RMN 59Co en champ interne pour l'étude de nanostructures de cobalt, analyse des interactions et anisotropies magnétiques

Pascal Scholzen

▶ **To cite this version:**

Pascal Scholzen. RMN 59Co en champ interne pour l'étude de nanostructures de cobalt, analyse des interactions et anisotropies magnétiques. Physique [physics]. Université Paris sciences et lettres, 2022. Français. NNT : 2022UPSLS087 . tel-03604413

HAL Id: tel-03604413
https://pastel.hal.science/tel-03604413

Submitted on 10 Mar 2022

HAL is a multi-disciplinary open access archive for the deposit and dissemination of scientific research documents, whether they are published or not. The documents may come from teaching and research institutions in France or abroad, or from public or private research centers.

L'archive ouverte pluridisciplinaire **HAL**, est destinée au dépôt et à la diffusion de documents scientifiques de niveau recherche, publiés ou non, émanant des établissements d'enseignement et de recherche français ou étrangers, des laboratoires publics ou privés.

PSL UNIVERSITÉ PARIS

THÈSE DE DOCTORAT
DE L'UNIVERSITÉ PSL

Préparée à l'Ecole Supérieure de Physique et de Chimie Industrielles de la ville de Paris (ESPCI Paris)

Internal field ^{59}Co NMR for the study of cobalt nanostructures, analysis of magnetic interactions and anisotropies

RMN ^{59}Co en champ interne pour l'étude de nanostructures de cobalt, analyse des interactions et anisotropies magnétiques

Soutenue par
Pascal SCHOLZEN
Le 19 janvier 2022

Ecole doctorale n° 397
Physique et Chimie des Matériaux

Spécialité
Chimie théorique, physique, analytique

Composition du jury:

Bradley, CHMELKA Professor University of California, Santa Barbara	*Président du jury*
Laurent, BINET Maître de conférences Chimie ParisTech	*Rapporteur*
Laurent, Le POLLES Maître de conférences Ecole nationale supérieure de Rennes	*Rapporteur*
Kai, LIU Professor Georgetown University	*Examinateur*
Sabine, WURMEHL Dr., Head of Department Leibniz-Institut for Solid State and Materials Research Dresden	*Examinatrice*
Jean-Baptiste, d'ESPINOSE de LACAILLERIE Professor ESPCI Paris	*Directeur de thèse*

ESPCI PARIS | PSL

Acknowledgements

First of all, I would like to thank all the jury members for having evaluated this PhD thesis and the interesting discussion after my PhD presentation. Especially I want to thank the two reviewers, Laurent Binet and Laurent Le Pollès, for their time investment and their feedback on the manuscript. I am also grateful to the examinators, Kai Liu and Sabine Wurmehl, and in particular to Bradley Chmelka who accepted to be the president of this jury.

My PhD thesis has been performed inside the SIMM (Sciences et Ingénierie de la Matière Molle) laboratory at the ESPCI in Paris. I would like to the thank its two directors during my time there, Christian Frétigny and Etienne Barthel, for welcoming me in the laboratory.

I am extremely grateful to my supervisor, Jean-Baptiste d'Espinose, who gave me the opportunity to do my PhD project with him on this interesting subject. First of all, for always being available when needed (despite having a very busy schedule) to answer questions about my PhD subject, but also to assist with the preparation of presentations, abstracts and journal articles. During the three years and more of my PhD, I learned a lot about NMR, other scientific topics, and the world of research in general. It was a pleasure for me to have such a pedagogic supervisor.

Even though not being my supervisor officially, a person that mentored me a lot during my PhD was Guillaume Lang. I must thank him for his help with performing the NMR experiments at low temperatures and providing the necessary set-up, but also for rich discussions and useful advice regarding NMR and magnetism.

I would also like to thank Andrey Andreev, who introduced me to the NMR technique during my master's internship and motivated me to apply for this PhD project. Even during my PhD thesis, he still gave me valuable advice.

Now, I would like to appreciate different people in the SIMM laboratory that contributed to the work of this PhD thesis. First of all, Ilya Iakovlev for his help with the NMR experiments and

fruitful exchanges on different occasions throughout our PhDs. Bruno Bresson for performing SEM measurements on different samples. Artem Kovalenko for the help with some experiments on Co NPs and rich discussions about this project. Finally, “my” intern Isaac Chin, who performed a big part of the ^{59}Co IF NMR experiments presented in the chapter about CoC composite materials.

This PhD thesis would not have been possible without the help of various collaborators, who provided me with samples for the different projects: Alberto Quintana and the whole team of Kai Liu at Georgetown University, Alexandre Sodreau, Arthur Moisset, Marc Petit and Christophe Petit from Sorbonne University, Gao-Feng Han and Jong-Beom Baek from UNIST South-Korea, and Dominique Larcher from LRCS Amiens.

There are plenty of people in the SIMM lab that I would like to acknowledge for their support and help on different levels. First of all, my different office mates over the course of the years. Starting with the “thesarium” where Sandrine helped me to get integrated in the lab life. In H203: Anne-Charlotte, Gaëlle, Helen and Yinjun from the “first generation”, and later Lola, Lucile (who both supported me for almost two and a half years! :D), Aaliyah, Caroline and Gabriel. Thank you for providing a good mood and motivation at work, despite the heat, the cold and the construction noise in the office. Especially during the periods of lockdown/curfew, this helped me a lot! In addition, there are many other SIMM lab members that allowed me to spend an amazing time in the lab, during lunch breaks, afterwork drinks, lab weekends, beer tasting events… I’d like to cite some of them in particular: Mehdi (frangin and best roommate), Miléna, Xavier (#TeamBelgium), Valentine, Pierre, Victoria (for giving me a home when I did not have an apartment), Gaétan (for always being motivated to get some drinks when others were lazy), Anusree and many more!

Finally, I would also like to thank my friends outside from the lab that made me enjoy my time here in Paris and supported me during difficult times! In addition thanks to everybody would deserves to be mentioned on this page but unfortunately has been forgotten by my side.

Zum Abschluss möchte ich noch meiner Familie danken, meinen Eltern, meinem Bruder und meinen Schwestern! Viel Dank für eure Unterstützung während meiner Doktorarbeit, aber auch auf meinem Weg dahin, ohne euch wäre das nicht möglich gewesen! Ich habe immer vollen Rückhalt erhalten, welchen Weg auch immer ich einschlagen wollte.

Table of content

Chapter 5: Magnetic structure and internal field nuclear magnetic resonance of cobalt nanowires 104

Chapter 6: ^{59}Co IF NMR study of assemblies of closely packed Co nanoparticles 132

List of Symbols and abbreviations

B	Magnetic induction or magnetic field
B_{dem}	Demagnetizing field
bcc	Body-centered cubic
B_{HF}	Hyperfine field
B_{int}	Internal magnetic field acting on a nucleus
CHG	Carbon hydrogasification
E_a	Magnetocrystalline anisotropy energy
η	Enhancement factor
EtOH	Ethanol
fcc	face-centered cubic
FID	Free-induction decay
FT	Fourier transform(ation)
γ	Gyromagnetic ratio
GC	Gas chromatography
FMR	Ferromagnetic resonance
FWHM	Full width at half maximum
H	Magnetization field
hcp	hexagonal close-packed
IF	Internal field

k_B	Boltzmann constant ($1.38 * 10^{-23} \frac{J}{K}$)
λ_m	Molecular field parameter/ Hyperfine interaction constant
M	Magnetization
μ_{dip}	Magnetic dipole moment
m.d.	multi-domain
N_d	Form factor/ demagnetizing factor
NMR	Nuclear Magnetic Resonance
(N)NN	(Next) nearest neighbor
NP	Nanoparticle
NQR	Nuclear quadrupolar resonance
OAm	Oleylamine
ω	(IF NMR) resonance frequency
Q(-factor)	Quality factor of a circuit
rf	radiofrequency
s.d.	single-domain
SEM	Scanning electron microscope/ microscopy
T_1	spin-lattice (longitudinal) relaxation time
T_2	spin-spin (transverse) relaxation time
T_{amb}	Ambient temperature
T_B	Blocking temperature
t_p	Pulse length
τ	Spin-echo interpulse delay
τ_m	Experimental measurement time
τ_N, τ_B	Néel, Brown relaxation time
t_{dead}	Electronic dead time of the probe
(HR) TEM	(High-resolution) transmission electron microscope/ microscopy
THF	Tetrahydrofuran
T_{irr}	Irreversibility temperature of ZFC/FC magnetometry
$[XCo(PPh_3)_3]$	Halogen-Tris(Triphenylphosphine) Cobalt(I)
XRD	X-ray diffraction
ZFC/FC	Zero-field-cooling/field-cooling

General introduction and context of the study

General introduction and context of the study

Cobalt containing materials and especially cobalt nanostructures are already commonly used or show great potential in many applications of the modern society. They can be designed to have various interesting properties, which makes them useful in different domains. Their applications include catalysis of different reactions [1]–[3], ultra-high-density recording[4], random access memories[5], medicine[6] and energy storage[7], just to name a few. As function of the application, different properties are targeted, meaning that the materials come in various shapes and crystalline structures. In the case of catalysis for example, a high Co surface should be available to the reactant and the material should contain small cobalt nanoparticles with a high surface-to-volume ratio. In addition, the efficiency of the catalytic reaction often depends on the crystalline structure of the Co particles. In random access memories, on the other hand, specific magnetic properties of the structures are targeted. For this type of application, a large variety of structures are considered: 1D or 2D structures of Co, pure or alloyed [5], or organized in multilayers[8] with different elemental composition.

As the optimization of different sample properties is necessary in order to obtain the best result based on the wanted application, several analytical techniques are used. The most common ones are X-ray diffraction when analyzing the crystalline structure, transmission electron microscopy in order to determine the size of Co nanostructures, magnetic hysteresis measurements to quantify the magnetic properties, but also many others. A powerful technique that is often overlooked is ^{59}Co internal field (IF) NMR, also called ferromagnetic NMR (FNR). In contrast to classical NMR techniques, it requires no applied constant external magnetic field as the internal field present in ferromagnetic compounds suffices to polarize the nuclear spins. As a result, the resonance frequency of the nuclei is directly related to the intensity of this internal field. This internal field depends on the Co crystalline structure and on the presence of foreign atoms in the Co proximity, but also on the magnetic structure of a material. ^{59}Co IF NMR therefore allows the simultaneously study of these properties, which is a big advantage over other analytical techniques. Taking into account the advantages and disadvantages of ^{59}Co IF NMR compared to other techniques, the results obtained by ^{59}Co IF NMR in the upcoming work are always compared to the ones of different techniques.

Despite being quite unknown, even in the NMR community, ^{59}Co IF NMR is not a new technique and it has been used for over 60 years now. While in recent years mainly catalysts and multilayer systems containing Co have been analyzed, in this work its area of application is extended by testing only rarely (or not at all) studied systems and using novel approaches. Overall, different geometries are explored: bulk composite systems, nanowires and nanoparticles.

A first system of interest are Co-C composite structures produced by ball milling during the carbon hydrogasification reaction with Co as catalyst. Using this process, lower value energy sources like coke,

coal or even waste materials can be transformed into methane, which is a valuable energy carrier in many applications. A remarkably strong carbon hydrogasification reaction rate is observed when using a ball milling process, much higher than the one of classical reaction types, using fixed-bed reactors for example. Using ^{59}Co IF NMR, the structural evolution of the cobalt catalyst with ongoing milling is analyzed and compared to the corresponding methane production rate. The aim is a better understanding of the reaction mechanisms happening during the carbon hydrogasification, which will also give information about the reason of the extremely high reaction rate obtained when using the mechanochemical process. Finally, this study also has a general interest, as no detailed study of C-rich Co-C composites by ^{59}Co IF NMR exists in the literature so far.

Secondly, systems of Co nanowires deposited into porous membranes are studied. Such systems are not only of interest to study fundamental questions about magnetism in anisotropic nanomaterials, but also because of their potential use in electromagnetic devices. In these systems, it is important to understand the influence of the deposition conditions on the Co crystalline structure inside the wires and how this influences their magnetic structure. In particular, the orientation of the magnetic domains and the structure and dynamics of the corresponding domain walls need to be characterized. Similar systems have already been studied in depth using different methods in the past, including ^{59}Co IF NMR [9]. However, in the current thesis we propose a new approach, based on the variation of the orientation of the *rf* field with respect to the wire axis. Besides gaining information on the crystalline wire structure, the goal of this thesis is therefore to use and exemplify this new approach in order to gain information on the magnetic structure and orientation.

The final object of this thesis are assemblies of close-packed cobalt nanoparticles. Co nanoparticles can be of interest in several domains of application, like catalysis and medicine, but the main motivation of this thesis is their occurrence in energy storage devices, in CoO/Li conversion reaction battery anode materials to be more precise [10], [11]. In these materials, CoO particles are transformed into Co metal during the discharge, forming a network of Co nanoparticles inside a Li_2O matrix. The big advantage of conversion reaction anodes is their higher energy storage density compared to typically employed intercalation reaction batteries anodes. However, a problem of these anodes is their low storage capacity retention over several charge and discharge cycles and therefore they still need to be improved. ^{59}Co IF NMR allows to obtain sample-wide information about the crystalline structure of the formed Co nanoparticles, as well as about their size. Their size can be studied thanks to the ferromagnetic - superparamagnetic transition with increasing temperature at the so-called blocking-temperature of nanoparticles of ferromagnetic materials. As the blocking temperature is directly dependent on the particle size, the analysis of this transition using experiments at varying temperatures can be related to a particle size distribution inside the system. When analyzing anodes

of conversion reaction battery materials by ^{59}Co IF NMR, a significant increase of the blocking temperature is observed, which might be due to particle interactions. In order to validate this hypothesis, ^{59}Co IF NMR experiments are performed on controlled model systems composed of close-packed Co nanoparticles with varying particle size and interparticle distance. While isolated Co nanoparticles have already been studied using ^{59}Co IF NMR and other techniques [12], [13], the influence of particle interactions on the blocking temperature is still not always clear. Besides the characterization of particle interactions, the aim of this thesis is therefore to be able to analyze systems of close-packed nanoparticles more precisely in the future.

The structure of this manuscript is the following:

In **Chapter 1**, the theoretical principles of ^{59}Co IF NMR are recalled and the parameters influencing the internal field are illustrated. Explanations about the excitation mechanisms and the origin of the nuclear magnetic resonance should help to better understand the fundamentals of this technique and the differences compared to traditional NMR. Detailed expressions of the internal field acting of the nucleus, including explanations about nanoscale effects on the magnetic structure of a ferromagnetic material, are given to demonstrate the ^{59}Co IF NMR spectra interpretation.

In **Chapter 2**, a bibliographic overview of ^{59}Co IF NMR studies is presented. Results from pure cobalt materials and also from Co containing composites are shown. The aim of this part is not simply to give a historical background, but to provide the basis of the spectrum interpretations for the experiments in this thesis.

In **Chapter 3**, technical details about the ^{59}Co IF NMR setups and the data treatment procedures used in this thesis are presented. This should help the reader and future potential user of this technique to get a better insight into the different parts for the experimental procedures.

Finally, the results of the three different systems studied in this thesis (already described earlier) are presented in separate chapters:

- **Chapter 4**: Cobalt/ carbon materials produced by mechanical alloying
- **Chapter 5**: Electrodeposited cobalt nanowires
- **Chapter 6**: Assemblies of close-packed cobalt nanoparticles

[1] Y.-P. Pei et al., “High Alcohols Synthesis via Fischer–Tropsch Reaction at Cobalt Metal/Carbide Interface,” ACS Catal., vol. 5, no. 6, pp. 3620–3624, Jun. 2015, doi: 10.1021/acscatal.5b00791.

[2] L. A. Calderón, E. Chamorro, and J. F. Espinal, “Mechanisms for homogeneous and heterogeneous formation of methane during the carbon–hydrogen reaction over zigzag edge sites,” Carbon, vol. 102, pp. 390–402, Jun. 2016, doi: 10.1016/j.carbon.2016.02.052.

[3] F. Chen et al., “Selective cobalt nanoparticles for catalytic transfer hydrogenation of N-heteroarenes,” Chem. Sci., vol. 8, no. 9, pp. 6239–6246, 2017, doi: 10.1039/C7SC02062G.

[4] A. Fert and L. Piraux, “Magnetic nanowires,” J. Magn. Magn. Mater., vol. 200, no. 1–3, Art. no. 1–3, Aug. 1999, doi: 10.1016/S0304-8853(99)00375-3.

[5] S. S. P. Parkin, M. Hayashi, and L. Thomas, “Magnetic Domain-Wall Racetrack Memory,” Science, vol. 320, no. 5873, pp. 190–194, Apr. 2008, doi: 10.1126/science.1145799.

[6] R. Hergt, S. Dutz, R. Müller, and M. Zeisberger, “Magnetic particle hyperthermia: nanoparticle magnetism and materials development for cancer therapy,” J. Phys. Condens. Matter, vol. 18, no. 38, pp. S2919–S2934, Sep. 2006, doi: 10.1088/0953-8984/18/38/S26.

[7] Z. Yan et al., “Co 3 O 4 /Co nanoparticles enclosed graphitic carbon as anode material for high performance Li-ion batteries,” Chem. Eng. J., vol. 321, pp. 495–501, Aug. 2017, doi: 10.1016/j.cej.2017.03.146.

[8] R. Sbiaa, H. Meng, and S. N. Piramanayagam, “Materials with perpendicular magnetic anisotropy for magnetic random access memory,” Phys. Status Solidi RRL - Rapid Res. Lett., vol. 5, no. 12, Art. no. 12, Dec. 2011, doi: 10.1002/pssr.201105420.

[9] G. J. Strijkers, J. H. J. Dalderop, M. A. A. Broeksteeg, H. J. M. Swagten, and W. J. M. de Jonge, “Structure and magnetization of arrays of electrodeposited Co wires in anodic alumina,” J. Appl. Phys., vol. 86, no. 9, Art. no. 9, Nov. 1999, doi: 10.1063/1.371490.

[10] P. Poizot, S. Laruelle, S. Grugeon, L. Dupont, and J.-M. Tarascon, “Nano-sized transition-metal oxides as negative-electrode materials for lithium-ion batteries,” Nature, vol. 407, no. 6803, Art. no. 6803, Sep. 2000, doi: 10.1038/35035045.

[11] S.-H. Yu, S. H. Lee, D. J. Lee, Y.-E. Sung, and T. Hyeon, “Conversion Reaction-Based Oxide Nanomaterials for Lithium Ion Battery Anodes,” Small, vol. 12, no. 16, Art. no. 16, Apr. 2016, doi: 10.1002/smll.201502299.

[12] I. V. Yakovlev et al., “Superparamagnetic behaviour of metallic Co nanoparticles according to variable temperature magnetic resonance,” Phys. Chem. Chem. Phys., vol. 23, no. 4, Art. no. 4, 2021, doi: 10.1039/D0CP05963C.

[13] Y. Liu et al., “Sampling the structure and chemical order in assemblies of ferromagnetic nanoparticles by nuclear magnetic resonance,” Nat. Commun., vol. 7, no. 1, Art. no. 1, Sep. 2016, doi: 10.1038/ncomms11532.

Chapter 1: Theoretical introduction to IF NMR and nanomagnetism

This first chapter is dedicated to the description of the theoretical principles of nuclear magnetic resonance (NMR), internal field (IF) NMR in particular. In Section 1, the general principles of NMR are briefly introduced. In Section 2, more details about IF NMR and what distinguished this technique from classic NMR are given. This includes a description of the excitation mechanisms and an introduction to the so-called enhancement factor, both for the case of magnetic domains and domain walls. Using the Bloch equations for a coupled nucleus-electron system allows to determine an expression of the resonance frequency and give more details about the signal enhancement. As the IF NMR frequency depends on the magnitude of the internal field, the different terms influencing the internal field inside a Co nucleus are described in Section 3. Besides the Co crystalline structure and influence of nearest neighbor atoms, the sample shape also has an influence. Finally, Section 4 contains an overview about how the size of a nanometric structure can have an influences on its magnetic properties. This section includes discussions about the magnetic anisotropy energy, superparamagnetism and the formation of magnetic domains and domain walls. The information from the two latter sections is crucial for the interpretation of IF NMR spectra and to understand the full capacity of this technique.

Before going on, readers that are not familiar with the concepts of the magnetic induction (B), the magnetizing field (H) and magnetization (M), are invited to read the introduction to these terms in the Appendix.

Chapter 1: Theoretical introduction to IF NMR and nanomagnetism

1. Brief introduction to NMR

Before explaining the particularities of IF NMR, a general introduction to the principles of NMR will be given. This should help the general reader to better understand the terms used in the following.

During an NMR analysis, the chemical environment on a nucleus is probed via the resonance frequency of the nuclear spins, which are exposed to a magnetic field (an external field B_0 in case of classic NMR). For non-zero spin isotopes, the interaction between the nuclear spins and the magnetic field generates an equilibrium of the nuclear magnetization alongside the magnetic field. Without removing this external magnetic field, the nuclear spins can be deviated from this equilibrium by a magnetic radiofrequency (*rf*) pulse with a frequency equal (or close) to their resonance frequency. This resonance frequency (Ω_0) depends on the gyromagnetic ratio of the nucleus (γ_n, an intrinsic property of the nucleus) and the intensity of the magnetic field seen by the nucleus B_0:

$$\Omega_0 = \gamma_n B_0 \qquad (1.1)$$

This frequency is also called the Larmor frequency. Out of equilibrium after the pulse, the nuclear magnetization will start a precession around the magnetic field at a frequency equal to the Larmor frequency Ω_0, as shown in **Figure 1**. In classic NMR, the presence of electrons in the environment of a nucleus will slightly modify the magnetic field seen by the nucleus by creating a small local internal field (B_{int}) in response to B_0, which will have an influence on the resonance frequency. For dia- or paramagnetic materials, this difference is typically around $10^6 - 10^4$ times smaller than B_0, but allows to distinguish different environments of the atom.

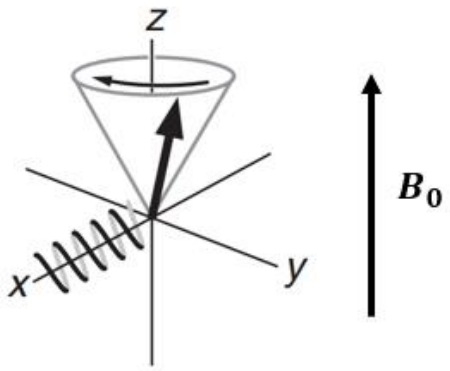

Figure 1: Precession of the nuclear magnetization vector around an external magnetic field (B_0) defined alongside the z-axis, when tilted from its equilibrium position. Alongside the x-axis a schema of the excitation/detection coil is represented. Modified from [1]

During NMR experiments the direction of B_0 is generally defined as the *z*-axis, as shown in **Figure 1**. The *rf* pulse for excitation is generated by a *rf* coil, in the plane perpendicular to the *z*-axis, in order to tilt the magnetization away from its equilibrium. The precession of the nuclear magnetization is detected by the same coil already used for the excitation.

2. Introduction to the particularities of IF NMR

In the upcoming section, a theoretical introduction to the principles of internal field (IF) NMR experiments in ferromagnets and the differences to classical NMR experiments is given. Most of the information described in the rest of this section was taken from books written by E.A Turov and M.P. Petrov : *Nuclear Magnetic Resonance in Ferro- and Antiferromagnets* (1972) [2] and by A.P. Guimarães *: Magnetism and Magnetic Resonance in Solids*, p.227 - 242 (1998)[3], where additional details can be found as well.

Letters in bold correspond to vectors.

2.1. Vector model

The general principles of IF NMR are similar to those of usual NMR on diamagnetic/paramagnetic materials, with the difference that the ferromagnetic material under consideration is not linear from the perspective of electromagnetism and that a significant internal magnetic field (B_{int}) is acting on the nuclei. In absence of a static (i.e., external) field B_0, it is solely this internal field that is responsible for the polarization of the nuclear spins and around which the nuclear magnetization precesses. A detailed expression of this internal field in ferromagnetic materials is presented in Section 3 of this chapter. A first consequence of this is the observation of peaks much broader than the ones observed for dia- and paramagnetic materials. The internal field is naturally inhomogeneous, resulting in a quite large distribution of the magnetic field seen by the probed nuclei. Secondly, this internal field is not static and will interact with the nuclear magnetization, as well as with the radio frequency (*rf*) field used to probe the resonance frequencies of the nuclear spins. This leads to interesting properties that are specific to IF NMR.

An additional point that needs to be mentioned is the orientation of the internal field and consequently of the nuclear magnetization with respect to *rf* excitation field. In the case of NMR with an applied

external field, the direction of the *rf* field is chosen to be perpendicular to this field, in order to have the most efficient excitation of the nuclear magnetic moment. In the case of IF NMR on the other hand, the orientation of the internal field potentially varies from one nucleus to the other and so does the orientation with respect to the *rf* field. This does not influence the resonance frequency but will decrease the excitation efficiency for most nuclei. The optimal excitation is therefore a mean value over the whole sample. The case of an oriented sample will be discussed in Chapter 5.

Domain excitation

A difference between classic and IF NMR can be observed during the excitation of the nuclear magnetization. In contrast to classic NMR, during IF NMR the nuclear magnetization is not directly excited and tilted away from its equilibrium by the *rf* pulse $\boldsymbol{B}_1 e^{i\omega t}$. Instead, the excitation is due to a time dependent transverse component of the internal field, arising from the *rf* pulse and therefore having the same frequency. The origin of this transverse component is shown in **Figure 2**. Initially, the nuclear magnetization $\boldsymbol{m}$ is aligned with the internal field $\boldsymbol{B}_{int}$, which itself is colinear with the electronic magnetization $\boldsymbol{M}$, but of opposite sign. $\boldsymbol{M}$ is aligned with the anisotropy field $\boldsymbol{B}_a$[1], and at equilibrium both define the quantification *z*-axis (left on **Figure 2**). As the transverse *rf* field is applied, $\boldsymbol{M}$ reorients along $\boldsymbol{B}_a + \boldsymbol{B}_1 e^{i\omega t}$ and an oscillating transverse component appears. This transverse component is small, but measurable, and depends on the strength of the magnetic anisotropy (~B_a) of the material. The frequency of the applied field is chosen close to the resonance of the nuclear magnetization and therefore far from (i.e., much lower than) the resonance frequency of the electronic magnetization. As a result, $\boldsymbol{M}$ can be considered to respond adiabatically to the *rf* field and oscillates with the same frequency. Consequently, an oscillating transverse component of the internal field $\boldsymbol{B}_{int}^{\perp}$ arises as well, which is responsible for the excitation of the nuclear spins and orders of magnitudes higher than the *rf* field. As shown in **Figure 2** for small deviations from the equilibrium position, the magnitude of $\boldsymbol{B}_{int}^{\perp}$ can be estimated via the deviation angle from the equilibrium position θ, defined by B_1/B_a. From this value we can determine the so-called enhancement factor (η), which is defined as the amplification of the excitation field seen by the nuclear magnetization:

$$\eta = \frac{B_{int}^{\perp}}{B_1} \approx \frac{B_{int}}{B_a} \tag{1.2}$$

[1] In a ferromagnetic material, there exist internal interactions between the magnetic moments that tend to align them in the same direction alongside a certain crystallographic axis (neglecting shape effect etc.), called easy axis of magnetization. These interactions can most simply be presented by an anisotropy field $\boldsymbol{B_a}$ oriented along this axis. The magnetic anisotropy energy E_a is function of the orientation between $\boldsymbol{B_a}$ and of the electron magnetization ($E_a = -\boldsymbol{B_a} \cdot \boldsymbol{M}$) and is minimum when the magnetization is oriented along the easy axis. For a stronger $\boldsymbol{B_a}$ it is therefore more difficult to deviate $\boldsymbol{M}$ from this easy axis.[2]

In cobalt magnetic domains, η is typically around 10-100. The higher the enhancement factor, the less power is needed for an optimal excitation of the nuclear spins, which gives an indication about the strength of the magnetic anisotropy of the material.[3] Reciprocally to the indirect excitation of the nuclear spins, the observed signal also does not come directly from the precession of the nuclear magnetization. Instead, it is the oscillation of the electronic magnetization, induced by a torque exerted by the precessing nuclear magnetization, that is observed. Besides a reduction in the power needed for the excitation, the enhancement factor thus also results in a sensitivity increase of the IF NMR. This simplifies the measurements but as a drawback, the amplitude of the observed signal does not depend directly on the number of nuclei in a certain environment, but also on the enhancement factor in that environment. The enhancement might vary inside a single sample and therefore needs to be taken into account when doing a quantitative analysis. [4]

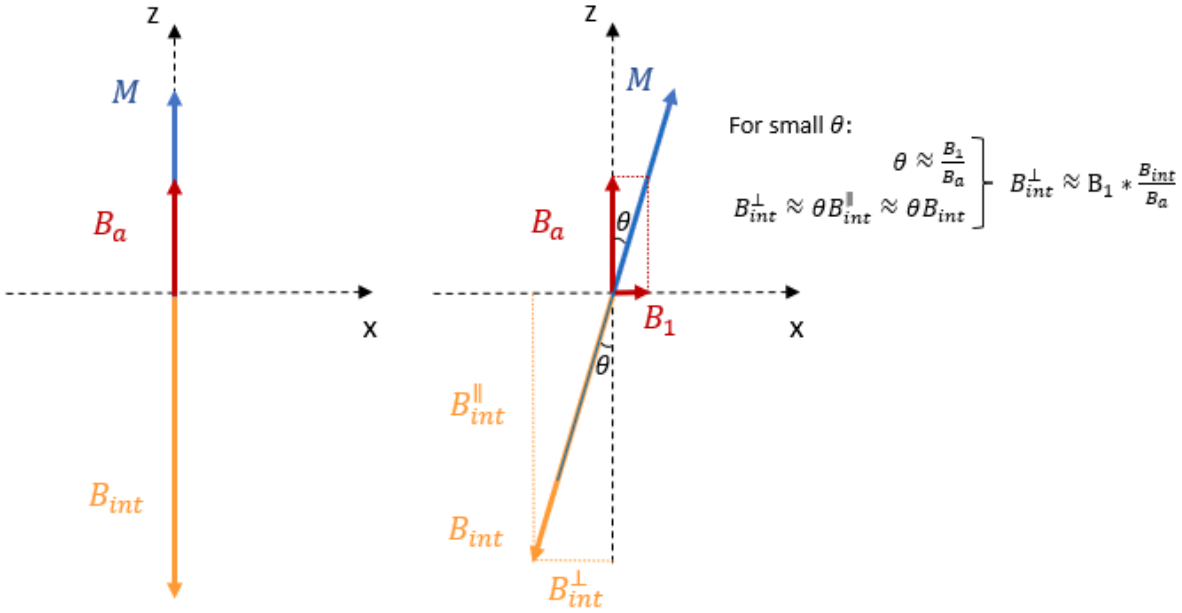

Figure 2: Description of the transverse component of the internal field in a ferromagnetic material under the influence of a *rf* field B_1 and in the absence of an external B_0 field. Modified from [2]

Domain wall excitation

The above description of the enhancement factor was about the case of magnetic domains. In reality, magnetic materials tend to be composed of not only a single magnetic domain, but to divide themselves into multiple domains, with so-called domain walls in between them. More information about the conditions of domain wall formation and their parameters can be found in the subsection 4.3. Within domain walls, an even more efficient enhancement effect than inside domains takes place. In the right of **Figure 3**, the response of a 180° domain wall to an external magnetic field parallel to

one of the domain directions is represented. The increase/decrease of the domain size with magnetization parallel/antiparallel to the external field causes a domain wall displacement. While under a static field this displacement is permanent, the application of an external *rf* field causes the wall to move back and forth due to the periodic change of direction of the external field. As illustrated in the right of **Figure 3**, this displacement corresponds to a rotation of the magnetic moments inside the domain wall, leading to an additional component of the magnetization ($\boldsymbol{\Delta M}$), and consequently also of $\boldsymbol{B}_{int}$ acting on the nuclei**,** in the direction of $\boldsymbol{B}_1$. Consequently, the part of $\boldsymbol{B}_{int}$ that is created alongside $\boldsymbol{B}_1$ is much bigger in the case of domain walls, than it is for simple domains, causing the η to take values from 1000 up to 10.000.[4], [5] As it can be seen, $\boldsymbol{\Delta M}$ and therefore also the enhancement are not constant and depends on the position inside the domain wall; it is maximum in the center and decreases towards the edges. [3]

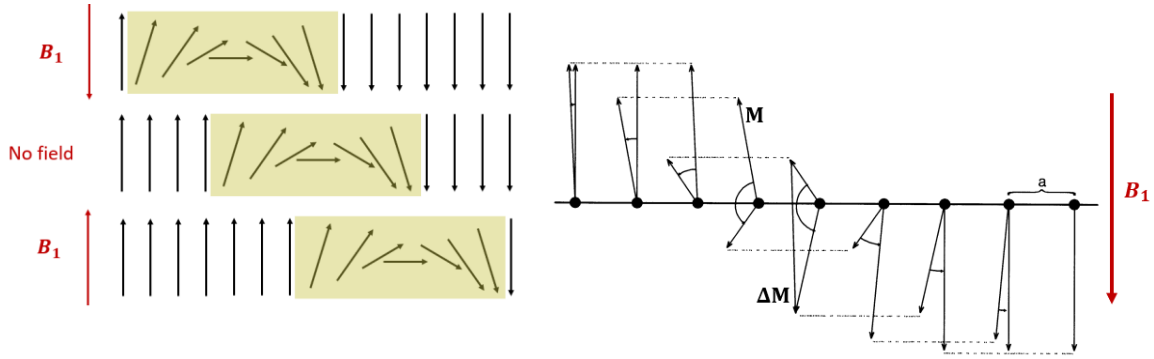

Figure 3: Left: Schematic representation of a 180° domain wall (light green background) and its displacement under the influence of an external magnetic field $\boldsymbol{B_1}$ (static or *rf*) in different direction. Right: Illustration of the rotation of the magnetic moments inside the domain (showing a local magnetization $\boldsymbol{M}$) and the resulting change of the local magnetization $\boldsymbol{\Delta M}$ (adapted from [3]). The domain walls illustrated here are Néel domain walls, but the mechanism is similar for different types of 180° walls (such as Bloch walls).

2.2. Resonance in a coupled nucleus – electron system

In the following, a theoretical introduction to the interactions inside a system of coupled nuclear and electronic magnetizations is given. Amongst other things, it allows determining the resonance frequencies of the nuclear and the electronic spin systems and introducing the enhancement factor in a different way.

Local magnetic fields & Bloch equations

In a simplified way, the total magnetic field acting on a nucleus, $\boldsymbol{b}$, during an NMR experiment can be approximated by:

$$\boldsymbol{b} = \boldsymbol{B}_0 + \boldsymbol{B}_1 e^{i\omega t} + \boldsymbol{B}_{int} \tag{1.3}$$

with $\boldsymbol{B}_0$ the external field, $\boldsymbol{B}_1$ the *rf* field of the excitation and $\boldsymbol{B}_{int}$ the internal field acting on the nucleus.

$\boldsymbol{B}_{int}$ will be discussed in more detail in the next section of this thesis, but for the moment it is approximated by the hyperfine field, namely the product of the magnetization of the electron system $\boldsymbol{M}$ and the molecular field parameter λ_m:

$$\boldsymbol{B}_{int} \sim \boldsymbol{B}_{hf} = \lambda_m \boldsymbol{M} \tag{1.4}$$

The magnetic response (precession) of the nuclear magnetization $\boldsymbol{m}$ to the fields acting on the nucleus (static and radiofrequency) can be treated linearly through the Bloch equation:

$$\frac{d\boldsymbol{m}}{dt} = \gamma_n \, \boldsymbol{m} \times \boldsymbol{b}(\boldsymbol{M}) + \boldsymbol{r} \tag{1.5}$$

with γ_n the gyromagnetic ratio and $\boldsymbol{r}$ the relaxation term of the nuclear spin system. From this, the nuclear Larmor precession frequency becomes:

$$\Omega_n = |-\gamma_n \boldsymbol{b}| \approx |-\gamma_n \boldsymbol{B_0}| \tag{1.6}$$

Usually, NMR experiments are performed on dia- and paramagnetic materials, where $\boldsymbol{M}$ is proportional to the applied external magnetic field via the local magnetic susceptibility χ. The internal magnetic field is therefore zero in absence of an external field. Even in presence of an external field, $\boldsymbol{B_{int}}$ is generally small compared to $\boldsymbol{B_0}$, justifying the simplification in (1.6). In ferromagnetic materials on the other hand, an internal field is also present when no external field is applied and it is non-negligible compared to $\boldsymbol{B_0}$ (if present). The simplification is therefore not valid for these materials.

As the nuclear and the electron spin systems are coupled, it is also important to define the magnetic field acting on the electron system $\boldsymbol{B}$, amongst other things dependent on the nuclear magnetization $\boldsymbol{m}$ via the molecular field parameter λ_m:

$$\boldsymbol{B} = \boldsymbol{B}_0 + \boldsymbol{B}_a + \boldsymbol{B}_1 e^{i\omega t} + \lambda_m \boldsymbol{m} \tag{1.7}$$

The dependence of the energy of an electronic magnetic moment with its orientation within the crystal is considered by an effective anisotropy field $\boldsymbol{B}_a$ which was already introduced in the preceding

section. This effective field also includes contributions due to the shape anisotropy of the particle. Similarly, the Bloch equation of the electron system writes as:

$$\frac{d\boldsymbol{M}}{dt} = \gamma_e \, \boldsymbol{M} \times \boldsymbol{B}(\boldsymbol{m}) + \boldsymbol{R} \tag{1.8}$$

with γ_e is the gyromagnetic ratio and $\boldsymbol{R}$ the relaxation term of the electron spin system. The two Bloch equations (1.5) and (1.8) represent the coupling between the electron and nuclear spin systems.

Linearization of Bloch equations

Setting the z-axis in the direction of the magnetizations at equilibrium, M_z and m_z at equilibrium are equal to the module of $\boldsymbol{M}$ and $\boldsymbol{m}$ respectively. The transverse components, defined as $\boldsymbol{M}_\pm = \boldsymbol{M}_x \pm \boldsymbol{M}_y$ and $\boldsymbol{m}_\pm = \boldsymbol{m}_x \pm \boldsymbol{m}_y$ are then equal to zero. During an NMR experiment, the spin systems are deviated from their equilibrium and the transverse magnetic fields become:

$$\boldsymbol{B}_\pm = \boldsymbol{B}_{1\pm} + \lambda_m \boldsymbol{m}_\pm \qquad\qquad \boldsymbol{b}_\pm = \boldsymbol{B}_{1\pm} + \lambda_m \boldsymbol{M}_\pm \tag{1.9}$$

By doing the assumption of small deviations away from the equilibrium configuration, the longitudinal terms are approximated to be equal to their equilibrium value ($M_z \cong M$, $m_z \cong m$), resulting in the magnetic fields along the *z*-axis:

$$B_z = B_0 + B_a + \lambda_m m \qquad\qquad b_z = B_0 + \lambda_m M \tag{1.10}$$

Linearizing the Bloch equations (1.5) and (1.8) with respect to the in-plane components of $\boldsymbol{M}$ and $\boldsymbol{m}$, one gets:

$$\frac{d\boldsymbol{m}_\pm}{dt} = \pm\gamma_n[-\boldsymbol{m}_\pm b_z - \boldsymbol{b}_\pm m_z] \qquad\qquad \frac{d\boldsymbol{M}_\pm}{dt} = \pm\gamma_e[-\boldsymbol{M}_\pm B_z - \boldsymbol{B}_\pm M_z] \tag{1.11}$$

neglecting the relaxation terms.

Under the assumption of a stationary regime (no relaxation), the transverse magnetizations are:

$$\boldsymbol{m}_\pm = \boldsymbol{m}_\pm(0)e^{i\omega t} \qquad\qquad \boldsymbol{M}_\pm = \boldsymbol{M}_\pm(0)e^{i\omega t} \tag{1.12}$$

Assuming that the excitation field is also solely in the transverse plane: $\boldsymbol{B}_1 = B_{1\pm}e^{i\omega t}$, (1.11) becomes:

$$\begin{aligned} \omega\, m_\pm &= \pm\gamma_n[-m_\pm(B_0 + \lambda_m M) - (B_{1\pm} + \lambda_m M_\pm)m\,] \\ \omega\, M_\pm &= \pm\gamma_e[-M_\pm(B_0 + B_a + \lambda_m m) - (B_{1\pm} + \lambda_m m_\pm)M\,] \end{aligned} \tag{1.13}$$

When neglecting the $B_{1\pm}$ terms, inserting B_{int} (as defined in (1.4)) and rearranging to a system of linear equations in $M_\pm$ and $m_\pm$:

$$\begin{aligned} -\gamma_n\lambda_m m M_\pm + [\pm\omega + \gamma_n(B_0 + B_{int})]m_\pm = 0 \\ -\gamma_e B_{int} m_\pm + [\pm\omega + \gamma_e(B_0 + B_a + \lambda_m m)]M_\pm = 0 \end{aligned} \quad (1.14)$$

In order to find the solutions of the system, its determinant must be equal to zero. The eigenvalues of the system give the normal modes of the coupled system (eigenfrequencies):

$$[\pm\omega + \gamma_e(B_0 + B_a + \lambda_m m)][\pm\omega + \gamma_n(B_0 + B_{int})] - \gamma_n\gamma_e\lambda_m m B_{int} = 0$$

$$\Rightarrow \quad \pm\omega^2 \pm \omega[\gamma_n(B_0 + B_{int}) + \gamma_e(B_0 + B_a + \lambda_m m)] + \gamma_n\gamma_e(B_0 + B_a + \lambda_m m)(B_0 + B_{int}) - \gamma_n\gamma_e\lambda_m m B_{int} = 0 \quad (1.15)$$

Resonance frequencies

The four solutions of this system form two pairs which differ in sign only and the two solutions with physical meaning correspond to the normal modes of ω. The first solution of this equation corresponds to the resonance frequency of the nuclear system, the NMR frequency, which can be simplified considering $m \ll M$ and the case of no external applied field (B_0 = 0):

$$\begin{aligned} \Omega_n = |\omega_1| &= \left|-\gamma_n\left[B_0 + B_{int}\left(1 - \eta\frac{m}{M}\right)\right]\right| \\ &= \left|-\gamma_n B_{int}\left(1 - \eta\frac{m}{M}\right)\right| \approx |-\gamma_n B_{int}| = |-\gamma_n\lambda_m M| \end{aligned} \quad (1.16)$$

with η the already previously defined enhancement factor, which under the influence of a static external field becomes:

$$\eta = \frac{B_{int}}{B_0 + B_a} \quad (1.17)$$

When looking at equation (1.16) without an external field, it can be seen that the IF NMR frequency Ω_n can be an easy way to measure B_{int}, when knowing the value of γ_n.[6] The term $\eta\frac{m}{M}$ becomes small compared to 1, due to a negligible nuclear magnetization with respect to the electron magnetization. In general, it is only at very low temperatures that this condition is not verified anymore (m being proportional to 1/T, while M saturates) and that a significant effect on the frequency of the term $\left(1 - \eta\frac{m}{M}\right)$ can be observed.[7]

The second solution of equation (1.15) gives the resonance of the electron system, represented here for the situations with and without an external applied field, as well as considering $m \ll M$:

$$\Omega_e = |\omega_2| = \left|-\gamma_e(B_0 + B_a)\left(1 + \eta\frac{m}{M}\right)\right|$$
$$= \left|-\gamma_e B_a\left(1 + \eta\frac{m}{M}\right)\right| \approx |-\gamma_e B_a| = |-\gamma_e \lambda_m m| \qquad (1.18)$$

This frequency is of interest during ferromagnetic resonance (FMR) experiments. Due to the fact that $\gamma_e \gg \gamma_n$ and $M \gg m$, the electron resonance frequency is much bigger than the nuclear one ($\Omega_e \gg \Omega_n$). To give an idea, without the application of an external field in ferromagnetic cobalt, the resonance frequency of ^{59}Co nuclear systems (IF NMR) is around 210 - 230 MHz, while the resonance frequency of the electron system (FMR) is around 4-10 GHz.

Transverse magnetizations and susceptibilities

In order to estimate the signal intensity observed during an NMR experiment, the transverse magnetization of the nuclear system, as well as of the electron system, are determined. $M_\pm$ is determined from the linear expression of the Bloch equation of the electron system, still including $B_{1\pm}$ (bottom equation in (1.13)). When rearranging the equation without the application of an external field ($B_0 = 0$), one finds:

$$M_\pm = \frac{\gamma_e(B_{int}m_\pm + B_{1\pm}M)}{\pm\omega + \gamma_e(B_a + \lambda_m m)} \approx \frac{B_{int}m_\pm + B_{1\pm}M}{B_a} \qquad (1.19)$$

neglecting $\lambda_m m$ compared to B_a. In addition, as in the upcoming descriptions we are only interested in ω in the frequency range of the nuclear and not of the electron resonance, the frequency term ω can also be neglected compared to $\gamma_e B_a \approx \Omega_e$, the electron resonance frequency. An expression of the transverse nuclear magnetization $m_\pm$ can be found by substituting the expression of $M_\pm$ in Eq.(1.19) into the linear Bloch equation of the nuclear system (top equation in (1.13)). After simplifications one obtains:

$$m_\pm = (1+\eta)\frac{\gamma_n B_{1\pm}m}{\pm\omega + \Omega_n} => m_\pm = -(1+\eta)\frac{\gamma_n B_{1\pm}m}{\omega - \Omega_n} \qquad (1.20)$$

Only the solution with the negative sign before ω is chosen, in order to obtain a resonance phenomenon (maximum amplitude of $m_\pm$ for $\omega = \Omega_n$), resulting in a transverse susceptibility of the nuclear magnetization of the form:

$$\chi_m^{\pm} = \mu_0 \frac{m_{\pm}}{B_{1\pm}} = -\mu_0(1+\eta)\frac{\gamma_n m}{(\omega - \Omega_n)} \quad (1.21)$$

with μ_0 the magnetic susceptibility of vacuum.

To compare this expression to the one of a nonmagnetic (diamagnetic) material, let us consider the case of an additional external field B_0. In that case, after inserting the expression of the static nuclear susceptibility ($\chi_n = \mu_0 \frac{m}{B_0}$) and of the static nuclear magnetic resonance ($\omega_0 = \gamma_n B_0$), we find:

$$\chi_m^{\pm} = -(1+\eta)\frac{\mu_0 m * \gamma_n}{(\omega - \Omega_n)}\frac{B_0}{B_0} = -(1+\eta)\frac{\omega_0}{(\omega - \Omega_n)}\chi_n \quad (1.22)$$

From this expression, it can be seen that the transverse susceptibility in a ferromagnetic material is enhanced by a factor $(1+\eta) \sim \eta$ compared to a nonmagnetic one. Due to the typically large value of η, less power is therefore generally needed for an optimal excitation in the case of an IF NMR experiment compared to NMR in a dia-/ paramagnetic material. In addition, the resonance of the nuclear system is confirmed as the susceptibility is maximum for $\omega = \Omega_n$.

2.3. Conclusion

The main information that should be retained from this first part are first of all that when doing NMR analysis on ferromagnetic materials, no external field is needed. Instead, it is the internal magnetic field ($\boldsymbol{B}_{int}$) present inside the materials that lifts the nuclear spin level degeneracy, hence the IF NMR name of the technique. As a result, the resonance frequency can be estimated by:

$$\Omega_n = |-\gamma_n B_{int}|$$

An additional characteristic of this technique is the indirect character of the excitation and of the detection, leading to an enhancement of both phenomena, defined by the enhancement factor η. This enhancement is function of the sample structure and especially differs between domains and domain-walls, due to a different excitation mechanism in both cases. Consequently, the distribution of the enhancement factor needs to be considered when doing a quantitative analysis of a sample. This allows to obtain additional information about the magnetic structure of a sample.

3. Internal field inside a ferromagnet

As presented in the previous Section 2, the resonance frequency in IF NMR is crucially dependent on the internal field acting on the nucleus. As a result, knowing the parameters and samples characteristics influencing it are of great importance to understand the obtained results. One of the first theoretical estimations of the internal field inside ferromagnets was published by Marshall in 1958, taking into account contributions from both, core and conduction electrons.[8] His estimations were later refined, notably by Watson and Freeman [9]. These theoretical estimations help to predict the value of the magnetic resonance of a nucleus and to understand which factors influence it. Let us remind that here, as before, bold symbols correspond to vectors.

The overall magnetic field $\boldsymbol{B_{tot}}$ acting on a ferromagnetic nucleus can be divided into different terms [4]:

$$\boldsymbol{B_{tot}} = \boldsymbol{B_0} + \boldsymbol{B_{int}} = \boldsymbol{B_{ext}} + \boldsymbol{B_{dip}} + \boldsymbol{B_{HF}} \tag{1.23}$$

$\boldsymbol{B}_0$ corresponds to an applied external field and $\boldsymbol{B_{int}}$ to the field originating from internal contributions.

$\boldsymbol{B}_{dip}$ corresponds to all dipolar fields resulting from magnetic dipolar moments of electron spins and orbital moments in the sample outside of the ion radius. It can be divided into three terms:

$$\boldsymbol{B}_{dip} = \boldsymbol{B}_{dem} + \boldsymbol{B}_{Lor} + \boldsymbol{B}_{Loc} \tag{1.24}$$

$\boldsymbol{B}_{dem}$ represents the demagnetizing field and is therefore dependent on the macroscopic magnetic structure of the sample. Depending on its size and shape, a particle inside the sample can be composed of a single or of multiple magnetic domains, with the formation of multiple domains reducing the demagnetizing field. It can be defined by (in CGS units)

$$\boldsymbol{B}_{dem} = 4\pi N_d \boldsymbol{M}_e \tag{1.25}$$

with $\boldsymbol{M}_e$ the total electronic magnetization of a continuous part of the sample and N_d the form factor, which varies between 0 and 1 as function of the particle shape. For example, in the case of a sphere, N_d is equal to 1/3, in the case of an infinite cylinder $N_d = 0$ along the axis and 1/2 in the directions perpendicular to the axis. [10] $\boldsymbol{B}_{Lor}$ is the classic isotropic Lorentz cavity field: $\frac{4\pi}{3}\boldsymbol{M}_e$. It has to be noted that for spherical samples, for which $N_d = \frac{1}{3}$, $\boldsymbol{B}_{Lor}$ and $\boldsymbol{B}_{dem}$ fully cancel each other out. $\boldsymbol{B}_{loc}$ is the small residue of the Lorentz field, which comes from all the other moments than the central moments of the Lorentz sphere. It is thus strictly zero for isotropic structures and, by symmetry, near-zero for

cubic crystals. It is therefore only significant for noncubic Cobalt. Even when its non-zero, this term is generally much smaller than (~0.1 % of $\boldsymbol{B}_{lor}$) and is therefore can often be neglected. [2], [4], [8]

The hyperfine field $\boldsymbol{B}_{HF}$ arises from the electron spins and orbital moments within the ion radius. As already stated in order to write equation (1.3), as a first approximation it is often defined as:

$$\boldsymbol{B}_{HF} = \lambda_m * \boldsymbol{M}, \tag{1.26}$$

with λ_m being the molecular field parameter (also called hyperfine interaction constant) and $\boldsymbol{M}$ the local magnetization, equal to the electron magnetic moment of the atom containing the nucleus to be analyzed. λ_m is generally of negative sign due to the fact that the hyperfine field is often of opposite sign to the magnetic moment.[2] When going more into detail, the hyperfine field can be subdivided into three components [4]:

$$\boldsymbol{B}_{HF} = \boldsymbol{B}_{HF,dip} + \boldsymbol{B}_{HF,orb} + \boldsymbol{B}_{HF,con} \tag{1.27}$$

$\boldsymbol{B}_{HF,dip}$ is due to the dipolar field from electron spins outside of the nucleus volume and $\boldsymbol{B}_{HF,orb}$ is the so-called orbital field and arises from a not fully quenched orbital moment. Both these terms contain an anisotropic component, in contrast to the upcoming term. $\boldsymbol{B}_{HF,con}$ is the Fermi contact field, which comes from the spin polarization of the electrons (mainly s-electrons) within the nucleus volume and can be divided further into different contributions. The first contribution to $\boldsymbol{B}_{HF,con}$ comes the polarization of the inner shell *s* electrons ($\boldsymbol{B}_{HF,core}$) due to interactions with magnetic moments of the atom itself (this includes the core polarization due to interactions with the d electrons). Two different contributions arise from of the polarization of *s* conduction electrons, polarized due to the magnetic moment of the atom itself ($\boldsymbol{B}_{HF,ce}$) or polarized due to the magnetic moment of the nearest neighbors (NN) surrounding the atom (transferred field $\boldsymbol{B}_{tran}$). This last contribution is strongly dependent on the NN structure surrounding the atom in question and therefore responsible for a variation of the local field inside alloys or for atoms at interfaces. Overall, $\boldsymbol{B}_{HF,con}$ is the largest contribution to the $\boldsymbol{B}_{HF}$ in ferromagnetic materials. In Co it is about 20 T (or 200 kG in CGS units), which corresponds to around 95% of the total magnetic field acting on the nucleus in case no external magnetic field is applied. In addition, it is generally antiparallel to the local magnetic moment of and therefore responsible for the negative sign of λ_m in equation (1.26).[4] It is noteworthy that Marshall [8] and Watson and Freeman [9] developed more detailed expressions for the different terms represented here, but such details are not necessary to the interpretation of ^{59}Co IF NMR spectra and they will not be discussed here.

To sum up for further discussions, the different factors influencing the internal field are:

- The nature of the atom to be analyzed: Obviously, the element that is analyzed, with its electron cloud, has a major influence on the internal field acting on the nucleus.
- The symmetry of the crystalline structure: Some terms of the hyperfine field (namely $\boldsymbol{B}_{HF,dip}$ and parts of $\boldsymbol{B}_{HF,orb}$) and $\boldsymbol{B}_{loc}$ are anisotropic. As a result, the internal field of an anisotropic structure is also anisotropic and depends on the orientation of the magnetization with respect to the crystallographic axes. In the IF NMR spectrum, this results in a much broader line for very anisotropic structures (*hcp* cobalt for example) than for higher symmetry structures (like *fcc* cobalt).
- The nearest neighbor structure: Mostly via $\boldsymbol{B}_{tran}$, the NN structure surrounding the atom to be analyzed influences the internal field seen by the nucleus. The study of the internal field via IF NMR therefore allows the study of nuclei at interfaces or inside different types of solid solutions and alloys. The variation of the resonance frequency of different crystalline configurations of the same element is also due to the difference of their respective NN structure.
- Sample shape: The demagnetizing field depends on the macroscopic magnetic structure and the presence and shape of magnetic domains. As a result, information about the sample shape and size can be obtained.

The above considerations lead to the idea that the study of the internal field inside a ferromagnetic material via IF NMR can provide information on a lot of different aspects of this material. Precise theoretical calculations of the internal field and the resulting peak positions inside the spectrum are however difficult, especially when the structure is more complex than a pure bulk structure. Therefore, the spectrum attribution in IF NMR, as usual in NMR, is often done empirically by comparison with reference materials. Nevertheless, the knowledge of the different terms influencing the internal field are crucial when analyzing and understanding a spectra, especially when studying systems that have not been studied in depth before. In Chapter 2, a bibliographic review of ^{59}Co IF NMR of cobalt containing samples is presented, with the focus on systems that are close to the ones studied in this work. This overview is important in order to study and understand the spectra analyzed during this work.

4. Size effect on ferromagnetism

As described in the previous paragraph, during IF NMR experiments the magnetic field acting on the nucleus is the internal field arising from the electron system, or more precisely from the ordered electronic magnetic moment of a sample. As a result, it is crucial to understand the factors that can influence the magnetic structure and behavior of a sample. In the following, an overview of two phenomena that lead to different magnetic behaviors as function of the size of a ferromagnetic structure is presented, namely the superparamagnetism and the magnetic domain formation. Understanding them not only allows a better spectrum interpretation, but also to gain more information on magnetic structures from IF NMR experiments. Before discussing the superparamagnetism and magnetic domains in detail, the magnetic anisotropy energy is examined in more detail, which help to better understand both.

4.1. Magnetic anisotropy energy

In order to understand the phenomenon of superparamagnetism, but also some other phenomena related to multi-domain formation, it is first important to describe the concept of the magnetic anisotropy energy. In a magnetically ordered material, the magnetic anisotropy energy defines the magnetic easy and hard axes of magnetization.[11] There are several types of anisotropies that contribute to the overall magnetic anisotropy energy of magnetic nanoparticles, namely: magnetocrystalline anisotropy, shape anisotropy, surface anisotropy and strain anisotropy for isolated particles, as well as dipole-dipole and exchange interactions for interacting particles. The following explications can be understood the best when considering single-domain particles but are also valid for multi-domain structures. More detailed descriptions of the different types of anisotropy can be found in [12], which is also the main reference for this part.

Magnetocrystalline anisotropy

The magnetocrystalline anisotropy originates from the spin-orbit coupling inside a crystalline lattice and results in preferential alignment of the magnetic moments alongside certain crystallographic directions. The direction and strength of this anisotropy is naturally function of the crystalline structure and most of them can be categorized in two: uniaxial and cubic anisotropies. In the case of cobalt, *hcp* Co corresponds to a uniaxial anisotropy with the *c*-axis the unique, strong easy axis, while *fcc* Co corresponds to a cubic anisotropy with three non-energetically equivalent easy axes. The difference

between the easy axis configuration of an *hcp* and an *fcc* crystalline structure can be observed when looking at the magnetization curves alongside the different directions for *hcp* Co and *fcc* Ni, shown in the left of **Figure 4**. The easy axis configuration of *fcc* Co is the same as the one of *fcc* Ni, even though with different absolute magnetization values. Mathematically the uniaxial magnetocrystalline anisotropy energy (E_a) of a particle with a volume V can be expanded in the form:

$$E_a = V * (K_{c1} sin^2(\theta) + K_{c2} \sin^4(\theta) + \cdots) \quad (1.28)$$

with θ the angle between the magnetic moment and the easy axis and K_{c1} and K_{c2} the 1st and 2nd uniaxial magnetocrystalline anisotropy constants. The terms above the 2nd term are often neglected, and sometimes even the 2nd term itself [12], resulting in a magnetic anisotropy energy as function of θ as shown for a *hcp* structure in the top right **Figure 4**. The energy barrier between the directions parallel and antiparallel to the easy axis is equal to $K_{c1}V$. For a cubic anisotropy, the mathematical description of the anisotropy energy is less straightforward due to the multiplicity of easy axes.

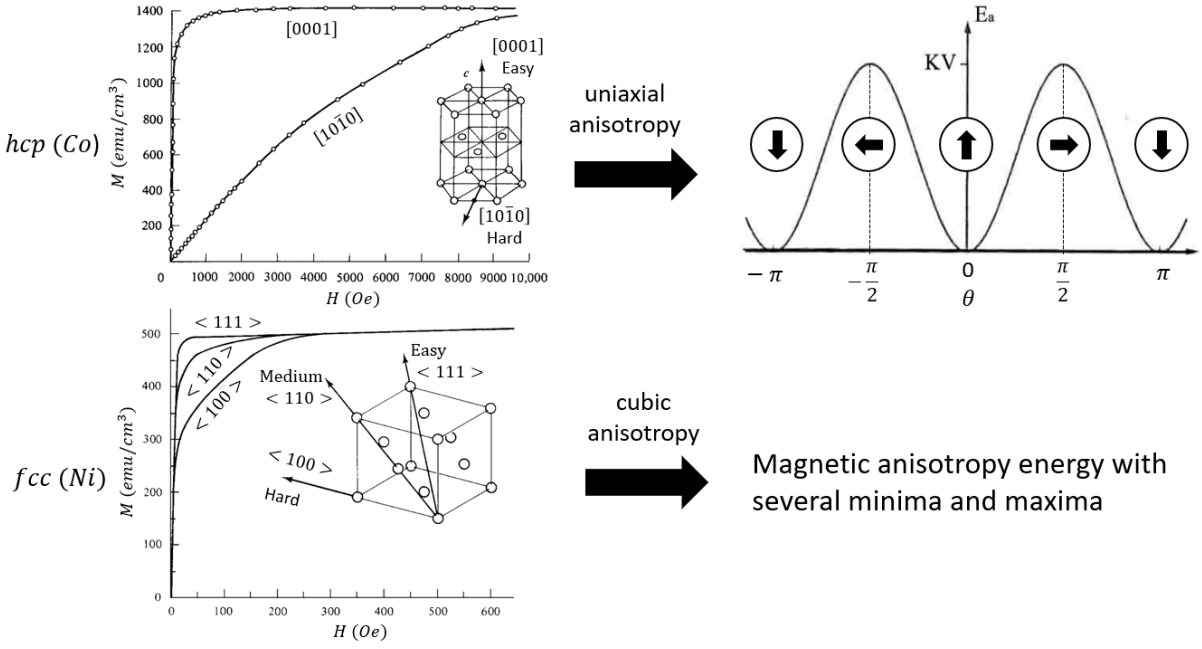

Figure 4: Left: Magnetization curves of *hcp* Co and *fcc* Ni alongside the different easy and hard axes of the structure. (adapted from [13]). Right: Evolution of the magnetic anisotropy energy for a uniaxial anisotropy as function of θ, the angle between the magnetic moment and the easy axis, adapted from [14].

Shape, surface and strain anisotropy

The shape anisotropy, also referred to as magnetostatic anisotropy, finds its origin in an anisotropic demagnetizing energy (also called magnetostatic energy). It is therefore zero for spherical particles, but strong for films and wires with a high aspect ratio, reaching values of the same order of magnitude and even above the ones of the magnetocrystalline anisotropy for those geometries. For example, in nanowires of high aspect ratios, the easy axis of magnetization is along the wire axis as the demagnetizing field and energy would be much higher in any other direction.[15], [16]

The surface anisotropy occurs from the surface atoms, which have a lower symmetry due to the missing of neighboring atoms. For nanoparticles, its relative importance increases with decreasing diameter and can lead to various spin structures depending on its strength compared to the magnetocrystalline anisotropy.[17] It has been studied for *fcc* Co NPs for various sizes[18] and embedded in different matrices [19] and was found to be higher for particles embedded in metal matrices compared to non-metallic ones. Its effect has not been studied for *hcp* Co NPs, but its values found for cubic Co were lower than the *hcp* magnetocrystalline anisotropy.[20]

The strain or stress anisotropy refers to all possible magneto-mechanical contributions of the anisotropy energy. Even though this phenomenon has been known for a long time, it is still largely unexplored for NPs. [12]

Particle interactions

So far, only the factors influencing the magnetic anisotropy of isolated particles have been discussed. The influence of particle interactions on the magnetic anisotropy can be divided into two categories: Dipole-dipole (dipolar) and exchange interactions. The magnetic moments of nanoparticles that are not in direct contact and embedded in a non-conducting medium interact only via dipolar interactions, whose energy is relative to $1/{r_{ij}}^3$, with r_{ij} the distance between the particle centers.[14] The range over which dipolar interactions may have an influence strongly depends on the magnetic moment of the particle and they generally add up to the magnetic anisotropy and increase the energy barrier for a fluctuation of the magnetic axis. The interacting particles can either form a so-called “dipole glass”, with the dipolar moments frozen in random directions, or forming a chain with aligned dipolar moments.[21] Interestingly, an energy barrier decrease has been observed in some cases for weak dipolar interactions, but the cause of this phenomenon is still debated. [22], [23]

Exchange interactions cannot be explained by dipolar interactions but are the result of the interactions between electron wave functions of neighboring atoms. They exist in different forms (direct exchange

coupling, superexchange coupling, RKKY (Ruderman, Kittel, Kasuya, Yosida) coupling) and usually only play a role for nanoparticles that are in contact. In general, they result in an increase of the magnetic anisotropy. [12] For nanoparticles embedded inside a conducting medium, RKKY interactions can also become significant. The sign of this interaction oscillates with the interparticle distance, but the amplitude of the corresponding energy decreases with $1/r_{ij}^3$.[14]

Summary

The total magnetic anisotropy energy density, coming from all the different contributions, is often approximated to result from an effective uniaxial anisotropy. Consequently, it can be written in the same form as the uniaxial magnetocrystalline anisotropy energy density in Eq. (1.28), with the magnetocrystalline anisotropy constants K_{ci} being replaced by the effective anisotropy constants $K_{eff,i}$. As all the terms above the 1st one are often neglected, the function describing the anisotropy energy dependence on the angle between the magnetic moment and the easy axis has the same allure as the one shown in **Figure 4** (top right), with an energy barrier of $K_{eff}V$.

4.2. Superparamagnetism

As described in the previous paragraph, the magnetic moment of a ferromagnet structure is oriented preferentially along one or several easy axis of magnetization, defined by the various contributions to the magnetic anisotropy energy. In order to deviate the magnetic moment from such an easy axis a certain energy is necessary. In the case of a single-domain ferromagnetic particle with a uniaxial anisotropy, an energy of K_{eff}V is necessary in order to switch the magnetic moment between the two directions of the easy axis (as represented in the top right of **Figure 4**). Note that the magnetic moment may be affected by the thermal fluctuations of the system, with a thermal energy of k_BT. If $k_BT \ll K_{eff}$V, then the thermal energy is too low to change the direction of the magnetization and the particle behaves like a stable ferromagnet. If on the other hand, the thermal energy is of the same order of magnitude or above $K_{eff}V$, then there exists a measurable chance that the thermal energy flips the magnetic moment between the two directions of the easy axis. On average over time, the particle might therefore lose its magnetization and exhibit what is called a superparamagnetic behavior.

This effect was first introduced by Néel in 1949 [24], who defined a characteristic superparamagnetic relaxation time τ (also often referred to as the Néel relaxation time) with an Arrhenius law:

$$\tau = \tau_0 \exp\left(\frac{K_{eff}V}{k_B T}\right) \quad (1.29)$$

with τ_0 the elementary flip time[12], or the average time between two attempts to jump over the energy barrier. As a result, the exponential factor gives the inverse probability of the attempt to succeed in jumping over the barrier.[14] Néel's approach has been refined by several authors for different anisotropy geometries and external fields [25], [26], as reviewed by Coffey et al.[27]. The expression (1.29) remains a good approximation for uniaxial anisotropies, but more developed expressions are necessary for cubic anisotropies.[26] In addition, the elementary flip time, usually considered to be constant and of the order of 10^{-12} to 10^{-9} s, is not constant with temperature and also depends on the intrinsic magnetic properties of the nanostructures.[28]

The Néel relaxation time described in Eq.(1.29) defines the time scale of flips of the magnetic moment of a particle. That this particle is considered to be superparamagnetic or not also depends on the timescale τ_m of the magnetic measurement. In case the relaxation is slower than the measurement time ($\tau \ll \tau_m$), no flip of the magnetic moment occurs throughout the measurement and the particle appears to be ferromagnetic. In the case of the reverse situation ($\tau \gg \tau_m$), the magnetic moment will flip several times over the duration of the measurement, resulting in an average zero magnetization over time. In between those cases, the temperature at which the relaxation of a given particle (K_{eff} and V) and the measurement time are equal, is defined as the so-called blocking temperature T_B. From Eq.(1.29) we obtain:

$$\tau_m = \tau_0 \exp\left(\frac{K_{eff}V}{k_B T_B}\right) => T_B = \frac{K_{eff}(T)\,V}{k_B \ln(\tau_m/\tau_0(T))} \quad (1.30)$$

At first sight, the particle volume and the blocking temperature might appear linearly related. However, the magnetic anisotropy constant (K_{eff}) as well as the elementary flip time (τ_0) are temperature dependent, resulting in a deviation from a simple linear law. However, since τ_0 is inside a logarithm the impact of its variation on T_B is reduced. In **Figure 5**, the theoretical evolution of T_B with the particle volume or diameter (since size is often an important parameter determining nanoparticles behavior, for example in catalysts) is given for spherical *hcp* cobalt particles, as determined for IF NMR measurements. The value of K_{eff}(T) is taken to be equal to the sum of the first two terms of the magnetocrystalline anisotropy constant ($K_{c1}(T) + K_{c2}(T)$) of *hcp* Co (uniaxial anisotropy). Their values are taken from [29], [30] and their evolution with temperature is represented in **Figure 6**. The other parameters are $\tau_0 = 10^{-11}$ s, considered constant with temperature, and $\tau_m = 1.8 * 10^{-5}$ s, which is the typical measurement time of a spin-echo ^{59}Co IF NMR experiment. In the left graph a pseudo-linear relationship between the particle volume and the blocking temperature can be

seen for low temperatures, due to K_{eff} being only weakly T°-dependent. For T_B above 200 - 300 K, a strong deviation from linearity is observed, due to a significant decrease of K_{eff}. Above 400 K, $K_{c1}(T)$ and $K_{c2}(T)$ become small. Experimentally, the contribution of other terms (K_{c3}, surface contributions…) becomes then significant and may even dominate the overall magnetic anisotropy. Logically, the evolution of T_B also does not vary perfectly as d^3. As represented in the graphs, for a given particle volume/diameter, the particle appears to be superparamagnetic for temperatures above the blocking temperature and ferromagnetic below T_B. Inversely, for a given temperature, a critical particle volume (V_c(T)) or diameter ($d_c(T)$) can be defined. All particles with an inferior volume or diameter, are considered to be superparamagnetic and therefore do not give a signal in IF NMR, all bigger particles appear to be ferromagnetic and result in an IF NMR signal.

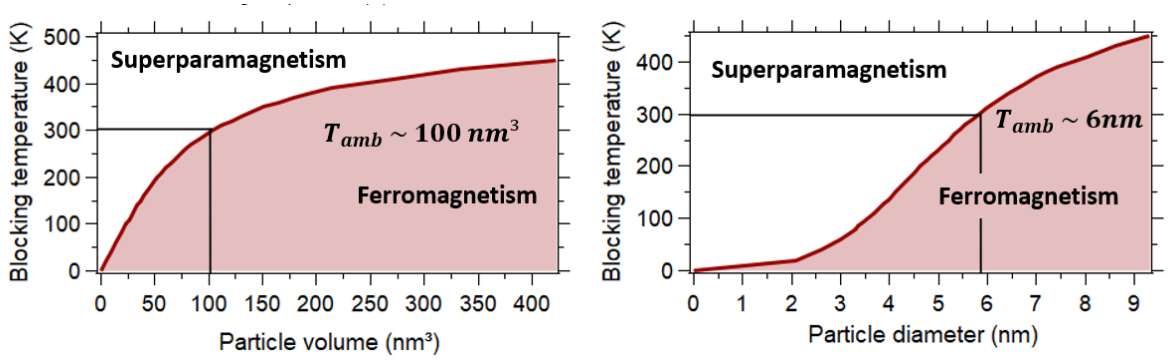

Figure 5: Evolution of the theoretical blocking temperature (T_B) with particle volume or diameter of spherical *hcp* Co particles, as determined for IF NMR measurements taking, as explained in the text, $\tau_0 = 10^{-11}$ s and $\tau_m = 1.8 * 10^{-5}$ s, the typical measurement time of a spin-echo ^{59}Co IF NMR experiment.

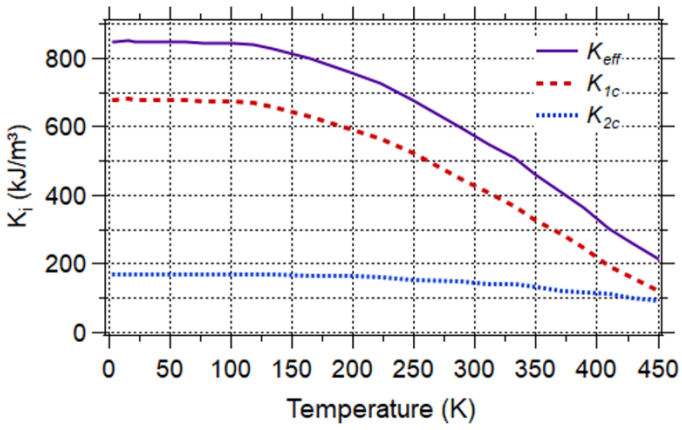

Figure 6: Evolution of $K_{eff}(T) = K_{c1}(T) + K_{c2}(T)$ with temperature for *hcp* Co particle. Data taken from [29], [30]

4.3. Magnetic domain formation

A detailed overview about the properties, formation and particle size dependence of the formation of magnetic domains in nanostructures has been published by Kittel in 1949 [31]. It shows that for ferromagnetic particles, there exists a critical size, above which it becomes energetically more favorable for the magnetic structure to split into so-called magnetic domains, as illustrated in **Figure 7**. The total magnetic energy (E_{tot}) of a ferromagnetic structure with no external applied magnetic field can be divided into different terms:

$$E_{tot} = E_{dem} + E_{exchange} + E_a \tag{1.31}$$

with E_{dem} the demagnetizing (or magnetostatic) energy, $E_{exchange}$ the exchange due to the coupling between the atomic magnetic moments, E_a the magnetocrystalline anisotropy energy.

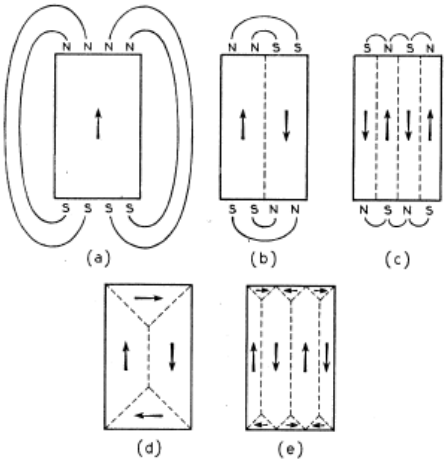

Figure 7: Illustration of the formation of domain walls in ferromagnetic particles and its influence on the demagnetizing field. Reproduced from [31].

The demagnetizing field energy comes from the interaction of the magnetic moments with the demagnetizing field $\boldsymbol{B}_{dem}$. In the case of a single-domain particle, also called saturation configuration and as shown in (a), only one magnetic pole exists on each side of the particle. This configuration has a high demagnetizing energy, due to the large demagnetizing field looping around the whole particle between the poles. This energy can already be cut roughly in half by dividing the crystal into two domains, magnetized in opposite directions. This is visualized in (b), where the presence of one of each pole reduces the demagnetizing field already significantly. Afterwards, the further division into even

smaller domains will decrease the demagnetizing energy even more, with N domains reducing the energy to approximately 1/N of the one of the saturated configuration.

Knowing that the formation of more and more domains reduces the magnetization energy further and further, one could naively think that it would be favorable for every ferromagnet to form a maximum number of domains in order to reduce its energy. This is not the case due to the exchange energy ($E_{exchange}$) between the individual magnetic moments, which is minimal if they are aligned and gradually increases with the angle in between them until it reaches a maximum for an antiparallel configuration. As a result, the change in the spin direction between magnetic domains does not occur in one discontinuous jump from one atomic plane to the next one, but rather gradually over many atomic planes, forming a so-called "domain wall" as represented in **Figure 8**. It can be proven that the total exchange energy of a directional change is lower, the more spins are involved in this change.

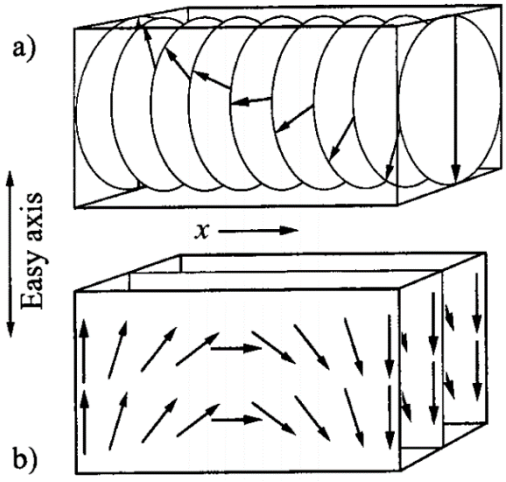

Figure 8: Graphical representation of the gradually changing spin direction in 180° domain walls: a) corresponds to a so-called "Bloch wall" and b) to a "Néel-wall". Reproduced from [32].

The fact that is limiting the domain wall to increase in width infinitely is the magnetocrystalline anisotropy energy (E_a). As discussed in subsection 4.1, in each crystalline configuration there exist one or several directions that are easier to magnetize, called easy axes (**Figure 4**). The spins inside the domain wall deviate from those easy axes and have therefore a higher energy. Consequently, the thickness of a domain wall is defined by a competition between the anisotropy energy, favoring thin walls, and the exchange energy, tending to increase their thickness. The overall domain and domain wall configuration is defined by a minimization of the total magnetic energy expressed in Eq. (1.31). [31]

In **Figure 8**, the two most common types of 180° domain walls are represented: a) Bloch walls and b) Néel walls. In both cases, the magnetization rotates along the wall thickness around an axis perpendicular to the easy axis. However, in Bloch walls the rotation axis is perpendicular to the wall, while in Néel walls the rotation occurs around an axis parallel to the wall. Bloch walls are generally the favored type of domain wall, but Néel walls are often observed in confined structures, such as thin films for example. Beside those two, other types of domain walls can also occur, especially in nanostructures.[32] Until now, only the case of domains with antiparallel spin directions has been considered here, but experiments show that there exist many different other and more complex configurations. One commonly studied domain shape is the so-called "domain of closure", shown in **Figure 7** (d) and (e). As there are no poles in the crystal without a counterpart next to it and no poles on the surface of the crystal, no demagnetizing field exists and the magnetization energy is reduced to zero. The factor that is often preventing those kind of domains to form is the anisotropy energy, for similar reasons limiting the width of domain walls, as explained in the previous paragraph. For uniaxial structures, such as cobalt *hcp* for example, a lot of energy is needed to form a domain of closure, in contrast to less anisotropic structures as *fcc* cobalt or nickel, or *bcc* iron.[31] In fact there are even more factors that influence the domain structure and it is rarely as simple as in the previously presented cases, especially for polycrystalline samples. However, for monocrystalline particles with simple structures, the minimum size of nanoparticles to form multiple domains has been estimated. In the case of spherical cobalt nanoparticles without shape anisotropy (like *fcc*), the critical diameter is 70 nm, while particles with significant shape anisotropy like nanorods for example can remain single-domain to much larger dimensions.[33]

The formation of domain walls has an important influence on the macroscopic magnetic properties of a ferromagnetic particle. First of all, without the application of an external magnetic field, a single-domain particle will have a magnetization along a unique direction, defined by the magnetic anisotropy. In a multi-domain particle on the other hand, the magnetic moments of the different domains will generally tend to cancel each other out, leading to an overall reduced magnetization. When an external magnetic field is applied, the magnetic moments tend to align with this field. In a multi-domain particle, the domain walls will move in order to increase the size of the domains aligned with the external field, at the expense of the ones oriented in a different direction. This displacement generally requires less energy than the coherent rotation of the magnetic moments, happening in single-domain particles. The formation of domain walls therefore decreases the coercivity of small magnetic particles, meaning that only a weaker external magnetic field intensity is needed to demagnetize them, *i.e.* obtain a magnetic induction equal to 0 inside the sample.[11], [34]

5. Summary of Chapter 1

The general principles of IF NMR studies are similar to the ones of classic NMR techniques, however, no external field is needed. When studying ferromagnetic materials (containing Co, for example), an important internal magnetic field ($\boldsymbol{B}_{int}$) is present that polarizes the nuclear spins. The resulting resonance frequency can be estimated by:

$$\Omega_n = |-\gamma_n B_{int}|$$

This internal field is not static but interacts with the excitation radiofrequency pulse, as well as the nuclear magnetic moments. This leads to an indirect character of the excitation and of the detection and consequently to an enhancement of both phenomena, defined by the enhancement factor η. This enhancement is function of the sample structure and especially differs between domains and domain-walls, due to a different excitation mechanism in each case. Consequently, the distribution of the enhancement factor needs to be considered when doing a quantitative analysis of a sample, but also allows to obtain additional information about the magnetic structure of a sample.

The internal field directly influences the resonance frequency and depends on different factors. First of all, it depends on the crystalline structure of the analyzed material, mainly *fcc* or *hcp* in the case of cobalt. This not only influences the magnitude of the internal field but also its anisotropy. Secondly, it is the nearest neighbor structure of the atom to be analyzed that influences the internal field. The presence of foreign atoms plays an important role when analyzing interfaces or different types of solid solutions and alloys. Finally, the shape and size of a sample has an influence on the internal field, due to a variation of the demagnetizing field. The intensity of the demagnetizing field strongly depends on the magnetic domain and domain-wall structure of a sample.

The magnetic structure of a sample is the consequence of an interplay between the demagnetizing, exchange and anisotropy energies, leading to the formation of domain-walls in rather big structures with a low aspect ratio. On the other hand, rather small nanostructures (for example, spherical *fcc* Co particles with d <70 nm) are composed of a single magnetic domain. When studying even smaller single domain Co nanostructures (d < 10 nm in the case of spheres to give an order of magnitude), the ferromagnetic - superparamagnetic transition needs to be considered. A superparamagnetic Co nanostructure does not show a ferromagnetic behavior due to thermal fluctuations of its magnetic moments. This effect depends on the total magnetic anisotropy of a particle and therefore on its size, but also its crystalline structure, its shape, and interactions with other particles.

Knowing how the different sample properties of cobalt containing structures influence their internal field and magnetic characteristics helps to understand how ^{59}Co IF NMR can provide information on a

lot of different aspects of these materials. The resonance frequency depends on the internal field inside a structure and therefore on the magnetic crystalline structure, the presence of foreign atoms and the domain/domain-wall structure. In addition, the ferromagnetic - superparamagnetic transition helps to study the size of cobalt containing nanoparticles. Precise theoretical calculations of the internal field and the resulting resonance frequency are difficult, especially when the structure is more complex than a pure bulk structure. As a result, the spectrum attribution in IF NMR, is often done empirically by comparison with reference materials. In the following Chapter 2, a bibliographic review of ^{59}Co IF NMR of cobalt containing samples is presented, which should help to better understand the spectrum interpretations done in this work.

6. References

[1] J. Keeler, *Understanding NMR Spectroscopy*. Univeristy of Cambridge, 2002.

[2] E. A. Turov and M. P. Petrov, *Nuclear Magnetic Resonance in Ferro- and Antiferromagnets*. Jerusalem: Israel Program for scientific translations (Halsted Press), 1972.

[3] A. P. Guimarães, *Magnetism and magnetic resonance in solids*. New York: John Wiley & Sons, 1998.

[4] P. Panissod, "Structural and Magnetic Investigations of Ferromagnets by NMR. Application to Magnetic Metallic Multilayers," in *Frontiers in Magnetism of Reduced Dimension Systems*, Dordrecht, 1998, pp. 225–270.

[5] A. M. Portis and A. C. Gossard, "Nuclear Resonance in Ferromagnetic Cobalt," *J. Appl. Phys.*, vol. 31, no. 5, pp. S205–S213, May 1960, doi: 10.1063/1.1984666.

[6] A. C. Gossard and A. M. Portis, "Observation of Nuclear Resonance in a Ferromagnet," *Phys. Rev. Lett.*, vol. 3, no. 4, pp. 164–166, Aug. 1959, doi: 10.1103/PhysRevLett.3.164.

[7] P. G. de Gennes, P. A. Pincus, F. Hartmann-Boutron, and J. M. Winter, "Nuclear Magnetic Resonance Modes in Magnetic Material. I. Theory," *Phys. Rev.*, vol. 129, no. 3, pp. 1105–1115, Feb. 1963, doi: 10.1103/PhysRev.129.1105.

[8] W. Marshall, "Orientation of Nuclei in Ferromagnets," *Phys. Rev.*, vol. 110, no. 6, pp. 1280–1285, Jun. 1958, doi: 10.1103/PhysRev.110.1280.

[9] R. E. Watson and A. J. Freeman, "Origin of Effective Fields in Magnetic Materials," *Phys. Rev.*, vol. 123, no. 6, Art. no. 6, Sep. 1961, doi: 10.1103/PhysRev.123.2027.

[10] J. A. Osborn, "Demagnetizing Factors of the General Ellipsoid," *Phys. Rev.*, vol. 67, no. 11–12, pp. 351–357, Jun. 1945, doi: 10.1103/PhysRev.67.351.

[11] C. Kittel, *Introduction to Solid State Physics*, 6th ed. New York: John Wiley & Sons, 1986.

[12] S. Bedanta, O. Petracic, and W. Kleemann, "Supermagnetism," in *Handbook of Magnetic Materials*, vol. 23, Elsevier, 2015, pp. 1–83. doi: 10.1016/B978-0-444-63528-0.00001-2.

[13] B. D. Cullity and C. D. Graham, *Introduction to magnetic materials*, 2nd ed. Hoboken, N.J: IEEE/Wiley, 2009.

[14] D. Peddis, "Nanostructured Magnets - Syntheis and characterization of CoFe2O4 nanoparticles," PhD Theis, Università degli Studi di Cagliari, cagliari, 2006.

[15] G. J. Strijkers, J. H. J. Dalderop, M. A. A. Broeksteeg, H. J. M. Swagten, and W. J. M. de Jonge, "Structure and magnetization of arrays of electrodeposited Co wires in anodic alumina," *J. Appl. Phys.*, vol. 86, no. 9, Art. no. 9, Nov. 1999, doi: 10.1063/1.371490.

[16] I. L. Prejbeanu, L. D. Buda, U. Ebels, M. Viret, C. Fermon, and K. Ounadjela, "Domain structures in epitaxial (1010) Co wires," *IEEE Trans. Magn.*, vol. 37, no. 4, Art. no. 4, Jul. 2001, doi: 10.1109/20.951068.

[17] Y. Labaye, O. Crisan, L. Berger, J. M. Greneche, and J. M. D. Coey, "Surface anisotropy in ferromagnetic nanoparticles," *J. Appl. Phys.*, vol. 91, no. 10, p. 8715, 2002, doi: 10.1063/1.1456419.

[18] M. Hillenkamp *et al.*, "Size effects of the magnetic anisotropy of fcc cobalt nanoparticles embedded in copper," *Eur. Phys. J. D*, vol. 71, no. 12, p. 330, Dec. 2017, doi: 10.1140/epjd/e2017-80299-x.

[19] A. Tamion *et al.*, "Magnetic anisotropy of embedded Co nanoparticles: Influence of the surrounding matrix," *Phys. Rev. B*, vol. 81, no. 14, p. 144403, Apr. 2010, doi: 10.1103/PhysRevB.81.144403.

[20] M. Respaud *et al.*, "Surface effects on the magnetic properties of ultrafine cobalt particles," *Phys. Rev. B*, vol. 57, no. 5, Art. no. 5, Feb. 1998, doi: 10.1103/PhysRevB.57.2925.

[21] S. Mørup, M. F. Hansen, and C. Frandsen, "Magnetic interactions between nanoparticles," *Beilstein J. Nanotechnol.*, vol. 1, pp. 182–190, Dec. 2010, doi: 10.3762/bjnano.1.22.

[22] S. Mørup and E. Tronc, "Superparamagnetic relaxation of weakly interacting particles," *Phys. Rev. Lett.*, vol. 72, no. 20, pp. 3278–3281, May 1994, doi: 10.1103/PhysRevLett.72.3278.

[23] J. L. Dormann, L. Bessais, and D. Fiorani, "A dynamic study of small interacting particles: superparamagnetic model and spin-glass laws," *J. Phys. C Solid State Phys.*, vol. 21, no. 10, pp. 2015–2034, Apr. 1988, doi: 10.1088/0022-3719/21/10/019.

[24] L. Néel, "Influence des fluctuations thermiques sur l'aimantation de grains ferromagnétiques très fins," *Comptes Rendus Hebdomadaires Des Seances De L Academie Des Sciences*, vol. 228, no. 8, pp. 664–666, 1949.

[25] W. F. Brown, "Thermal Fluctuations of a Single-Domain Particle," *Phys. Rev.*, vol. 130, no. 5, pp. 1677–1686, Jun. 1963, doi: 10.1103/PhysRev.130.1677.

[26] W. T. Coffey, D. S. F. Crothers, Yu. P. Kalmykov, E. S. Massawe, and J. T. Waldron, "Exact analytic formulae for the correlation times for single domain ferromagnetic particles," *J. Magn. Magn. Mater.*, vol. 127, no. 3, Art. no. 3, Oct. 1993, doi: 10.1016/0304-8853(93)90039-5.

[27] W. T. Coffey and Y. P. Kalmykov, "Thermal fluctuations of magnetic nanoparticles: Fifty years after Brown," *J. Appl. Phys.*, vol. 112, no. 12, Art. no. 12, Dec. 2012, doi: 10.1063/1.4754272.

[28] M. Respaud *et al.*, "Dynamical properties of non-interacting Co nanoparticles," *Europhys. Lett. EPL*, vol. 47, no. 1, Art. no. 1, Jul. 1999, doi: 10.1209/epl/i1999-00361-2.

[29] Y. Barnier, "Contribution à l'étude des propriétés magnétiques du cobalt et des alliages de fer-cobalt (Thèse d'Ingénieur-Docteur)," Université de Grenoble, Grenoble, 1963. [Online]. Available: https://tel.archives-ouvertes.fr/tel-03372927

[30] E. P. Wohlfarth, "Iron, Cobalt and Nickel," in *Ferromagnetic materials*, vol. 1, North-Holland Publishing Company, 1980, p. 70.

[31] C. Kittel, "Physical Theory of Ferromagnetic Domains," *Rev. Mod. Phys.*, vol. 21, no. 4, pp. 541–583, Oct. 1949, doi: 10.1103/RevModPhys.21.541.

[32] C. L. Dennis *et al.*, "The defining length scales of mesomagnetism: a review," *J. Phys. Condens. Matter*, vol. 14, no. 49, Art. no. 49, Dec. 2002, doi: 10.1088/0953-8984/14/49/201.

[33] D. L. Leslie-Pelecky and R. D. Rieke, "Magnetic Properties of Nanostructured Materials," *Chem. Mater.*, vol. 8, no. 8, Art. no. 8, 1996, doi: 10.1021/cm960077f.

[34] A. P. Guimarães, *Principles of Nanomagnetism*. Berlin, Heidelberg: Springer Berlin Heidelberg, 2009. doi: 10.1007/978-3-642-01482-6.

Chapter 2: Bibliographic overview of IF NMR on Co containing samples

In this second chapter, a literature overview of the IF NMR studies performed on cobalt containing compounds is presented. This overview will not only present to the reader the historical background of this technique but will also help to understand the decomposition of the different spectra presented in this work. Due to the difficulty of calculating theoretically the internal field and the resulting resonance frequency, many of the results presented below will be used as references for the peak assignment in this work. First, bulk and nanometric sized pure Co materials will be discussed, differentiating between the two main cobalt crystalline structure: *fcc* and *hcp*. In all cases the evolution with temperature of the resonances is presented, as in Chapter 6 of this work experiments at various are analyzed. Finally, cobalt containing composite materials of various nature are addressed.

Chapter 2: Bibliographic overview of IF NMR on Co containing samples

Before describing ^{59}Co IF NMR results, the three different cobalt crystalline phases that have been reported are described and represented in **Figure 1**: *hcp*, *fcc* and *bcc*. For bulk materials the *hcp* phase is the stable form at ambient temperature, while *fcc* Co becomes stable at temperatures above around 650 - 750 K.[1] In contrast to bulk materials, it was found that during the production of Co nanoparticles the *fcc* phase is the most stable one.[2] Kitakami et al.[3] studied this effect more in detail for particles produced by sputtering and observed a pure *fcc* phase for particles below 20 nm in diameter, an almost pure *hcp* phase for particles above 40 nm and mixture of both phases in between. This phenomenon can be explained by considering the internal and surface energy and the exact particle shape of the particles. The *bcc* phase is generally not stable in the case of pure Co and was only observed in cobalt alloys with iron.[4] A major difference between the two cubic structures and the hexagonal one is its anisotropy, which has a strong influence on its magnetic properties. As already discussed around Chapter 1 Subsection 4.1, *hcp* Co is strongly anisotropic with an easy axis alongside the *c*-axis, while the cubic structures have a much more isotropic character. As will be shown in the following, ^{59}Co IF NMR experiments also helped to determine magnetic properties of the different Co structures, like the amplitude of the internal field.

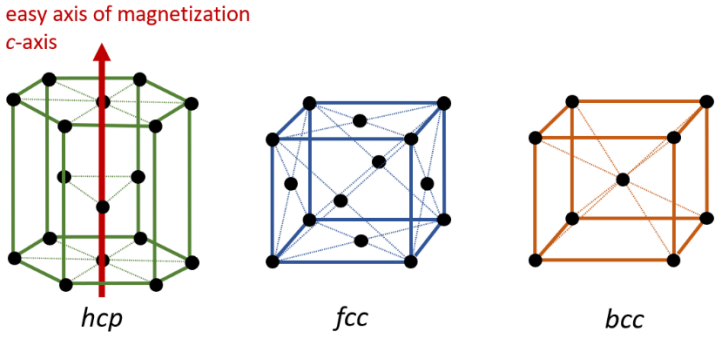

Figure 1: Schematic representation of the different Co crystalline structures that have been observed by ^{59}Co IF NMR: hexagonal close-packed (*hcp*), face-centered cubic (*fcc*) & body-centered cubic (*bcc*)

1. Pure Co materials

1.1. Bulk Co (multi-domain)

Face-centered-cubic (fcc)

The first published observation of nuclear magnetic resonance in a ferromagnet without the presence of an external magnetic field has been done by Gossard and Portis in 1959 at the University of California.[5] The particles that have been analyzed were produced by hydrogen reduction of cobalt oxide. Two types of particles were studied, spherical *fcc* Co particles with a size of 1-5 µm and *hcp* Co particles with a size of 5-10 µm. A ^{59}Co IF NMR signal could be detected from the *fcc* particles, but not from the *hcp* ones. After conversion of the crystalline structure of the 5-10 µm particles to *fcc* Co by annealing over 700 K, a ^{59}Co IF NMR signal with the same features as the 1-5 µm particles was obtained.[6] At ambient temperature, they observed a single IF NMR peak at 213.1 MHz, which was then attributed to *fcc* cobalt. This frequency corresponds to a magnetic field of 21.20 T (212.0 kG) at the cobalt nuclei. This was the first experimental determination of the internal magnetic field inside an *fcc* cobalt structure or an *fcc* metal in general.[5] The internal field inside *hcp* cobalt and Co alloys was determined around the same time by different authors using specific heat measurements [7], [8] and the field inside *fcc* Co was found to be slightly inferior to the one inside *hcp*.

Portis and Gossard continued their work on this subject, first by analyzing experimentally the effect of the temperature on the peak position of the resonance.[6] The analyzed cobalt particles are the annealed 5-10 µm Co particles described in the previous paragraph. Experiments have been performed at 77.4 K, 194.7 K and 296.5 K and a frequency-temperature dependence has been established. This dependence is found to be similar to the one of the relative magnetization in this temperature range, set up by Stoner [9]:

$$\nu(T) = \nu(0)\sqrt{1 - \left(\frac{T}{\theta}\right)^2} \qquad (2.1)$$

with $\nu(0)$ the frequency extrapolated to 0 K and θ the observed Curie temperature of bulk cobalt. The data could be fitted well with these two parameters being equal to 217.2 MHz and 1400 K, respectively. Another parameter analyzed by Portis and Gossard at different temperatures is the relaxation time. The spin-lattice relaxation time increased from 280 µs at room temperature to 600 µs at 77.4 K (liquid nitrogen temperature). The spin-spin relaxation time on the other hand was found to be 25 µs and independent of the temperature. Those times are shorter than predicted by the theory of Suhl [10] for

example, which was explained by the presence of domain walls in the samples. Koi et al. [11] extended the proposed frequency-temperature model to higher temperature temperatures. Even though the model's precision was lower at temperatures over 500 K, they still could conclude that the main dependence in frequency is due to the change in electronic magnetization. In the same paper, the influence of pressure on the frequency was analyzed. At different temperatures (282.3 K and 194.7 K), the samples were analyzed under pressures ranging from 1 to 8000 kg/cm² and a linear increase was observed. The authors attributed this to a change of the hyperfine interaction parameter λ_{HF}, linking the local field to the magnetization as represented in equation (1.26). In contrast, the pressure was shown to have no or only few influence on the electronic magnetization.

The assignation of the peaks corresponding to multi-domain (m.d.) *fcc* Co structures, around 213 MHz at ambient temperature or around 217 MHz close to 0 K, is widely accepted and used by many authors. [1], [12]–[16] More detailed studies about the frequency-temperature dependence for this peak have been performed at temperatures up to 850 K [1], [11], [17], [18] and are compared to the results obtained considering Stoner's theory in **Figure 2**. It can be seen that Stoner's theory is not experimentally valid at higher temperatures. In order to describe the evolution of the magnetization, and therefore also the resonance frequency, it is possible to use the spin wave approximation, resulting in equation (2.2).[19] When using only the first term of the approximation ($C_{3/2}\,T^{3/2}$), also known as the "three halves law" and first proposed by Bloch [20], a decent prediction can be obtained. However, a measurable deviation from this law is obtained by NMR measurements, leading to the introduction of a $T^{5/2}$ dependance and therefore to the introduction of a $C_{5/2}$ parameter. It can be explained by a more accurate expression of the spin wave energy compared to the law proposed by Bloch, taking also into account the inhomogeneous part of the dipole-dipole interaction of the magnetic moments. [1], [6]

$$\frac{\nu(0)-\nu(T)}{\nu(0)} = \frac{M(0)-M(T)}{M(0)} = C_{3/2}\,T^{3/2} + C_{5/2}T^{5/2} + \cdots \qquad (2.2)$$

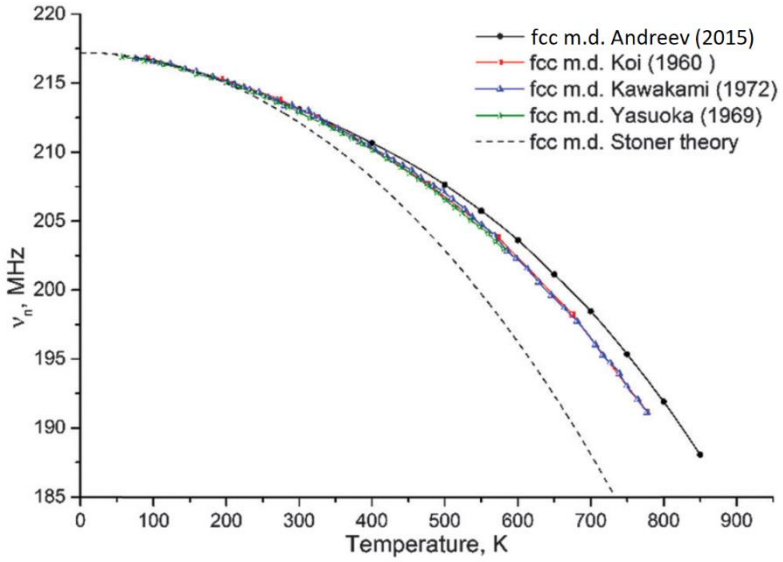

Figure 2: Temperature dependence of the resonance frequency for multi-domain (m.d.) *fcc* cobalt structures, reported in different articles by Andreev et al.[1], Koi et al. [11], Kawakami et al.[18] and Yasuaoka et al.[17]. The dashed line corresponds to the prediction by Stoner's theory [9]. (adapted from [1])

Hexagonal close packed (hcp)

The first published observation of ferromagnetic nuclear magnetic resonance of an *hcp* cobalt structure was done by Koi et al. in 1960 on well annealed and finely divided Co powder.[21] They assigned their success of observing a *hcp* resonance to the use of a spectrometer of higher sensitivity than Gossard and Portis.[5] A higher sensitivity is necessary due to the broader signal in *hcp* compared to *fcc* caused by the larger crystalline anisotropy (and therefore internal field anisotropy, as well) in *hcp* Cobalt.. A resonance occurred around 221.5 MHz at ambient temperature and by performing experiments at various temperatures they extrapolated the 0 K frequency to 228.0 MHz. The frequency was found to decrease more rapidly with temperature than for *fcc*. The *hcp* phase frequency has been measured and extrapolated only for temperatures up ~700K, probably because the *hcp* → *fcc* phase transition is known to occur around this temperature in bulk. Further experiments on bulk or micrometer sized samples, therefore having a m.d. structure, showed the appearance of a second peak at a frequency around 214 MHz at ambient temperature. Kawakami et al. [18] explained the appearance of this peak by the anisotropy of the hyperfine field in *hcp* cobalt, which leads to a different resonance frequency as function of the orientation of electronic magnetic moment with respect to the *c*-axis, the easy axis in hexagonal cobalt. The higher frequency peak therefore corresponds to spins in

the center of the domain wall (electron magnetization perpendicular to easy axis) and the lower frequency peak to spins on the edge of the domain wall (electron magnetization parallel to easy axis). This attribution was verified experimentally in different articles. [22]–[27] Kawakami et al. also studied the temperature dependence of both frequencies up to 730 K, as shown in **Figure 3**. Close to 0 K, the domain wall center frequency is confirmed to be ~228 MHz and the domain wall edge frequency is found to be ~220 MHz. While the center frequency can be predicted reasonably well by the "three halves law", the edge frequency shows some anomalies for temperatures above 40 K already.[18], [28] Some interesting properties of bulk *hcp* cobalt that can be deduced from this study are the change of the easy direction of magnetization from the *c*-axis into the *c*-plane, starting at 519K, as well as the *hcp* → *fcc* transition between 712K and 730K, both verified by other techniques. [29]–[32]

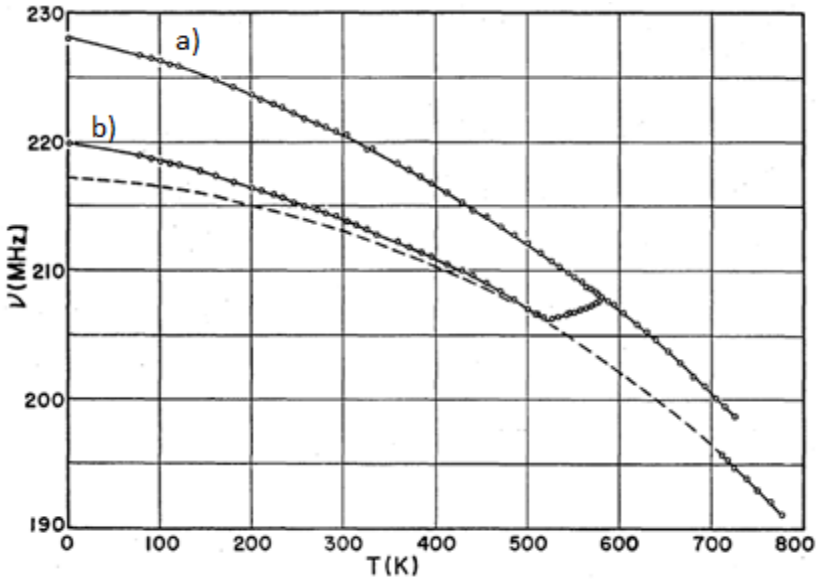

Figure 3: The evolution with temperature of the resonance frequencies of a) the domain wall center and b) the domain wall edge of multi-domain *hcp* cobalt structures. Dashed line = multi-domain *fcc* cobalt. (Adapted from [18])

1.2. Co Nanostructures

During the previous works, the only sample characteristics that was studied is the crystalline structure, *hcp* or *fcc*, and the particle sizes were all sufficiently big to consider those structures as bulk. The inconvenience of small nanoparticles is that they are more difficult to produce, to protect from oxidation and to control in size. Also, they give a weaker signal than their multi-domain counterpart due to the weaker enhancement of the pulse associated to domain wall occurrence.

Fcc nanostructures

The first ones to analyze small nanoparticles below the critical size for multi-domain magnetism have been again Gossard and Portis in collaboration with Rubinstein and Lindquist in 1965.[33] In order to produce stable cobalt nanoparticles, heterogeneous catalyst preparative techniques have been used where the nanoparticles are supported on γ alumina. The particle size can be controlled by the time and temperature of the reduction by hydrogen and is determined afterwards from XRD line width broadening. They revealed a new IF NMR resonance at 216.85 MHz at room temperature for particles between 10 and 15 nm and assigned it to single-domain (s.d.) cobalt. More details about the domain formation and the critical size has been given in Section 4.3 of Chapter 1 (and can be found in [34]), but this particle size is well below the critical size for s.d. cobalt nanoparticles. The difference in the resonance frequency of this s.d. structure, compared to the frequency around 213 MHz of a multi-domain (m.d.) structure, thus unequivocally resulted from the presence of the demagnetizing field in this case. The demagnetizing field is defined by equation (1.25) in Chapter 1, with its intensity depending linearly on the total electronic magnetization (M_e) and on the form factor (N_d). For a ferromagnetic material like cobalt a good approximation of M_e is the saturation magnetization, which is equal to 1400 emu/cm³ for *fcc* cobalt.[35] For spherical particles and N_d=1/3, this leads to a theoretical demagnetizing field ($B_{dem} = 4\pi N_d M_e$) of about 6 kG.[33] As both, the demagnetizing field and the hyperfine field are in the opposite direction of the electron magnetization, this would lead to an upwards shift of about 6 MHz giving the gyromagnetic ratio of ^{59}Co (1.005 MHz/kG). Experimentally however, a much smaller difference between m.d. and s.d. *fcc* signals is observed, 3.75 MHz in the work by Gossard et al. [33] for example. They explained the discrepancy between the theoretical and experimental value by the fact that the particles are not isolated, but there are particle-particle interactions. The presence of the magnetic poles of the s.d. particles in proximity to the s.d. particle under consideration reduces the intensity of the demagnetizing field. As a result, the shift of the resonance frequency compared to a m.d. particle is reduced as well. The estimation of this effect has been done by calculating the demagnetizing field of such a s.d. particle inside a medium of permeability μ.[33]

Further studies on single domain particles have been done by Yasuoka and Lewis [17]. They mostly studied samples with particle sizes below 25 nm, therefore single-domain (s.d.) ones. They studied the evolution of the s.d. frequency at different temperatures. The observed shift of the s.d. signal compared to the position of the already know domain wall signal was similar at all considered temperatures and close to the one previously observed.[33] The *fcc* s.d. peak position evolution could be fitted quite accurately by the first term ($C_{3/2}\,T^{3/2}$, "three halves law") of the spin-wave

approximation. For a sample also containing some bigger particles, an important signal assigned to domain walls coming from multi-domain (m.d.) particles has been observed. This shows that even the presence of a few large particles leads to a quite intense signal, which can be explained by the facts that the volume increases rapidly with increasing particle diameter and the more important enhancement of the domain wall signal. A more detailed study of the temperature dependence of the s.d. signal has been done by Andreev et al.[1] When studying nanosized metal clusters supported on $\beta - SiC$, peaks corresponding to m.d. *fcc* Co, as well as s.d. *fcc* Co particles have been observed, with a shift of about 3 MHz in between them. The evolution with temperature of both peaks is shown in **Figure 4**. The evolution of the m.d. signal already has been discussed in **Figure 2**, where a measurable deviation from the "three halves law" has been detected, explained by taking into account the $C_{5/2}\,T^{5/2}$ term of the spin-wave approximation shown in Eq.(2.2). A similar temperature dependence has been demonstrated for the s.d. signal, with the approximated frequency at 0 K being equal to $\nu_0 = 220.0 \pm 0.3\ MHz$. Several other authors observed such a peak corresponding to *fcc* s.d. structures. They did experiments at different temperatures and observed the peak at an upwards shift of 3-4 MHz compared to the m.d. peak.[36]–[38]

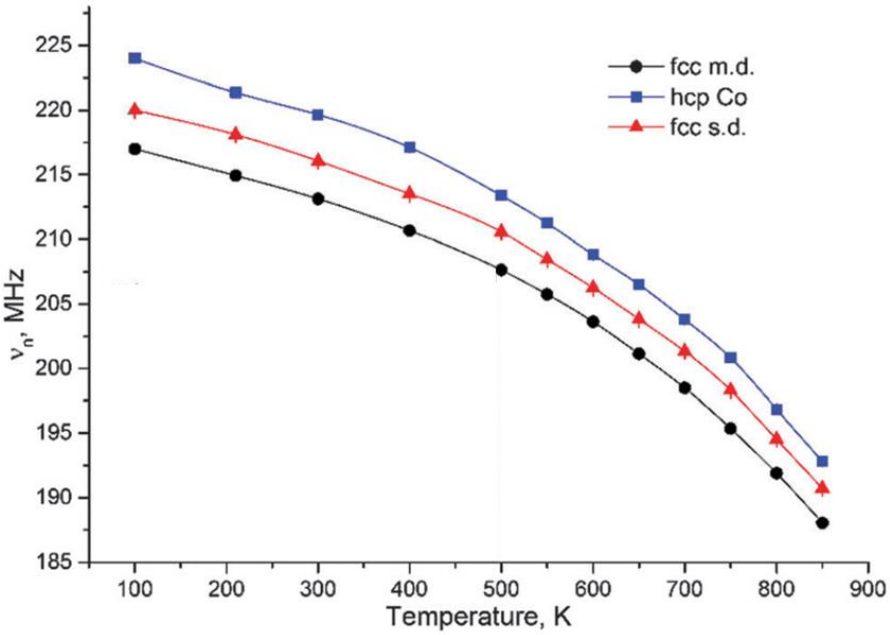

Figure 4: Evolution with temperature of the ^{59}Co IF NMR frequencies of different kinds of Co nuclei observed for Co metal supported on $\beta - SiC$. Black circles: *fcc* multi-domain (m.d.), Red triangles: *fcc* single-domain (s.d.), Blue squares: *hcp* Co. Reproduced from [1]

Hcp nanostructures

In contrast to bulk materials, in small nanoparticles the *fcc* structure is found to be the most stable one, which makes it more difficult to produce pure single-domain *hcp* nanoparticles.[2] Several authors that managed to produce *hcp*-containing nanoparticles and other nanostructures, report a large peak at frequencies above the resonance frequency of s.d. *fcc* rather than two well defined sharp peaks as observed by Kawakami et al. for bulk *hcp* cobalt [18] (**Figure 2**). The large peak width can be explained by the big anisotropy of the *hcp* crystalline structure and the often more irregular character of the crystallinity inside nanostructures. The exact position of this peak is therefore not always well defined. At ambient temperature the peak is generally observed between 218 and 225, at 77 K it is observed at a higher frequency between 223 and 230 MHz.[1], [37]–[40] As for the two peaks assigned to *fcc*, Andreev et al. [1] studied in detail the evolution with temperature of this peak, as represented in **Figure 4**. Again, it can be fitted quite well using the first two terms of the spin-wave approximation (Eq.(2.2)), with $\nu_0 = 223.0 \pm 0.3\ MHz$ and a resonance around 219 MHz at RT. Although for temperatures below 100 K the observed frequency seems to deviate slightly from this law.

In opposition to the case of *fcc* Co nanomaterials, the exact attribution of the different peaks corresponding to *hcp* cobalt in nanomaterials is still not unified in the literature. As a reminder, in bulk *hcp* a peak around 221.5 MHz corresponding to the domain wall center and sometimes an additional peak assigned to the domain wall edge around 214 MHz are observed at ambient temperature. [18] When studying nanomaterials, several authors distinguish a peak between 220 and 222 MHz at ambient temperature that they assign to signal coming from *hcp* domain walls. [14], [39], [41] A peak corresponding to the *hcp* domain wall edge around 214 MHz is not distinguished however, which can be rationalized by the fact that the enhancement is not constant over the domain wall and higher at its center.[42, p. 237] As the amount of domain walls is generally smaller in nanomaterials compared to in the bulk, the less enhanced domain wall edges cannot be distinguished in nanoparticles. Nevertheless, a peak corresponding to *hcp* s.d. structures is observed, which is shifted with respect to the domain wall peak due to the presence of the demagnetizing field, as already explained for *fcc* cobalt. For example, Choudhary, Manjunatha and coworkers [14], [41] claim to observe a s.d. peak around 223 MHz at RT, about 3 MHz above the additionally observed *hcp* multi-domain/ domain wall center peak at 220 MHz. In contrast, Andreev et al. [39] observed a s.d. *hcp* peak around 219 MHz, at a lower frequency than the *hcp* domain wall resonance. This seems a little surprising at first glance, as the demagnetizing field present for s.d. structures generally increases the magnetic field at the nucleus. However, the upwards shift in this case is considered to be with respect to the resonance of the *hcp* domain wall edge, observed around 214 MHz in bulk materials, which makes sense as in both cases the hyperfine field is along the easy axis of the *hcp* crystalline structure. In summary, two

different *hcp* s.d. peaks have been observed in the literature, distinguished by the orientation of the magnetization relative to the easy *c*-axis of the *hcp* structure. The signal is observed around 219 MHz for a magnetic moment colinear with the *c*-axis and around 223 MHz (both at RT) for a magnetic moment perpendicular to the *c*-axis. The exact positions can vary with the strength of the demagnetizing field. For small, isolated particles (mostly < 10 nm), which therefore should not contain any domain walls, Liu et al. [37] observed both of the above described peaks. However, the intensity of the peak of a perpendicular orientation is much lower than the one of a colinear orientation, as the magnetic moment is much more likely to be alongside the easy *c*-axis.

The previous paragraph showed the difficulty of differentiating the *hcp* peaks in *hcp* containing nanostructures. Especially the peaks corresponding to the domain wall center and to monodomains with a magnetic moment colinear with the *c*-axis tend to be at a similar position. For a better interpretation of a ^{59}Co IF NMR spectra and the region around 219 MHz in particular, the power needed for optimal excitation is often considered.[39], [41] It is known that the excitation of domain walls requires less power than the excitation of domains due to a higher enhancement factor. Knowing that the signal around 213 MHz is arising from nuclei inside *fcc* domain walls, the magnetic structure of the *hcp* peak can be determined by comparison. In case the optimal excitation power is comparable or to the one of the *fcc* multi-domain peak, the *hcp* signal can unambiguously be assigned to arise from domain walls as well. In contrast, if the optimal power in this region or a part of this region is significantly higher than the one for the signal around 213 MHz, it is assigned to a single-domain *hcp* structure.

Overview

In **Table 1** an overview of the different peaks that are distinguished when analyzing samples containing pure cobalt by IF NMR is presented. All the frequencies correspond to values observed at ambient temperature, but its evolution with temperature can generally be described using an approximation of the spin-wave theory (Eq. (2.2)), as presented in **Figure 3** and **Figure 4**. The peak assignment that is well-accepted in the literature is the *fcc* m.d. peak. The position of the *fcc* s.d. peak can vary as function of the strength of the demagnetizing field. Both peaks are in general relatively narrow, especially compared to the wider peaks assigned to the more anisotropic *hcp* structure. Two well distinguished *hcp* m.d. peaks are often not observed in nanosized Co samples. Instead, a broad peak above 219 MHz is observed. In order to distinguish m.d. and s.d. structures, the optimal excitation power is considered in this case, as the enhancement factor is higher for nuclei inside domain walls compared to domains.[42, p. 237], [43] An additional consequence of the enhancement factor difference is the fact

that when analyzing m.d. structures, the main contribution to the IF NMR signal comes from excitation of the domain walls, rather than the domains.

The influence on the resonance frequency of foreign atoms in the Co structure will be discussed in the following section.

Table 1. Summary of the ^{59}Co IF NMR peak position at ambient temperature of different crystalline structures that have been observed when analyzing pure cobalt samples

Crystalline Structure	*fcc* m.d.	*hcp* m.d. (//*c*-axis)	*fcc* s.d.	*hcp* nanostructures	*hcp* m.d. (⊥ *c*-axis)
Frequency (MHz) T_{amb}	213	214	~ 216	large peak 218 - 225	221.5

2. Co containing composites

Beside the study of pure cobalt by ^{59}Co internal field NMR, a large number of different Co-alloys has also been studied by this technique. Soon after its discovery by Portis and Gossard in 1959, the first IF NMR works on binary Co-X alloys in bulk form with different cobalt concentrations and varying mixing and annealing properties were published.[44], [45] One objective of these studies is the precise determination of the internal field at the cobalt nuclei in these alloys with different short range order and neighbor distributions in the crystalline structure, in combination with the detection and attribution of the corresponding NMR satellite lines. Other interests include the search of phases with extraordinary magnetic properties, as well as a precise phase determination for metallurgical purposes.

The hyperfine field ($\boldsymbol{B}_{HF}$) at a ^{59}Co nucleus will be disturbed when an impurity is introduced into the crystalline structure surrounding the Co atom in question. As described in a previous part of this manuscript when talking about the different terms of the $\boldsymbol{B}_{HF}$ inside a ferromagnet (Chapter 1, Section 3, Eq. (1.27)), it is mostly via the transferred field $\boldsymbol{B}_{tran}$ that the surrounding atoms influence the field seen by the nucleus. The replacement of a cobalt atom in the nearest neighbor (NN) structure of a cobalt atom will lead to a reduced $\boldsymbol{B}_{HF}$ seen by the corresponding Co nucleus for most foreign atoms, resulting in a resonance frequency shifted downwards compared to pure bulk cobalt. Only when a Co atom is replaced by an Fe is the $\boldsymbol{B}_{HF}$ at the nucleus increased and the resulting resonance frequency shifted upwards. The exact value of the shift depends on the nature of the foreign atom and has been calculated and verified experimentally for many different elements.[46] In most cases,

calculations are only precise for situations of extreme dilution and with a single impurity in the neighboring shell. On the other hand, experiments have shown that the contribution of additional foreign atoms in the NN shell can be approximated by an additional up- or downwards shift of the same value than the one observed when introducing the first foreign NN.[12] The contribution of further distant foreign atoms (next nearest neighbor, 3rd NN,…) on the $\boldsymbol{B}_{HF}$ of a ^{59}Co atom generally cannot be distinguished so clearly and only contributes to the broadening of the peaks in the NMR spectrum.

2.1. Binary alloys

Co/Fe composite materials have been studied in depth by ^{59}Co IF NMR, including bulk materials [4], [12], [44], [47]–[54], thin films and superlattices with interesting magnetic properties [55]–[61] and nanoparticle catalysts for carbon nanotube synthesis.[62] As an example, in **Figure 5** the ^{59}Co IF NMR results at 4.2 K of $Co_{60}Fe_{40}$ alloys are represented. The spectra were collected by Jay et al. [4] on samples prepared by arc melting. The sample on the left is called to be in a disordered state and corresponds to the sample directly after its synthesis, while the same sample is transformed into an ordered state by annealing. Both samples are fitted with 9 lines, corresponding to Co with 0 to 8 Fe as NN and with an upwards per additional NN Fe equal to 10.7 ± 0.5 MHz. Additional peaks corresponding to various numbers of Fe NNN or 3rd NN cannot be taken into account, as the fitting would become too complicated. Instead, the influence of these further distant neighbors accounts for the linewidth of each peak. The peak corresponding to a pure cobalt structure is centered at a frequency below 200 MHz and is assigned to body-centered cubic (*bcc*) Co, below the usually observed lines corresponding to *hcp* or *fcc* cobalt. *bcc* is not stable in pure Co, but is observed in different alloys or thin films, especially containing iron.[46], [57], [62] In fact, the stable iron crystalline structure is *bcc* and iron alloying causes the cobalt to form a *bcc* phase as well. The spectrum from the disordered alloy is mainly composed of Co with 3 or 4 Fe as NN and the NN distribution can be modelled by a binomial law. On the other hand, the main peak observed in the spectrum of the sample in an ordered state corresponds to Co with all 8 NN being Fe. The most stable form seems to be a perfect mixture of Co with only Fe as NN and only Co as NNN. Besides Co/Fe materials, different bulk composite materials that have been studied by IF NMR are made of Co-Cu[12], [44], [63]–[67], Co-Ni[44], [45], [68]–[70], Co-Cr[12], [44], [64], [69]–[71], Co-Mn[44], [64], [70]–[73], Co-V[69]–[71], [74], Co-Ru[12], [64], Co-Al[44], [69], Co-Ti [69]–[71], Co-Ge [69], Co-Si [69], Co-La[75].

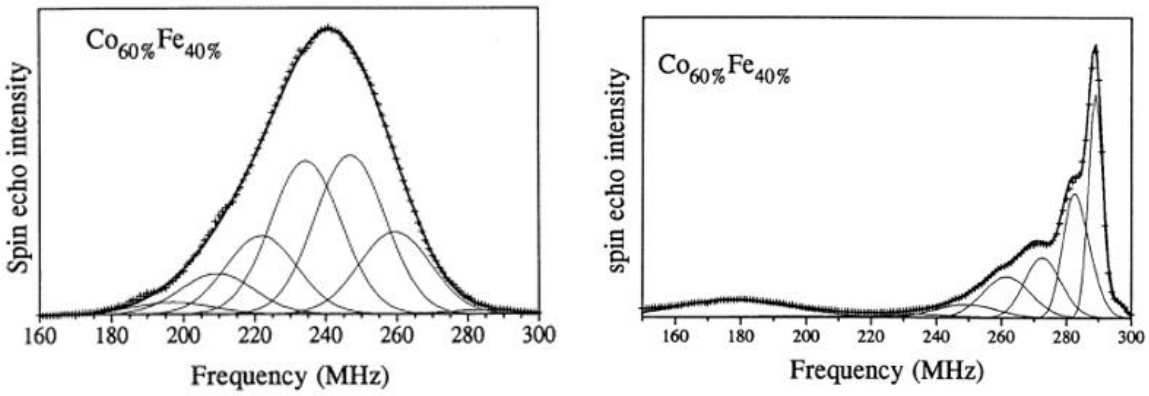

Figure 5: ^{59}Co IF NMR spectra at 4.2 K of $Co_{60}Fe_{40}$ alloys, in a disordered (left) and ordered state (right). Taken from [4]

A lot of information that has been obtained during the study of these different bulk alloy samples. They are of great use for the study of cobalt containing 2D materials: multilayers, superlattices and alloy thin films. 2D materials of Co combined with lots of different elements have been synthesized and studied and the main motivation is to seek materials with special magnetic properties like perpendicular anisotropy and giant magnetoresistance (GMR). The sample properties are influenced by many parameters, like the layer thicknesses, internal strain and interface topology, which can be indirectly studied by means of ^{59}Co IF NMR. In multilayer systems, different kinds of interfacial configurations are distinguished: continuous layered structures, discontinuous layered structures and granular systems, which have obviously an impact on the sample's magnetic behavior and the interlayer exchange coupling. All those sample characteristics are influenced by the synthesis method and parameters. The available synthesis methods include different sputtering techniques, molecular beam epitaxy (MBE), ion plasma spraying and ultrahigh vacuum (UHV) e-beam evaporation, at different temperatures, pressures and deposition rates and substrates.

2.2. Multilayers

The most studied cobalt containing multilayers are by far Co/Cu multilayers [55], [64], [76]–[86]. It has been found that due to the weak miscibility of Co and Cu, it is possible to form sharp interfaces by choosing the right synthesis parameters. This system is particularly well studied due to its pronounced GMR and the resulting application as magnetic field sensors in hard disk drives or sensors. In contrast, for elements that tend to form solid solutions or compounds with Co, inter-diffusion and interfacial mixing over several atomic planes can be observed. Those compounds are therefore often used as an alloy thin layer, instead of separated multilayers. One example are Fe-Co thin layers, which are used

for recording and sensing, due to their soft magnetic character.[59] Other Co containing binary systems studied in multilayer and thin film systems are synthesized in combination with Cr[55], [64], [79], Cr[55], [64], [79], Ni [76], Ag[76], [87], [88], Au[89], [90], Mn[64], [72], V[91], Ge[92], Mg[93], Al[94], Mo[95], Si[96]–[98], Pd[89] and Ir[89]. As an example of the multilayer study by ^{59}Co IF NMR, two spectra obtained from Co/Cu multilayers are represented in **Figure 6**. The left spectrum corresponds to a sample produced by magnetron sputtering and is taken from [78], where more information about the sample characteristics can be found. Besides the main peak of pure Co, the spectrum can be fitted with peaks corresponding to Co with 1 to 6 Cu as NN, which arise from Co at the Co/Cu interface. Per additional Cu NN, the peak is shifted downwards by 18 MHz. The peak intensity globally decreases with the amount of Cu as NN, only the 3 Cu NN peak is more intense than the one with 2 Cu NN. The relatively strong peak of this configuration can be explained by the fact that cobalt at a perfect Co/Cu interface will have 3 Cu atoms as NN. In the spectrum, peaks with a different amount of Cu NN are of a similar intensity than the 3 Cu NN one, representing a non-perfect interface with intermixing. The spectrum on the right is obtained from a sample produced by molecular beam epitaxy (MBE), as explained in [77]. No precise decomposition is presented; however, 3 peaks can clearly be distinguished and correspond to pure Co (216 MHz) and to Co with 1 (199 MHz) or 3 (169 MHz) Cu as nearest neighbor. The shift per additional Cu in the NN shell is around 16 MHz, which is a little lower than what was observed in the spectrum on the right. It can be seen that, in addition to the pure Co peak, the 3 Cu NN peak is the most intense, which is the sign of a good interface quality. Even though some signal coming from Co with different amounts of Cu NN can be observed, there is less intermixing at the Co/Cu interfaces than in the previously described sample.

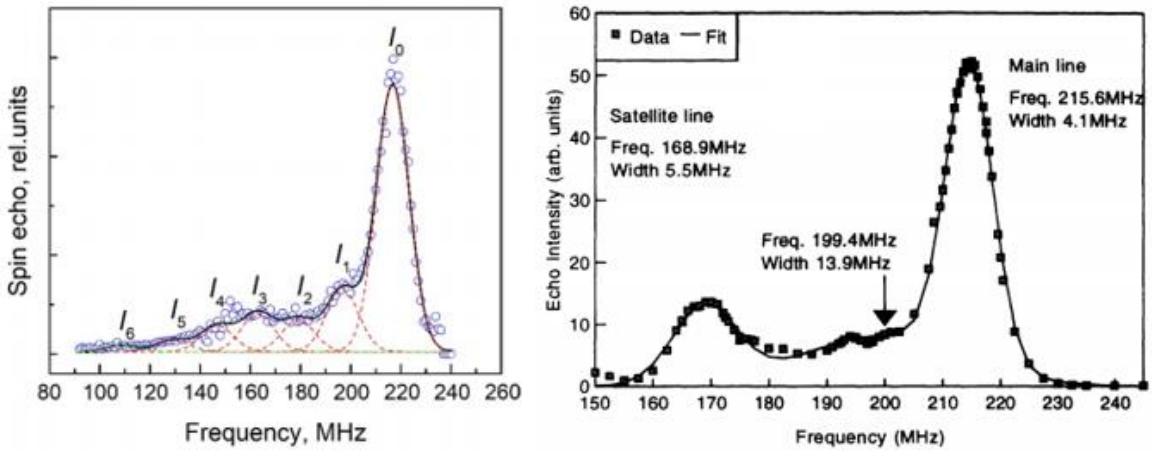

Figure 6: ^{59}Co IF NMR spectra collected from Co/Cu multilayers. Left: Sample produced by magnetron sputtering, spectrum taken from [78] Right: Sample produced by molecular beam epitaxy, spectrum taken from [77]

2.3. Other systems

Heusler alloys

Apart from all the binary alloy samples described in the sections above, different multi-atomic Heusler alloys have been analyzed by ^{59}Co NMR with a similar approach as in the case of binary alloys. First, different bulk samples have been analyzed in order to obtain more information about the hyperfine field distribution and the different observed satellite lines as function of the crystalline structure and atomic distribution inside the sample.[99]–[105] In later publications, also thin films constituted of different types of Heusler alloys have been investigated.[86], [106]–[108] The main drive for these studies is the better understanding of the local order inside materials with potential applications in spintronic devices as tunnel junctions or GMR elements.

Interstitial solid solutions

In all systems described in this section now, a foreign atom that enters a pure cobalt structure replaces a Co when forming alloys or intermixing at a surface. In contrast, small atoms, like carbon for example, do not replace atoms in the parent cobalt structure, but occupy interstitial sites when diffusing into it. The hyperfine field seen by a cobalt in such an interstitial solid solution is still strongly reduced, as the electron configuration of the Co structure is disturbed and the structure is expanding when a C atom is introduced. Such systems have been studied by few authors so far.[109]–[111] They found that the presence of a carbon on a cobalt nearest neighbor interstitial site leads to significant shift of the resonance frequency of this cobalt. A similar system will be the subject of Chapter 4, where the spectrum interpretation of such compounds will be explored in detail.

3. Summary

In this chapter, a literature overview of the ^{59}Co IF NMR studies of various systems was given. It will be the basis for the spectrum decomposition of the different types of samples studied in this thesis.

The ^{59}Co IF NMR resonance frequencies that correspond to signal from *fcc* cobalt are generally well-defined in the literature. At ambient temperature, a peak around 213 MHz can unambiguously be assigned to signal from *fcc* multi-domain (m.d.) structures. In comparison, the resonance frequency corresponding to *fcc* single-domain (s.d.) structures is slightly higher due to the presence of a demagnetizing field. The strength of the demagnetizing field and therefore the position of this peak depends on the size and shape of the Co structure, as well as the magnetic interactions with the surrounding. In the literature, the s.d. *fcc* peak is often observed around 216 MHz at ambient temperature. Both peaks are relatively narrow in general, especially compared to the peaks assigned to the more anisotropic *hcp* Co structures.

The assignment of the peaks corresponding to *hcp* Co structures is not as straightforward as for *fcc* Co structures and not always unified in the literature. In bulk materials, two well distinguished *hcp* m.d. peaks are sometimes observed, corresponding to signal form the center and the edge of domain walls (221.5 MHz and 214 MHz at ambient temperature, respectively). In reality, these two peaks are not always observed, especially for samples containing nanostructures. Instead, a broad peak around 219 MHz is often observed, which is then assigned to signal from *hcp* Co structures. Due to the large width of this peak, it is difficult to distinguish m.d. and s.d. *hcp* Co structures, unfortunately. In order to solve this issue, the power needed for an optimal excitation is analyzed, which is much lower for signal coming from domain-walls compared to signal coming from domains.

The evolution with temperature of the resonance frequencies corresponding to the different Co environments described above has been studied. They can all be approximated well using the first term of the spin-wave approximation, even though better fits can be obtained in some cases using the first two terms.

If inside a pure Co structure a nearest neighbor (NN) of a cobalt atom is replaced by a foreign atom, like in the case of alloying or at an interface, the internal field seen by this cobalt atom is changed. The consequence on the ^{59}Co IF NMR resonance frequency of such a substitution is often well approximated by a constant frequency shift per substituted NN atom. The value of this shift depends on the nature of this foreign atoms and was studied for many different elements, especially for copper (~ - 17 MHz) and iron (~ + 11 MHz). The case of interstitial solutions, with carbon for example, has only rarely been studied so far and is the subject of Chapter 4 of this work.

4. References

[1] A. S. Andreev, J.-B. d'Espinose de Lacaillerie, O. B. Lapina, and A. Gerashenko, "Thermal stability and hcp–fcc allotropic transformation in supported Co metal catalysts probed near operando by ferromagnetic NMR," *Phys. Chem. Chem. Phys.*, vol. 17, no. 22, pp. 14598–14604, 2015, doi: 10.1039/C4CP05327C.

[2] E. A. Owen and D. M. Jones, "Effect of Grain Size on the Crystal Structure of Cobalt," *Proc. Phys. Soc. Sect. B*, vol. 67, no. 6, pp. 456–466, Jun. 1954, doi: 10.1088/0370-1301/67/6/302.

[3] O. Kitakami, H. Sato, Y. Shimada, F. Sato, and M. Tanaka, "Size effect on the crystal phase of cobalt fine particles," *Phys. Rev. B*, vol. 56, no. 21, Art. no. 21, Dec. 1997, doi: 10.1103/PhysRevB.56.13849.

[4] J. Ph. Jay, M. Wójcik, and P. Panissod, "Hyperfine field and ordering in bcc CoFe bulk alloys studied by 59Co NMR and Monte-Carlo simulation," *Z. Für Phys. B Condens. Matter*, vol. 101, no. 4, Art. no. 4, Dec. 1996, doi: 10.1007/s002570050236.

[5] A. C. Gossard and A. M. Portis, "Observation of Nuclear Resonance in a Ferromagnet," *Phys. Rev. Lett.*, vol. 3, no. 4, pp. 164–166, Aug. 1959, doi: 10.1103/PhysRevLett.3.164.

[6] A. M. Portis and A. C. Gossard, "Nuclear Resonance in Ferromagnetic Cobalt," *J. Appl. Phys.*, vol. 31, no. 5, pp. S205–S213, May 1960, doi: 10.1063/1.1984666.

[7] V. Arp, D. Edmonds, and R. Petersen, "Hyperfine Coupling in CoFe and CoNi Alloys as Determined by Heat Capacity Measurements," *Phys. Rev. Lett.*, vol. 3, no. 5, pp. 212–214, Sep. 1959, doi: 10.1103/PhysRevLett.3.212.

[8] N. Kurti, "Experimental Determination of the Hyperfine Coupling in Ferromagnetic Metals and Alloys," *J. Appl. Phys.*, vol. 30, no. 4, pp. S215–S219, Apr. 1959, doi: 10.1063/1.2185895.

[9] E. C. Stoner, "Collective electron ferromagnetism," *Proc. Roy. Soc. Lond.*, vol. A165, pp. 372–414, 1938, doi: 10.1098/rspa.1938.0066.

[10] H. Suhl, "Effective Nuclear Spin Interactions in Ferromagnets," *Phys. Rev.*, vol. 109, no. 2, pp. 606–606, Jan. 1958, doi: 10.1103/PhysRev.109.606.

[11] Y. Koi, A. Tsujimura, and Y. Yukimoto, "The Temperature and Pressure Dependence of the Nuclear Resonance of 59Co in Face-Centered-Cubic Cobalt Metal," *J. Phys. Soc. Jpn.*, vol. 15, pp. 1342–1342, 1960, doi: 10.1143/JPSJ.15.1342.

[12] C. Meny, E. Jedryka, and P. Panissod, "Satellite structure of ^{59}Co NMR spectra in some Co alloys," *J. Phys. Condens. Matter*, vol. 5, no. 10, pp. 1547–1556, Mar. 1993, doi: 10.1088/0953-8984/5/10/012.

[13] P. Panissod and C. Mény, "Nuclear magnetic resonance investigations of the structure and magnetic properties of metallic multilayers and nanocomposites," *Appl. Magn. Reson.*, vol. 19, pp. 447–460, 2000, doi: 10.1007/BF03162388.

[14] H. K. Choudhary, M. Manjunatha, R. Damle, K. P. Ramesh, and B. Sahoo, "Solvent dependent morphology and ^{59}Co internal field NMR study of Co-aggregates synthesized by a wet chemical method," *Phys. Chem. Chem. Phys.*, vol. 20, no. 26, pp. 17739–17750, 2018, doi: 10.1039/C8CP01780H.

[15] R. Speight, A. Wong, P. Ellis, T. Hyde, P. T. Bishop, and M. E. Smith, "A 59Co NMR study to observe the effects of ball milling on small ferromagnetic cobalt particles," *Solid State Nucl. Magn. Reson.*, vol. 35, no. 2, pp. 67–73, Apr. 2009, doi: 10.1016/j.ssnmr.2008.12.001.

[16] M. Gellesch *et al.*, "Compositional analysis of multi-element magnetic nanoparticles with a combined NMR and TEM approach," *J. Nanoparticle Res.*, vol. 19, no. 9, Sep. 2017, doi: 10.1007/s11051-017-3975-7.

[17] H. Yasuoka and R. T. Lewis, "Temperature Dependence of Co 59 Nuclear Magnetic Resonance in Single-Domain Cobalt Particles," *Phys. Rev.*, vol. 183, no. 2, pp. 559–562, Jul. 1969, doi: 10.1103/PhysRev.183.559.

[18] M. Kawakami, T. Hihara, and Y. Koi, "The Co59 Nuclear Magnetic Resonance in Hexagonal Cobalt," *J. Phys. Soc. Jpn.*, vol. 33, pp. 1591–1598, 1972, doi: 10.1143/JPSJ.33.1591.

[19] E. A. Turov and M. P. Petrov, *Nuclear Magnetic Resonance in Ferro- and Antiferromagnets*. Jerusalem: Israel Program for scientific translations (Halsted Press), 1972.

[20] F. Bloch, "Zur Theorie des Ferromagnetismus," *Z. Für Phys.*, vol. 61, no. 3, pp. 206–219, Mar. 1930, doi: 10.1007/BF01339661.

[21] Y. Koi, A. Tsujimura, and T. Kushida, "NMR of Co59 in Ferromagnetic Hexagonal Cobal Metal," *J. Phys. Soc. Jpn.*, vol. 15, pp. 2100–2100, 1960, doi: 10.1143/JPSJ.15.2100.

[22] S. G. Bailey, D. C. Creagh, and G. V. H. Wilson, "Domain wall and 'domain' 59Co NMR in hexagonal cobalt," *Phys. Lett. A*, vol. 44, no. 3, pp. 229–230, Jun. 1973, doi: 10.1016/0375-9601(73)90895-5.

[23] C. W. Searle, H. P. Kunkel, S. Kupca, and I. Maartense, "NMR enhancement of a modulating field due to the anisotropic component of the hyperfine field in hcp Co and Y Co 5," *Phys. Rev. B*, vol. 15, no. 7, pp. 3305–3308, Apr. 1977, doi: 10.1103/PhysRevB.15.3305.

[24] D. Fekete, H. Boasson, A. Grayevski, V. Zevin, and N. Kaplan, "Anisotropic hyperfine interactions in ferromagnetic hcp Co," *Phys. Rev. B*, vol. 17, no. 1, pp. 347–354, Jan. 1978, doi: 10.1103/PhysRevB.17.347.

[25] H. Brömer and H. L. Huber, "Nuclear magnetic resonance in ferromagnetic HCP and FCC 59cobalt," *J. Magn. Magn. Mater.*, vol. 8, no. 1, pp. 61–64, Mar. 1978, doi: 10.1016/0304-8853(78)90077-X.

[26] H. P. Kunkel and C. W. Searle, "Experimental identification of domain-wall-center and domain-wall-edge NMR resonances in magnetically ordered materials," *Phys. Rev. B*, vol. 23, no. 1, pp. 65–68, Jan. 1981, doi: 10.1103/PhysRevB.23.65.

[27] H. Enokiya, "Nuclear Magnetic Resonance and Nuclear Relaxation in hcp Cobalt," *J. Phys. Soc. Jpn.*, vol. 42, no. 3, Art. no. 3, Mar. 1977, doi: 10.1143/JPSJ.42.796.

[28] M. Kawakami and H. Enokiya, "Anomaly in Temperature Dependence of 59Co NMR Frequency in HCP Co," *J. Phys. Soc. Jpn.*, vol. 55, no. 11, Art. no. 11, Nov. 1986, doi: 10.1143/JPSJ.55.4038.

[29] W. Sucksmith and J. E. Thompson, "The Magnetic Anisotropy of Cobalt," *Proc. R. Soc. Lond.*, vol. 225, no. 1162, Art. no. 1162, 1954, doi: 10.1098/rspa.1954.0209.

[30] E. F. Bertaut, A. Delpalme, and R. Pauthenet, "Rotation des spins dans le cobalt hexagonal," *J. Phys. France*, vol. 25, no. 5, pp. 610–614, 1964, doi: 10.1051/jphys:01964002505061000.

[31] C. R. Houska, B. L. Averbach, and M. Cohen, “The cobalt transformation,” *Acta Metall.*, vol. 8, no. 2, pp. 81–87, Feb. 1960, doi: 10.1016/0001-6160(60)90088-2.

[32] H. Bibring and F. Sebilleau, “Structure et transformation allotropique du cobalt,” *Rev. Métallurgie*, vol. 52, no. 7, pp. 569–578, Jul. 1955, doi: 10.1051/metal/195552070569.

[33] A. C. Gossard, A. M. Portis, M. Rubinstein, and R. H. Lindquist, “Ferromagnetic Nuclear Resonance of Single-Domain Cobalt Particles,” *Phys. Rev.*, vol. 138, no. 5A, pp. A1415–A1421, May 1965, doi: 10.1103/PhysRev.138.A1415.

[34] D. L. Leslie-Pelecky and R. D. Rieke, “Magnetic Properties of Nanostructured Materials,” *Chem. Mater.*, vol. 8, no. 8, Art. no. 8, 1996, doi: 10.1021/cm960077f.

[35] V. A. Bautin, A. G. Seferyan, M. S. Nesmeyanov, and N. A. Usov, “Magnetic properties of polycrystalline cobalt nanoparticles,” *AIP Adv.*, vol. 7, no. 4, Art. no. 4, Apr. 2017, doi: 10.1063/1.4979889.

[36] Y. D. Zhang, J. I. Budnick, W. A. Hines, S. A. Majetich, and E. M. Kirkpatrick, “Microstructure and magnetic behavior of carbon-coated Co nanoparticles studied by nuclear magnetic resonance,” *Appl. Phys. Lett.*, vol. 76, no. 1, Art. no. 1, Jan. 2000, doi: 10.1063/1.125667.

[37] Y. Liu *et al.*, “Sampling the structure and chemical order in assemblies of ferromagnetic nanoparticles by nuclear magnetic resonance,” *Nat. Commun.*, vol. 7, no. 1, Art. no. 1, Sep. 2016, doi: 10.1038/ncomms11532.

[38] I. V. Yakovlev *et al.*, “Superparamagnetic behaviour of metallic Co nanoparticles according to variable temperature magnetic resonance,” *Phys. Chem. Chem. Phys.*, vol. 23, no. 4, Art. no. 4, 2021, doi: 10.1039/D0CP05963C.

[39] A. S. Andreev *et al.*, “Magnetic and dielectric properties of carbon nanotubes with embedded cobalt nanoparticles,” *Carbon*, vol. 114, pp. 39–49, Apr. 2017, doi: 10.1016/j.carbon.2016.11.070.

[40] V. V. Matveev, D. A. Baranov, G. Yu. Yurkov, N. G. Akatiev, I. P. Dotsenko, and S. P. Gubin, “Cobalt nanoparticles with preferential hcp structure: A confirmation by X-ray diffraction and NMR,” *Chem. Phys. Lett.*, vol. 422, no. 4–6, pp. 402–405, May 2006, doi: 10.1016/j.cplett.2006.02.099.

[41] M. Manjunatha, G. S. Reddy, K. J. Mallikarjunaiah, R. Damle, and K. P. Ramesh, “Determination of Phase Composition of Cobalt Nanoparticles Using 59Co Internal Field Nuclear Magnetic Resonance,” *J. Supercond. Nov. Magn.*, Mar. 2019, doi: 10.1007/s10948-019-5083-7.

[42] A. P. Guimarães, *Magnetism and magnetic resonance in solids*. New York: John Wiley & Sons, 1998.

[43] P. Panissod, “Structural and Magnetic Investigations of Ferromagnets by NMR. Application to Magnetic Metallic Multilayers,” in *Frontiers in Magnetism of Reduced Dimension Systems*, Dordrecht, 1998, pp. 225–270.

[44] Y. Koi, A. Tsujimura, T. Hihara, and T. Kushida, “NMR of Co59 in Ferromagnetic Cobalt Alloys,” *J. Phys. Soc. Jpn.*, vol. 16, pp. 574–574, 1961, doi: 10.1143/JPSJ.16.574.

[45] L. H. Bennett and R. L. Streever, “Internal Magnetic Fields in Nickel-Rich Nickel-Cobalt Alloys,” *J. Appl. Phys.*, vol. 33, no. 3, Art. no. 3, Mar. 1962, doi: 10.1063/1.1728614.

[46] P. C. Riedi, T. Thomson, and G. J. Tomka, “Chapter 2 NMR of thin magnetic films and superlattices,” in *Handbook of Magnetic Materials*, vol. 12, Elsevier, 1999, pp. 97–258. doi: 10.1016/S1567-2719(99)12006-7.

[47] M. Rubinstein, “Hyperfine Field Spectra of Binary Fe-Co Alloys: Nuclear Magnetic Resonance of Fe 57 and Co 59,” *Phys. Rev.*, vol. 172, no. 2, Art. no. 2, Aug. 1968, doi: 10.1103/PhysRev.172.277.

[48] G. H. Strauss and D. W. Forester, “Short-Range Order Effects on ^{59} Co NMR Spectra in Equiatomic FeCo,” *J. Appl. Phys.*, vol. 42, no. 4, Art. no. 4, Mar. 1971, doi: 10.1063/1.1660228.

[49] G. H. Stauss, “Hyperfine Fields in Dilute Alloys of Co in Fe,” *Phys. Rev. B*, vol. 4, no. 9, Art. no. 9, Nov. 1971, doi: 10.1103/PhysRevB.4.3106.

[50] Y. Muaoka, M. Shiga, H. Yasuoka, and Y. Nakamura, “NMR Study of ordered and disordered Fe-Co Alloy,” *J. Phys. Soc. Jpn.*, vol. 40, no. 2, Art. no. 2, Feb. 1976, doi: 10.1143/JPSJ.40.414.

[51] V. Pierron-Bohnes, M. C. Cadeville, and F. Gautier, “Magnetism and local order in dilute FeCo alloys,” *J. Phys. F Met. Phys.*, vol. 13, no. 8, Art. no. 8, Aug. 1983, doi: 10.1088/0305-4608/13/8/014.

[52] I. G. Shmakov, O. I. Gorbatov, V. V. Serikov, N. M. Kleinerman, O. A. Golovnya, and Yu. N. Gornostyrev, “Short-range order formation in Fe-Co alloys: NMR study and first-principles calculations,” *J. Alloys Compd.*, vol. 782, pp. 1008–1014, Apr. 2019, doi: 10.1016/j.jallcom.2018.12.192.

[53] V. V. Serikov, N. M. Kleinerman, and O. A. Golovnya, “NMR and Mössbauer study of peculiarities of the structure formation in Fe–Co alloys,” *Phys. Met. Metallogr.*, vol. 118, no. 11, Art. no. 11, Nov. 2017, doi: 10.1134/S0031918X1711014X.

[54] J.-P. Jay, “Etude par résonance magnétique nucléaire de l’ordre à courte distance dans le système cobalt/fer: de l’alliage massif à la multicouche,” Université Louis Pasteur (Strasbourg I), Strasbourg, 1995. [Online]. Available: https://tel.archives-ouvertes.fr/tel-00003414/

[55] P. Panissod, J. P. Jay, C. Meny, M. Wojcik, and E. Jedryka, “NMR analysis of buried metallic interfaces,” *Hyperfine Interact.*, vol. 97–98, no. 1, Art. no. 1, Dec. 1996, doi: 10.1007/BF02150169.

[56] Ph. Houdy *et al.*, “Magnetic and structural properties of rf-sputtered Co/Fe and Co/Cr multilayers,” *J. Appl. Phys.*, vol. 69, no. 8, Art. no. 8, Apr. 1991, doi: 10.1063/1.347930.

[57] J. Dekoster, E. Jedryka, C. Mény, and G. Langouche, “Epitaxial growth of bcc Co/Fe superlattices,” *J. Magn. Magn. Mater.*, vol. 121, no. 1–3, Art. no. 1–3, Mar. 1993, doi: 10.1016/0304-8853(93)91151-V.

[58] Th. Mühge, Th. Zeidler, Q. Wang, Ch. Morawe, N. Metoki, and H. Zabel, “Structural and magnetic studies of $Fe_x Co_{1-x}$ (001) alloy films on MgO(001) substrates,” *J. Appl. Phys.*, vol. 77, no. 3, Art. no. 3, Feb. 1995, doi: 10.1063/1.358965.

[59] M. Wojcik, J. P. Jay, P. Panissod, E. Jedryka, J. Dekoster, and G. Langouche, “New phases and chemical short range order in co-deposited CoFe thin films with bcc structure: an NMR study,” *Z. Für Phys. B Condens. Matter*, vol. 103, no. 1, Art. no. 1, Mar. 1997, doi: 10.1007/s002570050327.

[60] N. A. Lesnik *et al.*, “Local structure in CoFe/Al2O3 multilayers determined by nuclear magnetic resonance,” *J. Magn. Magn. Mater.*, vol. 242–245, pp. 943–945, Apr. 2002, doi: 10.1016/S0304-8853(01)01306-3.

[61] H. G. Silva *et al.*, “Magnetic and transport properties of diluted granular multilayers,” *J. Appl. Phys.*, vol. 106, no. 11, Art. no. 11, Dec. 2009, doi: 10.1063/1.3266010.

[62] A. S. Andreev *et al.*, "Internal field 59Co NMR study of cobalt-iron nanoparticles during the activation of CoFe2/CaO catalyst for carbon nanotube synthesis," *J. Catal.*, vol. 358, pp. 62–70, Feb. 2018, doi: 10.1016/j.jcat.2017.11.025.

[63] E. H. C. P. Sinnecker, I. S. Oliveira, P. Tiberto, and A. P. Guimarães, "Magnetic and structural properties of Cu–Co granular alloys measured with NMR," *J. Magn. Magn. Mater.*, vol. 218, no. 2–3, Art. no. 2–3, Aug. 2000, doi: 10.1016/S0304-8853(00)00424-8.

[64] M. Malinowska, C. Mény, E. Jedryka, and P. Panissod, "The anisotropic first-neighbour contribution to the hyperfine field in hexagonal-close-packed Co: a nuclear magnetic resonance study of diluted alloys and multilayers," *J. Phys. Condens. Matter*, vol. 10, no. 22, Art. no. 22, Jun. 1998, doi: 10.1088/0953-8984/10/22/016.

[65] M. Malinowska *et al.*, "Identification of magnetic phases in granular Co10Cu90 alloy using 59Co NMR method," *J. Magn. Magn. Mater.*, vol. 198–199, pp. 599–601, 1999, doi: S0304-8853(98)01222-0.

[66] J. P. Jay, I.-S. Jurca, G. Pourroy, N. Viart, C. Mény, and P. Panissod, "59Co NMR study in Co–Fe alloys/Co magnetite composites," *Solid State Sci.*, vol. 3, no. 3, Art. no. 3, Mar. 2001, doi: 10.1016/S1293-2558(00)01100-6.

[67] S. Dhara, R. R. Chowdhury, and B. Bandyopadhyay, "Disorder in Co-Cu granular alloys studied by 59Co NMR," *J. Magn. Magn. Mater.*, vol. 471, pp. 355–358, Feb. 2019, doi: 10.1016/j.jmmm.2018.09.099.

[68] P. C. Riedi and R. G. Scurlock, "Satellite Lines in the ^{59} Co Resonance in Cobalt-Nickel Alloys," *J. Appl. Phys.*, vol. 39, no. 2, Art. no. 2, Feb. 1968, doi: 10.1063/1.1656243.

[69] S.-I. Kobayashi, K. Asayama, and J. Itoh, "Nuclear magnetic Resonance in Co Alloys," *J. Phys. Soc. Jpn.*, vol. 21, no. 1, Art. no. 1, Jan. 1966, doi: 10.1143/JPSJ.21.65.

[70] T. M. Shavishvili and I. G. Kiliptari, "Distribution of hyperfine fields and magnetic perturbation in cobalt alloys with 3d transition metals," *Phys. Status Solidi B*, vol. 92, no. 1, Art. no. 1, Mar. 1979, doi: 10.1002/pssb.2220920105.

[71] M. Kawakami, "Co-59 NMR in hexagonal cobalt-based dilute alloys with 3D-transition metals," *J. Phys. Soc. Jpn.*, vol. 40, no. 1, Art. no. 1, 1976, doi: 10.1143/JPSJ.40.56.

[72] T. Thomson, P. C. Riedi, Q. Wang, and H. Zabe, "59Co and 55Mn NMR of CoMn alloys and multilayers," *J. Appl. Phys.*, vol. 79, no. 8, Art. no. 8, 1996, doi: 10.1063/1.362044.

[73] H. Yasuoka, S. Hoshinouchi, Y. Nakamura, M. Matsui, and K. Adachi, "Nuclear Magnetic Resonance of Co59 in Co-Mn Alloys," *Phys. Status Solidi B*, vol. 46, no. 2, Art. no. 2, Aug. 1971, doi: 10.1002/pssb.2220460248.

[74] M. Kawakami and Y. Aoki, "Phase dependent NMR spectra of Co-rich CoV alloys," *J. Phys. F Met. Phys.*, vol. 10, no. 9, Art. no. 9, Sep. 1980, doi: 10.1088/0305-4608/10/9/023.

[75] H. Nakamura, A. Shimoda, T. Waki, Y. Tabata, and C. Mény, "Site-dependent cobalt electronic state in La–Co co-substituted magnetoplumbite-type ferrite: ^{59} Co nuclear magnetic resonance study," *J. Phys. Condens. Matter*, vol. 28, no. 34, Art. no. 34, Sep. 2016, doi: 10.1088/0953-8984/28/34/346002.

[76] E. A. M. van Alphen, S. G. E. te Velthuis, H. A. M. de Gronckel, K. Kopinga, and W. J. M. de Jonge, "NMR study of the strain in Co-based multilayers," *Phys. Rev. B*, vol. 49, no. 24, Art. no. 24, Jun. 1994, doi: 10.1103/PhysRevB.49.17336.

[77] T. Thomson, P. C. Riedi, and D. Greig, "Interfacial quality and giant magnetoresistance in MBE-grown Co/Cu(111) superlattices," *Phys. Rev. B*, vol. 50, no. 14, Art. no. 14, Oct. 1994, doi: 10.1103/PhysRevB.50.10319.

[78] S. A. Chuprakov *et al.*, "Nuclear Magnetic Resonance and X-ray Reflectometry of Co/Cu Superlattices," *Appl. Magn. Reson.*, vol. 50, no. 1–3, Art. no. 1–3, Mar. 2019, doi: 10.1007/s00723-018-1090-2.

[79] E. Jędryka, M. Wójcik, S. Nadolski, D. Kubinski, M. Parsons, and H. Holloway, "Effect of deposition sequence on interface intermixing in Cu/Co/Ru and Ru/Co/Cu multilayers studied by NMR," *J. Appl. Phys.*, vol. 91, no. 10, Art. no. 10, 2002, doi: 10.1063/1.1448801.

[80] C. Mény, P. Panissod, and R. Loloee, "Structural study of cobalt-copper multilayers by NMR," *Phys. Rev. B*, vol. 45, no. 21, Art. no. 21, Jun. 1992, doi: 10.1103/PhysRevB.45.12269.

[81] F. Schreiber, H. A. M. de Gronckel, I. A. Garifullin, P. Bödeker, K. Bröhl, and J. Pelzl, "Ferromagnetic and nuclear magnetic resonance studies of Co/Cu(111) superlattices: anisotropy and structural properties," *J. Magn. Magn. Mater.*, vol. 148, no. 1–2, Art. no. 1–2, Jul. 1995, doi: 10.1016/0304-8853(95)00187-5.

[82] H. A. M. de Gronckel, K. Kopinga, W. J. M. de Jonge, P. Panissod, J. P. Schillé, and F. J. A. den Broeder, "Nanostructure of Co/Cu multilayers," *Phys. Rev. B*, vol. 44, no. 16, Art. no. 16, Oct. 1991, doi: 10.1103/PhysRevB.44.9100.

[83] K. Le Dang, P. Veillet, E. Vélu, S. S. P. Parkin, and C. Chappert, "Influence of crystal structure on the magnetoresistance of Co/Cu multilayers," *Appl. Phys. Lett.*, vol. 63, no. 1, Art. no. 1, Jul. 1993, doi: 10.1063/1.109728.

[84] K. Le Dang, P. Veillet, Hui He, F. J. Lamelas, C. H. Lee, and R. Clarke, "NMR study of interface structure in epitaxial Co-Cu superlattices," *Phys. Rev. B*, vol. 41, no. 18, Art. no. 18, Jun. 1990, doi: 10.1103/PhysRevB.41.12902.

[85] K. Inomata, Y. Saito, and S. Hashimoto, "Giant magnetoresistance with low saturation fields in Co-Fe/Cu and Ni80Fe20/Cu multilayers induced by optimized Ar acceleration voltage in ion beam sputtering," *J. Magn. Magn. Mater.*, vol. 121, no. 1–3, Art. no. 1–3, Mar. 1993, doi: 10.1016/0304-8853(93)91219-W.

[86] S. Wurmehl, "Nuclear magnetic resonance studies of materials for spintronic applications," *Appl Phys*, p. 28, 2008, doi: 10.1088/0022-3727/41/17/173002.

[87] E. A. M. van Alphen and W. J. M. de Jonge, "Granular Co/Ag multilayers: Relation between nanostructure, and magnetic and transport properties," *Phys. Rev. B*, vol. 51, no. 13, Art. no. 13, Apr. 1995, doi: 10.1103/PhysRevB.51.8182.

[88] E. Jędryka *et al.*, "Heat-induced nanocluster formation in codeposited Ag1−xCox thin films: Nuclear magnetic resonance study," *J. Appl. Phys.*, vol. 95, no. 5, Art. no. 5, Mar. 2004, doi: 10.1063/1.1645997.

[89] H. A. M. de Gronckel, J. A. M. Bienert, F. J. A. den Broeder, and W. J. M. de Jonge, "Co/X multilayers, NMR study of microscopic structure and strain," *J. Magn. Magn. Mater.*, vol. 93, pp. 457–461, Feb. 1991, doi: 10.1016/0304-8853(91)90383-L.

[90] M. Wojcik, C. Christides, E. Jedryka, S. Nadolski, and I. Panagiotopoulos, "Formation of a Co nanostructure revealed by 59 Co nuclear magnetic resonance measurements in Co/Au multilayers," *Phys. Rev. B*, vol. 63, no. 1, Art. no. 1, Dec. 2000, doi: 10.1103/PhysRevB.63.012102.

[91] T. Thomson, P. C. Riedi, and R. Krishnan, "59Co nuclear magnetic resonance study of molecular-beam epitaxy grown Co/V multilayers," *J. Appl. Phys.*, vol. 87, no. 9, Art. no. 9, May 2000, doi: 10.1063/1.372781.

[92] G. S. Patrin *et al.*, "Synthesis and magnetic states of cobalt in three-layer Co/Ge/Co films," *Phys. Solid State*, vol. 56, no. 2, Art. no. 2, Feb. 2014, doi: 10.1134/S1063783414020255.

[93] M.-H. Hu *et al.*, "Investigation of the thermal stability of Mg/Co periodic multilayers for EUV applications," *Appl. Phys. A*, vol. 106, no. 3, Art. no. 3, Mar. 2012, doi: 10.1007/s00339-011-6681-9.

[94] H. A. M. de Gronckel, H. Kohlstedt, and C. Daniels, "Prerequisites for high-quality magnetic tunnel junctions: XPS and NMR study of Co/Al bilayers," *Appl. Phys. Mater. Sci. Process.*, vol. 70, no. 4, Art. no. 4, Apr. 2000, doi: 10.1007/s003390051063.

[95] P. Nawrocki, A. Pietruczik, A. Wawro, and M. Wojcik, "Epitaxial Co1-xMox thin film alloys studied by 59Co NMR," *J. Alloys Compd.*, vol. 788, pp. 559–564, Jun. 2019, doi: 10.1016/j.jallcom.2019.02.232.

[96] N. Yaacoub, C. Meny, C. Ulhaq-Bouillet, M. Acosta, and P. Panissod, "Short period magnetic coupling oscillations in Co ⁄ Si multilayers: Role of crystallization and interface quality," *Phys. Rev. B*, vol. 75, no. 17, Art. no. 17, May 2007, doi: 10.1103/PhysRevB.75.174402.

[97] N. Yaacoub, C. Meny, O. Bengone, and P. Panissod, "Reduced interfacial mixing and exchange coupling in Co/Si multilayers," *J. Magn. Magn. Mater.*, vol. 316, no. 2, Art. no. 2, Sep. 2007, doi: 10.1016/j.jmmm.2007.03.161.

[98] M. Vélez *et al.*, "Amorphous to polycrystalline transition in Co_xSi_1-x alloy thin films," *Eur. Phys. J. B*, vol. 41, no. 4, Art. no. 4, Oct. 2004, doi: 10.1140/epjb/e2004-00345-0.

[99] S. Wurmehl *et al.*, "Effects of random distribution of Mn,Fe in Co2Mn1−xFexSi Heusler compounds probed by Mn55 nuclear magnetic resonance," *J. Appl. Phys.*, vol. 103, no. 7, Art. no. 7, Apr. 2008, doi: 10.1063/1.2831359.

[100] S. Wurmehl *et al.*, "Local formation of a Heusler structure in CoFe–Al alloys," *Appl. Phys. Lett.*, vol. 98, no. 1, Art. no. 1, Jan. 2011, doi: 10.1063/1.3517490.

[101] A. Shinogi, "The origin of the positive hyperfine field at 59Co in a ferromagnetic Heusler Alloy: Co2TiAl," *J. Phys. Soc. Jpn.*, vol. 54, no. 1, Art. no. 1, Jan. 1985, doi: 10.1143/JPSJ.54.400.

[102] S. Wurmehl *et al.*, "Probing the random distribution of half-metallic Co2Mn1−xFexSi Heusler alloys," *Appl. Phys. Lett.*, vol. 91, no. 5, Art. no. 5, Jul. 2007, doi: 10.1063/1.2760158.

[103] A. Shinogi, M. Tanaka, and K. Endo, "Positive contribution to the Hyperfine Fields at Co nucleus in the Heusler Alloys; Co2TiSn and Co2-x(Ni,Fe)xTiSn," *J. Phys. Soc. Jpn.*, vol. 44, no. 3, Art. no. 3, Mar. 1978, doi: 10.1143/JPSJ.44.774.

[104] S. Wurmehl *et al.*, "Electronic structure and spectroscopy of the quaternary Heusler alloy $Co_2Cr_{1-x}Fe_xAl$," *J. Phys. Appl. Phys.*, vol. 39, no. 5, Art. no. 5, Mar. 2006, doi: 10.1088/0022-3727/39/5/S06.

[105] S. Wurmehl, J. T. Kohlhepp, H. J. M. Swagten, and B. Koopmans, "^{59}Co nuclear magnetic resonance study of the local distribution of atoms in the Heusler compound $Co_2FeAl_{0.5}Si_{0.5}$," *J. Appl. Phys.*, vol. 111, no. 4, Art. no. 4, Feb. 2012, doi: 10.1063/1.3684686.

[106] S. Wurmehl, J. T. Kohlhepp, H. J. M. Swagten, and B. Koopmans, "Hyperfine field distribution in the Heusler compound Co_2FeAl probed by ^{59}Co nuclear magnetic resonance," *J. Phys. Appl. Phys.*, vol. 41, no. 11, Art. no. 11, Jun. 2008, doi: 10.1088/0022-3727/41/11/115007.

[107] S. Wurmehl and J. T. Kohlhepp, "NMR Spectroscopy on Heusler Thin films - a review," *SPIN*, vol. 04, no. 04, Art. no. 04, Dec. 2014, doi: 10.1142/S2010324714400190.

[108] S. Wurmehl *et al.*, "Off-stoichiometry in Co_2FeSi thin films sputtered from stoichiometric targets revealed by nuclear magnetic resonance," *J. Phys. Appl. Phys.*, vol. 42, no. 8, Art. no. 8, Apr. 2009, doi: 10.1088/0022-3727/42/8/084017.

[109] M. C. Cadeville, F. Gautier, and C. Robert, "Cadeville et al. 1972 - Electronic Structure of nickel and cobalt-carbon interstitial alloys.pdf," in *Proc. 13th Low Temperature Conference*, Boulder, 1972, vol. 4, pp. 325–331.

[110] M. C. Cadeville and C. Lerner, "On the electronic structure of interstitial transition-metal based alloys with boron and carbon impurities: Part I. Experimental study," *Philos. Mag.*, vol. 33, no. 5, Art. no. 5, May 1976, doi: 10.1080/14786437608221917.

[111] K. Hiraoka, A. Oota, and H. Jinushi, "NMR and Magnetic Studies of Mechanically Alloyed $Co_{75}C_{25}$," *J. Phys. Soc. Jpn.*, vol. 77, no. 7, Art. no. 7, Jul. 2008, doi: 10.1143/JPSJ.77.074705.

Chapter 3: Materials and methods

In this chapter, a detail description of the ^{59}Co IF NMR experiments is given, including information about the experimental set-up, the NMR sequences and the data treatment. An objective of this description is to open up the use of this technique to potential future users, as the literature often lacks information about the experimental details.

First, the experimental set-up, including probe and spectrometer, and the used pulse sequences are described. In addition, this section contains explanations of the different parameters that need to be modified in some cases or taken into account when doing a quantitative analyses.

Afterwards, an example for the spectrum interpretation of a pure cobalt sample is shown in order to visualize the methodology of this step.

Finally, the data treatment procedure of a point-by-point acquisition is explained in detail. The different steps from the spin-echo signal to the intensity in the spectrum at the tested frequency are described.

Besides ^{59}Co IF NMR, different analytical techniques have been used in this work for verification and to obtain supplementary information. More detailed descriptions of these techniques are provided in the chapter corresponding to the samples studied by each technique

Chapter 3: Materials and methods

1. IF NMR

1.1. Experimental setup & sequences

NMR Probes

The main experiments performed on all samples in this work is ^{59}Co IF NMR, carried out without the application an external magnetic field. Most of the experiments have been performed using a commercial (NMR-service, Germany) low-temperature static NMR/NQR probe. The probe is equipped with a 5 mm solenoid coil, as shown in the top of **Figure 1**, and allows covering frequencies between 130 MHz and 250 MHz with tuning and matching trimmer capacitors without the necessity of changing a capacitor or the inductive coil. In addition, the probe allows to perform experiments at temperatures down to liquid Helium (4.2 K). The probe was inserted into an Oxford cryostat during all the experiments, even those carried out at ambient temperature, in order to assure a good shielding of the probe head and the sample. To perform experiment outside of the frequency range of this probe, two different probes have been used: A commercial Bruker (Germany) broadband probe with exchangeable capacitors and coils for the experiments between 80 MHz and 130 MHz and an NMR-Service (Germany) NQR-tabletop probe with exchangeable 5 mm coils for the experiments below 80 MHz. Those last two probes are suitable for ambient temperatures experiments only. A picture of the latter one can be found in the bottom of **Figure 1**, equipped with a home-made 5 mm coil of 64 turns and with a 15 Ω resistance in series, used for experiments at very low frequencies. For all experiments, the samples were put into shortened 5 mm glass NMR-tubes and the sample centered inside the coil. Due to the fact that metallic cobalt can easily oxidize, the cobalt inside the samples has to be protected in some way from the oxygen in the atmosphere. In some samples the cobalt is already protected inside a matrix, while in other cases the sample containing tubes had to be prepared inside a glovebox and sealed with a flame or a septum and epoxy glue. As a reminder, Cobalt oxides are antiferromagnetic and therefore do not give an NMR signal without the application of an external magnetic field.

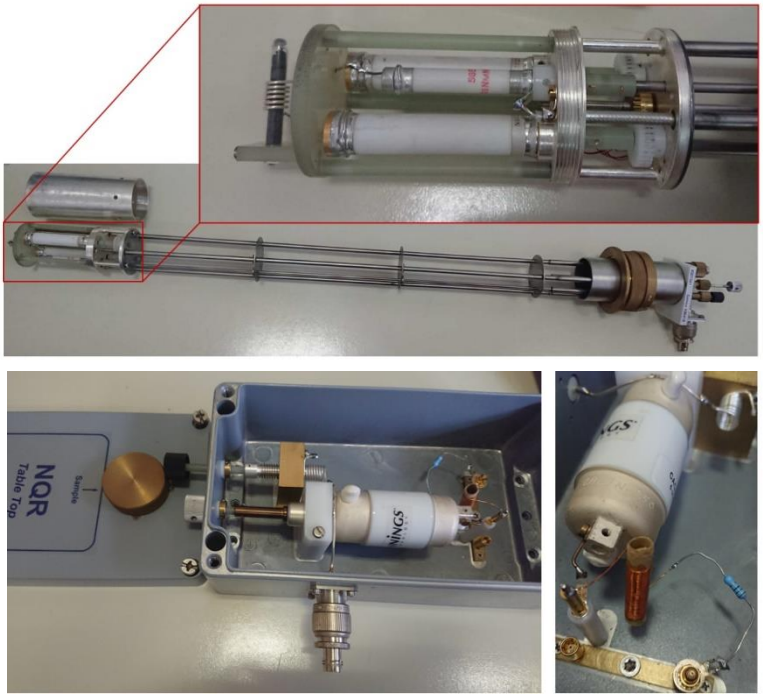

Figure 1: Pictures of two of the employed probes - Top: NMR-service low-temperature NMR/NQR probe, with a 5 mm coil. The sample is the black powder in the sealed glass tube. Bottom: NMR-service NQR tabletop probe, with a home-made 5 mm coil and a 15 Ω resistance in the circuit.

Spectrometer and sequences

The main part of the experiments has been performed on a TECMAG (USA) tabletop Scout spectrometer. Only for experiments in a small frequency range (14 – 80 MHz), a Bruker Avance III 500 spectrometer was used. In this frequency region, no adequate transcoupler was available to us for the TECMAG Scout spectrometer Due to the extremely broad character of the spectra, they have been recorded by a point-by point technique, with frequency steps between 0.5 MHz and 2 MHz generally. The signal intensity at each point has been determined with a solid spin-echo sequence, composed of two pulses of equal length: [$t_p - \tau - t_p$], as represented in **Figure 2**. After a time τ following the second pulse, the spins, which were precessing in the transverse plane and were distributed randomly due to field inhomogeneities, refocus and give a spin-echo signal.[1] In contrast to a classical [$\frac{\pi}{2} - \tau - \pi$] spin-echo sequence, this solid-echo sequence also allows to refocus the quadrupolar interaction part of the spins. The advantage of using an echo experiment is to dissociate the acquisition time from the instrumental dead time (t_{dead}), as will be discussed in the Supplementary Information of Chapter 4. To obtain the signal intensity, first a Fourier transformation (FT) on the second half of the echo signal

is performed. After phasing and baseline correction in the frequency domain, the signal intensity is determined by integration of the peak. More details about data acquisition and treatment for a point-by-point spectrum are presented later in Section 1.3. The pulse length was varied for some experiments but was generally equal to 1 µs. The interpulse delay (τ) and the repetition rate were generally equal to 8 µs and 100 Hz, respectively, but were varied for some experiments, especially those performed at low temperature.

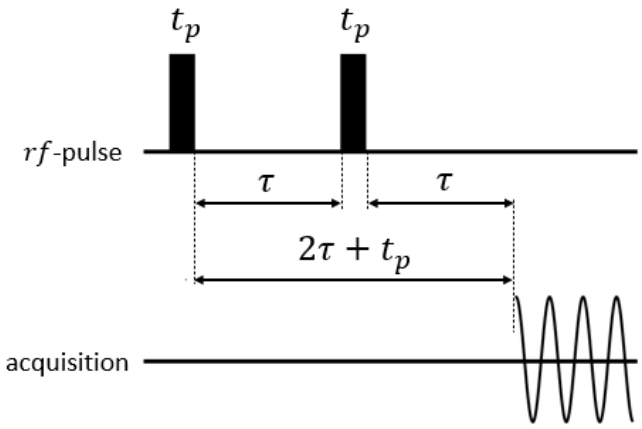

Figure 2: Schematic representation of a solid spin-echo sequence. t_p is the pulse length and τ is the interpulse delay. Adapted from [2].

To choose the acquisition parameters, one needs to consider the lifetime of the spin coherence, that is of the transverse magnetization, and its variation with temperature and frequency. There are two phenomena that lead to a random distribution of the nuclear spins in the transverse plane. The first one is due to constant field inhomogeneities and defines the maximum length of an FID/ spin-echo signal, $T_2{}'$. This effect is time independent and is therefore perfectly refocused in the spin-echo. The second one is the transverse relaxation T_2, which is due to random fluctuations of the local magnetic fields and is not refocused by the spin-echo due to its entropic nature.[3] Both effects lead no near-exponential decays and the times $T_2{}'$ and T_2 mentioned above are the characteristic times of these exponential phenomena. Both times are taken into consideration when choosing the length of τ. τ has to be longer than T_2' for all spins to be oriented randomly in the transverse plane before the 2nd pulse, which is important to avoid interference of the FID generated by the first pulse with the one generated with the second one. In addition, $2\,\tau$ has to be shorter than the transverse relaxation time T_2 in order to avoid a big reduction of the signal intensity due to transverse relaxation. A supplementary condition is that τ has to be longer than t_{dead}.

Practically, it is important to realize that the acquisition parameters need to be changed with temperature. At low temperatures, the relaxation times (longitudinal T_1 & transverse T_2) of the nuclear

spins [4] and the probe dead time (t_{dead}) increase. Consequently, it is necessary to decrease the repetition rate and to increase the interpulse delay of the echo sequence with decreasing temperature.

Intensity corrections

To obtain a spectrum as quantitative as possible, the echo intensity points obtained at each frequency must be corrected for relaxation, frequency and enhancement effects.

The T_2 relaxation time was thus measured systematically in each frequency region corresponding to a resonance of interest, in order to correct the spectrum intensity for variations of this parameter. It was measured by varying the interpulse delay of the echo sequence between 4 and 100 µs and fitting the signal decrease as function of the time between the 1st pulse and the detected signal ($2\tau + t_p$, as shown in **Figure 2**) with an exponential decay. Knowing the value of τ used when measuring the spectrum, the signal in each region of the spectrum was then extrapolated to zero interpulse spacing ($I(0)$) to obtain the corrected spectrum. In **Figure 3** a) a typical fitting is shown for an experiment at 213 MHz on a specific sample. The sample was a commercially available cobalt oxide powder (provided by OMG) which contained a non-negligible amount of metallic Co particles of various sizes and that was stabilized inside a polymer matrix. Even though in the literature T_2 relaxation decays differing from a purely exponential law have been observed [5], the decays observed in this work could all be fitted well with a simple exponential law.

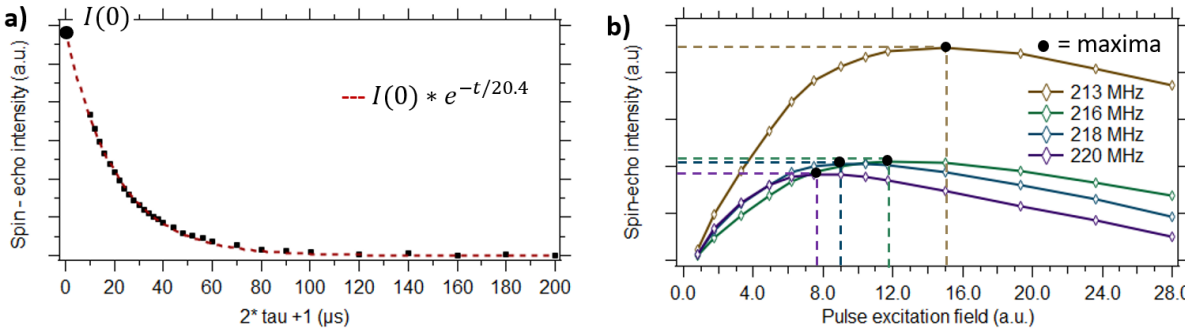

Figure 3: Both graphs were obtained from a CoO/Co OMG powder sample. **a)** Variation of the spin-echo intensity with varying interpulse delay (τ) at 213 MHz. The data is represented as function of $2\tau + t_p$ (with $t_p = 1$), the time during which the spins relax after the first pulse, and is fitted with a simple exponential: $I(t) = I(0) * e^{-t/T_2}$, with T_2 = 20.4 µs in this case. **b)** Evolution of the spin-echo intensity with increasing amplitude of the excitation *rf* field at different frequencies. The maxima of each graph are marked and give the intensity of the final spectra as well as the optimal field for the different frequencies, which are represented in **Figure 4**.

In order to obtain a quantitative spectrum, it is necessary to consider the influence of the resonance frequency on the signal intensity. There are two effects that lead to an overall ω^2 dependence of the signal intensity. This is a well-known fact in NMR that has been discussed for example in [6], [7]. First, the signal is the current induced in the coil by the precessing nuclear magnetization. Since the induced voltage is proportional to the rate of change of the magnetic flux, these result in a linear dependence with frequency. Second, the induced voltage amplitude is also directly proportional to the amplitude of the nuclear magnetization. The magnetization is the result of the polarization of the spins that varies in turn proportionally to the field in the high temperature limit (Boltzmann distribution). Due to the linear relationship between B_{int} and the resonance frequency ($\omega \sim \gamma B_{int}$), the amplitude of the magnetization is thus also proportional to the resonance frequency. In total, the induction voltage is thus proportional to ω^2. To compare intensities over the whole frequency range, a ω^{-2} correction must thus be applied to the point-by-point echo amplitudes. For NMR in diamagnetic materials, the spectra are sufficiently narrowband for this correction to be neglected but this is not the case for IF NMR where the spectra can span tens or even hundreds of MHz.

As described in the first chapter of this work, in IF NMR the optimal excitation power is dependent on the magnetic and crystalline structure around the nucleus and can therefore vary for different nuclei inside a sample. The reason is the so-called enhancement factor, which, in particular, is much higher for nuclei situated inside domain walls than for the ones situated inside a domain.[8] Therefore, at each measured frequency point, the pulse power has been varied over up to 20 dB (i.e., over two orders of magnitude for the *rf* power or one order of magnitude for the *rf* field B_1 amplitude) and the corresponding spin-echo intensity has been measured (**Figure 3 b)**). The maximum intensity is chosen at each frequency to obtain a so-called optimum spectrum and the corresponding excitation field amplitudes are noted. The distribution with frequency of this optimal field can give important information about the magnetic structure inside the sample and is of importance when doing a quantitative analysis of the spectrum. As shown by Panissod and Mény [9], the signal intensity is directly proportional to the enhancement factor, which in turn is inversely proportional to the optimal excitation field. As a result, the signal intensity at each point should be multiplied by the optimal excitation field in order to obtain a quantitative spectrum. However, for most conducted experiments, the observed optimal excitation spectrum was pretty flat and thus no correction for the enhancement factor was necessary. It has to be noted that the spectrometer/amplificatory setup used with the Tecmag Scout spectrometer did not allow a precise regulation of the pulse power around the low power needed for an optimal excitation of the cobalt nuclei using a 1 µs pulse. Especially for nuclei situated inside domain walls, optimal excitation was already reached for a power close to the minimum power interval the setup can produce. In order to have a more precise variation of power around the

optimal excitation and to determine the optimal power more precisely, a variable power attenuator was connected between the amplifier and the transcoupler. The attenuation value could be varied, allowing the investigation of samples composed of a multi-domain structure for which the intensity of the optimal excitation field is much lower than in the case of samples containing only single-domain particles. However, for the same type of samples, the attenuation value was kept constant in order to be able to factor out the effect of the attenuator.

1.2. Spectrum interpretation

In the order to visualize the methodology of the spectrum interpretation for the analysis of pure cobalt, the different steps of the interpretation are presented here on a specific sample. The analyzed sample was a cobalt oxide powder (provided by OMG) containing a non-negligible amount of metallic Co particles of various sizes, already presented in the previous section in the discussion of **Figure 3**. **Figure 4** shows the optimal ^{59}Co IF NMR spectrum obtained from pure cobalt metal, as well as the distribution of the power needed for optimal excitation. The spectrum has been corrected for the ω^2 dependence, as well as the variation of the T_2 and η as justified above. The NMR signal comes solely from the metallic Co particles and not from the cobalt oxide, which is antiferromagnetic. The main peak that was observed around 213 MHz. Based on its position, it could unambiguously be assigned to the signal coming from the domain walls of *fcc* multi-domain (m.d.) structures. The peak was rather narrow due to the nearly isotropic character of the *fcc* structure. A second peak was apparent at 215.5 MHz, around 2.5 MHz above the main peak, which corresponded to the signal coming from *fcc* single-domain (s.d.) structures. The upwards shift between the multi- and s.d. *fcc* signal is due to the presence of a demagnetizing field at the s.d. particles. It was however smaller than the one observed by Gossard et al. [10] for example, which meant that the demagnetizing field was weaker for the particles in the current sample. This peak was small compared to the main peak and when analyzing the evolution of the optimal excitation power, no variation was observed in this zone.

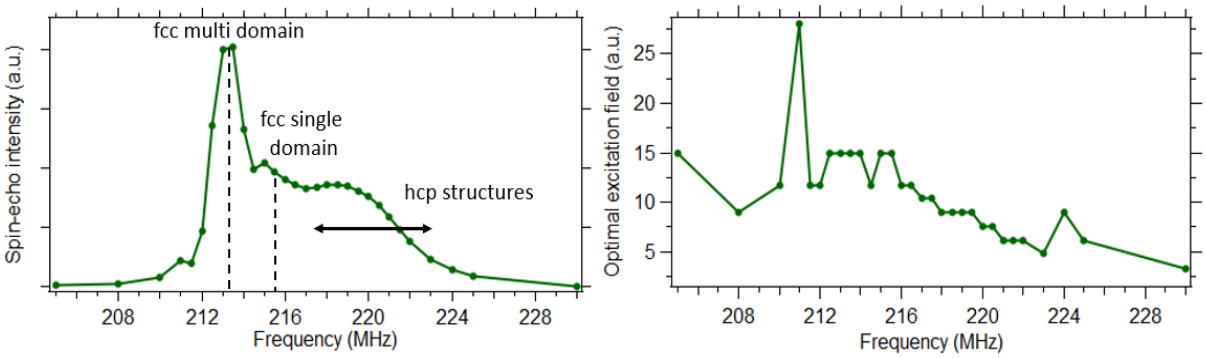

Figure 4: ^{59}Co IF NMR analysis of a CoO/Co OMG powder sample containing Co particles of various sizes. Left: Optimal spectrum, right: Optimal Power. Different peaks can be distinguished, giving information about the crystalline (*fcc* or *hcp*) and magnetic structure (single- or multi-domain) of the cobalt inside the sample.

In the frequency area above the *fcc* peaks, a very large peak centered around 218.5 MHz was observed, which is at a position that is assigned to *hcp* cobalt. The broadened nature of this resonance can be explained by the anisotropic character of the *hcp* crystalline structure and the overlapping of different peaks. As explained in Subsection 1.2 of Chapter 2, a detailed attribution of different peaks in this region cannot be done directly from references in the literature. When looking at the optimal power distribution, the power in this region was even a little lower than the one of the *fcc* m.d. peak, meaning that most signal originated from *hcp* domain walls. A different *hcp* peak, corresponding to *hcp* cobalt in s.d. particles for example, could not be distinguished due the broad character of the peak, but a small fraction might have been present as well. Lastly, a small bump around 211 MHz was observed, which in the literature often has been assigned to grain boundaries or a defect in the structure, leading to a reduce hyperfine field.[11], [12] In addition, a high power was needed for an optimal excitation in this region. Overall, it is concluded that the metallic cobalt in this sample was composed of a mixture of *hcp* and *fcc* structures. A big part of the sample was made of particles large enough to form a multi-domain magnetic structure. However, a part of the *fcc* cobalt was also situated inside s.d. structures, as a corresponding IF NMR peak clearly can be distinguished. If the *hcp* part of the sample also formed some s.d. particles, they could not be distinguished.

1.3. Data treatment

In the following, the data acquisition and treatment for the point-by-point acquisition is explained in detail, using the commercial TNMR program (TecMag, USA). The experiments corresponding to the presented data were performed on the same CoO/Co powder sample whose spectrum has already

been presented in **Figure 4**. As a reminder the spectrum acquisition is done point by point using a solid spin-echo sequence: [$t_p - \tau - t_p$]. As a result, after a time around τ following the second pulse, an echo signal is observed, as shown in **Figure 5** a) for experiments at a frequency of 213 MHz. As the Fourier Transformation (FT) of the signal is only done on the second half of the echo (~ free-induction decay (FID) signal), a left shift (LS) is performed to shift the echo maximum to the time 0 and cut the first half of the echo. In theory, the echo maximum should be at a time τ after the second pulse. In the present case, giving $\tau = 8\ \mu s$ and a delay of 4 µs before the start of the data acquisition, the echo maximum should theoretically be after 4 µs. In reality, it was generally observed about 1 µs after its theoretical value, as can be seen in **Figure 5** a), which can be explained by the pulse length being of the same order of magnitude than τ. The echo signal after LS is represented in **Figure 5** b). After FT, the peak in the frequency domain is represented in **Figure 5** c), including an exponential line broadening (LB) of 50 kHz in order to decrease the relative contribution from the noise occurring after the echo region. After phasing (ϕ) and baseline (BL) correction, the real part of the signal is integrated (INT) of the whole peak range (**Figure 5** d). This same procedure is done for several pulse powers at each frequency and the one giving the maximum integral is chosen in order to obtain the optimal spectrum as previously explained.

The echo signal represented in **Figure 5** a) has quite clean FID shape, resulting in relatively clean absorption and dispersion mode line shapes after FT. However, during the IF NMR spin-echo experiments we performed, the echo signal tends to get distorted for high pulse powers, especially for low intensity signals (away from the main 213 MHz peak in example of **Figure 4**). This effect is represented in **Figure 6** for data collected at 216 MHz from the same CoO/Co sample discussed earlier. It can be seen that with increasing pulse power the echo starts losing its double-FID shape and begins to adopt a square from. For even higher powers, more than one peak appears for the echo signal, with a hole appearing around the time where previously the summit was situated. All this happens while the height of the echo signal continues increasing. Due to the echo distortion, oscillations around the main peak start to arise after FT, which are also included in the integration of the peak. The optimal excitation power for these spin-echo experiments (resulting in the highest peak integral) often does not give a good echo shape. The shift values and the integral span was thus taken to be the same for all tested frequencies and pulse powers of a sample, with the shift value being chosen from the maximum of the non-distorted echo signal.

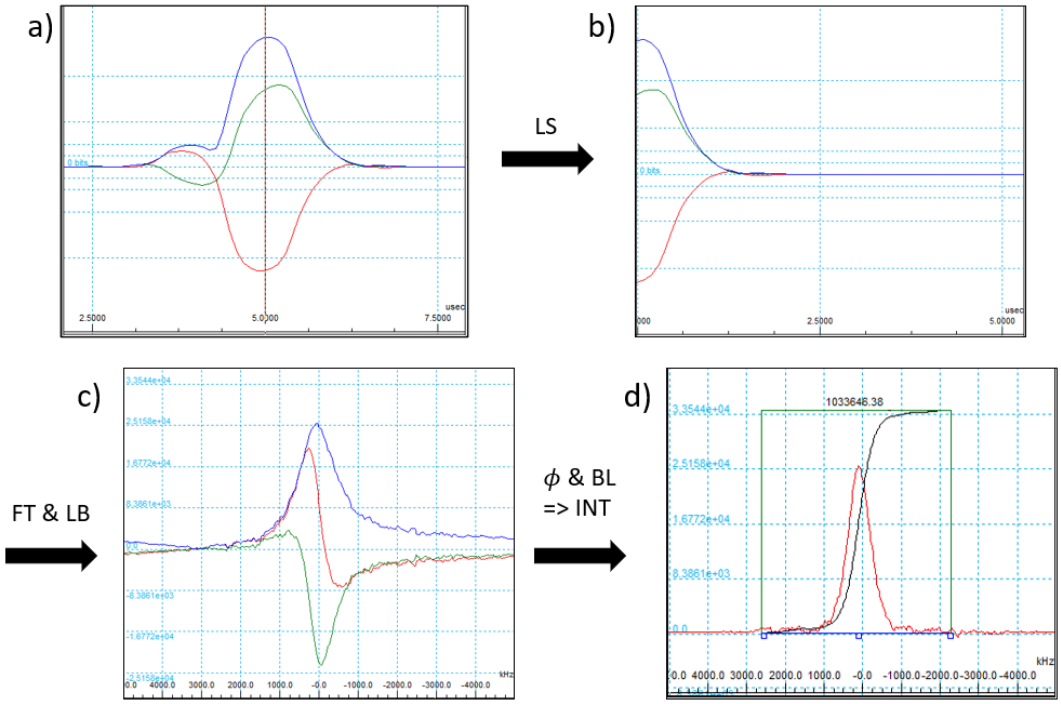

Figure 5: Typical data treatment procedure for the point-by-point spectrum acquisition using a spin-echo sequence. The signal was obtained from a CoO/Co sample at 213 MHz Red line: real part, green line: imaginary part, blue line: magnitude of the signal. Top left: the detected echo signal. LS: Left shift, FT: Fourier transformation, LB: line broadening, ϕ: phasing, BL: baseline correction, INT: integration.

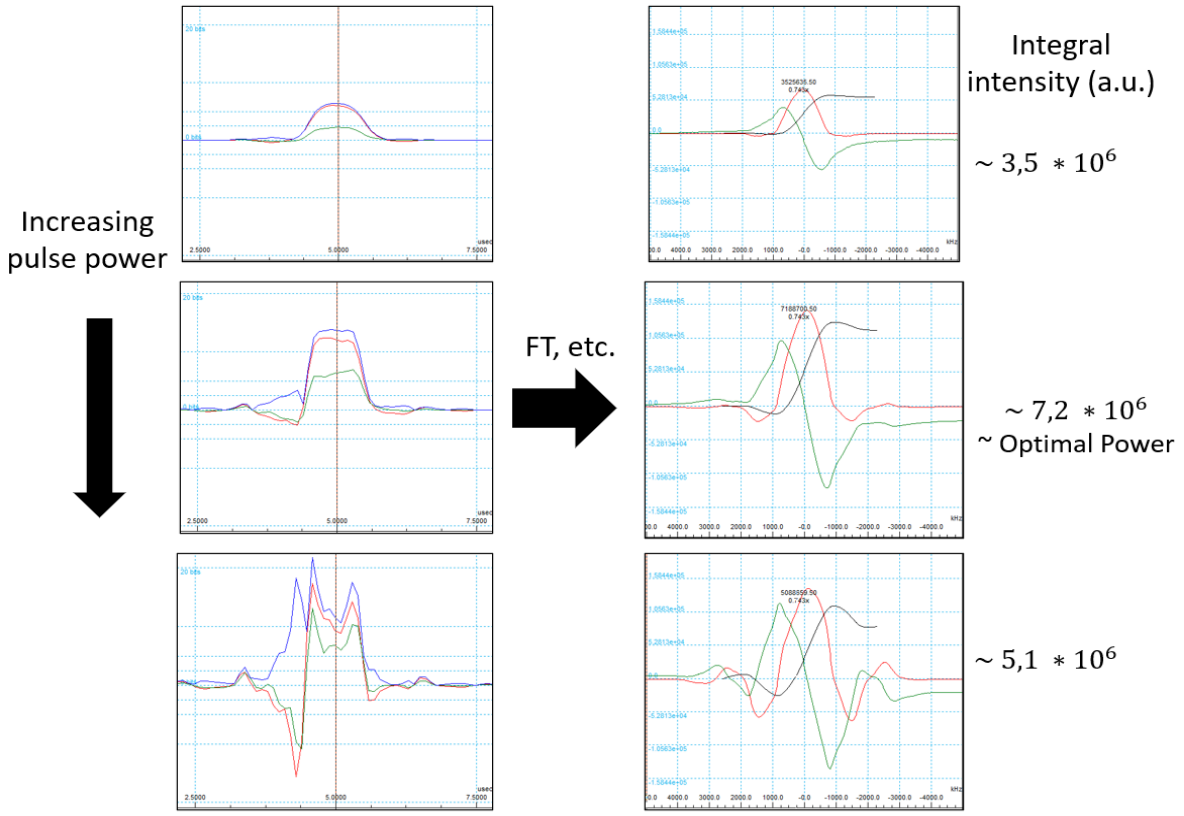

Figure 6: Evolution of the echo shape (left) and the resulting peak (right) after LS, FT, LB, ϕ and BL. The signal was obtained from a CoO/Co sample at 216 MHz with different pulse powers (increasing from top to bottom). Red line: real part, green line: imaginary part, blue line: magnitude of the signal.

The data treatment procedure has been automated using .VBS scripts for the TNMR program in order to perform all the different steps. In addition, all the procedures after the FT have been automated using MATLAB, finding automatically the optimum integral and the corresponding excitation power. The FT of the results were exported as .txt files, which were then treated by MATLAB.

2. Complementary experimental techniques

Besides the main experimental method ^{59}Co IF NMR, various other techniques were applied in order to obtain complementary information on the studied samples or to verify the results obtained by NMR. These experiments include x-ray diffraction (XRD), transmission (TEM) and scanning electron microscopy (SEM), Field-cooling/ zero field cooling (FC/ZFC) and magnetic hysteresis measurements. More detailed descriptions of these techniques are provided when needed in the chapter covering the sample studied by each technique.

3. References

[1] E. L. Hahn, "Spin Echoes," *Phys. Rev.*, vol. 80, pp. 580–594, Nov. 1950, doi: 10.1103/PhysRev.80.580.

[2] J. Keeler, *Understanding NMR Spectroscopy*. Univeristy of Cambridge, 2002.

[3] C. P. Slichter, *Principles of Magnetic Resonance*, vol. 1. Berlin, Heidelberg: Springer Berlin Heidelberg, 1990. doi: 10.1007/978-3-662-09441-9.

[4] A. M. Portis and A. C. Gossard, "Nuclear Resonance in Ferromagnetic Cobalt," *J. Appl. Phys.*, vol. 31, no. 5, pp. S205–S213, May 1960, doi: 10.1063/1.1984666.

[5] T. Thomson, P. C. Riedi, and D. Greig, "Interfacial quality and giant magnetoresistance in MBE-grown Co/Cu(111) superlattices," *Phys. Rev. B*, vol. 50, no. 14, Art. no. 14, Oct. 1994, doi: 10.1103/PhysRevB.50.10319.

[6] J. Mispelter, M. Lupu, and A. Briguet, *NMR Probeheads for Biophysical and Biomedical Experiments*. Imperial College Press, 2006.

[7] A. Webb, "Increasing the Sensitivity of Magnetic Resonance Spectroscopy and Imaging," *Anal. Chem.*, vol. 84, no. 1, pp. 9–16, Jan. 2012, doi: 10.1021/ac201500v.

[8] P. Panissod, "Structural and Magnetic Investigations of Ferromagnets by NMR. Application to Magnetic Metallic Multilayers," in *Frontiers in Magnetism of Reduced Dimension Systems*, Dordrecht, 1998, pp. 225–270.

[9] P. Panissod and C. Mény, "Nuclear magnetic resonance investigations of the structure and magnetic properties of metallic multilayers and nanocomposites," *Appl. Magn. Reson.*, vol. 19, pp. 447–460, 2000, doi: 10.1007/BF03162388.

[10] A. C. Gossard, A. M. Portis, M. Rubinstein, and R. H. Lindquist, "Ferromagnetic Nuclear Resonance of Single-Domain Cobalt Particles," *Phys. Rev.*, vol. 138, no. 5A, pp. A1415–A1421, May 1965, doi: 10.1103/PhysRev.138.A1415.

[11] H. K. Choudhary, M. Manjunatha, R. Damle, K. P. Ramesh, and B. Sahoo, "Solvent dependent morphology and ^{59} Co internal field NMR study of Co-aggregates synthesized by a wet chemical method," *Phys. Chem. Chem. Phys.*, vol. 20, no. 26, pp. 17739–17750, 2018, doi: 10.1039/C8CP01780H.

[12] A. S. Andreev, O. B. Lapina, and S. V. Cherepanova, "A New Insight into Cobalt Metal Powder Internal Field 59Co NMR Spectra," *Appl. Magn. Reson.*, vol. 45, no. 10, Art. no. 10, Oct. 2014, doi: 10.1007/s00723-014-0580-0.

Chapter 4: ^{59}Co IF NMR study of cobalt-carbon composite materials produced by mechanical alloying

In this first experimental chapter, the ^{59}Co IF NMR analysis of Co-C composite materials is presented. The materials were produced by ball milling of carbon under a hydrogen atmosphere with the purpose of doing a carbon hydrogasification reaction with Co as a catalyst. As a reminder, Co-C composite materials are only rarely studied by ^{59}Co IF NMR in the literature, so far. This analysis could therefore be the basis for future studies of Co-C containing systems.

In a first part, the results of the ^{59}Co IF NMR analysis of samples synthesized under different conditions are presented. This analysis allows to determine the predominant crystalline phase, as well as different Co-C intermediates: Co/C solid solution or a Co_3C phase. These results are compared to the ones obtained by X-ray diffraction (XRD) and photoemission spectroscopy (PES) in order to the consolidate the spectrum decomposition of the NMR analysis. In addition, this comparison shows the potential of ^{59}Co IF NMR compared to other techniques to differentiate various Co phases simultaneously.

After confirmation of the ^{59}Co IF NMR methodology, it is presented how this technique was used to monitor the evolution of the cobalt material over the course of a single milling process. This includes the evolution of the predominant Co phase, as well as the amount of the different Co-C intermediates. In addition, these results are compared to the carbon hydrogasification rate, obtained by measuring the amount of methane produced over a certain period of time. This comparison allows to obtain more information about the reaction mechanisms during a carbon hydrogasification reaction.

This work was performed in collaboration with Dr. Gao-Feng Han and Prof. Jong-Beom Baek from Ulsan National Institute of Science and Technology (UNIST, South Korea), who synthesized the samples and performed the XRD and PES analysis. An article discussing the details of the synthesis and the potential of this process is in preparation. This chapter is written in the form of an article, which is planned to be submitted in the near future.

Chapter 4: Cobalt-carbon composite materials produced by mechanical alloying

1. Introduction

^{59}Co internal field nuclear magnetic resonance (IF NMR) is a powerful technique in order to study the crystalline structure of not only pure cobalt materials [1]–[5], but also of cobalt containing alloys and multiphasic systems, where it provides information about the alloy composition or the formed interfaces. Especially multilayer structures [6]–[9] and alloy thin films [10]–[12] have been studied in depth due to their interesting magnetic properties and potential as data storage and sensor materials. So far, published ^{59}Co IF NMR studies focused almost exclusively on pure cobalt or alloyed systems containing another metallic compound, especially copper or iron. On the other hand, systems composed of cobalt and a non-metallic compound, carbon for example, have been much less investigated. Existing works on Co-C containing systems concern bulk systems [13], as well as nanoparticles synthesized by different routes [14], [15], but the assignment of the different phases in the ^{59}Co IF NMR spectrum are sometimes contradicting.

Nanosized composite materials containing carbon and cobalt are nevertheless of great interest for different applications. Adding carbon to cobalt increases its coercivity and therefore results in harder magnetic materials, either as layered structures [16], [17] or as Co_xC (x=2,3) nanoparticles[18]–[21]. In addition, cobalt is used as a catalyst for various reactions involving small carbon molecules which are of great interest in the current context of carbon capture and utilization, for example: Fisher-Tropsch synthesis [22], [23] and carbon hydrogasification (CHG) for clean methane production from coke or coal [24]–[26]. For these reactions the carbon debonding from the cobalt, by reaction with hydrogen, is not the rate determining step and the amount of alloyed carbon remains therefore low throughout the reaction.[27], [28] As a result, it is difficult to study the cobalt-carbon interactions and the formed Co-C intermediates by ^{59}Co IF NMR under these reaction conditions. In a recent article, Han et al. (*in preparation*) show the potential of methane production by ball milling of graphite with cobalt under hydrogen atmosphere, a process requiring no heating. During this process, an unusually large amount of Co-C phases is formed and those phases seem to have a strong influence on the reaction. As a result, this process presents a unique opportunity in order to study by cobalt NMR the nature and quantity of the Co-C species formed during a catalytic CHG reaction. This will also help to better understand the influence and role of Co-C during the reaction, which is of great importance in order to elucidate the mechanisms happening during the methanation reaction.

In the paper by Han et al. (*in preparation*), some ^{59}Co IF NMR results already are presented and prove the simultaneous presence of both, a Co/C solid solution and a Co_3C phase during the CHG process. In the present article, the NMR analysis of those samples is discussed in more detail. Furthermore, the in-depth NMR analysis on samples with several different milling times is presented, with the aim of

monitoring the evolution of the different phases inside the sample. Beside the interest for the analysis of these particular samples, an additional goal is to present a solid basis for future analysis of cobalt-carbon composite materials.

2. Experimental details

2.1. Sample preparation

The sample synthesis and preparation are not part of this PhD work. They were realized by Dr. Gao-Feng Han at UNIST. Nevertheless, they are reported here for clarity. A detailed explanation of the ball milling procedure can be found in the paper by Han et al. (*in preparation*).

In order to avoid cobalt oxidation, all manipulations were performed under inert atmosphere. All samples were prepared by ball milling of commercially available cobalt (~25.3 g) and graphite (~3 g => 10.6 wt.%) powder using a Planetary Mono Mill (Pulverisette 6 classic line, Fritsch GmbH, Germany). WC balls (ø 5 mm, 1000 g) were used for the main experiments, while ZrO_2 balls (ø 5 mm, 423 g) were used for some experiments for comparison. The milling speed was adapted to the density difference of the balls and set to 300 r.p.m. and 400 r.p.m., respectively. Before the start of the hydrogasification process, the reactants inside the mill were first activated (as shown in the top of **Figure 1**). This was done by milling for 12 – 15 h under an H_2 or Ar atmosphere with the goal of decreasing the size of the metal granules and of the graphite particles. Even when the milling is performed under an H_2 atmosphere, the goal of this activation process is not methane production. In fact, only little carbon (about 5% of the initial amount in the present case) was consumed and all the hydrogen present inside the mill reacted to form methane. Therefore, the most part of the activation process was performed under an inert methane atmosphere. Afterwards, the gas present inside the milling container was evacuated, the CH_4 fraction inside determined and the container refilled with 8 bar H_2 before the start of the CHG process. During the CHG process (bottom of **Figure 1**), the sample was milled for 1 to 8 h, at which point the same gas exchange as after the activation process was performed. The CHG reaction was thus conducted in a succession of batch reactions where the gaseous reactant was renewed but not the solid phase. The CH_4 content inside the outflowing gas was measured after each step, which allows to monitor by difference the carbon content in the container and the hydrogasification rate over time. Besides this measurement, a small part of the cobalt/carbon mixture was removed from the container after the activation process and after some of the milling steps before the H_2 – refill, in order to perform NMR and other analyses on these samples. For the ^{59}Co IF NMR analyses, a part of the solid

mixture was put into a 5 mm NMR glass tube and sealed with a torch under inert atmosphere to prevent oxidation.

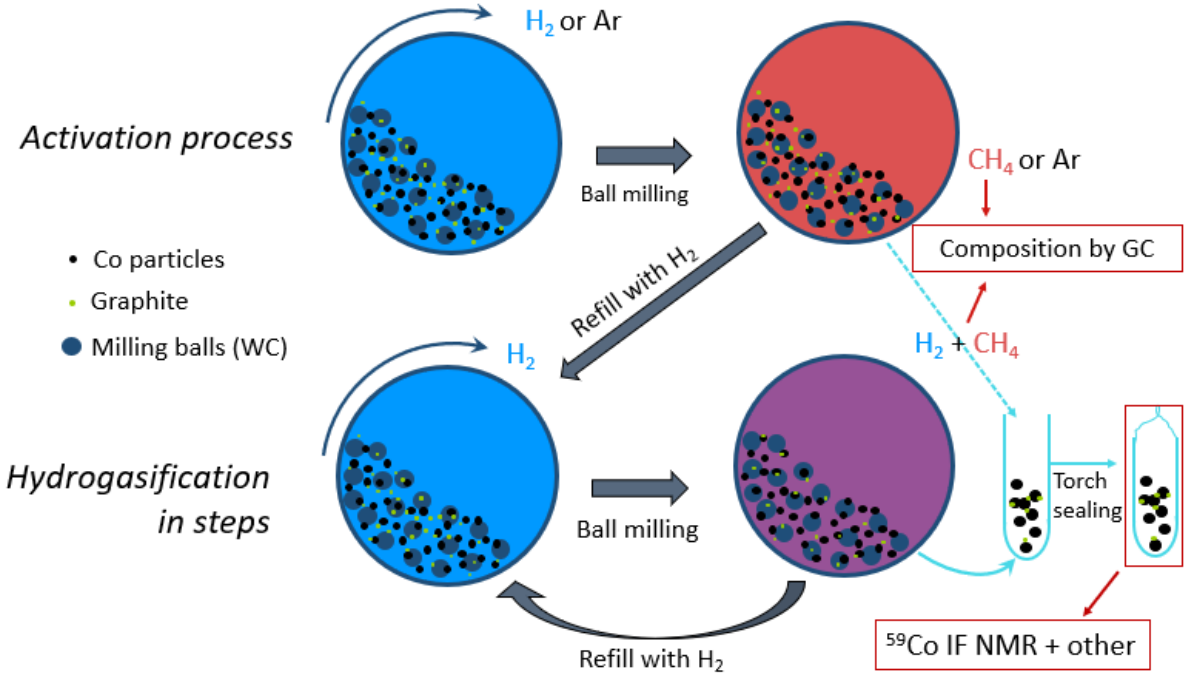

Figure 1: Schematic representation of the milling process. Top: Activation process (one step), during which most of the milling is performed under an inert atmosphere => Only little C consumption. Bottom: Hydrogasification (CHG) process (multiple steps), during which the milling container is refilled with H_2 before all of it is consumed. After the activation step and the CHG steps, a small part of the solid phase is sometimes taken out to be tested by ^{59}Co IF NMR and other techniques. The CH_4 content inside the gaseous phase after each step is tested systematically by gas chromatography (GC).

2.2. IF NMR

The general principles of IF NMR are similar to those of classic NMR; however, no external static magnetic field is applied during the experiments. Instead, the internal hyperfine field present in ferromagnetic compounds is responsible for lifting the degeneracy of the nuclear spin levels. The resulting spectra are extremely broad compared to conventional solid-state NMR and therefore generally measured point-by-point, with frequency steps between 0.5 and 2 MHz. At each frequency, the spectral intensity corresponds to the integral of the spin-echo signal. In the present experiments, the spin-echo sequence was composed of two equal 1 µs radio frequency pulses with an interpulse delay of 8 µs and a repetition rate of 100 Hz. The experiments were performed at ambient temperature

(T = 293K) using two different spectrometers (TECMAG Scout, USA, and Bruker Avance III, Germany). Depending on the frequency range, three different static 5 mm broadband probes had to be used: a broadband 130 – 230 MHz low temperature probe and a NQR 5-80 MHz (with exchangeable coils) tabletop probe, both provided by NMR-Service, Germany, and a broadband 80 – 130 MHz (with exchangeable capacitors/coils) probe provided by Bruker. When changing the probe or the spectrometer, a sufficient number of overlapping frequency points were collected, in order to factor out the instrumental functions of the different probe-spectrometer set-ups. The spectra presented here are so-called optimum spectra, meaning that at each frequency point the pulse power was varied over 20 dB. The signal obtained at the power value maximizing the response, and therefore corresponding to the optimal excitation conditions, was retained to plot the spectrum. The optimal excitation power is related to the enhancement factor of the NMR signal and consequently needs to be considered in order to relate the signal intensity to a number of nuclei.[29] In addition, in order to give a quantitative spectrum, the intensities were corrected for the classic ω^2 factor, as well as for the T_2 spin-spin relaxation time.

2.3. Complementary analytical techniques

All the experiments in this section have been performed under the responsibility of Gao-Feng Han and Jong-Beom Baek at Ulsan National Institute of Science and Technology (UNIST).

The X-ray diffraction (XRD) measurements were obtained on a D/max2500V (Rigaku, Japan, Cu-Kα radiation, λ = 1.5418 Å). A step scan mode was adopted with a step of 0.02 °, and an accumulation time of 3 s. The scan window ranged from 36 to 60 °. The samples were prepared for the XRD measurement in a glovebox and sealed with tape to prevent oxidation. After being removed from the glovebox, the samples were measured immediately.

The composition of the gaseous product inside the milling container was done using a gas chromatograph (GC, 7890B, Agilent), equipped with a 10Ft 1/8 2mm HayeSep Q 80/100 µm column.

The Photoemission spectroscopy (PES) measurements were carried out at the 4D PES beamline, Pohang Light Source (PLS), Pohang Accelerator Laboratory (PAL), South Korea. The samples were first packed into a vacuum-sealed container in a glovebox, which was unpacked under N_2 flow and directly connected to the instrument. The analysis was recorded with a photoemission electron analyzer (R3000, Scienta Omicron, Sweden at room temperature with a pressure better than 4×10^{-10} Torr. The PES spectra were taken at *hv* = 350 eV from a synchrotron radiation source.

3. IF NMR Spectrum interpretation

As already mentioned in the introduction part of this chapter, the ^{59}Co IF NMR spectrum interpretation of Co and C containing compounds is not unified in the literature; especially the position of the peak corresponding to Co_3C varies.[13]–[15] In order to strengthen the spectrum interpretation, the ^{59}Co IF NMR spectra obtained from three different samples synthesized by ball milling of cobalt and graphite are first compared to the results of the XRD and PES analysis of the same samples. Building on this, a lot of original information can be obtained from ^{59}Co IF NMR that might prove useful during further studies.

3.1. Sample overview

In **Table 1** the synthesis conditions of the three samples produced (at UNIST) by ball-milling that are analyzed in this section are given. The initial content in the ball mill was the same for all samples (25.3 g Co, 3 g C), but the activation and milling conditions were different each time. First of all, the ball material was varied, together with the corresponding milling speed. In addition, the time and atmosphere of the activation process was changed, as well as the milling time after the activation. Naturally, the milling time, not considering the activation, directly influences the final carbon content inside the milling container, determined by measuring the CH_4 content in the outflowing gas. As all samples were produced under different conditions and different milling times, the influence of the different milling parameters on the sample properties is difficult to determine. However, it is discussed in an upcoming section, by comparison to another set of samples. Some of the data are also compared to results obtained from the initial pure cobalt powder that was not milled at all.

Table 1: Overview of the synthesis conditions of the different samples tested by ^{59}Co IF NMR, XRD and PES. Milling time, is the time after the end of the activation.

Sample	Ball material	Activation	Milling time (h)	C_{mill} (wt.%)
I	ZrO_2	15 h in H_2	0	10
II	ZrO_2	15 h in Ar	15.5	3.2
III	WC	12 h in H_2	30.5	~0

3.2. Results

XRD, PES

In **Figure 2** a), the diffraction patterns of the XRD analysis on the initial Co powder and on the different samples prepared by ball milling are represented. The different crystalline phases present are determined by comparison to reference files of *hcp* Co, *fcc* Co and Co_3C. In these reference files, the peaks corresponding to pure Co phases that can be distinguished for the studied reflection angles are: 44.22° (111), 51.52° (200) for *fcc* Co; 41.68° (100), 44.76° (002), 47.57° (101) for *hcp* Co. Given the close position of the two reflections around 44.5°, it is difficult to differentiate the crystalline phase based on these peaks, especially when the peaks are broad. Consequently, the predominant crystalline phase is mainly distinguished considering the reflections at the other angles.

It can be seen in **Figure 2** a) that the initial Co was composed of a mixture of *hcp* and *fcc* phases, with an important contribution from both phases. All the peaks were narrow, indicating large crystalline domains and particles, with few defaults. Just after the activation process (sample **I**) the predominant Co phase clearly became *hcp* Co, as the characteristic reflection of *fcc* Co at 51.52° almost disappeared. The increase of the peak width is a sign of a decreasing crystallite domain size during the milling. However, no evidence of a Co_3C phase could be observed. In sample **II**, milled for 15.5 h after the activation process, the predominant crystalline phase was now *fcc* Co, with almost no sign of the characteristic *hcp* Co peaks (41.68°, 47.57°). In addition, a Co_3C phase was also observed for this sample, indicated by the small and broad reflections at different angles, but especially marked by one around 45.5° close to the main *fcc* Co peak. This main *fcc* Co peak was much larger than in the previous samples, indicating even smaller crystallites. The peak enlargement was amplified by the overlap with the Co_3C peaks, but was probably also due to the presence of C in solid solution inside the cobalt, leading to diffraction at lower angles.[30] Sample **III** was milled for a longer time, until almost no C was present anymore inside the milling container. Its crystalline phase was still *fcc* Co, but with narrower peaks compared to sample **II** and no sign of a Co_3C phase. Small quantities of a Co/C solid solution could not be excluded, however.

In **Figure 2** b), the results of the PES analysis on sample **I** and **II** are shown. When comparing both signals, it can be seen that the peak is shifted towards lower energies for **II**, compared to **I**. This implies that in sample **II** the relative amount of free carbon present inside the milling container was reduced at the expense of carbon bond to Co. This is not surprising when comparing the C wt.% inside both samples but consolidates the conclusions drawn from XRD, that is the occurrence of a significant amount of Co-C phases inside sample **II**.

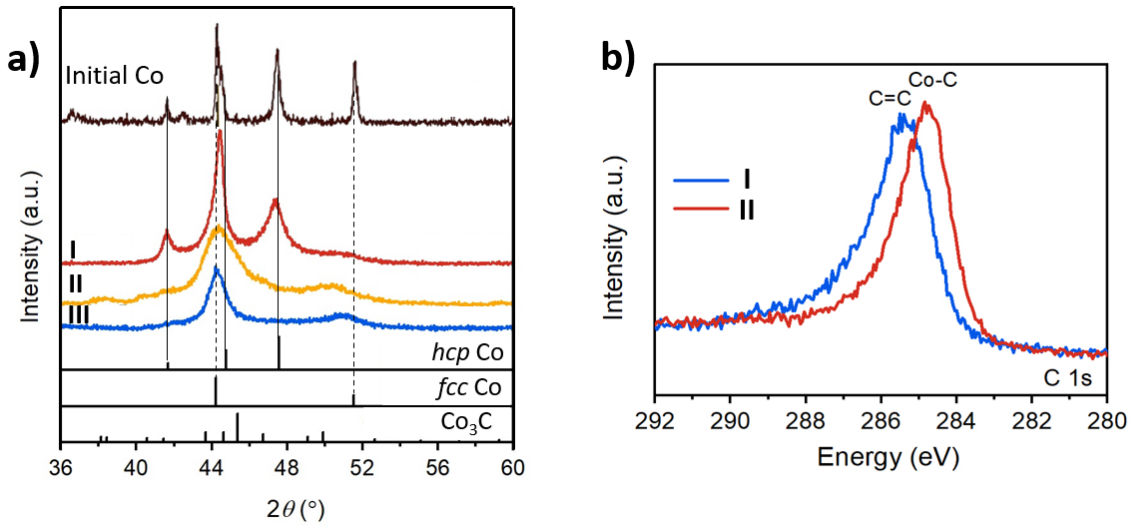

Figure 2: a) Results of the XRD analysis on the initial Co powder, as well as on the samples with different synthesis conditions. The reference files for the decomposition of the different Co structures are: *hcp* Co (05-0727), *fcc* Co (15-0806), Co_3C (26-0450) b) Results of the carbon PES analysis on sample **I** and **II**.

^{59}Co IF NMR

In **Figure 3**, the NMR spectrum of sample **II**, milled for 15.5 h after activation is represented, including a proposition for the spectrum decomposition into different cobalt environments (dotted lines). The main peak centered around 213.5 MHz is assigned to pure *fcc* cobalt, as well-accepted in the literature.[1], [2] In addition, the decomposition shows a small peak around 219 MHz, indicating the presence of a small amount of *hcp* cobalt as well.[2] In the same figure, the spectrum is compared to the one of the initial, non-milled Co powder. It exhibited the same features in this frequency range but was much narrower, which can be explained by a variation of the quality of the crystalline structure and of the crystallite size. While in the initial Co powder the cobalt was composed of big grains with few crystalline defaults, in the activated sample the milling for several hours has reduced the crystallite size and increased the default density. All these factors increased the width of the *fcc* peak, which might cover some signal arising from stacking faults or more *hcp* Co in the upper frequency region of the peak. [31]

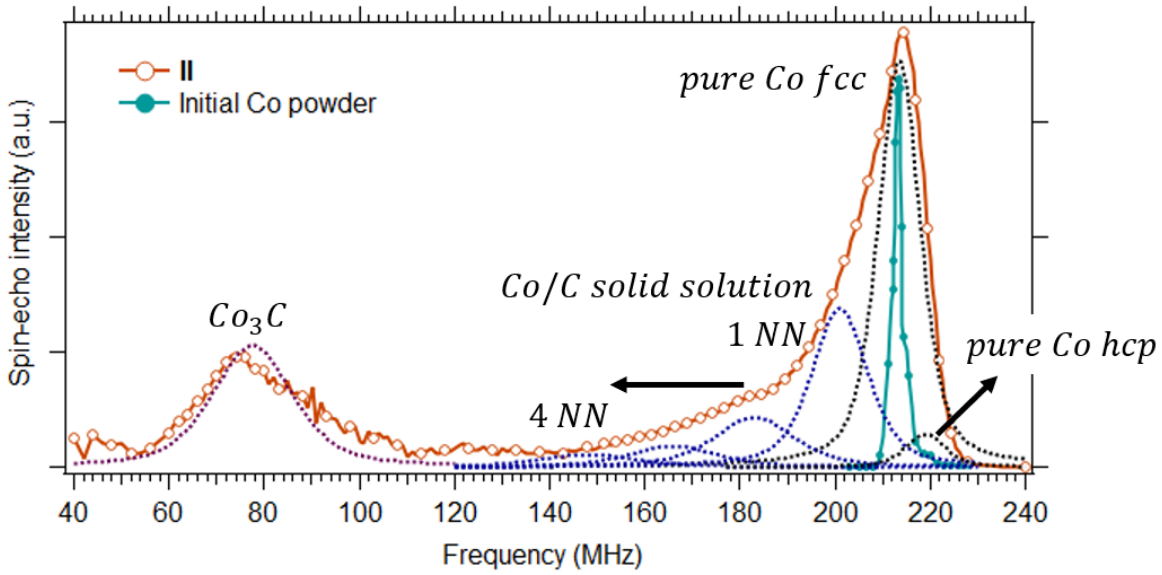

Figure 3: ^{59}Co IF NMR spectrum of the sample **II**: orange line with hollow circles. It is compared to the spectrum obtained from the initial cobalt powder, without any milling: turquoise line with filled circles. The dotted lines correspond to the proposed decomposition of the spectrum after activation → black: pure *fcc* Co & *hcp* Co, blue: *fcc* cobalt with 1 – 4 carbon as NN in solid solution (neglecting contributions from further neighbors), purple: Co_3C.

The main conclusion to be drawn from the spectrum is not the predominant Co crystalline phase, but the occurrence of cobalt carbides. In the spectrum of the sample **II** in **Figure 3**, the signal decreased only slowly in the frequency region below the main Co *fcc* peak. The signal in this region is assigned to a cobalt/ carbon solid solution, with the presence of one or several carbons on a Co nearest neighbor interstitial site disturbing the cobalt electron structure and therefore reducing the magnetic field seen by the ^{59}Co nucleus. For the study of Co/metal interfaces or alloys, the effect of the introduction of different atoms into the Co nearest neighbor (NN) structure is well studied and approximated by a constant shift per foreign NN of the NMR signal.[6], [7], [32] However, the correlation with those kinds of systems has to be taken with caution due to the different nature of the foreign NN (substitutional), compared to the current system (interstitial). ^{59}Co IF NMR analyses on carbon containing cobalt systems produced by rapid quenching were performed by Cadeville et al. [13], [33] for a carbon content up to 1.1 at.% (~ 0.19 wt.%). Besides the main *fcc* line, they observed satellite lines assigned to cobalt with one and two carbons on its NN octahedral interstitial sites, with a downwards shift compared to pure *fcc* of 14 MHz and 34 MHz, respectively. The spectrum of the sample **II** in **Figure 3** can be fitted well with two peaks with a similar downwards shift at 201 MHz and 183 MHz, therefore assigned Co with one and two C NN, respectively. The spectrum below these frequencies is fitted with two additional peaks at 165 MHz and 148 MHz, corresponding to cobalt with three and four C NN,

respectively. The positions are chosen with the same frequency downwards shift than the one between the previous peaks, namely, 18 MHz per additional C NN, but the exact peak positions and width are purely speculative due to the poor resolution at these lower frequencies. In the papers by Cadeville et al., the additional contribution from 2nd and 3rd NN is taken into account for Co with one NN, leading to additional peaks when fitting the spectra. However, especially for cobalt with more than one C NN however, a lot of different situations become possible and many different peaks with positions close to each other would be needed to correctly fit the spectra, which is not possible given the low resolution. For the purpose of this work and given the close position of those peaks, the fitting with large peaks considering only the amount of C NN seems well adapted.

The last signal that still needs to be assigned is the broad bump centered around 80 MHz. A signal at such a frequency already has been observed by Hiraoka et al. [14] when analyzing Co-C alloys, produced by ball-milling, and assigned to the presence of a Co_3C phase. It is noteworthy that the obtained signal in the lower frequency region was weak due to the ω^2 dependence of the signal intensity. In addition, the T_2 measurements showed a decrease of the relaxation from about 17.5 µs at the peak maximum to around 12 µs in the Co_3C region. These factors lead to a noisy signal in the lower frequency region.

Overall, four different Co environments can be differentiated by ^{59}Co IF NMR: *fcc* Co, *hcp* Co, Co/C solid solution (which can be divided into Co with 1 - 4 C as NN) & Co_3C. The peak weights of the fitting in **Figure 3** corresponding to the different environments are shown in **Table 2**. It can be seen that the main component was pure *fcc* Co, while only about 5 % corresponded to *hcp* Co. 26 % were inside a Co_3C phase and the remaining part had at least one C on its NN interstitial sites, forming a solid solution. Note that given the low resolution of the spectrum and the position of the peaks not always being well- defined, the precision of this decomposition is limited.

Table 2: Fraction of the different Co environments inside sample **I** according to the ^{59}Co IF NMR spectrum decomposition

fcc Co	*hcp* Co	Co_3C	1 NN	2 NN	3 & 4 NN
37 %	5 %	26 %	17 %	9 %	6 %

In **Figure 4** the ^{59}Co IF NMR spectra of samples **I** – **III** are represented. On the left the spectra over the whole tested frequency range are represented, while on the right a zoom on the main peak of the three spectra is shown. First of all, it can be observed that sample **II** is the only one where a Co_3C signal can be distinguished, as for the two other samples no signal is observed below 165 MHz. When comparing sample **III** to sample **II**, it can be seen that both have a predominant *fcc* Co crystalline phase,

with even less signal in the frequency region corresponding to *hcp* Co (219 MHz) for sample **III**. In addition, the amount of Co in Co/C solid solution is also inferior in sample **III** compared to sample **II**. The spectrum characteristics of sample **I** are completely different compared to the two other ones. Its main crystalline peak corresponded to *hcp* Co and almost no signal corresponding to Co/C solid solution could be observed.

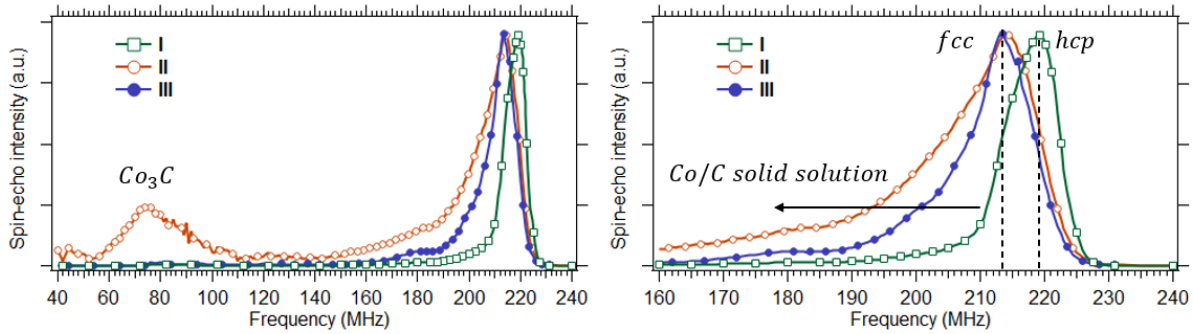

Figure 4: ^{59}Co IF NMR spectrum of the samples **I** – **III**: Left: entire spectrum, right: zoom on the main peak region. No detailed decomposition is shown, but the different Co environments are indicated.

Overview

Regarding the analysis of the pure Co phase, the XRD experiments allowed to distinguish the Co crystalline phases present inside the different samples. It suggested a predominantly *fcc* Co phase for samples **II** and **III** and a predominantly *hcp* Co phase for sample **I**. These observations were confirmed by the ^{59}Co IF NMR experiments. On the other hand, the results obtained from the initial non-milled Co powder slightly differ between XRD and ^{59}Co IF NMR. While the XRD diffractogram indicated an *fcc*/*hcp* Co mixture with significant contributions from both phases, the NMR analysis showed a much stronger signal corresponding to *fcc* Co. Finally, both methods revealed a decrease of the Co crystallite size of the milled sample compared to the initial Co powder.

When studying the presence and nature of Co-C intermediates, the XRD results showed the presence of a strong Co_3C phase in sample **II** only, which was confirmed by the PES and ^{59}Co IF NMR analysis. Compared to the XRD analysis, an advantage of the ^{59}Co IF NMR experiments is a better description of the Co/C solid solution. While in XRD, the reflections originating from Co/C solid solutions might be hidden by the broad *fcc* Co peak, the Co/C solid solution resonances can clearly be distinguished using NMR. In sample **I** almost no Co/C in solid solution was observed by ^{59}Co IF NMR. In contrast, in sample **III** a high amount of this phase was distinguished and even more in sample **II**. The ^{59}Co IF NMR even allows a quantitative estimation of the different phases, although the precision is limited due to the low resolution and poorly defined peak positions. The ^{59}Co IF NMR therefore gives a more complete

image of the sample than XRD and PES. Its results generally agree with the results of the different techniques, validating the peak attribution.

4. Comparison between sample reactivity and structure

In this section variation of the sample properties over the course of a single series of experiments is studied. In contrast to the samples of the previous section where all samples correspond to different series with various milling conditions, in this case a small part of the sample was removed after certain steps of the ball milling procedure before continuing the milling on the same sample. By monitoring the reactivity using CH_4 measurements of the outflowing gas, the sample properties could be compared to the CH_4 production rate and therefore its reaction rate.

4.1. Sample synthesis + reactivity measurement

The carbon hydrogasification was performed as described in the experimental part, with WC as ball material. The sample was activated for 15 h under H_2 atmosphere, after which the carbon content in the sample was slightly reduced to 10.0 wt.% due to the transformation into methane of a part of the carbon as already explained in the experimental section. Afterwards, the ball milling with the aim of methane production by CHG started. The evolution of the carbon content over the course of this reaction, at the end of each successive batch reaction, is represented in **Figure 5**, with batch time 0 being directly after the activation process. As apparent, the carbon content decreased rapidly at the beginning, before reaching a zone of constant decline after about 4 h of milling. After the carbon content in the container reached around 1 wt.% after 24 h of milling, one can consider that the curve went asymptotically towards 0 wt.% and the C content became negligible for the last two points. The evolution with milling time of the C consumption rate, approximated by finite differences over the batch time intervals, is also represented in the same graph. After a relatively high initial reaction rate, it dropped by a factor of four before reaching a quasi-constant hydrogasification rate for a duration of around 20 h. Then, it slowly decreased towards a negligible reaction rate at the end. Since the approximated reaction rates are the mean value over each interval, the true reaction rate at the very beginning might be even higher and it is difficult to determine exactly the start and end of the plateau of constant reaction rate.

The capital letters **A - F** in **Figure 5** correspond to the moments when a small part of the sample was taken out of the milling container to perform ^{59}Co IF NMR analysis, namely after 0, 4, 10, 16, 24 and 48 h of milling.

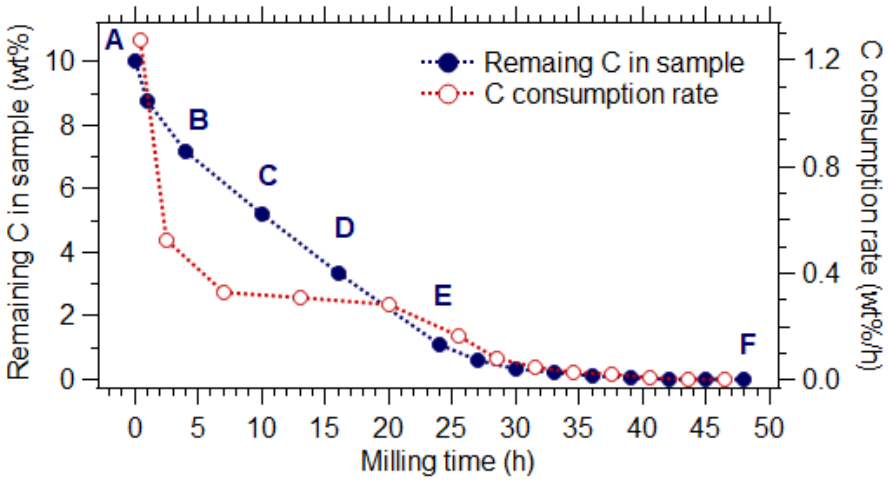

Figure 5: Analysis of a series of experiments on a single sample: Milled with WC balls and activated for 15 h under H_2 atmosphere. In blue, the evolution with milling time (0 h = directly after the activation process) of the carbon content remaining inside the milling container is represented. It was measured each time a gas exchange is performed (blue filled circles). The letter **A** - **F** correspond to the moments a small amount of the sample was taken out of the mill in order to do NMR experiments. The corresponding carbon consumption rate in between the measurements is represented in red (hollow circles).

4.2. ^{59}Co IF NMR results

The spectra shown in **Figure 6** correspond to the ^{59}Co IF NMR analysis of the samples described in the previous subsection. As a reminder, they were all produced during a series of milling on a single sample, but a small part of the sample was taken out at several points during the milling process, as represented in **Figure 5**. In the top of **Figure 6**, the spectra over the whole tested frequency range are represented, while in the bottom a zoom on the main peak is represented. The red line with hollow circles (**A**) corresponds to the ^{59}Co IF NMR spectrum of the sample after just the activation process, while the green line with filled circles (**B**) came from a sample milled for 4 h after activation. First of all, it can be seen that these two samples were the only ones for which a small signal around 80 MHz was observed, which was assigned to Co_3C. When comparing both spectra, it can be seen that the relative signal intensity in the regions corresponding to Co-C intermediates (Co_3C & Co/C solid solution) was reduced during the milling. In addition, for **B** a small shoulder was observed around 219 MHz,

which suggests the presence of some *hcp* Co. The spectra of the sample after 10 h (**C**, blue filled triangles) and 16 h (**D**, purple hollow squares) overlap almost perfectly. In both, the amount of Co/C solid solution components was even more reduced compared to the previous spectra with shorter milling time, while the shoulder corresponding to *hcp* was even stronger. When now looking at the yellow line with hollow triangles (**E**, 24 h of milling), it can be seen that the amount of Co/C in solid solution slightly increased, while the amount of *hcp* Co was close to zero. Finally, in the spectrum represented by an orange line with filled squares (**F**, 48 h of milling), almost no presence of carbon could be seen anymore. The *hcp*-peak around 219 MHz became the major one, but the presence of some *fcc* Co could still be clearly seen.

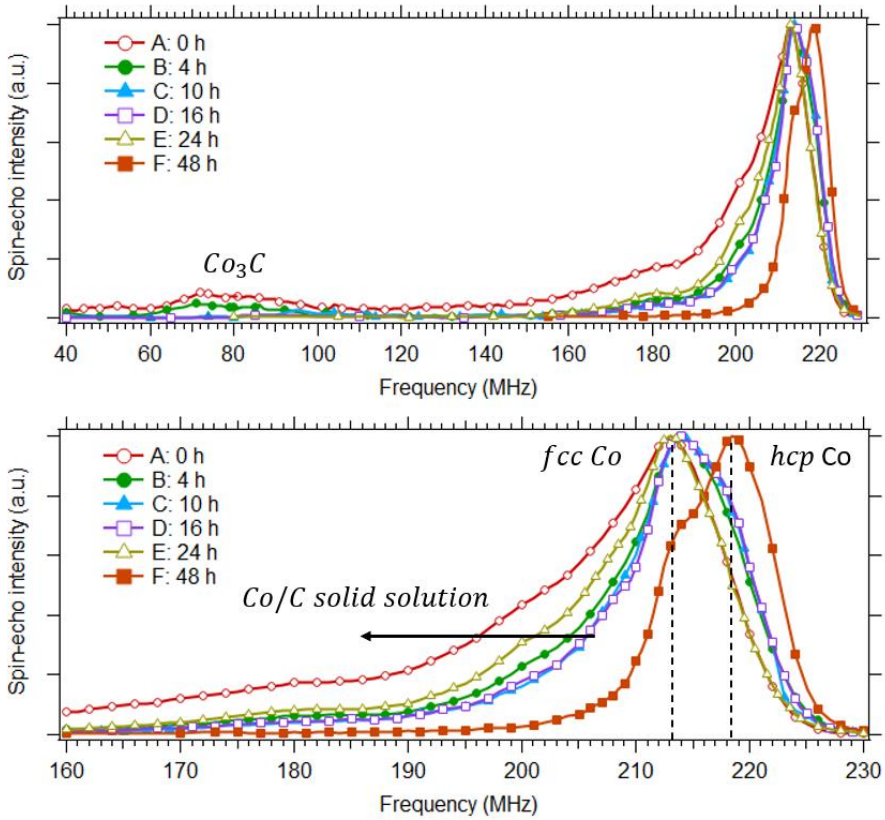

Figure 6: ^{59}Co IF NMR spectra of the samples **A, B, C, D, E** & **F**, milled for 0, 4, 10, 16, 24 & 48 h after activation, respectively. In the top spectrum, the region corresponding to Co_3C is highlighted. In the bottom a zoom of the spectra is shown, including indications of the different Co environments.

In **Figure 7**, the percentage of each of the different phases present in the samples with different milling times is indicated, determined by fitting (as described in Subsection 2.3) of the ^{59}Co IF NMR spectra in **Figure 6**. It allows to monitor the evolution of the pure cobalt phase (*fcc* or *hcp*), the amount of cobalt with one or several carbon on its NN interstitial sites forming a solid solution, as well as the quantity of cobalt in Co_3C during the course of the reaction. For most of the samples, the amount of cobalt

bound to carbon (Co_3C & Co/C solid solution) decreased with ongoing milling, which means that carbon was leaving the cobalt particles during the hydrogasification. In parallel, the amount of *hcp* Co, also compared to the quantity of *fcc* Co, increased. For samples **C** & **D** (10 h & 16 h of milling) all phases were present in pretty much the same relative amount, as the spectra overlapped. The only sample that did not follow the overall trend is **E**, which despite its long milling time (24 h) contained a higher amount of Co/C solid solution and no *hcp* Co. However, no Co_3C was observed for this sample. It has to be noted that the quantification of the different NN peaks does not allow a straightforward quantification of the amount of carbon inside the sample, due to the fact that a carbon can be NN to a cobalt with one or several C NN simultaneously. In addition, the weak signal and the strong correction in the Co_3C region led to a low precision for the quantification of this peak.

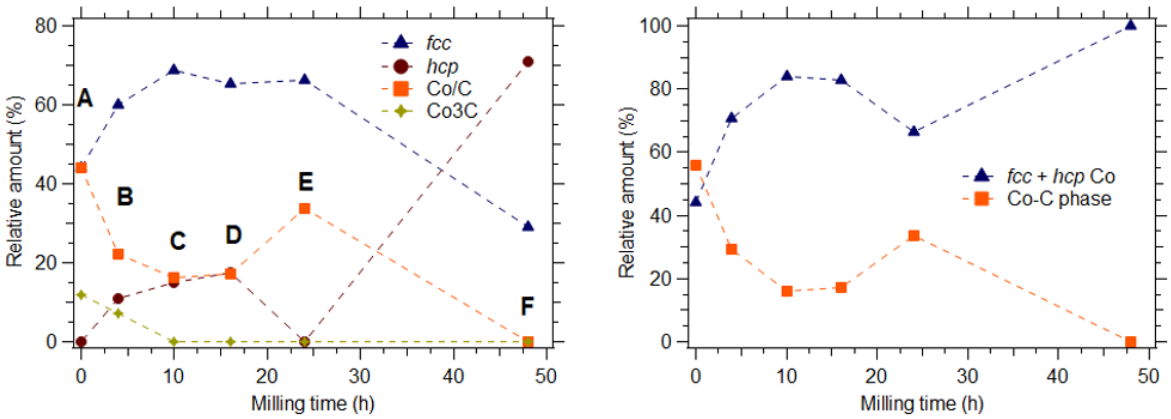

Figure 7: Left: Estimation from IF NMR of the different Co environments: pure *fcc* & *hcp* cobalt, Co/C solid solution (sum of the peaks of Co with 1-4 C NN), Co_3C. Right: Evolution of the total amount of pure Co (*hcp* + *fcc*) compared to Co-C intermediates (Co/C + Co_3C).

4.3. Discussion

Cobalt phase evolution during milling and reaction

The first observation to be discussed is the transformation of the pure cobalt phase. While the initial cobalt powder is a mixture of a *fcc* and *hcp*, even though with only few *hcp*, in the sample after activation only *fcc* was observed. With further milling, more *hcp* was observed until it became the main phase at the very end of the milling. In the literature about ball-milling of pure cobalt, the transformation in both directions (*hcp* → *fcc* & *fcc* → *hcp*) has been reported.[31], [34]–[36] Due to the fact that *hcp* is the thermodynamically stable phase at ambient temperatures, this phase is often observed for less intense milling conditions. On the other hand, the non-equilibrium *fcc* phase is generally observed after milling at a high intensity. An explanation for the stabilization of the *fcc* phase

is the decreasing crystallite size with milling. Indeed, this phase is known to be the stable one for Co grains/ crystallites with a diameter below 20 – 30 nm due to the influence of surface energies.[37], [38] This would explain the pure *fcc* structure in the sample after the activation treatment, where NMR and XRD (for sample **II** – **III** only) showed a clearly reduced crystallite size compared to the initial Co powder. Conversely, the slow reoccurrence of a *hcp* phase with further milling would suggest that the crystallite size grew after the activation step, which could be explained by cold welding and crystallite agglomeration [39]. However, this phenomenon is generally not observed to the extent that *hcp* becomes the major phase, as observed for sample **F**. Another reason that could explain these phase transformations is the presence of carbon, as **Figure 7** shows that the amount of *hcp* was inversely proportional to the quantity of C inside the Co particles. It already has been observed that carbon in solid solution tends to stabilize *fcc* Co [40], which is less dense that *hcp* Co. Therefore, the carbon reacting with and diffusing into the cobalt particles during the activation process initiates or helps with the transformation into *fcc*. When the carbon in the Co particles got consumed to form methane, more and more particles could relax to their equilibrium *hcp* phase.

Cobalt carbides formation and reactivity

The second observation of interest is the influence of the amount of carbon in the cobalt particles on the reaction rate. When comparing the rate of carbon consumption in **Figure 5** with the evolution of the total Co quantity with C in solid solution or forming an Co_3C phase in **Figure 7** (right), the shape of both lines seems similar. Both start at a very high value, decrease rapidly towards a steady-state, and then went down again to reach (almost) zero at the very end. Only the NMR results obtained on sample **E** (24 h of milling) did not follow this trend and an increased Co-C content compared to the previous samples was observed. The close relationship between the particles carbon content and the CHG reaction (carbon consumption) rate allows concluding about the reaction mechanisms and why methane production by mechanochemistry is so fast compared to classic hydrogasification reactions. During the CHG in fluidized or fixed bed reactors with a cobalt containing catalyst, it was found that carbon (C-C) dissociation is the rate-determining step and assumed to be catalyzed.[26] The H_2 adsorption on the catalyst and its reaction with carbon (by hydrogen spillover) turned out to be much faster in these cases, resulting in the absence of carbon on the catalyst after the reaction.[28] Here, the ball-milling increased the rate of the carbon dissociation by grain refining of cobalt and carbon and by keeping them in close contact. In addition, the formation of a large amount of defects inside the cobalt is known to enhance its reactivity with carbon, increase massively the carbon solubility and allow the formation of metastable phases, like Co_3C.[21], [41] The rate of carbon dissociation is increased to the point that it becomes of the same order of magnitude than the hydrogen – carbon reaction, as the amount of Co-C intermediates stays high during most of the milling process and even

reaches a steady-state at one point during the reaction. The Co-C intermediates are either in the form of a solid solution or as a Co_3C phase. The latter one is only present in the first hours after the activation steps, also the region of the highest reactivity, and disappears afterwards, which can be explained either by a higher reactivity of this phase or simply the fact that it is formed only close to the Co particle surface. The samples containing Co_3C also contain a lot of carbon in solid solution, which means that the higher reactivity in this zone is not necessarily only related to the presence of Co_3C.

Mechanochemical activation

In order to further study the influence of the ball material on the activation process, the spectra of samples **I** (**Figure 4**) and **A (Figure 6**) can be compared. As already been described previously, both samples and have been activated during 15 h under an H_2 atmosphere, but using ZrO_2 and WC balls, respectively (as summarized in **Table 3**). After the activation, the total amount of carbon remaining inside the milling container was ~10 wt.% in both cases. It can be seen that the amount of Co-C intermediates was very high (Co/C solid solution and even Co_3C) for sample **A** with a predominant *fcc* structure, while sample **I** was predominantly composed of *hcp* Co with almost no C in the Co structure. The reaction rate of sample **I** during the CHG reaction following the activation was reduced compared to the sample **A**, which confirms the importance of Co-C intermediates during the CHG process. The activation step therefore seems to be an important part of the CHG process.

Table 3: Overview of the synthesis conditions of the different samples compared in this subsection. Milling time, is the time after the end of the activation. All samples have already been described previously: Sample **I** in **Table 1** and sample **A** and **F** in **Figure 5**.

Sample	Ball material	Activation	Milling time (h)	C_{mill} (wt.%)
I	ZrO_2	15 h in H_2	0	10
A	WC	15 h in H_2	0	10
F	WC	15 h in H_2	48	~0

An interesting observation can be made when comparing the ^{59}Co IF NMR spectrum of sample **I** to the one sample **F**, milled for 48 h after activation (with WC balls, as described in **Figure 5** and summarized in **Table 3**). As shown in **Figure 8**, both these spectra look very similar, with a very low amount of cobalt/ carbon intermediates and a preferential *hcp* phase. Given the very different milling history and amount of C inside the ball mill, this is quite surprising and suggests that the reaction between C and Co was poor in sample **I**. Overall, it can be said that the sample **I** was only poorly activated for the CHG reaction, which seems to be due to the ZrO_2 balls. At this stage, this observation remains unexplained

and requires further investigation. An idea could be comparing experiments with different milling speeds or relative load of milling balls compared to the sample mass, in order to compensate for the lower density of ZrO_2 compared to WC.

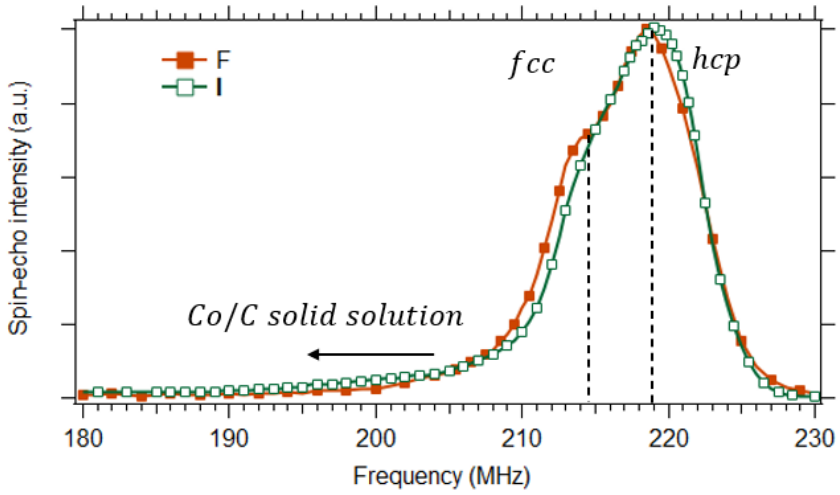

Figure 8: Comparison of the ^{59}Co IF NMR spectra of sample **F**: Activated for 15 h (WC balls, H_2 atmosphere) & milled for 48 h for CHG; with the one of sample **I**: Activated for 12 h (ZrO_2 balls, H_2 atmosphere), without any milling for CHG. The lines and arrows indicate the different Co environments.

5. Conclusions

In the present chapter, the potential of ^{59}Co IF NMR for the analysis of cobalt/ carbon containing systems has been presented on samples produced by ball milling for the purpose of carbon hydrogasification. Besides the differentiation of the main pure Co phases (*fcc* and *hcp*) ^{59}Co IF NMR allowed to evidence the presence of different Co-C intermediates. For a Co/C solid solution, different peaks corresponding to Co with 1 – 4 C at its nearest neighbor interstitial site have been observed around 201, 183, 165 and 148 MHz, respectively. On the other hand, the presence of a Co_3C phase resulted in a large resonance around 80 MHz. This spectrum decomposition was confirmed by X-ray diffraction (XRD) and photoemission spectroscopy (PES) experiments, which also showed the potential of ^{59}Co IF NMR compared to these techniques, especially to study the Co/C solid solution.

Over the course of the milling, phase transformations between *fcc* and *hcp* Co have been observed in both directions, which appeared to be in a close relationship with the amount of Co-C intermediates. The presence of carbon inside the particles tended to stabilize the *fcc* phase, an effect that seemed to

counterbalance the influence of a long milling. Milling the sample for a long time in absence of carbon results in *hcp* Co, probably due to an increasing crystallite size.

Lastly, as revealed by ^{59}Co IF NMR, the CHG reaction rate was closely related to the amount of Co-C intermediates present in the sample. The energy of the ball milling likely helped with the carbon dissociation and formation of Co-C bonds, which is known to be the rate determining step during a CHG reaction under classical conditions. This could explain why the mechanochemical process presented here was much more efficient than classical ones with respect to the CHG reaction. It also explained the crucial role of the activation step: activated by milling under an inert atmosphere maximizes the initial amount of Co-C intermediates. Some milling parameters, like the ball material for example, seem to have an influence on the efficiency of Co-C intermediate formation and therefore on the reaction rate. This influence might be studied in the future by further ^{59}Co IF NMR experiments.

6. Supplementary information

6.1. Low-Frequency signal

Besides the results previously shown, a strong resonance signal at frequencies below 60 MHz was also observed for some samples, which is a novelty for IF NMR measurements of cobalt-containing materials. This signal was different from the one at higher frequencies due to the very high pulse power needed for an optimal excitation and will further be described in the following

Materials and Methods

For the experiments at low frequencies, a NQR tabletop probe (NMR-Service, Germany) was used. The probe comes with exchangeable coils, but complementary handmade coils were also used to cover certain frequency ranges. Most acquisition parameters are the same as the ones described in Subsection 2.2. However, as a very high pulse power seemed to be needed for an optimal excitation at frequencies below 60 MHz, it actually could not be reached with the used setup, so the length of the two pulses in the echo sequence was increased to 2 µs to increase the signal. Nevertheless, the resulting spectra could not be considered quantitative. Due to the fact that such low frequencies are uncommon in NMR measurements, the available setup was not suitable to cover certain frequency ranges. As a result, there is a gap in the spectrum and the lower end of the spectrum could not be measured. In addition, the quality of the matching was sometimes poor and a long electronic dead time (t_{dead}) of the probe was observed for very low frequencies, making it necessary to increase the interpulse delay (τ) in some cases. More details about the dead time and how to solve this issue will be addressed in the next Section 6.2.

All the samples previously presented in this chapter have been tested in this low-frequency region and in addition, a ^{13}C enriched sample was analyzed. This sample was produced in a similar way than the previously described samples, however, but this time 1.0 g ^{13}C power (99 at.% ^{13}C, Sigma-Aldrich) were mixed with 12.7 g of Co granules and 423 g of ZrO_2 balls inside the container. Afterwards the sample was activated for 12 h in H_2 atmosphere, before being milled for 15 min in H_2. During this time, the ^{13}C transformed into CH_4 and its relative amount reduced to around 5.3 wt%. (more details can be found in the paper by Han et al., *in preparation*). The synthesize conditions of this sample (called **^{13}C** from now on) are compared to the ones of the samples **A** and **II** in the following table:

Table 4: Overview of the synthesis conditions of the different samples compared in this section. Milling time, is the time after the end of the activation. The samples **A** (**Figure 5**) and I**I (Table 1**) have already been described previously.

Sample	Carbon source	Ball material	Activation	Milling time (h)	C_{mill} (wt.%)
^{13}C	^{13}C powder	ZrO_2	12 h in H_2	0.25	5.3
A	Graphite	WC	15 h in H_2	0	10
II	Graphite	ZrO_2	12 h in Ar	15.5	3.2

Results

The first sample to give a significant IF NMR signal at frequencies below 60 MHz, was the one synthesized with ^{13}C as carbon source (**^{13}C**). The IF NMR spectrum at higher frequencies of this sample is presented in **Figure 9** a) and indicates that it is mainly composed of pure *fcc* Co, but also a big amount of Co/C solid solution and Co_3C. When comparing the spectrum to the one of sample **A** (already described in Section 4), it can be seen that the relative amount of Co-C intermediates was higher in **^{13}C**. Besides **^{13}C**, sample **A** was the only other sample to give a significant signal in the region below 60 MHz.

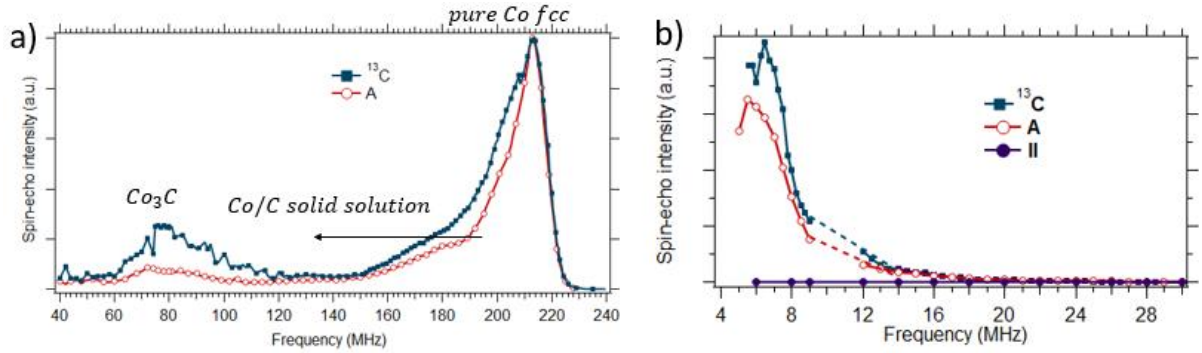

Figure 9: Comparison of the ^{59}Co IF NMR spectra of the sample synthesized with ^{13}C as carbon source (**^{13}C**: Blue squares) and the first sample of the series of samples, taken out immediately after activation (**A**: red hollow circles). a) High-frequency region. The signal intensity below 60 MHz of sample **A** is not optimal signal, but the one using the power giving the optimal signal at 75 MHz. This is due to the appearance of a low-frequency signal, as explained when discussing **Figure 10**. b) Low-frequency signal obtained from samples **^{13}C** and **A**, also compared to the sample **II** milled for 15.5 h after activation, showing no signal in this region.

In **Figure 9** b) the signals obtained from these two samples at frequencies below 30 MHz are represented. As the power needed for an optimal excitation was not reached in this frequency region,

the signal obtained using the highest power possible with the used setup is represented. Therefore, it cannot be assured that the spectra are quantitative. The spectra were obtained using different probe setups, but no complete spectrum could be obtained due to the unavailability of adapted transcouplers (< 5 MHz & 9 – 12 MHz). It can be seen that for both samples the signal intensity increased drastically towards the lower end of the spectrum before starting to drop at the very end. Unfortunately, this drop could not be followed further with the used setup. In comparison, the results of sample **II** in this frequency region are also shown, for which no signal was observed. In order to get an idea of the signal intensity in the low-frequency region compared to the high-frequency region (> 60 MHz), the whole spectrum of sample **A** from 12 MHz up to 230 MHz is represented in **Figure 10** a). The optimal spectrum is represented by a solid red line in this figure, also corrected for the ω^2 dependence of the signal. It can be seen that the spectrum intensity was very low in the high-frequency region compared to the low-frequency region. In **Figure 10** b) the signal intensity is plotted in a logarithmic scale, indicating that the signal intensity at 213 MHz was about 200 times lower than the one at 12 MHz. In order to show the influence of the correction for the ω^2 dependence, the raw signal intensity, without this correction, is represented in purple in this graph. It can be seen that without this correction the signals at 12 MHz and 213 MHz almost have the same intensity, manifesting the huge influence of the ω^2 correction due to the large frequency range.

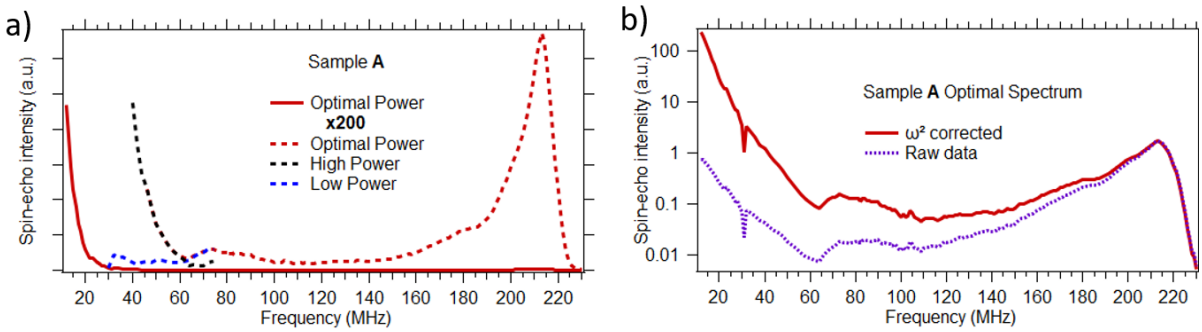

Figure 10: a) ^{59}Co IF NMR analysis of sample **A**: Optimal spectrum from 12 – 230 MHz (solid red line). The dotted red line corresponds to the high-frequency region multiplied by 200. The blue and black dotted lines correspond to the signal obtained using a low and a high pulse power respectively, and multiplied by 200. The low and high powers are chosen to be equal to the one given the strongest signal at 75 MHz and 12 MHz, respectively. b) Optimal spectra of sample **A** over the whole frequency range using a log scale for the *y*-axis. The red line corresponds to the signal intensity after ω^2 correction and the purple one to the raw data without this correction.

As previously described, the optimal power in the low-frequency (< 60 MHz) region was much stronger compared to the one in the high-frequency region (> 60 MHz). In the low-frequency region, the optimal

power could not even be reached with the used setup. In order to visualize the transition between the low- and high-power regime, two spectra are compared in **Figure 10** a): acquired using a high (dotted black line) and low power (dotted blue line). The power difference is equal to 15 dB. It can be seen that the black line (high power) is below the optimal signal around 75 MHz but becomes the optimal signal below 60 MHz and then rises quickly towards lower frequencies. The blue line (low power) on the other hand corresponds to the optimal signal from 75 MHz to 60 MHz but becomes small below. It is also this blue line (low power) that is represented in the high-frequency spectrum in **Figure 9** a), in order to correctly represent the Co_3C peak. To sum up, it can be said that the optimal power changes abruptly around a frequency of 60 MHz, going from a relatively low power above 60 MHz to a very high power for frequencies below. This is an indication that the signal in the low-frequency region might be of a different nature than the signal in the high-frequency region.

Discussions

There are several hypothesis to explain this strong signal at very low frequencies. Given the fact that this signal was firstly observed on a sample milled with enriched ^{13}C as carbon source and not for different other samples milled with graphite, the first idea that comes to mind is that this signal corresponded to a resonance from the ^{13}C. As no external field was applied, the magnetic field acting on the ^{13}C nuclei must be the field generated by the surrounding Co. Such a signal has never been observed in the literature to our knowledge. Considering the peak maximum to be around 6 MHz and a ^{13}C gyromagnetic ratio of 10.705 MHz/T, the magnetic field seen by C nuclei would therefore be about 0.56 T. What disproved this hypothesis, however, was the signal obtained from sample **A**, milled with non-enriched graphite.

A second hypothesis for the origin of the low-frequency signal comes to mind when comparing the synthesis conditions of both samples that gave an IF NMR signal in the low-frequency region (**A** & **^{13}C**). It can be seen that both samples were taken out of the container almost immediately after the activation pretreatment (**Table 4**). As during the activation process all H_2 was quickly consumed, very little C was hydrogasified during the remaining time and C could only react with the Co particles. This fact is also responsible for the high amount of Co-C intermediates present in both samples. A possible origin of the low-frequency signal could therefore be the formation of an unstable Co-C phase that is quickly consumed in presence of H_2 and therefore not present any more for the samples exposed to further C hydrogasification. This phase could be Co_2C, which has a low magnetic moment compared to pure Co and Co_3C, as suggested by Zhang et al. [42] and would therefore correspond to ^{59}Co with a low resonance frequency. Nevertheless, it seems unlikely that such a huge signal compared to pure Co and Co_3C would be obtained from a new phase that was not detected at all in the other samples. In

addition, given the high power needed for excitation, the NMR signal enhancement was low, which means that an enormous amount of this phase would be present in the sample.

In conclusion it can be said that the exact origin of this low-frequency signal is not understood at the moment. Two hypothesis for its origin have been proposed (i.e., it being due the resonance of the ^{13}C nucleus inside the field induced by the cobalt or the presence of a metastable Co_2C phase) without giving a satisfactory explanation. As such a signal has never been observed to the best of our knowledge, it would be interesting to further investigate its origin in the future. A first step to improve this investigation is the use of an NMR setup optimized to the low-frequency region and with a low t_{dead}.

6.2. Electronic dead time:

Different phenomena can occur during an NMR experiment that introduce a measurement dead times after a *rf* pulse during which no reliable signal acquisition is possible, such as acoustic ringing, piezoelectric ringing and the electronic dead time of a resonance circuit, for example. [43] Acoustic ringing only occurs in the presence of an external field [44] and piezoelectric ringing only for piezoelectric samples, so both phenomena are not expected in the case of IF NMR of metallic Co. On the other hand, the electronic dead time needs to be considered. In fact, during a pulsed NMR experiments, only a small part of the energy of the pulse is stored inside the sample via the excitation of the nuclear spins. The other part is stored inside the circuit of the probe, which will be released during a time that is called electronic dead time (t_{dead}) of the probe. During this time no NMR signal detection is possible, as it would be covered by the generally much higher signal due to the energy stored in the circuit. The characteristic length of t_{dead} can be estimated by the equation:

$$t_{dead} = \frac{20 * Q}{2\pi * \omega} \tag{4.1}$$

with Q the probe quality factor and ω the resonance frequency.[43] For experiments in the usual frequency range of ^{59}Co IF NMR (> 200 MHz) and for a probe with a Q < 120, which is the case for the probes used in this work at T_{amb}, t_{dead} will be inferior to 2.5 µs. This is shorter than the T_2 generally measured for ^{59}Co and an influence of t_{dead} can simply be avoided by using a spin-echo sequence. However, for some samples, experiments at frequencies down to 5 MHz have been performed, which should correspond to a t_{dead} of around 75 µs for $Q = 120$ and makes signal detection very difficult. In **Figure 11** a), the example of a spin-echo signal obtained from a Co-C sample (sample **A** in Section 4).

at 6.1 MHz using a 48-turn coil is represented. Strong noisy oscillations can indeed be observed up to a time of around 34 µs, which is longer than a usual T_2 time in cobalt and therefore strongly reduces the signal intensity at the opening of the receiver. Note that in the following, t_{dead} correspond to the period of time during which the oscillations are above the usual probe noise. In order to reduce t_{dead}, the Q - factor of the probe circuit can be cut down. The resonance circuit of the probe used at such low frequencies (NQR tabletop probe provided by NMR-Service, Germany) is a RLC circuit with exchangeable coils, where R is generally only due to the inner resistance of the different components. The easiest way to reduce the Q - factor without strongly influencing the resonance frequency is therefore to increase the resistance of the coil by using a thinner wire or even adding an external resistance in series. In **Figure 11** the effect of those changes is presented for experiments on the same sample: **b)** When using a thinner wire (0.3 mm diameter instead of 0.71 mm) and adding a 5 Ω resistance, t_{dead} was reduced to around 18 µs, **c)** when adding another 10 Ω it was further reduced to around 9.5 µs. We were therefore able to reduce the interpulse delay (τ) below the usual T_2 time of the ^{59}Co nucleus (typically a few tens of µs), which is important to get a strong signal. Unfortunately, the introduction of a resistance also reduced the matching quality and no good matching could be obtained in that manner.

A phenomenon that was observed for different probes is a reduced matching quality and Q - factor when introducing a sample containing a lot of Co into the *rf* coil. As a result, a small t_{dead} was obtained for these kind of samples even without the introduction of a resistance into the circuit. For example, for a sample obtained by ball milling of Co particles and ^{13}C powder for 12 h under H_2 atmosphere (sample **^{13}C** described in **Table 4**), a t_{dead} of only 10 µs was observed at 6 MHz using the same 48-turn coil as for the experiment in **Figure 11** a). This phenomenon can probably be explained by the increased coil inductance due to the introduction of a metallic core inside the coil.

An influence of the probe-head temperature on the probe Q - factor was also observed for a 5 mm broadband low-T probe (provided by NMR-Service, Germany). The Q - factor grew with decreasing temperature, probably due to the lower resistance of the circuit components at lower temperature. This led to an increasing t_{dead} from below 3 µs at T_{amb} to around 10 µs at 4 K, all at frequencies above 200 MHz. These dead times were still lower than the measured T_2 times, but still led to a signal loss.

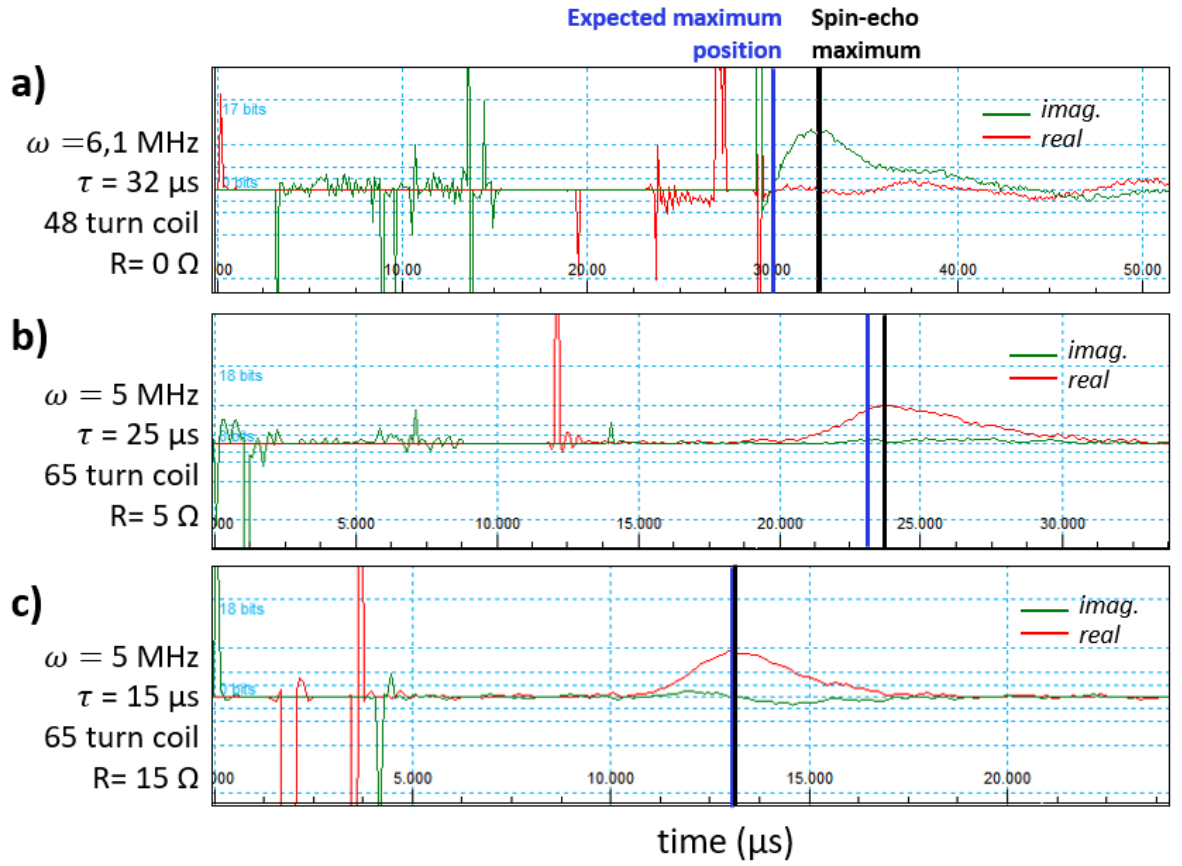

Figure 11: Imaginary and real IF NMR spin-echo signals obtained from a sample obtained by ball milling of Co particles and graphite for 12 h under H_2 atmosphere (sample **A** in this chapter). The three signals were collected at different frequencies and using different interpulse delays (τ). All measurements were performed using an NQR tabletop probe (provided by NMR-Service, Germany) with different 5 mm coils made of Cu: 48 turns (ø 0.71 mm wire) & 65 turns (ø 0.3 mm wire). There is a delay of 4 µs between the last pulse and the start of the acquisition (time 0 µs), which has to be considered when determining t_{dead}. It can be seen that for the 48-turn coil, strong noisy oscillations (~t_{dead}) are observed up to more than 30 µs. Using the 65-turn coil with a 5 Ω or 15 Ω resistance, this time can be reduced to about 18 µs or 9.5 µs, respectively. The black vertical lines correspond to the observed maximum of the echo signal, while the blue vertical lines correspond to its expected position at a time ~(τ + t_p) after the second pulse (t_p is the pulse length of 2 µs). This expected position was deduced from experiments in this thesis with a negligible t_{dead} (Chapter 3, Subsection 1.3 for example). Taken into the account the 4 µs delay of the acquisition, both seem to deviate from each other with longer t_{dead}.

7. References

[1] A. C. Gossard and A. M. Portis, “Observation of Nuclear Resonance in a Ferromagnet,” *Phys. Rev. Lett.*, vol. 3, no. 4, Art. no. 4, Aug. 1959, doi: 10.1103/PhysRevLett.3.164.

[2] A. S. Andreev, J.-B. d’Espinose de Lacaillerie, O. B. Lapina, and A. Gerashenko, “Thermal stability and hcp–fcc allotropic transformation in supported Co metal catalysts probed near operando by ferromagnetic NMR,” *Phys. Chem. Chem. Phys.*, vol. 17, no. 22, Art. no. 22, 2015, doi: 10.1039/C4CP05327C.

[3] I. V. Yakovlev *et al.*, “Superparamagnetic behaviour of metallic Co nanoparticles according to variable temperature magnetic resonance,” *Phys. Chem. Chem. Phys.*, vol. 23, no. 4, pp. 2723–2730, 2021, doi: 10.1039/D0CP05963C.

[4] G. J. Strijkers, *Magnetic nanostructures: an experimental study of structural, magnetic and transport properties*. Eindhoven: Technische Universiteit Eindhoven, 1999.

[5] Y. Liu *et al.*, “Sampling the structure and chemical order in assemblies of ferromagnetic nanoparticles by nuclear magnetic resonance,” *Nat. Commun.*, vol. 7, no. 1, Art. no. 1, Sep. 2016, doi: 10.1038/ncomms11532.

[6] P. Panissod, J. P. Jay, C. Meny, M. Wojcik, and E. Jedryka, “NMR analysis of buried metallic interfaces,” *Hyperfine Interact.*, vol. 97–98, no. 1, Art. no. 1, Dec. 1996, doi: 10.1007/BF02150169.

[7] P. C. Riedi, T. Thomson, and G. J. Tomka, “Chapter 2 NMR of thin magnetic films and superlattices,” in *Handbook of Magnetic Materials*, vol. 12, Elsevier, 1999, pp. 97–258. doi: 10.1016/S1567-2719(99)12006-7.

[8] S. A. Chuprakov *et al.*, “Nuclear Magnetic Resonance and X-ray Reflectometry of Co/Cu Superlattices,” *Appl. Magn. Reson.*, vol. 50, no. 1–3, Art. no. 1–3, Mar. 2019, doi: 10.1007/s00723-018-1090-2.

[9] Ph. Houdy *et al.*, “Magnetic and structural properties of rf-sputtered Co/Fe and Co/Cr multilayers,” *J. Appl. Phys.*, vol. 69, no. 8, Art. no. 8, Apr. 1991, doi: 10.1063/1.347930.

[10] Th. Mühge, Th. Zeidler, Q. Wang, Ch. Morawe, N. Metoki, and H. Zabel, “Structural and magnetic studies of $Fe_x Co_{1-x}$ (001) alloy films on MgO(001) substrates,” *J. Appl. Phys.*, vol. 77, no. 3, Art. no. 3, Feb. 1995, doi: 10.1063/1.358965.

[11] M. Wojcik, J. P. Jay, P. Panissod, E. Jedryka, J. Dekoster, and G. Langouche, “New phases and chemical short range order in co-deposited CoFe thin films with bcc structure: an NMR study,” *Z. Für Phys. B Condens. Matter*, vol. 103, no. 1, Art. no. 1, Mar. 1997, doi: 10.1007/s002570050327.

[12] S. Wurmehl and J. T. Kohlhepp, “NMR Spectroscopy on Heusler Thin films - a review,” *SPIN*, vol. 04, no. 04, Art. no. 04, Dec. 2014, doi: 10.1142/S2010324714400190.

[13] M. C. Cadeville and C. Lerner, “On the electronic structure of interstitial transition-metal based alloys with boron and carbon impurities: Part I. Experimental study,” *Philos. Mag.*, vol. 33, no. 5, pp. 801–824, May 1976, doi: 10.1080/14786437608221917.

[14] K. Hiraoka, A. Oota, and H. Jinushi, “NMR and Magnetic Studies of Mechanically Alloyed $Co_{75} C_{25}$,” *J. Phys. Soc. Jpn.*, vol. 77, no. 7, Art. no. 7, Jul. 2008, doi: 10.1143/JPSJ.77.074705.

[15] K. N. Mikhalev *et al.*, "Magnetic state and phase composition of carbon-encapsulated Co@C nanoparticles according to ^{59}Co, ^{13}C NMR data and Raman spectroscopy," *Mater. Res. Express*, vol. 5, no. 5, Art. no. 5, May 2018, doi: 10.1088/2053-1591/aac1f3.

[16] J. Shi, M. Azumi, and O. Nittono, "Structural and magnetic properties of Co-C composite films and Co/C multilayer films:," *Appl. Phys. Mater. Sci. Process.*, vol. 73, no. 2, pp. 215–218, Aug. 2001, doi: 10.1007/s003390000682.

[17] T. Hayashi, S. Hirono, and M. Tomita, "Magnetic thin films of cobalt nanocrystals encapsulated in graphite-like carbon," *Nature*, vol. 381, pp. 772–774, Jun. 1996, doi: doi.org/10.1038/381772a0.

[18] K. J. Carroll *et al.*, "Magnetic properties of Co_2C and Co_3C nanoparticles and their assemblies," *Appl. Phys. Lett.*, vol. 101, no. 1, p. 012409, Jul. 2012, doi: 10.1063/1.4733321.

[19] V. G. Harris *et al.*, "High coercivity cobalt carbide nanoparticles processed via polyol reaction: a new permanent magnet material," *J. Phys. Appl. Phys.*, vol. 43, no. 16, p. 165003, Apr. 2010, doi: 10.1088/0022-3727/43/16/165003.

[20] Y. Zhang *et al.*, "Controlled synthesis and magnetic properties of hard magnetic CoxC (x=2, 3) nanocrystals," *J. Magn. Magn. Mater.*, vol. 323, no. 11, pp. 1495–1500, Jun. 2011, doi: 10.1016/j.jmmm.2011.01.006.

[21] Z. Turgut, M. S. Lucas, S. Leontsev, S. L. Semiatin, and J. Horwath, "Metastable Co3C nanocrystalline powder produced via reactive ball milling: Synthesis and magnetic properties," *J. Alloys Compd.*, vol. 676, pp. 187–192, Aug. 2016, doi: 10.1016/j.jallcom.2016.03.095.

[22] Y.-P. Pei *et al.*, "High Alcohols Synthesis via Fischer–Tropsch Reaction at Cobalt Metal/Carbide Interface," *ACS Catal.*, vol. 5, no. 6, pp. 3620–3624, Jun. 2015, doi: 10.1021/acscatal.5b00791.

[23] M. Rahmati, M.-S. Safdari, T. H. Fletcher, M. D. Argyle, and C. H. Bartholomew, "Chemical and Thermal Sintering of Supported Metals with Emphasis on Cobalt Catalysts During Fischer–Tropsch Synthesis," *Chem. Rev.*, vol. 120, no. 10, pp. 4455–4533, May 2020, doi: 10.1021/acs.chemrev.9b00417.

[24] A. Tomita, "Hydrogenation of carbons catalyzed by transition metals," *J. Catal.*, vol. 27, no. 2, pp. 293–300, Nov. 1972, doi: 10.1016/0021-9517(72)90271-0.

[25] K. J. Hüttinger and P. Schleicher, "Kinetics of hydrogasification of coke catalysed by Fe, Co and Ni," *Fuel*, vol. 60, no. 11, pp. 1005–1012, Nov. 1981, doi: 10.1016/0016-2361(81)90040-5.

[26] S. Yan, J. Zhang, X. Yan, D. Pan, H. Ren, and X. Qu, "Catalytic coal hydrogasification by cobalt-calcium catalyst in a pressurized fluidized bed: Role of hydropyrolysis and catalysis process," *J. Anal. Appl. Pyrolysis*, vol. 135, pp. 251–259, Oct. 2018, doi: 10.1016/j.jaap.2018.08.028.

[27] S. Yan, J. Bi, and X. Qu, "The behavior of catalysts in hydrogasification of sub-bituminous coal in pressured fluidized bed," *Appl. Energy*, vol. 206, pp. 401–412, Nov. 2017, doi: 10.1016/j.apenergy.2017.08.189.

[28] F. Zhang *et al.*, "The evolution of Fe and Fe-Ca catalysts during char catalytic hydrogasification," *Fuel*, vol. 257, p. 116040, Dec. 2019, doi: 10.1016/j.fuel.2019.116040.

[29] P. Panissod and C. Mény, "Nuclear magnetic resonance investigations of the structure and magnetic properties of metallic multilayers and nanocomposites," *Appl. Magn. Reson.*, vol. 19, pp. 447–460, 2000, doi: 10.1007/BF03162388.

[30] T. Tanaka, K. N. Ishihara, and P. H. Shingu, "Formation of metastable phases of Ni-C," *Metall. Trans. A*, vol. 23, no. 9, Art. no. 9, Sep. 1992, doi: 10.1007/BF02658046.

[31] J. Sort *et al.*, "Role of stacking faults in the structural and magnetic properties of ball-milled cobalt," *Phys. Rev. B*, vol. 68, no. 1, Art. no. 1, Jul. 2003, doi: 10.1103/PhysRevB.68.014421.

[32] S. Nasu, H. Yasuoka, Y. Nakamura, and Y. Murakami, "Hyperfine field distribution in Co-Cu alloy: 59Co nuclear magnetic resonance," *Acta Metall.*, vol. 22, no. 9, Art. no. 9, Sep. 1974, doi: 10.1016/0001-6160(74)90060-1.

[33] M. C. Cadeville, F. Gautier, and C. Robert, "Cadeville et al. 1972 - Electronic Structure of nickel and cobalt-carbon interstitial alloys.pdf," in *Proc. 13th Low Temperature Conference*, Boulder, 1972, vol. 4, pp. 325–331.

[34] K. O. Hara, E. Yamasue, H. Okumura, and K. N. Ishihara, "Molecular dynamics study of the milling-induced allotropic transformation in cobalt," *Philos. Mag.*, vol. 92, no. 16, Art. no. 16, Jun. 2012, doi: 10.1080/14786435.2012.669058.

[35] W. S. Yeo, Z. Nur Amirah, H. S. C. Metselaar, and T. H. Ong, "X-Ray Powder Diffraction Studies of Mechanically Milled Cobalt," *Adv. Mater. Res.*, vol. 626, pp. 913–917, Dec. 2012, doi: 10.4028/www.scientific.net/AMR.626.913.

[36] J. A. Betancourt-Cantera, F. Sánchez-De Jesús, A. M. Bolarín-Miró, G. Torres-Villaseñor, and L. G. Betancourt-Cantera, "Magnetic properties and crystal structure of elemental cobalt powder modified by high-energy ball milling," *J. Mater. Res. Technol.*, vol. 8, no. 5, Art. no. 5, Sep. 2019, doi: 10.1016/j.jmrt.2019.07.048.

[37] E. A. Owen and D. M. Jones, "Effect of Grain Size on the Crystal Structure of Cobalt," *Proc. Phys. Soc. Sect. B*, vol. 67, no. 6, pp. 456–466, Jun. 1954, doi: 10.1088/0370-1301/67/6/302.

[38] O. Kitakami, H. Sato, Y. Shimada, F. Sato, and M. Tanaka, "Size effect on the crystal phase of cobalt fine particles," *Phys. Rev. B*, vol. 56, no. 21, Art. no. 21, Dec. 1997, doi: 10.1103/PhysRevB.56.13849.

[39] A. L. Rominiyi, M. B. Shongwe, and B. J. Babalola, "Development and characterization of nanocrystalline cobalt powder prepared via high energy ball milling process," *IOP Conf. Ser. Mater. Sci. Eng.*, vol. 430, p. 012029, Oct. 2018, doi: 10.1088/1757-899X/430/1/012029.

[40] M. C. Cadeville and M. F. Lapierre, "Etude aux rayons X de la solution solide cobalt-carbone," *Scr. Metall.*, vol. 6, no. 5, pp. 399–404, May 1972, doi: 10.1016/0036-9748(72)90211-6.

[41] B. Li, Q. Zhang, L. Chen, P. Cui, and X. Pan, "Vacancy-mediated diffusion of carbon in cobalt and its influence on CO activation," *Phys. Chem. Chem. Phys.*, vol. 12, no. 28, Art. no. 28, 2010, doi: 10.1039/b925764k.

[42] Y. Zhang *et al.*, "Controlled synthesis and magnetic properties of hard magnetic CoxC (x=2, 3) nanocrystals," *J. Magn. Magn. Mater.*, vol. 323, no. 11, Art. no. 11, Jun. 2011, doi: 10.1016/j.jmmm.2011.01.006.

[43] H. Förster, "Probe parameters," *Bruker Solids Experiments - NMR Guide & Encyclopedia*, 2001 1998. http://triton.iqfr.csic.es/guide/nmr/solids/solids1_7_2.html (accessed Nov. 03, 2021).

[44] I. P. Gerothanassis, “Methods of avoiding the effects of acoustic ringing in pulsed fourier transform nuclear magnetic resonance spectroscopy,” *Prog. Nucl. Magn. Reson. Spectrosc.*, vol. 19, no. 3, pp. 267–329, Jan. 1987, doi: 10.1016/0079-6565(87)80005-5.

Chapter 5: Magnetic structure and internal field nuclear magnetic resonance of cobalt nanowires

In this chapter, the study of cobalt nanowires electrodeposited into the parallel pores of membranes is presented. Two types of membranes are used as a template: polycarbonate (PC) membranes with 50 nm pores and a low pore density, as well as anodized aluminum oxide (AAO) membranes with 200 nm pores and a high pore density. In addition, samples deposited into both membrane types are synthesized with two different deposition conditions: with and without the presence of organic additives in the electrolyte. The focus of this chapter is the study of the crystalline and the magnetic structure of the nanowires.

First, the impact of the organic additives and the membrane type on the Co crystalline is presented. In this context, the results of X-ray diffraction (XRD) and ^{59}Co IF NMR are compared, which allows to obtain complementary information. Further, the influence of the crystalline structure and the geometry of the wire on its magnetic structure is studied. This information is obtained using magnetic hysteresis measurements, a technique commonly used for this type of system. In addition, these results are compared to the ones obtained using a novel ^{59}Co IF NMR approach. During this approach, the excitation efficiencies as function of the orientation between the *rf* field and the wire axis are compared, which gives information about the orientation of the magnetic domains and domain walls inside the wire. Besides obtaining valuable information about the wire properties, the goal of this chapter is therefore to confirm the validity of this novel ^{59}Co IF NMR approach.

This work was performed in collaboration with Dr. Alberto Quintana, Christopher Jensen and James Malloy from the team of Prof. Kai Liu from Georgetown University, who synthesized the samples and performed the magnetic hysteresis measurements. This chapter is a slightly modified version of a paper that is under review by the PCCP journal editors.

Chapter 5: Magnetic structure and IF NMR of cobalt nanowires

Chapter 5: Magnetic structure and IF NMR of cobalt nanowires

*Pascal Scholzen,[1] Guillaume Lang,[2] Andrey S. Andreev,[3] Alberto Quintana,[4†] James Malloy,[4] Christopher J. Jensen,[4] Kai Liu,[4] and Jean-Baptiste d'Espinose de Lacaillerie[1]**

(1) Soft Matter Science and Engineering, ESPCI Paris, Université PSL, UMR CNRS 7615, Sorbonne Université, 75005 Paris, France.

(2) Laboratoire de Physique et d'Étude des Matériaux, UMR CNRS 8213, ESPCI Paris, Université PSL, Sorbonne Université, 75005 Paris, France.

(3) TotalEnergies One Tech Belgium (TEOTB), Zone Industrielle C, 7181 Feluy, Belgium

(4) Physics Department, Georgetown University, Washington, DC 20057, USA

KEYWORDS. ^{59}Co NMR, internal field NMR, ferromagnetism, metallic nanostructures, nanomagnetism, FNR.

ABSTRACT:

The magnetic properties of cobalt metal nanowires grown by electrodeposition in porous membranes depend largely on the synthesis conditions. Here, we focus on the role of electrolyte additives on the magnetic anisotropy of the electrodeposited nanowires. Through magnetometry and internal field nuclear magnetic resonance (IF NMR) studies, we compared both the magnetic and crystalline structures of 50 and 200 nm diameter Co nanowires synthesized in presence or absence of organic additives. The spectral characteristics of IF NMR were compared structurally to x-ray diffraction patterns, and the anisotropy of the NMR enhancement factor in ferromagnetic multidomain structures to magnetometry results. While the magnetic behavior of the 50 nm nanowires was dominated, as expected, by shape anisotropy with magnetic domains oriented on axis, the analysis of the 200 nm proved to be more complex. ^{59}Co IF NMR revealed that the determining difference between the samples electrodeposited in presence or in absence of organic additives was not the dominant crystalline system (*fcc* or *hcp*) but the coherent domain sizes and boundaries. In the presence of organic

additives, the cobalt crystal domains are smaller and with defective grain boundaries as revealed by resonances below 210 MHz. This prevented the development of the strong magnetocrystalline anisotropy in the Co *hcp* part of the sample, that was observed in the absence of organic additives. In the presence of organic additives, even in nanowires as wide as 200 nm, the magnetic behavior remained determined by the shape anisotropy with a positive effective magnetic anisotropy and strong anisotropy of the NMR enhancement factor.

1. Introduction

Ferromagnetic nanowires with tunable magnetic properties have been the focus of intense research efforts, not only because they raise interesting fundamental physics questions but also because they are used in nano- or microscale electromagnetic devices.[1] For example, they can be used for ultra-high density recording[2] or in magnetic field sensors (e.g. read heads) or random-access memories, exploiting the giant magnetoresistance observed in the case of multilayered nanowires.[3]–[6] Progress in producing arrays of ferromagnetic materials by electrodeposition into porous membranes made of polycarbonate (PC) or anodized aluminum oxide (AAO) has stimulated research by providing model systems to study the structural and electromagnetic properties of metallic nanowire assemblies.[7]–[10]

Of particular interest is the issue of domain wall structure and dynamics. In soft magnetic nanowires, magnetic domain walls form perpendicularly to the wire axis and can propagate collectively along the wire under the drive of magnetic fields[11], spin-polarized currents[12] or electric fields[13]. This property lies at the basis of racetrack memory devices.[14] Most studies so far have explored the dynamic and static structures of domains and domain walls by magnetometry[10], [15], [16], pulsed resistometry[17]–[19] and magnetic imaging[12], [20], [21]. In this work however, we probed the magnetic structure of arrays of parallel cobalt nanowires by ^{59}Co internal field nuclear magnetic resonance (IF NMR), with a particular focus on the domain wall response to radiofrequency (*rf)* fields. This particular form of solid-state NMR is as old as NMR itself[22] but has raised a renewed interest because to its ability to probe cobalt nanoparticles in catalysts or battery materials.[23]–[25] For the study of cobalt nanowires, IF NMR represents a well-adapted technique due to the possibility to simultaneously analyze the crystalline and magnetic properties of the samples. Strijkers et al.[26] successfully adopted this approach to determine the crystalline structure and crystal orientation inside the samples, as well as the influence of the dipole-dipole interactions on the magnetic structure. For

this, they used a combination of experiments at zero field and in the presence of an external field oriented parallel or perpendicular to the wire axis. Others have addressed nanowires made of pure cobalt as well as Co-Cu alloys and multilayers.[27]–[30] In combination with x-ray diffraction (XRD) measurements, they studied the crystalline structure of those three kinds of samples for different synthesis parameters. They found that a fast deposition rate favors the appearance of a *fcc* crystalline structure, while a pure *hcp* phase is formed using slow deposition rates.

Nevertheless, in cobalt nanowires, how synthesis conditions determine precisely the magnetic domain structure inside the wires remains an open question. In this chapter, we study the magnetic and crystalline structures of cobalt nanowires electrodeposited inside the 50 nm and 200 nm cylindrical pores of PC and AAO membranes, respectively. The samples were studied by IF NMR experiments (without an applied field), supported by XRD, scanning electron microscopy (SEM) and magnetometry as complementary experiments. The first goal was to obtain new information on the crystalline and magnetic structure for nanowires obtained with different electrodeposition conditions, focusing on the influence of additives. Secondly, we wished to exemplify the methodological potential of simple IF NMR experiments in strongly anisotropic ferromagnetic structures, such as nanowires. The NMR spectral features complemented XRD for crystalline phase determination, while the analysis of the anisotropy of the enhancement of the *rf* field revealed the orientation of the magnetic domains inside the nanowires.

2. Materials and methods

2.1. Sample Synthesis.

All reagents have been used without any further purification: Cobalt sulfate heptahydrate ($CoSO_4 \cdot 7H_2O$ ReagentPlus ≥99%), Cobalt chloride hexahydrate ($CoCl_2 \cdot 6H_2O$ ACS reagent, 98%), Boric Acid (H_3BO_3 ACS reagent, ≥99.5%), Polyethylene Glycol (PEG – Mn 20000), 1-(2-Hydroxyethyl)-2-Imidazolidinethione ($C_5H_{10}N_2OS$), Thioglycolic Acid ($C_2H_4O_2S$ ≥98%), Janus Green B (3-Diethylamino-7-(4-dimethylaminophenylazo)-5-phenylphenazinium chloride.

Cobalt nanowires of 50 nm and 200 nm diameter were synthesized by template-assisted electrodeposition using a Princeton Applied Research Potentiostat 263A. For the 50nm diameter nanowires, 6µm thick polycarbonate membranes (PC) with a pore density of 6×10^8 cm^{-2} were used,[31] after coating with Au back electrodes. For the 200 nm diameter nanowires, 60 µm thick

anodized aluminum oxide (AAO) membranes with a pore density of 10^9 cm^{-2} were used,[32] after coating with Cu back electrodes.

Electrolytes formulation used in this project were adapted from prior studies.[4], [32], [33] For the additive-free electrolyte, a Watts-like[34] electrolyte with Ni replaced by Co precursors was employed. Specifically, the electrolyte was composed of 240 g/L $CoSO_4 \cdot 7H_2O$ + 50 g/L $CoCl_2 \cdot 6H_2O$ + 40 g/L H_3BO_3. For the additive-containing electrolyte, the same recipe as the additive-free solution was used, with the addition of a mixture of 60 mg/L PEG + 34 µg/L Janus Green B + 34 µg/L 1-(2-Hydroxyethyl)-2-Imidazolidinethione + 12 µg/L Thioglycolic Acid. In both solutions, pH was left unaltered and neither of the solutions were deaerated nor stirred prior to or during the growth. All samples were grown potentiostatically at -1.1V relative to an Ag^+/AgCl reference electrode. Deposition time was controlled to avoid overplating. After the synthesis, the Cu back electrodes on the AAO membranes were etched away using 2M $FeCl_3$, while the Au electrodes on PC membranes were not removed.

2.1. SEM

Scanning Electron Microscopy images were obtained on two different microscopes. The two 200 nm AAO samples were imaged on a Magellan 400 (ThermoFisher Scientific, USA) in a high vacuum. The 50 nm PC sample was analyzed on a Quattro ThermoFisher under a 100 Pa water vapor atmosphere, in order to avoid charge accumulation at the sample surface due to the lower cobalt content of the sample. Both instruments were used in secondary electron mode with a Field Emission Gun at a voltage of 5 kV.

2.2. XRD

X-ray diffraction was performed using a X'Pert (Philips) diffractometer with a PW3050 (θ/2θ) goniometer between 35° and 100° and with Cu as the anode material operated at 40 mA, 40 kV. The samples were positioned with the plane of the membrane in the reflection plane of the XRD experiment. As a result, mainly the crystallographic planes perpendicular to the wire axis diffracted, as shown in **Figure 1**, with small deviations expected due to imperfect alignment of the pores in the membranes. The ICDD reference files for spectra corresponding to *fcc* and *hcp* Co are PDF cards No. 00-015-0806 and 00-005-0727, respectively. Note that the gold electrode remaining on the 50 nm PC sample saturated the signal, masking the cobalt nanowire signal. As a result, no structural analysis of the cobalt by XRD could be performed on this sample.

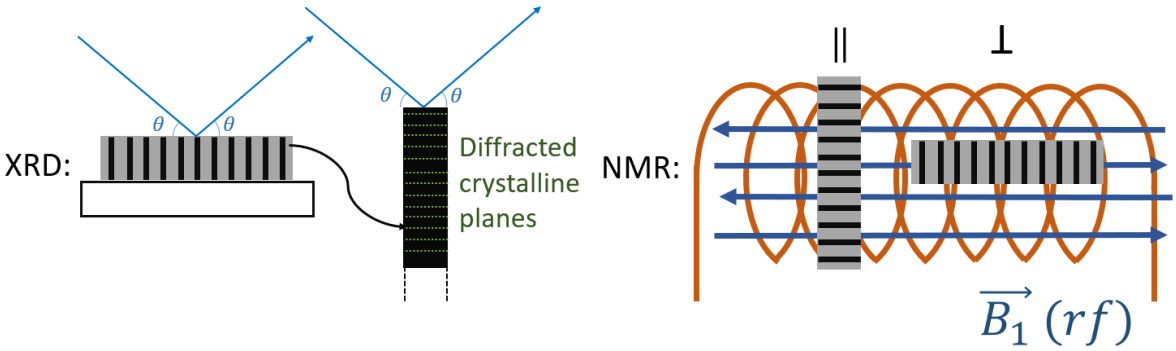

Figure 1: Schematic representation of the XRD and IF NMR experimental geometries. The membrane templates are shown in grey and the cobalt nanowires in black. XRD: The membrane sample was situated in the diffraction plane, i.e., diffraction came mainly from the crystallographic planes parallel to the membrane, or perpendicular to the wire axis. NMR: The samples were tested with two different orientations between the wire axis and the axis of the excitation and pick-up coil: Parallel (||) and Perpendicular (⊥) to the excitation magnetic field B_1 inside the coil.

2.3. ^{59}Co IF NMR

All NMR experiments were carried out at zero external field, using a SCOUT spectrometer (TECMAG, USA) and a commercial static broadband probe with a 5 mm solenoid excitation/pick-up coil (NMR-Service, Germany). Although the experiments were performed at ambient temperature, the probe was inserted inside a cryostat (Oxford Instruments, UK) for *rf* shielding purposes. The spectra were acquired point-by-point using spin-echo with frequency steps of 0.5 MHz. The spin-echo sequence was composed of two equal *rf* pulses of 1 µs with an interpulse delay of 8 µs. The repetition rate of the sequence was 67 Hz, thanks to the very short relaxation time of ferromagnetic cobalt, and the number of transients per point was equal to 4 k. In order to obtain quantitative spectra, the pulse power was varied over 20 dB (i.e., over two orders of magnitude for the *rf* power or one order of magnitude for the *rf* field B_1 amplitude) at each frequency point. The signal from the pulse power giving the maximum signal intensity at each frequency was chosen and used for the spectrum. The lower this power for a certain frequency, the higher the so-called enhancement factor and *vice-versa*. The enhancement factor is defined by the ratio of the excitation field seen by the nuclear spins during an impulsion and the magnitude of the *rf* field itself and allows to obtain additional information about the magnetic structure of the cobalt.[35], [36] In order to quantify the pulse power, the peak voltage was measured using an oscilloscope, which allowed to calculate the effective pulse power. At each frequency, the T_2 relaxation time of the main peaks was estimated by varying the interpulse delay and the spectral intensities was corrected accordingly as well as for the frequency (ω^2) dependence of the signal

intensity. To facilitate their insertion in a glass NMR tube fitting the 5 mm coil, the membranes containing the nanowires were cut into strips. In the case of the 200 nm AAO samples, the quantity of Co inside a single strip was already sufficiently high to obtain a good NMR signal. This was not the case for the 50 nm nanowire samples which have smaller nanowires with a lower density, and for which 6 of the membrane strips were stacked inside the NMR tube. As the orientation of the excitation field with respect to the wire main axis is crucial, each sample was tested at two different orientations, as shown in **Figure** . Since the nanowires are oriented normal to the membrane, for the first orientation, called *parallel*, the membranes were put perpendicular to the coil axis. This corresponded to a parallel orientation of the nanowire axis with respect to the excitation field. Similarly, for the *perpendicular* orientation, the membranes were placed parallel to the coil axis.

2.4. Magnetic characterization

Magnetic properties of the synthesized samples were studied by vibrating sample magnetometry (VSM) using a Princeton Measurement Corporation MicroMag 3900, as well as a Quantum Design Materials Property Measurement System (MPMS3). Hysteresis loops were measured at room temperature with an external field, up to 1.8 T, applied either parallel or perpendicular to the wire axis.

3. Results

3.1. SEM.

In order to verify the pore diameter, spacing and regularity, SEM analysis was performed on the samples. As shown in the tilted view of **Figure 1** a), the 200 nm pores inside the AAO samples were not completely filled with cobalt, in order to avoid overplating. In addition, the upper end of the pores, close to membrane surface, seemed to be quite defaulted due to a damaged surface, which was without consequence because of their incomplete filling. The AAO membranes, produced by anodic oxidation of aluminum in acidic solution, had interpore separations smaller than the pore diameter. On the other hand, as shown in **Figure 1** b), the 50 nm pores inside the PC membranes, being produced by track etching, had interpore spacings that were on average much larger than the pore diameter.

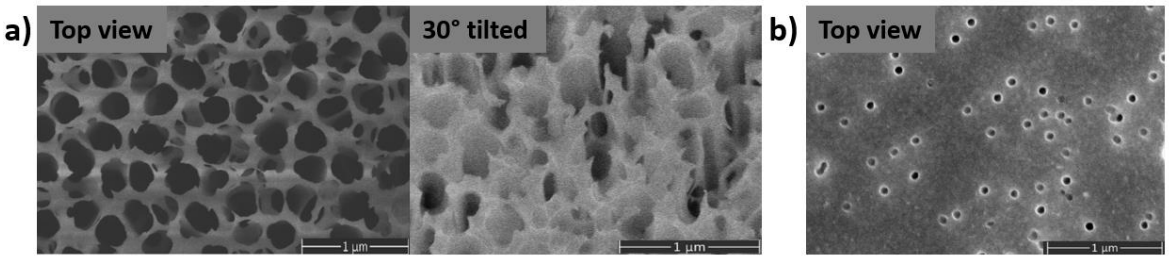

Figure 2: SEM images for two different membrane samples filled with cobalt nanowires. a) 200 nm AAO membrane sample under high vacuum (top view and 30° tilted with respect to the top view). b) 50 nm PC membrane sample under 100 Pa vapor pressure atmosphere.

3.2. XRD

The XRD patterns of the two 200 nm samples grown in AAO membranes (with and without additives) are represented in **Figure 2**.

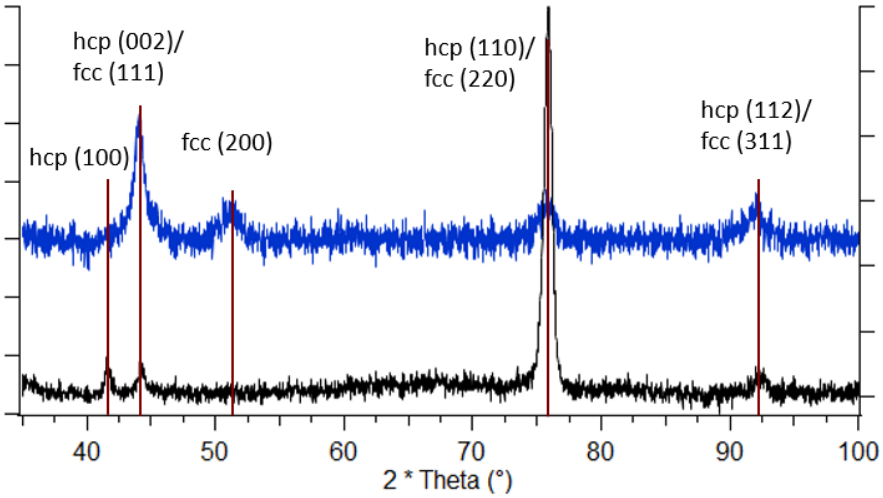

Figure 3: XRD patterns collected on 200 nm Co nanowires grown in AAO membranes (top/blue: with; bottom/black: without organic additives). The samples are analyzed with the membrane plane being in the XRD diffraction plane.

All the observed peaks in the diffraction pattern are from cobalt, either in the *fcc* or *hcp* phase. Three peaks are observed around 44.3°, 75.9° and 92.4°, which can be assigned to either *fcc* or *hcp*, irrespective of the presence of organic additives in the electrolyte during electrodeposition or not. In

the reference files, the theoretical positions of the cobalt *fcc* (111) and *hcp* (002) reflections are 44.2° and 44.8°, respectively, suggesting that this peak mainly came from *fcc* Co. Nevertheless, even a significant contribution to this peak from *hcp* Co cannot be excluded. Besides these three peaks, a fourth peak around 51.5° is observed in the diffraction pattern of the sample synthesized with additives and can unambiguously be assigned to *fcc* Co (200). While this peak is not present for the sample without additives, another peak at 41.6° is observed that corresponded this time unambiguously to *hcp* Co (100). These observations suggest that the additives changed the main crystalline form of the wire from *hcp* to *fcc*-rich. Further useful information could also be drawn about the crystal orientation with respect to the wire axis, as exposed earlier when describing the XRD setup (**Figure 1**). This is particularly interesting in the case of *hcp* cobalt in order to determine the relative orientation of the *c*-axis with respect to the wire axis because the *c*-axis is the magnetic easy axis of *hcp* Co. The *hcp* Co parts of the samples without organic additives were oriented with the *c*-axis mainly perpendicular to the wire axis since the relative intensity of the peaks corresponding to *hcp* Co (110) vs. *hcp* Co (002) is significantly higher than in polycrystalline samples. Overall, the reflections of the 200 nm sample electrodeposited with additives were broader than the one without, indicating smaller crystallite sizes. The XRD spectrum of the 50 nm PC membrane sample can be found in the Supporting Information 6.1 (**Figure 7**). Unfortunately, the reflections from the gold electrode still attached to the membrane masked those from cobalt and consequently, no conclusions could be drawn regarding the crystalline structure of this sample.

3.3. Magnetic hysteresis measurement.

The magnetic properties of the wires were studied at room temperature with a magnetic field applied perpendicularly (⊥) or parallel (||) to the wire axis, as shown in **Figure 4**. The 50 nm Co nanowires grown in a PC membrane exhibited squared hysteresis loops with a coercivity of about 500 Oe measured on-axis (i.e. parallel), about an order of magnitude larger than that in typical Co films. This coercivity enhancement is due to the small nanowire diameter, which impedes the domain wall propagation mechanism during magnetization reversal.[37]–[39] The magnetic easy axis of the wires can be determined by comparing the applied magnetic fields needed for saturation for the different directions of the applied field.

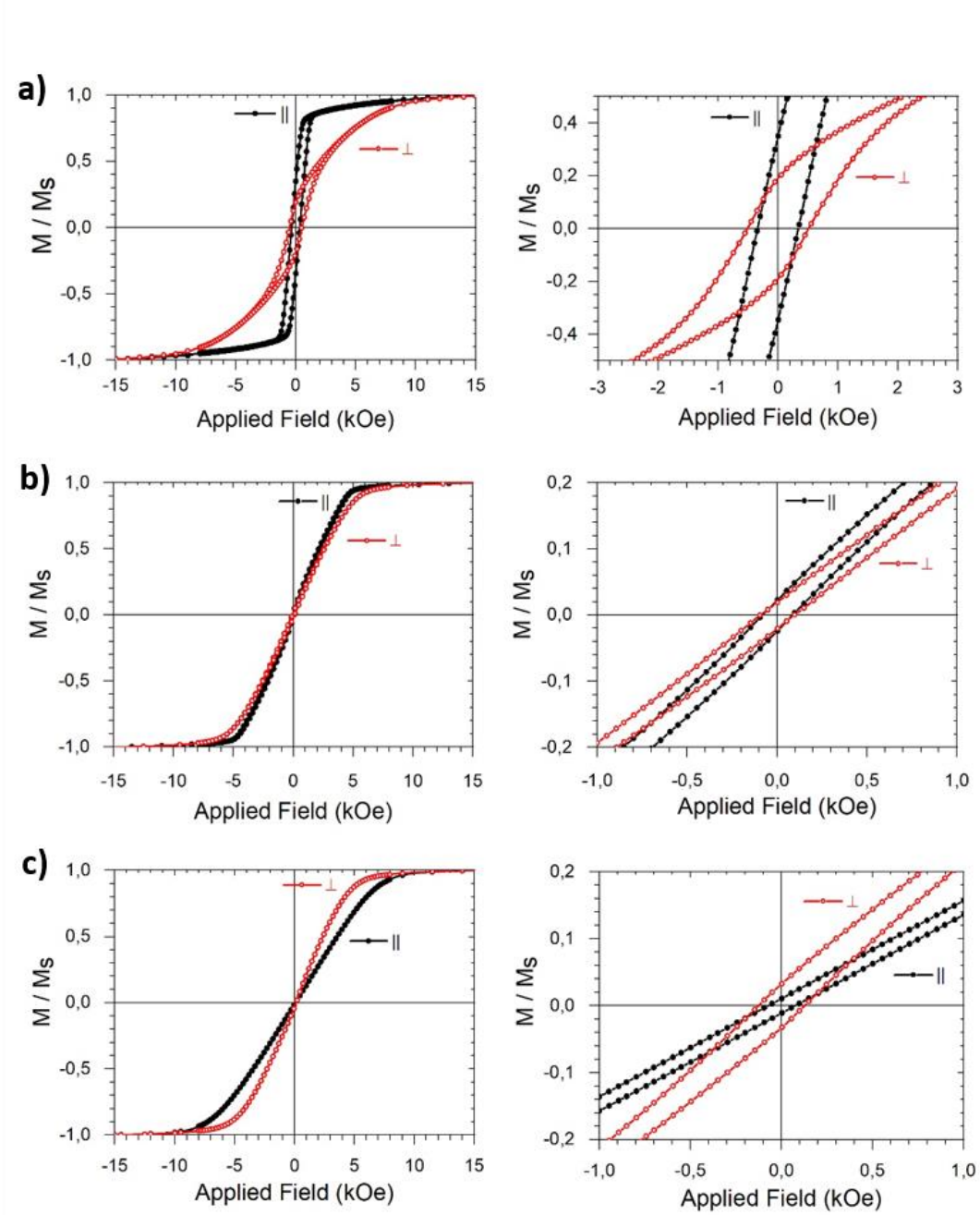

Figure 4: Magnetic hysteresis loops recorded at ambient temperature with the field applied perpendicular (⊥, red hollow symbols) or parallel (||, black full symbols) to the cobalt wires. a) 50 nm Co nanowires grown in a PC membrane, b) 200 nm Co nanowires grown in AAO membranes with additives, and c) 200 nm Co nanowires grown in AAO membranes without additives in electrolyte. Left: full loops. Right: Zoom-in views of the full loops.

A clear magnetic easy axis parallel (positive magnetic anisotropy) to the nanowires is observed for the 50 nm sample, due to the shape anisotropy resulting from the strong saturation field ($2\pi M_S$) of 8.8 kOe required to orient the magnetization away from the wire axis (**Figure 4** a)).[21] In the 200 nm Co

nanowire samples grown in AAO membranes, the magnetic properties exhibited significant differences. The coercivity enhancement was reduced to values below 120 Oe, due to the larger nanowire diameters. Furthermore, when cobalt was electrodeposited in the presence of additives, i.e. *fcc*-rich according to XRD, the nanowire axis (parallel geometry) was still the magnetic easy axis. However, its difference with the perpendicular geometry was much smaller (**Figure 4** b)), as the much closer spacing between nanowires leads to strong dipolar interaction that prefers antiferromagnetic alignment.[10], [40], [41] In contrast, the *hcp*-rich 200 nm sample, synthesized without additives, exhibited a magnetic easy axis perpendicular to the wire axis (negative magnetic anisotropy) (**Figure 4** c)). This is a manifestation of the *hcp* c-axis being perpendicular to the nanowires[42], [43], as suggested by the XRD diffraction patterns of **Figure 2**.

3.4. ^{59}Co Internal field NMR.

In metallic cobalt structures, valuable information may be obtained from the IF NMR spectrum, such as the crystalline and magnetic structure. Although not as commonly used as XRD or magnetometry, it nicely complements these methods due to its very local (nanoscale) character. The general spectral features of IF NMR in *fcc* or *hcp* cobalt nanostructures are as follows. At room temperature, the peak around 213 MHz can be assigned to signal coming from ^{59}Co nuclei in *fcc* multidomain structures.[22], [24] By symmetry of the *fcc* structure, this peak is generally narrow and well defined. A small peak around 216 MHz can be distinguished, which is in the literature sometimes assigned to Co in a single-domain magnetic structures, with the difference compared to the multidomain *fcc* being due to the demagnetizing field effect.[24], [44] However, this peak assignment is generally done when analyzing Co nanoparticles and not for oriented systems like nanowires. In nanowires the form factor is not the same one as in spheres[45] and consequently the demagnetizing field would lead to a different frequency shift in single-domain *fcc*. Possible origins of this peak could therefore be *fcc* stacking faults with a higher internal field compared to pure *fcc*[46], [47] or *fcc* structures with a residual demagnetizing field. The signal coming from anisotropic *hcp* structures is generally much broader than the one corresponding to *fcc*.

A broad peak between 217 MHz and 222 MHz is often assigned to *hcp* cobalt without distinction between signal arising from mono- and multidomain structures.[24], [48], [49] Additional information about the magnetic structure can be obtained from the variation of the optimal power with frequency, which is inversely proportional to the enhancement factor. As the enhancement is much stronger for nuclei situated inside a domain-wall structure than for those inside the domain itself, less power is

needed for the optimal excitation of the former.[35], [36], [48] In a similar fashion, the signal arising from ^{59}Co nuclei inside domain walls will also be enhanced much more than from the ones inside the domains, which means that the main signal observed when analyzing multidomain structures will be from the excitation of the domain walls and not from the domains. [35], [46]

Figure 5 displays the IF NMR spectra in the frequency range associated with ^{59}Co resonances. For all samples, the spectral features were similar and supported the conclusion that both *hcp* and *fcc* structures coexisted (**Figure 5** a-c)). While the XRD analysis suggests the presence of *fcc*- or *hcp*-rich structures in the 200 nm samples, depending on the presence of additives in the electrolyte during the wire deposition or not, this difference was not distinguished by NMR. Indeed, in all cases, a significant resonance in the 217-222 MHz range together with a peak around 213 MHz revealed the presence of both *hcp* and *fcc* components, with similar weights for both samples (The comparison of the weights in the decomposition can be found in the Supporting Information 6.3 (**Figure 11**)). The distribution of the optimal power, and hence of the enhancement factor, was constant over the whole spectrum range for all studied samples (**Figure 5** d-f)). No distinction in that respect could be made between the 213 MHz resonance of the *fcc* multidomain structures and the rest of the spectra. One could thus conclude that most of the signal in the spectrum, also in the *hcp* Co part, arose from the excitation of the walls in multidomain structures, establishing that the magnetic structure of the nanowires was broken up into magnetic domains. The signal was dominated by the excitation of the domain walls.[35], [46]

Experiments with different radio frequency (*rf*) field orientations relative to the wire axis have been performed, but the shape of the resulting spectra was identical for both orientations for all analyzed samples. However, a change in the power needed for an optimal excitation could be observed for some samples. For the samples for which the VSM measurements revealed a magnetic easy axis parallel to the wire axis (50 nm Co wires & 200 nm wires grown with additive), the enhancement factor (inversely related to the optimal power) was stronger for the *rf* field *parallel* to the wire axis than for the *perpendicular* orientation (**Figure 5** d-e)). In contrast, the 200 nm Co wires grown without additives, for which VSM revealed an easy axis perpendicular to the wire axis, had a similar enhancement factor for both orientations (**Figure 5** f)). These results provided more information on the magnetic domain structure, as will be discussed in the following section.

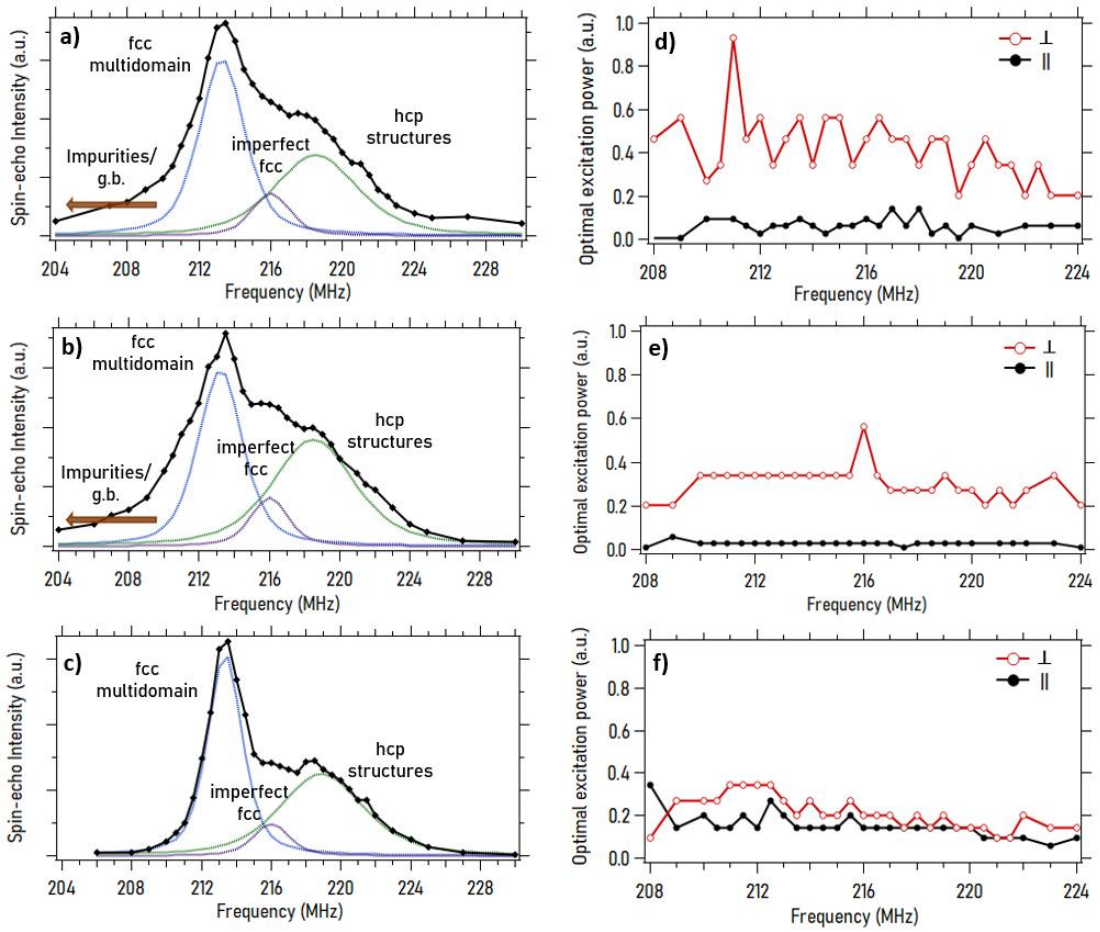

Figure 5: ^{59}Co IF NMR room temperature spectra: a) 50 nm Co nanowires grown in PC membrane, b) 200 nm Co nanowires grown in AAO membranes with organic additives (XRD *fcc*-rich), and c) 200 nm Co nanowires grown in AAO membranes without organic additives (XRD *hcp*-rich). A tentative decomposition into peaks corresponding to different crystalline and magnetic structures is also presented (g.b. = grain boundaries). The spectral shape is identical regardless of the orientation between the *rf* pulse and the wire axis, so only one orientation is represented here. The numerical comparison of the decomposition can be found in the Supporting Information 6.3 (**Figure 11**). The graphs d), e) and f) correspond to the optimal excitation power for each of the left-side graphs for different orientations: The red line (hollow spheres) corresponds to a perpendicular (⊥) orientation between the direction of the *rf* pulse and the wire axis, the black line (full spheres) to a parallel (||) one.

4. Discussions

4.1. Crystalline structure

From XRD and magnetometry measurements, it was apparent that the samples had different crystalline and therefore magnetic structures. Concerning the crystalline structure, XRD suggested that the 200 nm nanowires produced with organic additives had an enriched *fcc* structure, while the 200 nm nanowires produced without organic additives had a *hcp*-rich structure with a *c*-axis perpendicular to the wire axis. However, due to the oriented character of the sample during the XRD experiments and the overlapping of the main *fcc* and *hcp* Co peaks, a quantitative phase determination was not unambiguously possible. In addition, XRD experiments only detect signal coming from relatively large cobalt coherent domains, while NMR is sensible to the whole sample. Indeed, the IF NMR spectra revealed that, at the nanoscale, both crystalline structures were present in more or less the same relative amount.

4.2. Magnetic structure

Concerning the magnetic structures, magnetometry and IF NMR results supported each other. The M(H) hysteretic behavior has already been observed in previous articles analyzing cobalt wires of different diameters inside track-etched polymer membranes.[10], [21], [26] The physical basis for the observed magnetic anisotropy of soft ferromagnetic materials is well known.[50] It results from the superposition of shape anisotropy, magnetocrystalline anisotropy and wire-wire interactions (see for example the discussions of magnetic anisotropy in Co nanowires in references [21], [26]). Since the nanowire shape anisotropy favors a magnetization alongside the wire axis, this is the preferred configuration for wires with a weakly anisotropic crystalline structure, like *fcc* cobalt. On the other hand, a strong crystalline anisotropy (like *hcp* Co) perpendicular to the wire axis will be in competition with the shape anisotropy, possibly leading to a magnetic easy axis perpendicular to the wires.[42], [43], [51], [52]

50 nm nanowires

The case of the Co nanowires with a relatively narrow diameter of 50 nm grown in a PC membrane was the most straightforward as it was dominated by shape anisotropy. In this instance, the dipolar field acting on a wire due to its neighbors can safely be neglected because of the large interwire distances. Furthermore, the small 50 nm diameter, combined with the µm-scale wire length, resulted in a strong shape anisotropy[21], [26], as reflected in the saturation field difference of the sample

(**Figure 4** a)). It could be inferred that at zero field, the magnetic structure, confined by the wire diameter, was broken up into magnetic domains with on-axis remanent magnetic moments. This conclusion was strongly supported by the anisotropy of the IF NMR enhancement factor as function of the orientation of the wire axis to the excitation field (**Figure 5** d)). It must be recalled that the flat frequency dispersion of the enhancement factor established that the IF NMR signal of our samples arose predominantly from the excitation of domain walls. In this case, the enhancement factor finds its origin in the periodic displacement of the domain walls under the effect of the *rf* field, a displacement which is favored when the field is oriented along the domain magnetization[35], as represented schematically in **Figure 1** a). *Rf* fields with a different orientation compared to the domain axes will displace the walls less efficiently.[53] Consequently, the higher enhancement recorded when the *rf* field was applied on axis with the nanowires supported the conclusions that the magnetic domains were magnetized along the wires. Note that the same experiments have been performed on 50 nm wires deposited without the presence of organic additives in the electrolyte, leading to the same results regarding the magnetic anisotropy (Supporting Information 6.2 **Figure 9** & **Figure 10**). In contrast, the magnetic properties of the 200 nm samples strongly depended on the synthesis conditions, indicating that the magnetic behavior of the 50 nm wires is controlled indeed by the shape anisotropy.

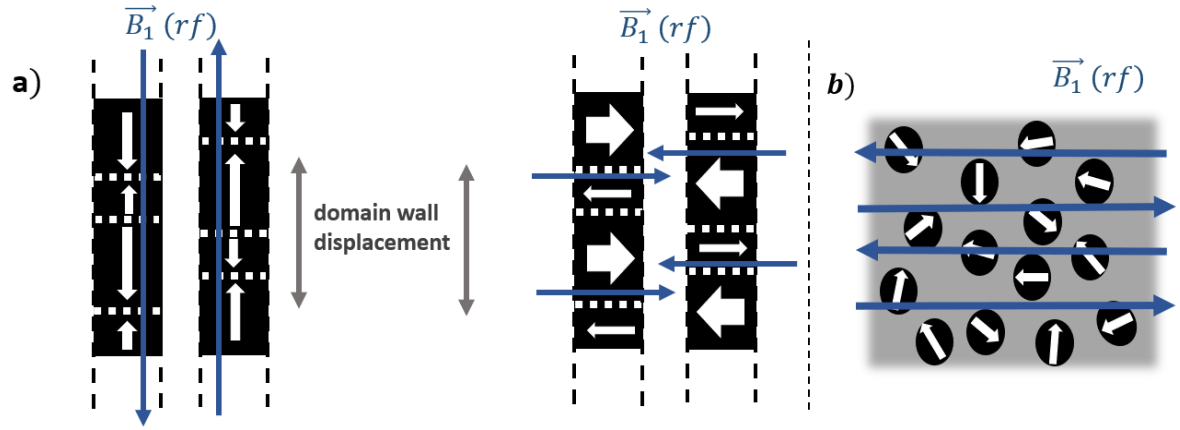

Figure 6: a) Orientation of the optimal excitation field as function of the domain wall structure. A *rf* field (B_1) with this orientation will efficiently displace the domain walls back and forth by favoring the growth of domains, as shown schematically. Left: domains alongside the wire axis: 50 nm & 200 nm nanowires with additives. Right: domains perpendicular to the wire axis: 200 nm without additives. b) Random orientations of the in-plane magnetic domains for the sample without additives, which are therefore more or less aligned with the orientation of the *rf* field perpendicular to the wire axis.

200 nm nanowires

For the two samples of 200 nm Co nanowires grown in AAO membranes, the same analysis as for the previously described 50 nm Co nanowires could be performed. For the sample electrodeposited in presence of additives in the electrolyte, the enhancement factor was higher for a *rf* field orientation along the wire axis (**Figure 5** e)), consistent with the magnetic easy axis along the nanowires detected by VSM (**Figure 4** b)). In contrast, for the 200 nm sample electrodeposited without additives, VSM revealed a magnetic easy axis perpendicular to the nanowires (**Figure 4** c)), while the enhancement factor did not reveal any strong anisotropy (**Figure 5** f)).

These observations raised two questions. First, why did the latter sample show no anisotropy of the IF NMR enhancement factor? Actually, this apparent contradiction can be explained on simple geometrical considerations. While the c-axis of the *hcp* crystallites (easy magnetic axis) was preferentially oriented perpendicular to the wire axis, its azimuthal angle was evenly distributed because of the axial symmetry of the wires, as already observed by magnetic torque measurements.[21], [51] As represented in the membrane top view of **Figure 6** b), even when the *rf* field was perpendicular to the wire axis, it could not coincide with all possible the orientations of the magnetic domains. As a result, the enhancement factor had an intermediate value between the one for a perpendicular and a parallel orientation. Due to angular symmetry, the overall enhancement factor can be approximated by:

$$\eta_{mean} = \frac{2}{\pi} * \int_0^{\frac{\pi}{2}} \eta(\theta) d\theta$$

with θ the angle between the domain orientation and the *rf* field. Approximations of the expression of the enhancement factor as function of θ, $\eta(\theta)$, have been proposed by Stearns et al.[53]. The power needed for an optimal excitation was therefore intermediate between the one needed for a perpendicular and a parallel orientation between the excitation field and the domain direction, observed for the samples with organic additives. Nevertheless, this reduced enhancement factor for experiments with a *perpendicular* orientation still does not fully explain why it is the same as for experiments performed with a *parallel* orientation. In the case of a parallel orientation between the wire and *rf* field, the *rf* field would be perpendicular to all the domains normal to the wire axis, independently of their azimuthal angle, resulting in an even lower enhancement. An additional explanation is the fact that the wires were composed of a mixture of *hcp* and *fcc* Co crystalline structures, as deduced from the IF NMR spectrum (**Figure 5** c)). Due to competition between the shape anisotropy and the perpendicular crystalline anisotropy (only from the *hcp* Co phases), the overall easy magnetic axis perpendicular to the wire was not very strong. This led to a situation with mixed domain

orientations, where, besides their predominant perpendicular orientation, a significant part of the domains was also oriented alongside the wire axis.

Second, what is the origin of the different magnetic behaviors of the two samples of 200 nm Co nanowires grown in AAO membranes? This can be discussed in terms of competition between shape and magnetocrystalline anisotropy, as well as the effect of dipolar interactions. From geometrical considerations, the shape anisotropy was reduced and the dipolar interactions increased in the 200 nm samples compared to the 50 nm one. As a result, the magnetic easy axis was distributed more off axis, the coercivity, the remanence and the effective magnetic energy were reduced. As both samples had the same geometrical configuration, the different magnetic behavior must originate from a variation in their crystalline anisotropy. The XRD results (shown in **Figure 2**) suggested a first explanation: The sample grown in presence of additives appeared to be *fcc*-rich, resulting in a low crystalline anisotropy and a magnetic easy axis alongside the wire due to the effect of the shape anisotropy. The sample grown in absence of additives on the other hand, appeared to be *hcp*-rich with a *c*-axis perpendicular to the wire axis, leading to a strong crystalline anisotropy and magnetic easy axis perpendicular to the wire. The analysis of the IF NMR spectra proposes an alternative explanation, however, as it shows an almost equal distribution of cobalt atoms between *fcc* and *hcp* crystallites for all the samples studied (**Figure 5** a-c)). Nevertheless, a significant difference between the IF NMR spectra of the samples is that the ^{59}Co resonances of the 200 nm sample without additives were sharper, in particular with no extension towards the 210 MHz frequency range. Signal from such a low frequency range is generally attributed to grain boundaries, impurities or interfaces[47], [54] From IF NMR this sample appeared thus more crystallized than the two others deposited with additives. When studying the deposition of cobalt thin films under similar conditions, it has been observed that the addition of organic additives, such as PEG, tends to inhibit the crystalline growth.[55], [56] As a result, the size of the cobalt crystallites decreases, as reflected in the broader XRD and NMR peak width. In addition more grain boundaries are created and organic impurities from the additives, such as sulfur, tend to be incorporated inside the structure[56], explaining the additional NMR peak at lower frequencies. Besides differences in crystal symmetry (*fcc* or *hcp*), for the cobalt nanowires under consideration a crucial structural parameter to control magnetic anisotropy appeared to be differences in the crystallite size and grain boundaries.

5. Conclusions

Despite being easy to perform on a standard commercial solid-state NMR spectrometer, IF NMR is not a widespread method to characterize cobalt magnetic structures. While concerning the magnetic structure, magnetometry and IF NMR provided essentially the same information regarding anisotropy, concerning the crystalline structure, IF NMR nicely complemented XRD characterization. Indeed, in our study of cobalt nanowires, it provided a more accurate picture of the distribution of *fcc* and *hcp* domains as well as of the presence and influence of defects at coherent domain boundaries. This allowed to better understand the influence of the presence of additives during the electrodeposition of cobalt on the magnetic properties of the formed nanowires. It was established that the organic additives determine the magnetic anisotropy of the nanowires more through the control of the grain boundaries than by modifying the *fcc* / *hcp* balance.

Acknowledgement

NMR equipment at ESPCI Paris is funded in part by the Paris Region. This project has received funding from the European Union's Horizon 2020 research and innovation program under the Marie Skłodowska-Curie grant agreement No 754387. Work at Georgetown University has been supported by the US NSF (ECCS-1933527). The acquisition of a Magnetic Property Measurements System (MPMS3) at GU, which was used in this investigation, was supported by the US-NSF (DMR-1828420). Bruno Bresson (ESPCI) is thanked for performing the SEM analysis.

6. Supporting information

6.1. 50 nm with additives

The following X-ray diffraction (XRD) pattern comes from the analysis of Co nanowires grown in the 50 nm pores of a PC membrane, in presence of organic additives in the electrolyte. The precise synthesis conditions, as well as more details about the XRD experiments are presented in Section 2 of this chapter. As highlighted in the graph, the only four peaks that can be distinguished (44.5°, 64.5°, 77.5°, 81.9°) correspond to signal from the gold (Au) electrode attached to the bottom of the membrane, probably covering peaks corresponding to signal from *fcc*/*hcp* cobalt. No determination of the Co crystalline phase was therefore possible.

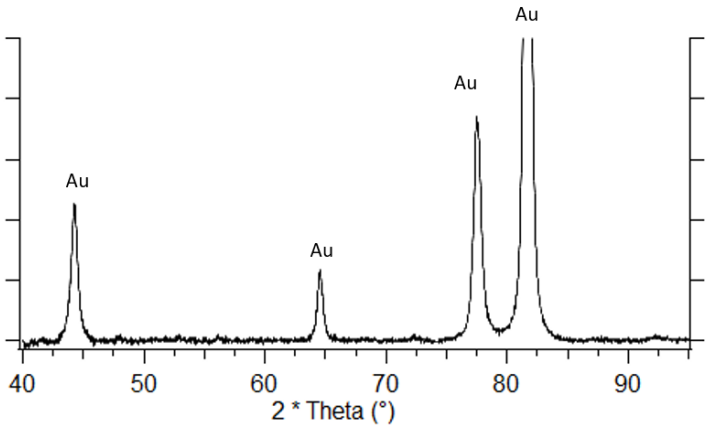

Figure 7: XRD pattern collected on 50 nm Co nanowires grown in the pores of a PC membrane in presence of organic additives in the electrolyte. The samples are analyzed with the membrane plane being in the XRD diffraction plane (*i.e.* the wire axis normal to the diffraction plane).

6.2. 50 nm without additives

The following results were obtained from wires grown into the 50 nm pores of a PC membrane, in absence of organic additives in the electrolyte. The characteristics of the membrane were the same as of the one used for the production of 50 nm nanowires deposited in presence of organic additives and are described in the main article. The composition of the electrolyte was the same as the one of the 200 nm nanowires without additives, namely: 240 g/L $CoSO_4 \cdot 7H_2O$ + 50 g/L $CoCl_2 \cdot 6H_2O$ + 40 g/L H_3BO_3.

XRD

The XRD pattern of the above presented sample is shown in **Figure 8**. Besides the 4 peaks corresponding to signal form the Au electrode still attached to the membrane, 3 peaks assigned to cobalt clearly can be distinguished: 41.5° (*hcp* (100), 75.9° (*hcp* (110)/ *fcc* (220)) and 92.3° (*hcp* (112)/ *fcc* (311)). The two peaks around 52.5° and 56.0° cannot be assigned to neither Co, nor Au structures, even though the former one is close to the characteristic peak of *fcc* Co (200) around 51.5°. Due to the strong Au signal around 44.5°, peaks corresponding to *hcp* (002)/ *fcc* (111) cobalt might be covered, which makes it difficult to analyze the crystalline structure by XRD. Nevertheless, the relatively strong *hcp* (100) Co peak indicates that a significant part of the sample had a hexagonal crystalline structure with its *c*-axis perpendicular to the wire axis.

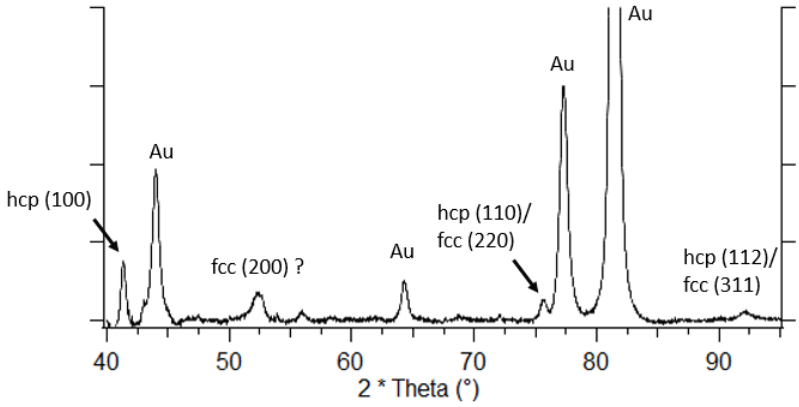

Figure 8: a XRD pattern collected on 50 nm Co nanowires grown in the pores of a PC membrane in absence of organic additives in the electrolyte. The samples are analyzed with the membrane plane being in the XRD diffraction plane.

Magnetic hysteresis measurement

The magnetic properties of the 50 nm Co nanowires deposited in absence of organic additives were studied at room temperature with a magnetic field applied perpendicularly (⊥) or parallel (**||**) to the wire axis, as shown in **Figure 4**. The loops are fairly similar to the ones observed on 50 nm Co nanowires deposited in presence of organic additives, shown in **Figure 4** a). Squared hysteresis loops with a coercivity of about 500 Oe measured on-axis (i.e. parallel) can be seen, as well as a clear magnetic easy axis parallel to the nanowires.

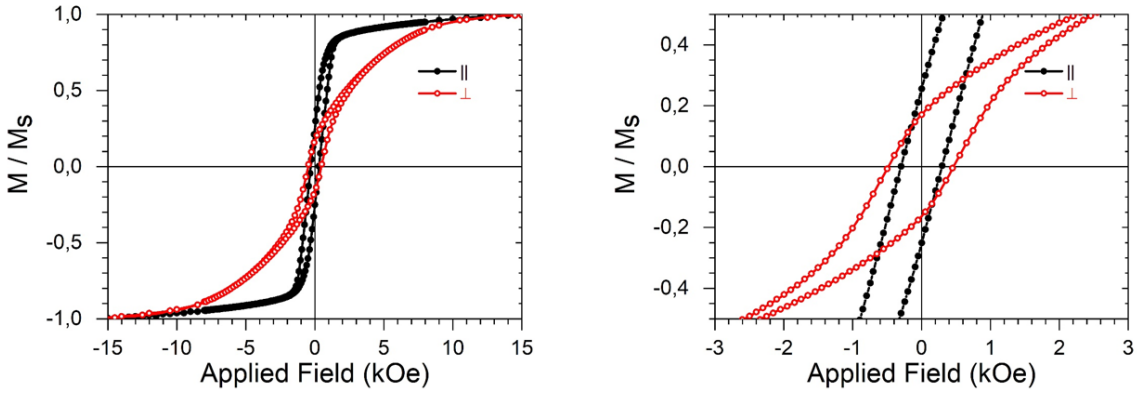

Figure 9: Magnetic hysteresis loops recorded on 50 nm Co nanowires grown in the pores of a PC membrane in absence of organic additives. The measurements were performed at ambient temperature with the field applied perpendicular (⊥, red hollow symbols) or parallel (||, black full symbols) to the cobalt wires. Left: full loops. Right: Zoom-in view of the full loops.

In **Figure 10**, the internal field (IF) NMR analysis in the frequency range associated with 59Co resonances obtained from 50 nm nanowires without additives is represented. The spectrum (left) is mainly composed of two peaks, corresponding to cobalt in fcc multi-domain and hcp structures. In addition, a small peak around 216 MHz can be distinguished, which could be assigned to fcc stacking faults or fcc structures with a residual demagnetization field. The amount of hcp Co detected by NMR was significantly bigger than the amount of fcc, which differentiated this samples from all the other ones analyzed, where both phases were present in more or less the same quantity (**Figure 11**). The narrow peak width and the absence of a significant signal below 210 MHz (especially compared to the samples grown in presence of additives) suggest that cobalt was well crystallized, with big crystalline domains and few grain boundaries/ impurities. As the signal around 213 MHz can unambiguously be assigned to signal from fcc multi-domain structures and the optimal power is pretty much flat over the whole frequency range, it can be concluded that a major part of the signal arose from multi-domain structures and therefore the excitation of domain walls. The power needed for an optimal excitation and consequently also the enhancement factor is anisotropic, with less power needed for a parallel orientation between the rf field and the wire axis. This was the result a multi-domain structure and an easy axis of magnetization colinear with the wire, as confirmed by the magnetic hysteresis measurements (**Figure 4**). It could be concluded that the strong shape anisotropy of the 50 nm wires results was dominant over the *hcp* Co crystalline anisotropy (dipolar interactions could be neglected due to the big interwire distance), in contrast to the 200 nm sample synthesized under the same conditions. The NMR results showed the presence of a big amount of *hcp* Co in the sample but gave no information about the orientation of its *c*-axis (easy axis of magnetization). The XRD analysis with

the membrane plane in the diffraction plane, shown in **Figure 8**, suggested that a significant part of the sample had a hexagonal crystalline structure with its *c*-axis perpendicular to the wire axis. However, the presence of the gold electrode at the bottom of the membrane made it difficult to obtain more information by XRD.

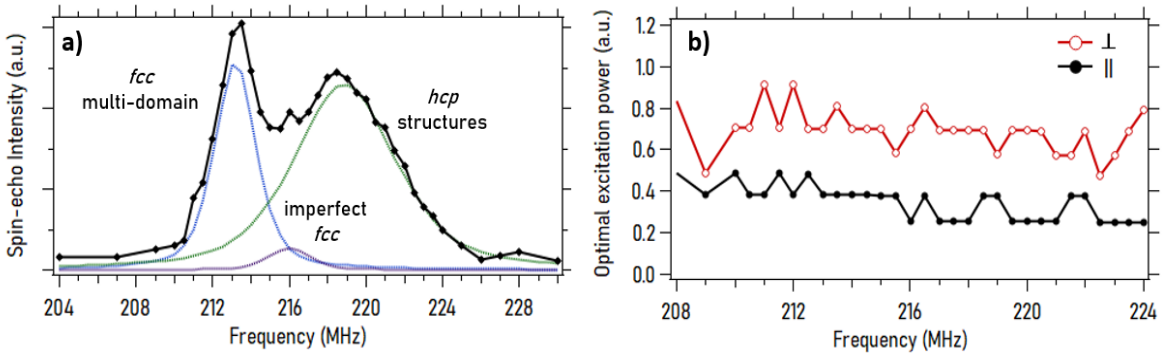

Figure 10: a) ^{59}Co IF NMR room temperature spectrum of 50 nm Co nanowires grown in PC membrane in absence of organic additives in the electrolyte. A tentative decomposition into peaks corresponding to different crystalline and magnetic structures is also presented, with the relative amounts of the different phases given in **Figure 11**. The spectral shape is identical regardless of the orientation between the *rf* pulse and the wire axis, so only one orientation is represented here. The graphs b) corresponds to the optimal excitation power for the same sample for different orientations: The red line (hollow spheres) corresponds to a perpendicular (⊥) orientation between the direction of the *rf* pulse and the wire axis, the black line (full spheres) to a parallel (||) one.

6.3. All sample overview

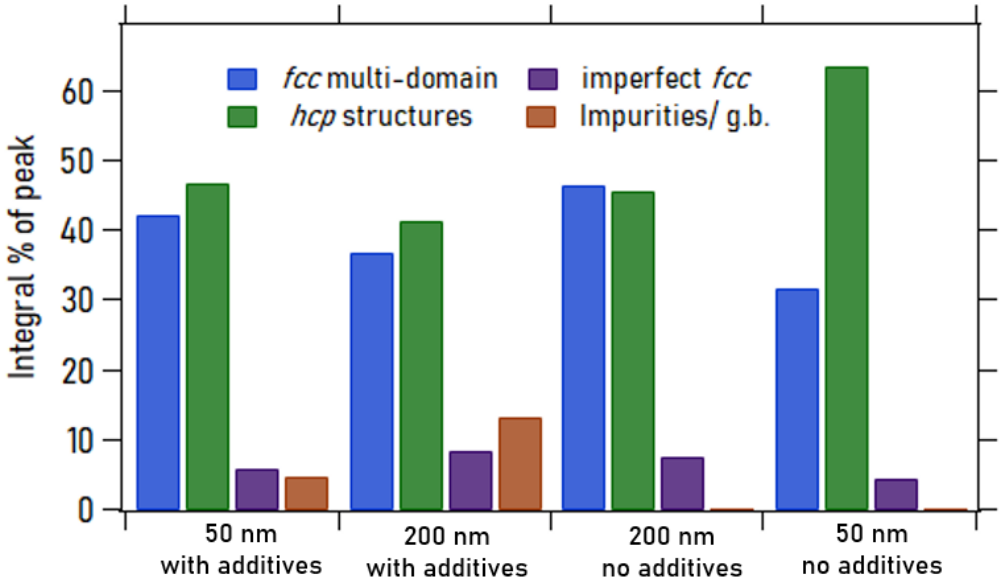

Figure 11: Quantitative distribution of the different crystalline/ magnetic phases detected by ^{59}Co IF NMR for the samples presented in this work. The corresponding spectra are shown in **Figure 5** and **Figure 10**.

7. References

[1] M. Staňo and O. Fruchart, “Magnetic Nanowires and Nanotubes,” in *Handbook of Magnetic Materials*, vol. 27, Elsevier, 2018, pp. 155–267. doi: 10.1016/bs.hmm.2018.08.002.

[2] A. Fert and L. Piraux, “Magnetic nanowires,” *J. Magn. Magn. Mater.*, vol. 200, no. 1–3, Art. no. 1–3, Aug. 1999, doi: 10.1016/S0304-8853(99)00375-3.

[3] A. Blondel, J. P. Meier, B. Doudin, and J. -Ph. Ansermet, “Giant magnetoresistance of nanowires of multilayers,” *Appl. Phys. Lett.*, vol. 65, no. 23, pp. 3019–3021, Dec. 1994, doi: 10.1063/1.112495.

[4] K. Liu, K. Nagodawithana, P. C. Searson, and C. L. Chien, “Perpendicular giant magnetoresistance of multilayered Co/Cu nanowires,” *Phys. Rev. B*, vol. 51, no. 11, Art. no. 11, Mar. 1995, doi: 10.1103/PhysRevB.51.7381.

[5] J.-L. Maurice *et al.*, “Microstructure of magnetic metallic superlattices grown by electrodeposition in membrane nanopores,” *J. Magn. Magn. Mater.*, vol. 184, no. 1, pp. 1–18, Apr. 1998, doi: 10.1016/S0304-8853(97)01104-9.

[6] J. Wong, P. Greene, R. K. Dumas, and K. Liu, “Probing magnetic configurations in Co/Cu multilayered nanowires,” *Appl. Phys. Lett.*, vol. 94, no. 3, Art. no. 3, Jan. 2009, doi: 10.1063/1.3073740.

[7] J.-L. Déjardin, A. Franco, F. Vernay, and H. Kachkachi, “Ferromagnetic resonance of a two-dimensional array of nanomagnets: Effects of surface anisotropy and dipolar interactions,” *Phys. Rev. B*, vol. 97, no. 22, p. 224407, Jun. 2018, doi: 10.1103/PhysRevB.97.224407.

[8] H. Zhang, W. Jia, H. Sun, L. Guo, and J. Sun, “Growth mechanism and magnetic properties of Co nanowire arrays by AC electrodeposition,” *J. Magn. Magn. Mater.*, vol. 468, pp. 188–192, Dec. 2018, doi: 10.1016/j.jmmm.2018.08.013.

[9] B. Das, K. Mandal, P. Sen, A. Bakshi, and P. Das, “Directional change of magnetic easy axis of arrays of cobalt nanowires: Role of non-dipolar magnetostatic interaction,” *Phys. B Condens. Matter*, vol. 407, no. 18, pp. 3767–3773, Sep. 2012, doi: 10.1016/j.physb.2012.05.058.

[10] E. C. Burks *et al.*, “3D Nanomagnetism in Low Density Interconnected Nanowire Networks,” *Nano Lett.*, vol. 21, no. 1, Art. no. 1, Jan. 2021, doi: 10.1021/acs.nanolett.0c04366.

[11] M. Hayashi, L. Thomas, C. Rettner, R. Moriya, and S. S. P. Parkin, “Real time observation of the field driven periodic transformation of domain walls in Permalloy nanowires at the Larmor frequency and its first harmonic,” *Appl. Phys. Lett.*, vol. 92, no. 11, p. 112510, Mar. 2008, doi: 10.1063/1.2890036.

[12] S. S. P. Parkin, M. Hayashi, and L. Thomas, “Magnetic Domain-Wall Racetrack Memory,” *Science*, vol. 320, no. 5873, p. 190, avril 2008, doi: 10.1126/science.1145799.

[13] L. Herrera Diez *et al.*, “Nonvolatile Ionic Modification of the Dzyaloshinskii-Moriya Interaction,” *Phys. Rev. Appl.*, vol. 12, no. 3, p. 034005, Sep. 2019, doi: 10.1103/PhysRevApplied.12.034005.

[14] S. Parkin and S.-H. Yang, “Memory on the racetrack,” *Nat. Nanotechnol.*, vol. 10, no. 3, pp. 195–198, Mar. 2015, doi: 10.1038/nnano.2015.41.

[15] M. Kac *et al.*, “Effect of the template-assisted electrodeposition parameters on the structure and magnetic properties of Co nanowire arrays,” *Mater. Sci. Eng. B*, vol. 211, pp. 75–84, Sep. 2016, doi: 10.1016/j.mseb.2016.06.004.

[16] V. R. Caffarena, A. P. Guimarães, W. S. D. Folly, E. M. Silva, and J. L. Capitaneo, "Magnetic behavior of electrodeposited cobalt nanowires using different electrolytic bath acidities," *Mater. Chem. Phys.*, vol. 107, no. 2–3, Art. no. 2–3, Feb. 2008, doi: 10.1016/j.matchemphys.2007.07.016.

[17] R. Ferré, K. Ounadjela, J. M. George, L. Piraux, and S. Dubois, "Magnetization processes in nickel and cobalt electrodeposited nanowires," *Phys. Rev. B*, vol. 56, no. 21, Art. no. 21, Dec. 1997, doi: 10.1103/PhysRevB.56.14066.

[18] J.-E. Wegrowe, D. Kelly, A. Franck, S. E. Gilbert, and J.-Ph. Ansermet, "Magnetoresistance of Ferromagnetic Nanowires," *Phys. Rev. Lett.*, vol. 82, no. 18, Art. no. 18, May 1999, doi: 10.1103/PhysRevLett.82.3681.

[19] L. Piraux *et al.*, "Anisotropic transport and magnetic properties of arrays of sub-micron wires," *J. Magn. Magn. Mater.*, vol. 165, no. 1–3, Art. no. 1–3, Jan. 1997, doi: 10.1016/S0304-8853(96)00553-7.

[20] W. Wernsdorfer *et al.*, "Nucleation of Magnetization Reversal in Individual Nanosized Nickel Wires," *Phys. Rev. Lett.*, vol. 77, no. 9, Art. no. 9, Aug. 1996, doi: 10.1103/PhysRevLett.77.1873.

[21] Y. Henry, K. Ounadjela, L. Piraux, S. Dubois, J.-M. George, and J.-L. Duvail, "Magnetic anisotropy and domain patterns in electrodeposited cobalt nanowires," *Eur. Phys. J. B*, vol. 20, no. 1, pp. 35–54, Mar. 2001, doi: 10.1007/s100510170283.

[22] A. C. Gossard and A. M. Portis, "Observation of Nuclear Resonance in a Ferromagnet," *Phys. Rev. Lett.*, vol. 3, no. 4, Art. no. 4, Aug. 1959, doi: 10.1103/PhysRevLett.3.164.

[23] Y. Liu *et al.*, "Sampling the structure and chemical order in assemblies of ferromagnetic nanoparticles by nuclear magnetic resonance," *Nat. Commun.*, vol. 7, p. 11532, May 2016, doi: 10.1038/ncomms11532.

[24] A. S. Andreev, J.-B. d'Espinose de Lacaillerie, O. B. Lapina, and A. Gerashenko, "Thermal stability and hcp–fcc allotropic transformation in supported Co metal catalysts probed near operando by ferromagnetic NMR," *Phys. Chem. Chem. Phys.*, vol. 17, no. 22, Art. no. 22, 2015, doi: 10.1039/C4CP05327C.

[25] I. V. Yakovlev *et al.*, "Superparamagnetic behaviour of metallic Co nanoparticles according to variable temperature magnetic resonance," *Phys. Chem. Chem. Phys.*, vol. 23, no. 4, pp. 2723–2730, 2021, doi: 10.1039/D0CP05963C.

[26] G. J. Strijkers, J. H. J. Dalderop, M. A. A. Broeksteeg, H. J. M. Swagten, and W. J. M. de Jonge, "Structure and magnetization of arrays of electrodeposited Co wires in anodic alumina," *J. Appl. Phys.*, vol. 86, no. 9, pp. 5141–5145, Nov. 1999, doi: 10.1063/1.371490.

[27] H. De Riedmatten, V. Scarani, and J.-P. Ansermet, "Effect of oxidation of cobalt-based nanowires on NMR spin-lattice relaxation," *Appl. Magn. Reson.*, vol. 19, no. 3–4, pp. 439–445, Jul. 2000, doi: 10.1007/BF03162387.

[28] V. Scarani, H. De Riedmatten, and J.-P. Ansermet, "59Co nuclear magnetic resonance studies of magnetic excitations in ferromagnetic nanowires," *Appl. Phys. Lett.*, vol. 76, no. 7, Art. no. 7, Feb. 2000, doi: 10.1063/1.125624.

[29] V. Scarani, B. Doudin, and J.-P. Ansermet, "The microstructure of electrodeposited cobalt-based nanowires and its effect on their magnetic and transport properties," *J. Magn. Magn. Mater.*, vol. 205, no. 2–3, p. 8, Nov. 1999, doi: 10.1016/S0304-8853(99)00513-2.

[30] B. Doudin *et al.*, "Magnetic and transport properties of electrodeposited nanostructured nanowires," *IEEE Trans. Magn.*, vol. 34, no. 4, Art. no. 4, Jul. 1998, doi: 10.1109/20.706328.

[31] D. A. Gilbert *et al.*, "Tunable Low Density Palladium Nanowire Foams," *Chem. Mater.*, vol. 29, no. 22, Art. no. 22, Nov. 2017, doi: 10.1021/acs.chemmater.7b03978.

[32] J. Malloy, A. Quintana, C. J. Jensen, and K. Liu, "Efficient and Robust Metallic Nanowire Foams for Deep Submicrometer Particulate Filtration," *Nano Lett.*, vol. 21, no. 7, pp. 2968–2974, Apr. 2021, doi: 10.1021/acs.nanolett.1c00050.

[33] A. Vicenzo and P. L. Cavallotti, "Growth modes of electrodeposited cobalt," *Electrochimica Acta*, vol. 49, no. 24, pp. 4079–4089, Sep. 2004, doi: 10.1016/j.electacta.2004.04.001.

[34] O. P. Watts, "Rapid nickel plating," *Trans. Am. Electrochem. Soc*, vol. 29, pp. 395–403, 1916.

[35] A. P. Guimarães, *Magnetism and magnetic resonance in solids*. New York: John Wiley & Sons, 1998.

[36] E. A. Turov and M. P. Petrov, *Nuclear Magnetic Resonance in Ferro- and Antiferromagnets*. Jerusalem: Israel Program for scientific translations (Halsted Press), 1972.

[37] T. M. Whitney, P. C. Searson, J. S. Jiang, and C. L. Chien, "Fabrication and Magnetic Properties of Arrays of Metallic Nanowires," *Science*, vol. 261, no. 5126, Art. no. 5126, Sep. 1993, doi: 10.1126/science.261.5126.1316.

[38] M. T. Rahman *et al.*, "Controlling magnetization reversal in Co/Pt nanostructures with perpendicular anisotropy," *Appl. Phys. Lett.*, vol. 94, no. 4, p. 042507, Jan. 2009, doi: 10.1063/1.3075061.

[39] K. Liu and C. L. Chien, "Magnetic and magneto-transport properties of novel nanostructured networks," *IEEE Trans. Magn.*, vol. 34, no. 4, pp. 1021–1023, 1998, doi: 10.1109/20.706344.

[40] X. Kou *et al.*, "Memory Effect in Magnetic Nanowire Arrays," *Adv. Mater.*, vol. 23, no. 11, pp. 1393–1397, Mar. 2011, doi: 10.1002/adma.201003749.

[41] M. R. Zamani Kouhpanji, A. Ghoreyshi, P. B. Visscher, and B. J. H. Stadler, "Facile decoding of quantitative signatures from magnetic nanowire arrays," *Sci. Rep.*, vol. 10, no. 1, p. 15482, Dec. 2020, doi: 10.1038/s41598-020-72094-4.

[42] F. Chen *et al.*, "Periodic magnetic domains in single-crystalline cobalt filament arrays," *Phys. Rev. B*, vol. 93, no. 5, p. 054405, Feb. 2016, doi: 10.1103/PhysRevB.93.054405.

[43] Z. Liu, P.-C. Chang, C.-C. Chang, E. Galaktionov, G. Bergmann, and J. G. Lu, "Shape Anisotropy and Magnetization Modulation in Hexagonal Cobalt Nanowires: Magnetization Modulation in Cobalt Nanowires," *Adv. Funct. Mater.*, vol. 18, no. 10, pp. 1573–1578, May 2008, doi: 10.1002/adfm.200701010.

[44] A. C. Gossard, A. M. Portis, M. Rubinstein, and R. H. Lindquist, "Ferromagnetic Nuclear Resonance of Single-Domain Cobalt Particles," *Phys. Rev.*, vol. 138, no. 5A, Art. no. 5A, May 1965, doi: 10.1103/PhysRev.138.A1415.

[45] J. A. Osborn, "Demagnetizing Factors of the General Ellipsoid," *Phys. Rev.*, vol. 67, no. 11–12, pp. 351–357, Jun. 1945, doi: 10.1103/PhysRev.67.351.

[46] P. Panissod, “Structural and Magnetic Investigations of Ferromagnets by NMR. Application to Magnetic Metallic Multilayers,” in *Frontiers in Magnetism of Reduced Dimension Systems*, Dordrecht, 1998, pp. 225–270.

[47] J. Sort *et al.*, “Role of stacking faults in the structural and magnetic properties of ball-milled cobalt,” *Phys. Rev. B*, vol. 68, no. 1, Art. no. 1, Jul. 2003, doi: 10.1103/PhysRevB.68.014421.

[48] A. S. Andreev, O. B. Lapina, and S. V. Cherepanova, “A New Insight into Cobalt Metal Powder Internal Field 59Co NMR Spectra,” *Appl. Magn. Reson.*, vol. 45, no. 10, Art. no. 10, Oct. 2014, doi: 10.1007/s00723-014-0580-0.

[49] V. V. Matveev, D. A. Baranov, G. Yu. Yurkov, N. G. Akatiev, I. P. Dotsenko, and S. P. Gubin, “Cobalt nanoparticles with preferential hcp structure: A confirmation by X-ray diffraction and NMR,” *Chem. Phys. Lett.*, vol. 422, no. 4–6, Art. no. 4–6, May 2006, doi: 10.1016/j.cplett.2006.02.099.

[50] M. T. Johnson, P. J. H. Bloemen, F. J. A. den Broeder, and J. J. de Vries, “Magnetic anisotropy in metallic multilayers,” *Rep. Prog. Phys.*, vol. 59, no. 11, pp. 1409–1458, Nov. 1996, doi: 10.1088/0034-4885/59/11/002.

[51] K. Ounadjela *et al.*, “Magnetization reversal in cobalt and nickel electrodeposited nanowires,” *J. Appl. Phys.*, vol. 81, no. 8, Art. no. 8, Apr. 1997, doi: 10.1063/1.364568.

[52] I. L. Prejbeanu, L. D. Buda, U. Ebels, M. Viret, C. Fermon, and K. Ounadjela, “Domain structures in epitaxial (1010) Co wires,” *IEEE Trans. Magn.*, vol. 37, no. 4, Art. no. 4, Jul. 2001, doi: 10.1109/20.951068.

[53] M. B. Stearns, “Spin-Echo and Free-Induction-Decay Measurements in Pure Fe and Fe-Rich Ferromagnetic Alloys: Domain-Wall Dynamics,” *Phys. Rev.*, vol. 162, no. 2, Art. no. 2, Oct. 1967, doi: 10.1103/PhysRev.162.496.

[54] M. C. Cadeville and J. Deportes, “Saturation magnetizations and high field susceptibilities of C and C interstitial solid solutions,” *Phys. Lett. A*, vol. 41, no. 3, pp. 237–238, Sep. 1972, doi: 10.1016/0375-9601(72)90275-7.

[55] X. Ni *et al.*, “Investigation of polyvinylpyrrolidone as an inhibitor for trench super-filling of cobalt electrodeposition,” *J. Taiwan Inst. Chem. Eng.*, vol. 112, pp. 232–239, Jul. 2020, doi: 10.1016/j.jtice.2020.06.010.

[56] Y. Hu, S. Deb, D. Li, and Q. Huang, “Effects of organic additives on the impurity and grain structure of electrodeposited cobalt,” *Electrochimica Acta*, vol. 368, p. 137594, Feb. 2021, doi: 10.1016/j.electacta.2020.137594.

Chapter 6: ^{59}Co IF NMR study of assemblies of closely packed Co nanoparticles

In this final chapter, the study of assemblies of close-packed monodisperse Co nanoparticles (NPs) in is presented. The NPs are synthesized in suspension by a disproportionation reaction, allowing a variation of the particle size and the of interparticle distance. The aim of this chapter is to study the influence of Co particle interactions on their superparamagnetic – ferromagnetic transition at the so-called blocking temperature (T_B) using ^{59}Co IF NMR. The main motivation is to be able to study CoO/Li conversion reaction battery materials, which contain Co NPs and for which an increase of T_B was observed.

In the first part of this chapter, the synthesis of the assemblies of Co NPs is described. In addition, the basic principles of the superparamagnetic – ferromagnetic transition are reminded and it is explained how this phenomenon allows to estimate the size of Co NPs using ZFC/FC magnetometry and ^{59}Co IF NMR measurements.

Afterwards, the characteristics of the different samples studied in this work are compared. The distribution of the NP size and the interparticle distance are determined using transmission electron microscopy (TEM) and the overall T_B of the samples obtained using ZFC/FC magnetometry is compared to these results.

Finally, the results of the ^{59}Co IF NMR experiments at various temperatures are presented, including their interpretation: The spectrum decomposition allows to obtain a sample-wide overview of the Co NP crystalline structure. In addition, the evolution of the signal intensity with varying temperature gives an estimation of the particle size distribution, which is then compared to the results obtained using TEM. This comparison allows to examine the influence of particle interactions on T_B. This last part also contains a discussion about the limits of the performed ^{59}Co IF NMR experiments, including suggestions of improvement for future studies.

This work was performed in collaboration with Dr. Alexandre Sodreau and Prof. Christophe Petit (Monaris laboratory) and Arthur Moisset and Dr. Marc Petit (IPMC laboratory) from Sorbonne Université. They synthesized the samples and performed the ZFC/FC magnetometry and TEM measurements.

CoO/Li conversion reaction battery electrode materials have been provided by Dominique Larcher from the LRCS laboratory in Amiens and preliminary ^{59}Co IF NMR experiments on these materials have been performed by Andrey Andreev during his time in the SIMM laboratory at ESPCI in Paris.

Chapter 6: ^{59}Co IF NMR study of assemblies of closely packed Co nanoparticles

1. Introduction and context

Assemblies of cobalt nanoparticles (NPs) find application in numerous scientific domains, for example in spintronics[1]–[3], catalysis[4]–[8], medicine [9]–[11] and energy storage[12]–[14]. In most of these applications, the crystalline structure and size of the nanoparticles are crucial parameters. In particular, together with the interparticle distance and interactions, these parameters have an influence on the magnetic properties of an assembly of nanoparticles. Efficient and preferentially non-destructive studies of these properties are of great importance for an optimal use. In the literature, different techniques have been applied to characterize the particle size and morphology of various Co NP systems, including different microscopy techniques (especially transmission electron microscopy (TEM)) [15]–[17], X-ray diffraction (XRD)[18], ferromagnetic resonance (FMR)[19],[20] and ^{59}Co internal field nuclear magnetic resonance (IF NMR)[21]–[27]. The resulting magnetic properties of those systems have been studied by zero-field-cooling (ZFC)/ field-cooling (FC) magnetometry [8],[18],[28] and magnetic hysteresis measurements [10], [18] for example. All those techniques have their advantages and drawbacks.

Comparison of analytical techniques

TEM is a commonly used technique and has the advantage of giving a visual representation of the particles, including their size and shape. Its drawback is that it only gives a local image of the sample and requires special sample preparation. XRD is a commonly used tool in order to determine the crystalline phase of various materials but is less adapted for studying very small crystallites with defects, due to peak broadening. The FMR signal of small superparamagnetic particles is sharp, but bigger particles are often not distinguishable. ZFC/FC magnetometry gives a sample-wide overview of the blocking temperature (T_B), which can be related to an average particle size. However, this measurement lacks precision for samples with a large particle size dispersion.

The signal intensity of ^{59}Co IF NMR is relative to the particle volume, thus having a higher sensitivity to bigger particles inside a given size distribution. In addition, if some particles large enough to be multi-domain are present in the sample, their signal will be strongly enhanced due to the excitation of domain walls, which will make it difficult to distinguish small particles in the sample. However, an advantage of IF NMR experiments is that no special sample preparation is necessary, which limits the risk of sample degradation during the preparation and allows to study samples close to *in-situ*. Another big advantage of this technique is that it allows to study the crystallite structure and size simultaneously. Cobalt nuclei in different crystalline structures will show resonance at different

frequencies, while experiments at different temperatures allow to study the particle size via the superparamagnetic transition.

Goals and applications

Systems where Co NPs play a crucial role, are *CoO-Li* conversion reaction anode materials. These anodes are initially made of cobalt oxide particles (CoO or even Co_3O_4, only the former case being considered here for simplicity), with a size of several 100 nm. During the first lithiation reaction, the CoO is reacting with lithium, resulting in the formation of Co metal and lithium oxide (Li_2O) in a displacive redox reaction, as shown in Eq. (6.1). The lithiation reaction of CoO is thermodynamically favorable, while the reaction in the reverse direction is not expected to happen. However, experiments have proven the reversibility of this conversion reaction, which can be explained by the nanometric size of the created Co metal.[14] Indeed, as represented schematically in **Figure 1**, during the lithiation process of the CoO particles, small Co metal NP are created inside an Li_2O matrix. The resulting high contact area between the Co and Li_2O is responsible for the reversibility of the reaction as it compensates the chemical inactivity of Li_2O.[14]

$$\begin{array}{c} CoO + 2\,Li^+ + 2e^- \leftrightarrow Co + Li_2O \\ \underline{2\,Li \leftrightarrow 2\,Li^+ + 2e^-} \\ CoO + 2\,Li \leftrightarrow Li_2O + Co \end{array} \qquad (6.1)$$

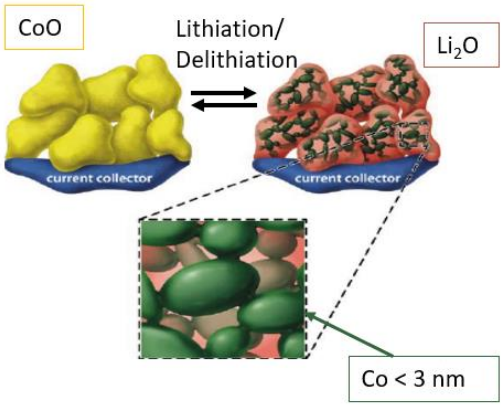

Figure 1: Schematic representation of the discharge/ charge reaction of conversion reaction CoO/Li anode materials. Adapted from [29].

The big advantage of conversion reaction anodes is their higher energy storage density compared to usual intercalation reaction batteries anodes. However, a difficulty for these types of anodes is to retain their storage capacity over several charge and discharge cycle, especially because of the big

volume changes happening during these cycles.[30] Even though this type of electrode has already been discovered over 20 years ago [14], it is still the subject of research up to this day.[31]–[34]

As during the lithiation process Co metal NPs are created, these electrodes are well adapted to be analyzed by ^{59}Co IF NMR. In our laboratory, Andrey Andreev performed ^{59}Co IF NMR experiments on CoO/Li conversion reaction electrodes at different points in the charge/discharge cycle (personal communication). He observed a strong ferromagnetic signal, even at ambient temperature, and was able to distinguish the different Co metal crystalline structures (*fcc*/*hcp*) inside the electrodes. However, given the small size of these Co metal particles, generally measured to be inferior to 3 nm by microscopy measurements [14], [35], they are expected to be superparamagnetic at ambient temperature on size contribution alone (Eq.(1.30), Chapter 1) and should then not give a ferromagnetic signal. This observation can probably be explained by magnetic interactions between the particles, resulting in a ferromagnetic behavior even above the theoretical blocking temperature (T_B). An unusually high T_B of magnetic particles in conversion reaction electrodes has already been evidenced by ZFC/FC magnetometry [29] or by magnetic hysteresis measurements [36]. Given the close packing of these particles, dipolar interactions are very likely to occur. In addition, the exchange interaction might also have an influence, as the Co particles are often considered to form a network, as presented in **Figure 1**.

Considering the complexity of electrode materials, in order to study this issue, this chapter will focus on a model system of interacting Co NPs. Its characteristics will be studied by ^{59}Co IF NMR and compared to TEM and FC/ZFC magnetometry results. In the literature, ^{59}Co IF NMR has already been used for the study of systems of non-interacting Co nanoparticles[20], [27], but the goal of this work is to extend it to the study of interacting particles. By using model systems with defined particle size distributions, the influence of the interparticle distance and interactions on T_B will be studied. In addition, while in previous studies only experiments with large temperature variations in between two NMR experiments have been presented, the use of smaller temperature variations has been tested, with the aim of a more precise particle size discrimination. It was chosen to analyze pure *hcp* cobalt NPs, whose strong uniaxial crystalline anisotropy leads to a better-defined superparamagnetic behavior than nanoparticles with a cubic structure and less well-defined crystalline anisotropies. The objective of studying interacting particles is not only of a fundamental nature, but also in order to extend the use of this technique to the study of systems where close-packed ferromagnetic particles occur, as in the above described conversion reaction batteries for example.

2. Materials and methods

2.1. Sample synthesis

The sample preparation, as well as the microscopy and ZFC/FC magnetometry measurements were performed by Alexandre Sodreau (IPCM laboratory, Sorbonne Université) and Arthur Moisset (MONARIS laboratory, Sorbonne Université). All analyzed samples where synthesized *via* a disproportionation process of a Halogen-Tris(Triphenylphosphine) Cobalt(I) ($[XCo(PPh_3)_3]$), with $X = Cl, Br$) precursor, in different solvents and using different stabilizing agents. The reaction mechanism is therefore the following:

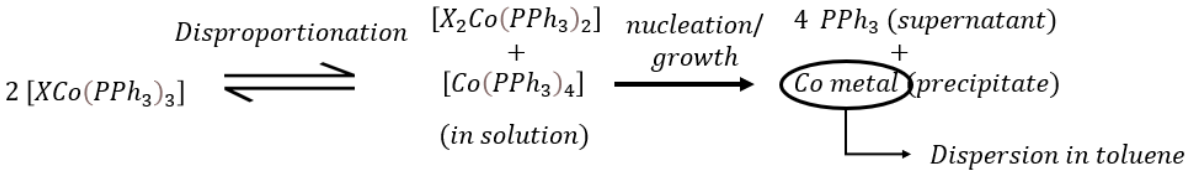

Figure 2: Schematic representation of the disproportionation reaction mechanism for the synthesis of monodisperse nanoparticles.

All the syntheses have been performed in a glovebox under a N_2 atmosphere. In a first type of synthesis, oleylamine (OAm) was used as a solvent and stabilizing agent/ ligand simultaneously. The precursor ($[XCo(PPh_3)_3]$) was dissolved in degassed oleylamine and heated up to 190°C under a N_2 flux for 1 h. The color of the solution changed to black, indicating the appearance of metallic Co. After cooling down to ambient temperature, the NPs were collected by washing with ethanol (EtOH) and centrifugation and dispersed in an apolar solvent, toluene in our case. The synthesized Co NPS had a spherical shape with an average diameter of 8 - 9 nm and a quite monodisperse distribution when using $[ClCo(PPh_3)_3]$ as precursor. The particle diameter can be varied by using a different halogen in the precursor molecule, but the interparticle distance is fixed to about 4.1 nm by the OAm. More information about this synthesis can be found in the works by Meziane et al. [37], [38].

A variation of the synthesis protocol allowed to perform it at ambient temperature, to drastically decrease the reaction time and to vary the interparticle distance, all by keeping a good spherical shape of the particles. For this, the ligand (OAm or tridecanol in our case) was dissolved in tetrahydrofuran (THF), which was then added to the precursor under agitation. The color of the solution changed to black quickly and the reaction is already stopped after only 6 min in some cases. The solution is washed with EtOH and centrifugated and the separated Co NPs are dispersed inside toluene. Besides its

influence on the interparticle distance, the choice of the ligand and its relative amount compared to the solvent also has a strong influence on the reaction time and the characteristics of the synthesized NPs. When using tridecanol, the reaction is fast (< 45 min) and the created particles are very closely together. With OAm on the other hand, the reaction time is strongly increased (several hours) and the interparticle distance is around 4.1 nm. In order to combine both properties, a ligand exchange can be performed. The tridecanol ligand can be replaced by OAm by simply adding the later to the synthesized particles. The excess of ligands is removed by EtOH washing. Like for the previous synthesis, the particle diameter is function of the halogen in the precursor. The detailed synthesis protocol and parameter study can be found in the work by Sodreau et al.[18].

In all cases, the particle size of the synthesized nanoparticles was determined by transmission electron microscopy (TEM). In **Figure 3**, the HRTEM analysis of such Co NPs is shown, including the size determination in a), as well as the crystalline phase determination by Fourier transform (FT) of a single particle in b) and c). The FT results indicate reticular distances corresponding to *hcp* Co, which confirms the results obtained by electron diffraction measurements using TEM shown in d).

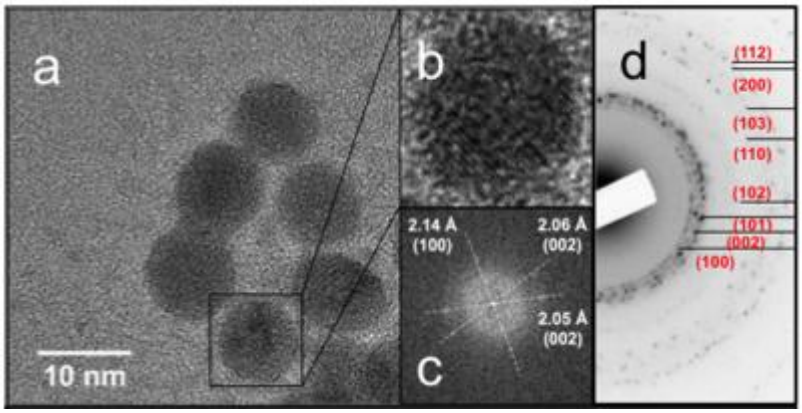

Figure 3: a) – c) Full HRTEM analysis of Co NPs with an average diameter of 8.7 nm, stabilized by a fatty alcohol: a) HRTEM pictures for size determination, b) Zoom on a single particle and c) the Fourier transform (FT) of this particle. d) Electron diffraction results obtained by TEM on similar particles, including the assignment of the reticular distances. Taken from [18].

2.2. Sample analysis

TEM analysis

The high-resolution microscopy images of the nanoparticles were obtained using a 200 kV transmission electron microscope (JEOL JEM 2100 with a digital camera Gatan). A small amount of the dispersed

solution was deposited on the TEM grid, followed by evaporation of the solvent. Detailed information about the procedure can be found in the supporting information of [18].

ZFC/FC magnetometry

The zero-field cooling/ field cooling (ZFC/FC) magnetometry measurements were performed using a SQUID magnetometer (Cryogenic S600). For the measurement, the NP samples were aggregated on a silicon wafer (solvent evaporation). (SI of [18]). The temperature was varied from 3 K to 350 K and the applied external field was 20 Oe. This technique is a standard technique to measure the blocking temperature (T_B) of an assembly of magnetic nanoparticles. Explanations about superparamagnetic/ ferromagnetic transition and the blocking temperature can be found in Subsection 4.2 of Chapter 1. As a reminder, T_B of a magnetic particle is defined by the following equation:

$$\tau_m = \tau_0 \exp\left(\frac{K_{eff}(T)\,V}{k_B T_B}\right) => T_B = \frac{K_{eff}(T)\,V}{k_B \ln(\tau_m/\tau_0(T))} => V_{crit} = \frac{T * k_B \ln(\tau_m/\tau_0(T))}{K_{eff}(T)} \quad (6.2)$$

with V the particle's volume, T the absolute temperature, K_{eff} the effective anisotropy constant, k_B the Boltzmann constant, τ_0 the elementary flip time and τ_m the characteristic time of the measurement. For a particle with a given volume V, the particle is observed to be superparamagnetic above T_B, while below T_B it behaves ferromagnetically. The critical volume V_{crit} is a term defined in a similar fashion: At a given temperature T, all particles with a volume below V_{crit} are observed to be superparamagnetic, while all particles with a volume above behave ferromagnetically.

For all the calculations in this chapter, τ_0 is considered to be temperature independent and equal to 10^{-11} s [20], while K_{eff} is equal to the sum of the first and second terms of the magnetocrystalline anisotropy of *hcp* Co ($K_{c1}(T) + K_{c2}(T)$) and varies with the temperature (values can be found in [39]–[41]). This choice of K_{eff} is done under the hypothesis of a perfect *hcp* Co crystalline structure and negligible particle shape or particle interaction contributions. The calculations are therefore only valid for spherical and non-interacting *hcp* Co nanoparticles. Deviations of the experimental results from these calculations might therefore be attributed to these factors.

For the ZFC measurement, the sample is cooled down without the application of an external field from a temperature above T_B down to a temperature well below T_B. The external magnetic field is then switched on, and the magnetization is measured as the temperature is progressively raised. At temperatures below T_B, all the magnetic moments will be frozen with a random orientation defined by their magnetic easy axis, leading to an overall zero magnetization and susceptibility. The magnetic moments of the particles are hindered from aligning with the external magnetic field by their magnetic

anisotropy. When reaching T_B, the thermal agitation energy (k_BT) will become superior to the magnetic anisotropy energy of the particles, allowing the magnetic moments of the particles to rotate freely and to align with the external field (phenomenon described in Subsection 4.2 of Chapter 1). These superparamagnetic particles have a high magnetic susceptibility, resulting in a relatively strong magnetization. When increasing the temperature further, the overall magnetization will decrease due to a reducing susceptibility with temperature. During the field cooling (FC) measurement, the sample is cooled under the presence of the same applied field than the one present during the heating of the ZFC measurement. The magnetization curve is either measured during the cooling down or heating of the sample under the presence of the field, generally leading to the same results.[42] In the superparamagnetic regime above T_B, the FC curve generally overlaps with the ZFC curve, but in the ferromagnetic regime below T_B the NPs are blocked in a magnetically ordered state with a high magnetization.

In **Figure 4**, the typical shape of FC/ZFC curves are represented. The graph on the left corresponds to the optimal case of sample with perfectly monodisperse particles, which therefore all "deblock" at the same temperature. Consequently, the magnetization of the ZFC line is zero until it jumps up at T_B and then monotonously decreases. The FC curve is flat below T_B and perfectly overlaps with the ZFC curve above. In reality however, all samples will contain particles with size distribution and the particles will gradually become superparamagnetic during the heating. The result is a curve like the one shown in the right of **Figure 4**, with a gradually increasing magnetization during the ZFC measurement and wide peak around the maximum. The temperature of the ZFC curve maximum is characteristic of the average sample blocking temperature (T_B). Another effect of the polydispersity will be an upwards shift from T_B of the temperature where the ZFC/FC curves start to overlap, also called splitting or irreversibility temperature (T_{irr}). This discrepancy is coming from the fact that the particles with a blocking temperature above the average will still be oriented randomly above T_B during the ZFC measurements, but oriented with a positive magnetic susceptibility during the FC measurement. The difference between T_{irr} and T_B is a qualitative indication of the particle size distribution.[42]

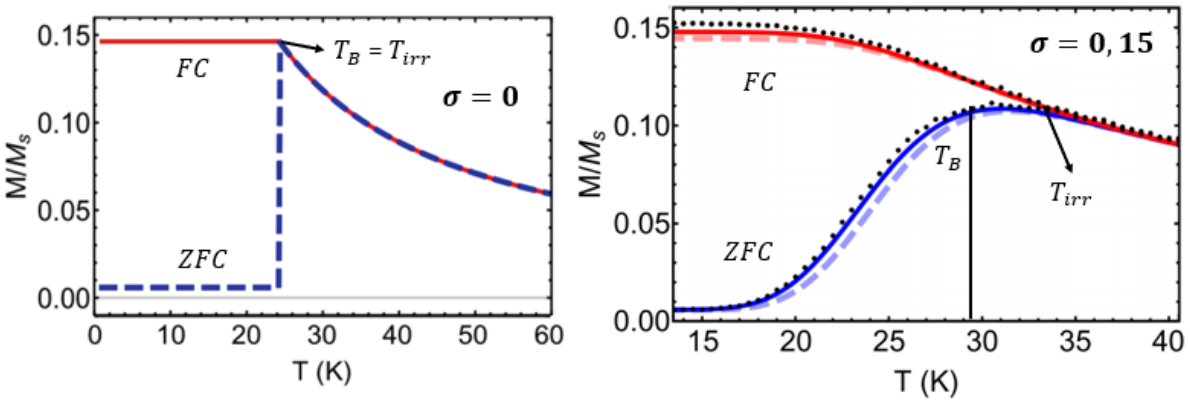

Figure 4: Typical shapes of zero-field cooling and field cooling (ZFC/FC) curves, monitoring the sample magnetization as function of the temperature. Curves based on theoretical calculations for: Left) a perfectly monodisperse sample ($\sigma = 0$); Right) a sample with particle size distribution ($\sigma = 0.15$). T_B = Blocking temperature, T_{irr} = irreversibility temperature. Adapted from [43].

The magnitude of the external applied field has of course an influence on the blocking temperature observed by the ZFC/FC magnetometry measurement. The external field will change the energy barrier ($\Delta E = K_a V$ without an applied external magnetic field) necessary to overcome in order to flip the magnetic moments. In general, a monotonically decreasing T_B with increasing magnetic field is observed, as expected. Nevertheless, a slight increase T_B at low fields is observed in some cases.[42], [44] Normally the applied external field during the ZFC/FC experiments is chosen small enough to only have a limited influence on the energy barrier and the blocking temperature. The observation of a superparamagnetic behavior also depends on the measurement time of the experiment (τ_m), as shown in Eq.(6.2), which is generally chosen to be equal to 100 s for a typical ZFC/FC experiment.

2.3. ^{59}Co IF NMR

Experimental configurations

All the IF NMR experiments were performed using the static, 5 mm NMR-service low-temperature probe (previously described in Chapter 3, Subsection 1.1) inside an Oxford cryostat and with an Oxford temperature controller. A heating unit and a temperature sensor on the bottom of the cryostat, close to the sample, were used to measure and control the sample temperature. The precision of the temperature sensor was high (0.2 K), however, the effect of a temperature gradient between the sample and the sensor introduced an error of the sample temperature measurement, potentially

reaching up to several Kelvins at higher temperatures, which could not be taken into account precisely. The cooling fluids were liquid nitrogen and helium for experiments down to 77 K and 4.2 K, respectively. The transfer in the cryostat of the liquid-state cooling fluid, as well as the evacuation of the evaporated fluid was done through a two-way transfer cane, driven by a pressurized liquid reservoir. The experimental procedure and pulse sequences were the same as the ones described in the main materials and methods section of this manuscript in Chapter 3. The interpulse delay (τ) of the solid-echo [$t_p - \tau - t_p$] sequence was varied as function of the temperature due to shorter T_2 relaxation times with increasing temperature and longer electronic dead times at lower temperatures. The dead time increase can be explained by the higher conductivity of the circuit at lower temperatures, resulting in a higher quality factor. More details about the dead time are given in Chapter 4, Subsection 6.2. The repetition rate of the experiments was decreased for the experiments at low temperatures, due to the increasing T_1 relaxation time. [45]

In order to perform the ^{59}Co IF NMR experiments, a part of the solution containing the Co NPs was transferred into a 5 mm NMR tube in a glovebox under an argon atmosphere. The tube had been cut to a length of about 4 cm in order to fit into the probe and the cryostat. To prevent oxidation during the sample transfers and the NMR experiments, it was crucial to seal the tube tight. Factors making the quality of the sealing crucila were the low temperatures (down to 4 K) during the experiments and the horizontal position of the sample in the NMR setup. As a result, a bad sealing would lead to the solvent pouring out during the experiment, leading to a potential loss of sample. In addition, movement of the NP suspension inside the coil could lead to a variation of the number of NPs in the coil center and falsify the quantitative measurements. The sample was first sealed with a septum and epoxy glue. Additionally, as the epoxy glue might break during the experiments at low temperatures, the sample tube and the septum were fixed to the coil with Teflon tape, as shown in **Figure 5**. This Teflon tape holds the septum in place on top of the tube during the experiments. Another advantage of the Teflon tape is that it reduces arcing, possibly occurring during the experiments at low temperatures in an He atmosphere, by covering naked metal surfaces. In order to avoid sample oxidation in case of a bad sealing, the samples were not taken out of the cryostat in between the experiments at different temperatures and kept under a constant flux of cryogenic gas. If the sample was kept above the freezing temperature of toluene for a longer period of time (overnight for example), a comparison experiment at the same temperature as the previous one was performed, in order to avoid the influence on the results of a potential oxidation or movement of the particles inside the coil during this time.

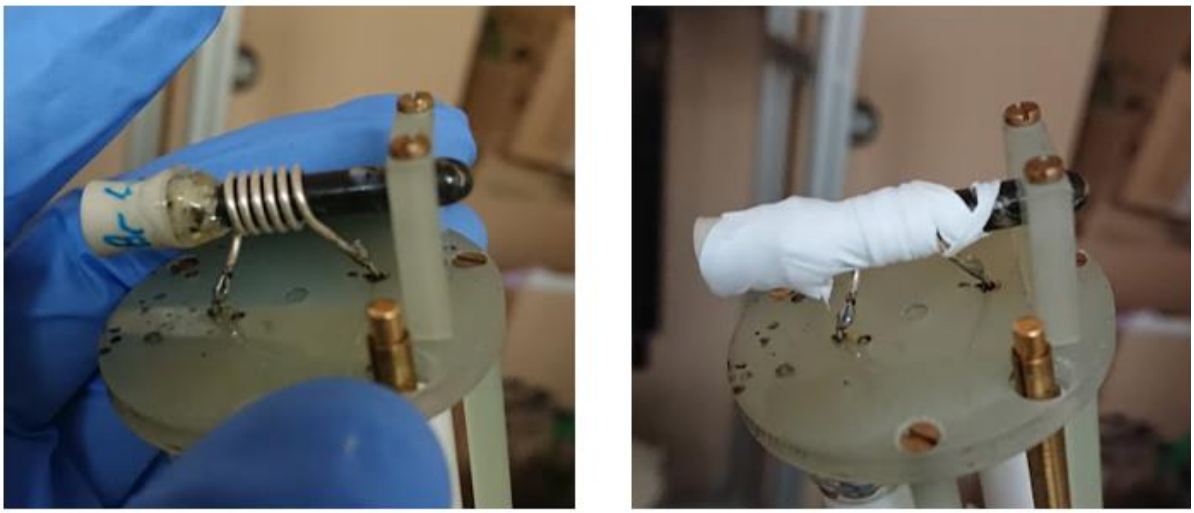

Figure 5: Sealing and fixing of the sample tube for the IF NMR experiments.

Particle size determination

For each sample, ^{59}Co IF NMR experiments at various temperatures have been performed. Due to the superparamagnetic to ferromagnetic transition, it is considered that only particles at temperatures below their T_B give a signal. For temperatures above, the thermal energy induces a flipping of the particle's magnetic moment, which is faster than the IF NMR the measurement time. This particle appears to be superparamagnetic and will therefore not contribute to the observed signal. When now comparing the spectra observed at two different temperatures (T_X and T_y for example), we can derive different information. Because the spectra at T_x and T_y correspond to the signal from all particles with a blocking temperature below T_x and T_y, respectively, the subtraction of both spectra represents the signal of all the particles with an intermediate T_B.

Similar to the ZFC/FC magnetometry measurements, T_B can be related to the particle volume by comparing the characteristic time of the magnetic moment flipping and the measurement time, shown in Eq.(6.2). For the NMR measurements the measurement time (τ_m) is different than for the ZFC/FC magnetometry and is taken to be equal to time between the first pulse and the FID detection, namely ($2*\tau + t_p$), with τ the interpulse delay and t_p the pulse duration. As a result, IF NMR can theoretically be used to determine the particle size distribution inside a sample of Co NPs. The signal difference between the spectra at the temperatures T_x and T_y is relative to the number of nuclei inside particles with a volume corresponding to a T_B in between those two temperatures.[20], [27]

Data treatment and correction factors

In order to quantitatively compare the signal obtained at different temperatures, various factors need to be considered and corrections to be made. First of all, the spin distribution at equilibrium is dependent on the temperature, following the Boltzmann law:

$$\frac{N_\uparrow}{N_\downarrow} = \exp\left(\frac{\Delta E}{k_B T}\right) = \exp\left(\frac{h * \omega}{k_B T}\right) = \exp\left(\frac{h/2\pi * \gamma B}{k_B T}\right) \cong 1 + \frac{h/2\pi * \gamma B}{k_B T} \qquad (6.3)$$

with $N_\uparrow, N_\downarrow$ the number of spins in the spin up and down state, respectively, h Planck's constant, γ the gyromagnetic ratio, B the field acting on the nucleus, k_B the Boltzmann constant and T the absolute temperature. For IF NMR measurements of Co, the linear approximation $\left(\frac{h/2\pi*\gamma B}{k_B T}\right) \ll 1$ is valid and the net longitudinal magnetization per nuclei $\langle \mu_z \rangle$ can be approximated by [46]:

$$\langle \mu_z \rangle \cong \left(\frac{(h/2\pi)^2 \gamma^2 B}{4\, k_B T}\right) \qquad (6.4)$$

The signal intensity, which is directly dependent on the longitudinal magnetization, will be stronger for experiments at low temperatures by a factor $1/T$. For quantitative comparison, the spectrum intensities are therefore all multiplied by the measurement temperature (often referred to as the correction for the Boltzmann factor). For NMR measurements of the Co at temperatures down to 4 K, the factor $\left(\frac{h/2\pi*\gamma B}{k_B T}\right) < 0.001$, which justifies the linear approximation.

Another factor that needs to be considered is the lateral relaxation time (T_2), which is of the same order of magnitude than τ and varies with temperature. Corrections for the spin-lattice relaxation time have not been considered in the literature, as it is generally much larger than τ. [45] Here, T_2 was measured at each temperature at the frequency given the maximum signal and fitted using a simple exponential function, as explained in Subsection 1.1 of Chapter 3. Knowing τ of the measured signal, it was then extrapolated to zero interpulse spacing to obtain the corrected spectrum. Note that this correction takes into account for the variation of τ at different temperatures.

A last correction that needs to be made, independently of the temperature variation is the ω^2 dependence of the signal. After all these corrections, the spectra can be considered to be a quantitative representation of the number of nuclei in an environment and a range of particle sizes.

3. Results

There are four different types of samples that will be presented in the following, with different particle diameters and interparticle distances. First of all, the sample synthesis conditions and its characterization by classic analysis techniques (TEM and ZFC/FC magnetometry), are described. Afterwards, the results of the IF NMR analysis are presented in detail.

3.1. Sample synthesis and characterization

All syntheses, as well as the ZFC/FC magnetometry and TEM measurements were performed by Alexandre Sodreau (Monaris laboratory) and Arthur Moisset (IPMC laboratory) at Sorbonne Université.

NP_9nm sample

This synthesis targeted the formation of nanoparticles with a diameter of around 9 nm. The sample was synthesized using the high-temperature procedure described in Section 2.1, with OAm as solvent and stabilizing agent. In the reaction recipient, 0.25 mmol of $[ClCo(PPh_3)_3]$ was dissolved in 10 ml of OAm. After 1 h of reaction at 190 °C, washing and centrifugation, the sample was redispersed in toluene. First of all, the particle size and shape were verified using TEM measurements.

In **Figure 6** a), a representative TEM picture of the sample is shown, indicating a fairly spherical shape of the particles. The particles appear to be closely packed on the TEM grid, with an interparticle distance of 4.1 nm due to the stabilizing agent OAm. From TEM pictures with many particles (> 1000), the particle size distribution was determined. The resulting histogram in **Figure 6** a) shows a distribution of the particle diameter, which is close to a normal distribution with an average diameter of 8.6 nm and a standard deviation of 0.4 nm.

ZFC/FC magnetometry of the sample was performed between 3 K and 350 K in order to estimate the T_B of the sample. However, the mean T_B of the sample could not be reached in the measured temperature range. Given the particle size distribution, this is in accordance with the theoretical estimation of T_B using Eq.(6.2): For $\tau_m = 100$ s (the typical measurement time of a ZFC/FC magnetometry experiment), only the spherical *hcp* Co particles with a diameter below 8 nm should be superparamagnetic at 350 K. The vast majority of the particles in the sample were therefore still ferromagnetic at this temperature.

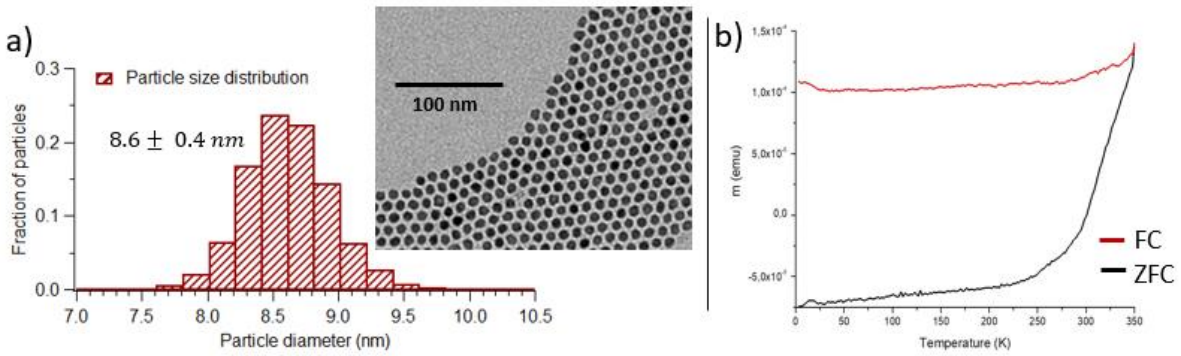

Figure 6: TEM and ZFC/FC magnetometry study of the *NP_9nm* sample. a) A representative TEM picture of the sample and the histogram of the particle diameter distribution, obtained from TEM pictures. b) ZFC/FC magnetometry of the sample between 3 K and 350 K using a 20 Oe applied field.

NP_6nm sample

This synthesis targeted the formation of nanoparticles with a diameter of around 6 nm. The sample was synthesized using the ambient temperature procedure described in Section 2.1, with THF as solvent and OAm as stabilizing agent. A solution of 0.0375 mmol of oleylamine inside 6 ml of THF was added to 0.15 mmol of $[ClCo(PPh_3)_3]$ in the reaction recipient. The reaction time was 18 h at ambient temperature and after washing and centrifugation, the NPs were dispersed in toluene.

The TEM picture of the sample shown in **Figure 7** suggests that the Co NPs in the sample were less spherical than the ones of the previous sample, but most of them with a low aspect ratio cross-section. The corresponding particle diameter distribution was $5.5 \pm 0.9\ nm$. The particles of this sample are therefore smaller, but with a wider distribution compared to the previous sample. No ZFC/FC magnetometry measurements have been performed for this sample, but the theoretical value defined by the mean particle size and Eq. (6.2) is equal to about 170 K $\tau_m = 100\ s$ (the typical measurement time of a ZFC/FC magnetometry experiment).

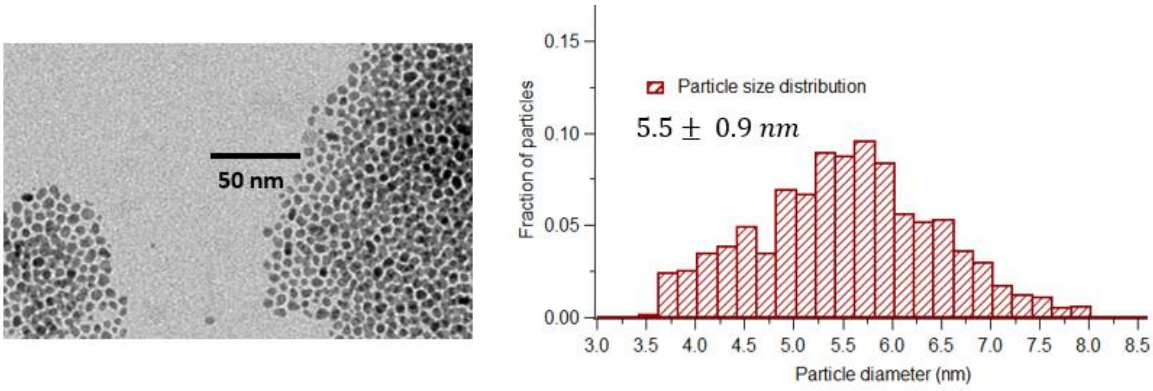

Figure 7: TEM analysis of the *NP_6nm* sample. Left: A representative TEM picture of the sample. Right: The histogram of the particle diameter distribution, obtained from TEM pictures.

NP_4nm_C13 sample and NP_4nm_OAm sample

This synthesis targeted the formation of nanoparticles with a diameter of around 6 nm with different interparticle distances. The first synthesis steps were the same for both of these samples. They were synthesized using the ambient temperature procedure described in Section 2.1, with THF as solvent and tridecanol as ligand. A solution of 0.45 mmol of tridecanol inside 6 ml of THF was added to 0.15 mmol of $[BrCo(PPh_3)_3]$ in the reaction recipient. The reaction time was 12 min in both cases. In the case of the *NP_4nm_C13* sample, it was simply washed with EtOH, centrifugated and redispersed in toluene after the reaction. The NPs were therefore still stabilized by the tridecanol. For the *NP_4nm_OAm* sample on the other hand, 1 ml of OAm was added to the reaction medium after the 12 min of reaction, in order to stop the reaction and perform a ligand exchange. The excess ligand was removed by washing with EtOH and after centrifugation, the NPs were redispersed in toluene. The NPs were stabilized by OAm in this case.

TEM pictures of both sample are shown in the top of **Figure 8**. They indicate a similar particle size and distribution for both ligands: a) *NP_4nm_C13* $d = 4.4 \pm 0.4$ nm, b) *NP_4nm_OAm* $d = 4.5 \pm 0.5$ nm. The shape of the particles could be considered to be spherical, even though their shape is less well defined than for the *NP_9nm* sample. As expected, the ligand had a strong influence on the NP organization and the interparticle distance. With tridecanol, the particles were closely packed and organized in clusters. After the ligand exchange to OAm, the interparticle distance increased significantly and was similar to the particle diameter.

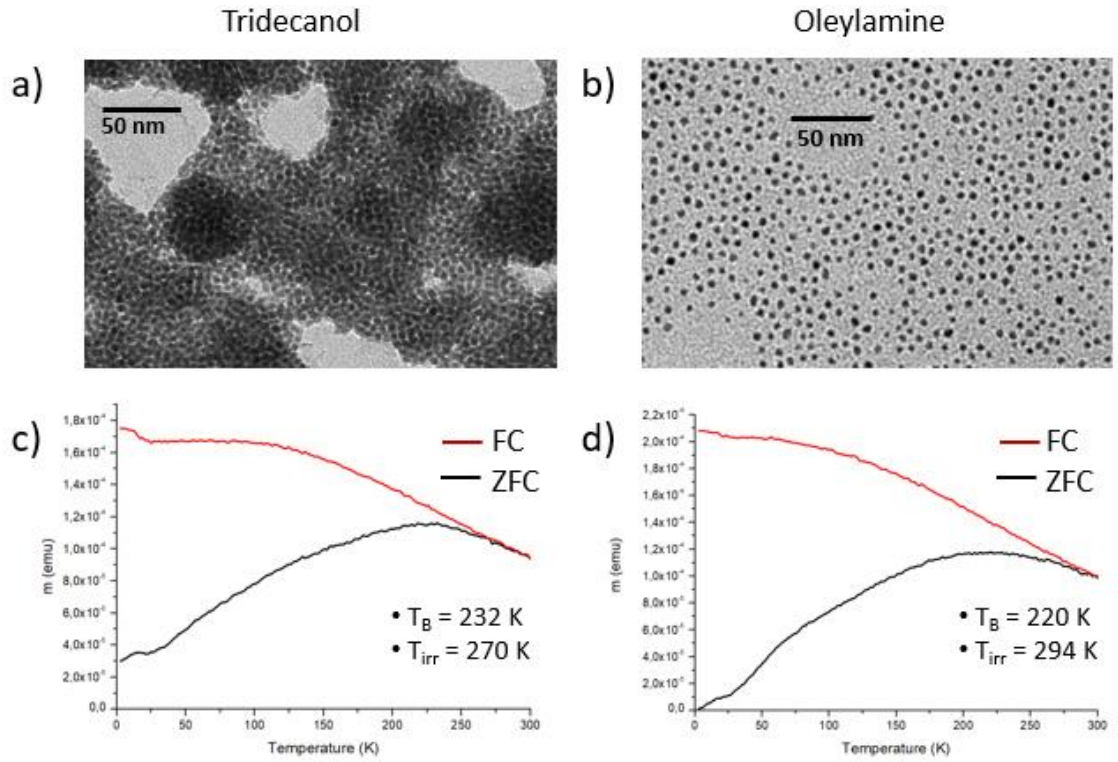

Figure 8: TEM and ZFC/FC magnetometry analysis of the *NP_4nm* samples with two different ligands. Top: TEM images. a) Tridecanol as ligand => Small interparticle distance. Particle size $d = 4.4 \pm 0.4$ nm. b) OAm as ligand => Large interparticle distance. Particle size $d = 4.5 \pm 0.5$ nm.
Bottom: ZFC/FC magnetometry with the corresponding blocking (T_B) and irreversibility (T_{irr}) temperature of the sample with c) Tridecanol and d) OAm as ligand.

In the bottom of **Figure 8**, the results of the ZFC/FC magnetometry measurements are represented, indicating the values of T_B and T_{irr} of these samples. In both cases, the measured T_B (232 K for *NP_4nm_C13* and 220 K for *NP_4nm_OAm*) was much superior to the theoretical value based on the particle size measured by TEM, which is around 90 - 100 K for spherical particles with $d = 4.4 - 4.5$ nm (using $\tau_m = 100$ s as applicable for ZFC/FC data). An explanation for such an increase of the blocking temperature could be particle interactions, as especially in *NP_4nm_C13* the particles are very closely packed. However, this explanation is questionable as one could expect a bigger difference in T_B between both samples, given the strong variation of the interparticle distance due to the ligand exchange. The difference between T_B and T_{irr} is relative to the polydispersity of the particles, which was therefore bigger for *NP_4nm_OAm* according to these measurements.

Chapter 6: ^{59}Co IF NMR study of assemblies of closely packed Co nanoparticles

Overview

In **Table 1**, the synthesis conditions, as well as the properties determined by TEM and ZFC/FC magnetometry are summarized for the samples presented in this chapter. Of the four samples presented, three were stabilized with OAm and are therefore considered to have an interparticle distance of around 4.1 nm. These samples differed in their average size. The fourth sample had a particle size distribution similar to that of an OAm sample, but was stabilized by tridecanol, resulting in a much closer packing. T_B values measured by ZFC/FC magnetometry were only available for the two samples with a particle size of 4.4 - 4.5 nm and were higher than the theoretical value. The crystalline structure of samples synthesized under similar conditions was determined using electron diffraction by TEM and high-resolution TEM (HRTEM) measurements and suggested an *hcp* crystalline phase for all analyzed samples.[17], [18], [37] However, these measurements have not been performed specifically for the samples presented here. In the following, the IF-NMR analysis of these samples will be presented with the goal of obtaining different information. First of all, this technique will provide a sample-wide study of the crystalline structure of the synthesized NPs. In addition, the evolution of the ferromagnetic signal with temperature will be studied, with the aim of establishing the distribution of T_B and its origin, taking especially into account the particle size distribution.

Table 1: Overview of the synthesis conditions and of the properties (determined by TEM and ZFC/FC magnetometry) of the studied NP samples.

Sample name	*NP_9nm*	*NP_6nm*	*NP_4nm_OAm*	*NP_4nm_C13*
Precursor	$[ClCo(PPh_3)_3]$		$[BrCo(PPh_3)_3]$	
Reaction conditions	190°C in OAm as solvent	T_{amb} in THF as solvent		
Reaction time	1 h	18 h	12 min	12 min
Ligand	OAm			Tridecanol
Particle size	8.6 ± 0.4 nm	5.5 ± 0.9 nm	4.5 ± 0.5 nm	4.4 ± 0.4 nm
T_B from ZFC/FC	> 350 K	/	220 K	232 K

3.2. ^{59}Co IF NMR study

The results of the ^{59}Co IF NMR study on the different samples will be presented in the following according to the experimental procedure described in Subsection 2.2. In **Figure 9**, the spectra of the different samples are compared at some of the temperatures at which experiments were performed. The spectra of the experiments at additional temperatures are presented in the Supplementary Information 5.2 (**Figure 17**). Samples *NP_9nm* and *NP_6nm* were tested for temperatures down to 85 K using liquid N_2, while experiments on the samples *NP_4nm_OAm* and *NP_4nm_C13* were performed down to 4 K using liquid He.

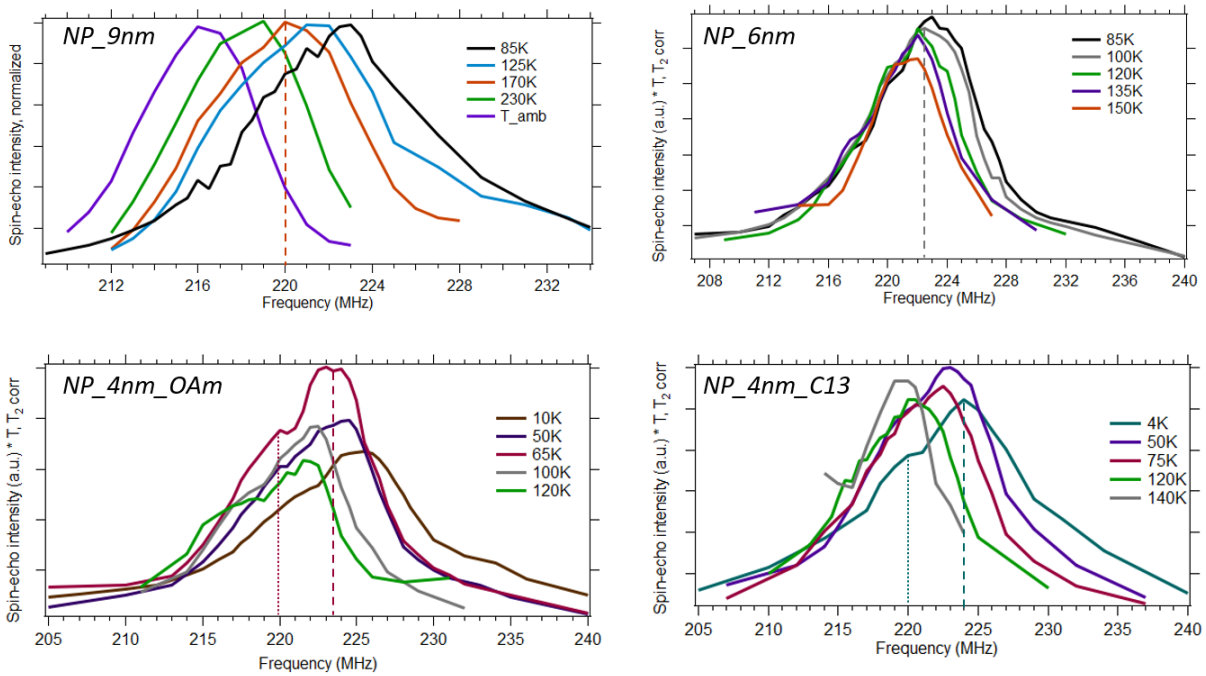

Figure 9: ^{59}Co IF NMR spectra taken at different temperatures of the four Co NPs samples presented in this work. Except for the *NP_9nm* sample, all spectra have been corrected for the Boltzmann distribution (multiplication by the temperature (K)) and the spin-spin relaxation (i.e., T_2) variation. The NP_9nm spectra have been normalized by their maximum. One or two main peaks can be differentiated in the spectra, indicated for one temperature for each sample as exemplification: dashed line = *hcp* Co, dotted line = *fcc* Co or *hcp* Co with defects, only differentiated for low temperature experiments.

For the sample *NP_9nm*, no T_2 measurements were performed and as a result no quantitative comparison of the different spectra was possible. In addition, this sample was the only one for which experiments above the freezing temperature of the solvent (toluene → 178 K) are presented, which might lead to an intensity loss due to Brownian motion at high temperatures, as described in

Supplementary Information 5.1. The spectra of this sample are therefore presented normalized by their maximum. The spectra of all the other samples were corrected for the Boltzmann distribution (using Eq. (6.4)) as well as for the decrease of the signal intensity due to the T_2 relaxation. As the T_2 time was temperature dependent and the interpulse delay (τ) was varied with temperature, this signal intensity decrease needs to be considered at each temperature to obtain quantitative information. The resulting spectra can therefore be considered to be a quantitative representation of the number of atoms inside ferromagnetic Co NPs. In the upcoming sections, more details about the results of the NMR analyses and their interpretation will be given.

Crystalline structure

The first sample property to be analyzed is its crystalline structure. Given the small particle size, one can expect all the signal to come from single-domain (s.d.) structures. Consequently, the peak generally assigned to *fcc* multi-domain (around 217 MHz at 4 K or 213 MHz at T_{amb} [47]) was not observed in the spectra. Two different factors can be considered for the crystalline structure study: the peak position and the peak width. In all the spectra a large main peak can be distinguished (marked by a dashed line), with a smaller bump present at lower frequencies (marked by a dotted line), especially for experiments at low temperatures. The evolution with temperature of the position of the main peak maximum for the different samples is represented in **Figure 10** a). As expected, the resonance frequency decreased with increasing temperature due to the reduction of the electron magnetization. For comparison, the laws of the temperature dependence of the resonance frequency of *fcc* Co s.d. particles obtained by Yasuoka et al. [25] and Andreev et al.[47] are plotted. The laws have been set up using the first and second terms of the spin waves theory, as explained in Subsection 1.2 of Chapter 2. For *hcp* Co s.d. particles, no such law has been set up in the literature so far. It can be seen that the main resonance was almost systematically above the frequency expected for *fcc* Co, especially for low temperatures. This suggested that the sample is mainly composed of *hcp* Co, which generally corresponds to a higher resonance than *fcc* Co. Towards higher temperatures, the frequency decreased faster than the *fcc* Co temperature dependence laws and the peak position approaches the one predicted by these laws. For experiments on Co NPs at temperatures below 100 K, different authors attributed resonances in a similar frequency range than the main peaks in this work to *hcp* Co s.d. [20], [22], [27]. The smaller bump observed at frequencies to the left of the main peak (dotted line) in some spectra (**Figure 9**), could be due to a smaller amount of *fcc* s.d. Co or defaulted *hcp* crystalline structures, which are less well-ordered and therefore have a lower internal field.

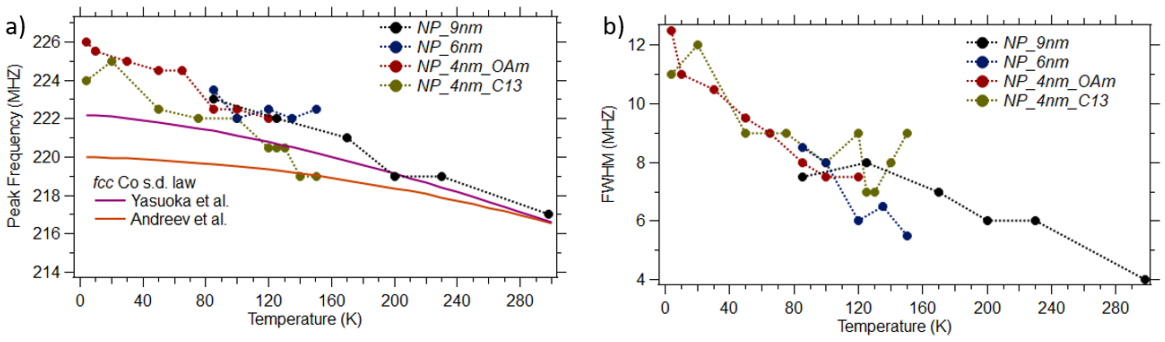

Figure 10: Evolution with temperature of a) the position of the main peak and the b) Full width at half maximum (FWHM) of the spectra for the ^{59}Co IF NMR analysis of the four samples. The two solid lines in the graph a) correspond to the fitting of the evolution with temperature of the *fcc* Co single-domain (s.d.) peak position proposed by Yasuoka et al. [25] and Andreev et al.[47].

Given the proximity of the main peak position to the position of an *fcc* s.d. Co peak, especially at higher temperatures, one could think that this peak arises from *fcc* Co structures. However, this can be disproved when considering the influence of the demagnetizing field. As a reminder, the exact position of a Co s.d. peak depends on the strength of the demagnetizing field, responsible for a frequency shift compared to the multi-domain peak position of the same crystalline structure (explained in Subsection 1.2 of Chapter 2 and [24]). This upwards shift is theoretically around 6 MHz for an isolated Co particle, but declines in line demagnetizing fields, due to particle interactions.[24] Close-packed and therefore interacting s.d. Co particles will thus correspond to a lower frequency than isolated ones. As a result, if the particles in this work had an *fcc* structure, they would show a resonance at frequencies below the one predicted by the laws set up for isolated *fcc* particles, and not higher as observed here [25][47]. The demagnetizing field is hpwever a possible explanation for the frequency shift between the peaks of the two *NP_4nm* samples shown in **Figure 10** a): In *NP_4nm_C13* the particles were closer and probably interacting stronger compared to *NP_4nm_OAm*, resulting in a lower demagnetizing field and resonance frequency. The peak frequencies of the three samples stabilized by the same ligand (OAm) on the other hand, seem to follow a same evolution with temperature. It can be concluded that the ligand and the resulting interparticle distance have a strong impact on the resonance frequency, probably due to an influence on the strength of the demagnetizing field.

In **Figure 10** b), the evolution with temperature of the full width at half maximum (FWHM) of the spectra obtained from the different samples is presented. It can be seen that the spectral width decreases systematically with the temperature, going from very large values, up to 12 MHz at 4 K, down to only 4 MHz at T_{amb}. The very large nature of the peak is another indication for the presence

of *hcp* Co, due to its anisotropic crystalline structure. In addition, factors like the surface anisotropy or inhomogeneities of the particle interactions further increased the width of the spectrum. One reason for the decline of the peak width temperature is probably the fact that some NPs become superparamagnetic at temperatures below the one of the others. If the NPs that become superparamagnetic at lower temperatures have a different resonance frequency that the others, the line width will decrease when they became superparamagnetic and therefore do not give an IF NMR signal anymore. An example is the lower frequency bump corresponding to *fcc* or defaulted *hcp* s.d. Co. As NPs with a non-perfect *hcp* crystalline structure are generally considered to have a lower energy barrier for the flipping of the magnetic moment compared to NPs with an anisotropic *hcp* structure, they should be become ferromagnetic at a lower temperature. In addition, *hcp* Co particles with slightly different particle sizes or interparticle distances might also correspond to different resonance frequencies, due to demagnetizing field effects for example.

To sum up, it can be said that the ^{59}Co IF NMR study of the samples indicates an *hcp* Co structure of the NPs. The position of the main peak and the large width of the spectrum, especially of experiments at low temperatures where the signal intensity is the strongest, support this conclusion. This is in line with the results of electron diffraction and HRTEM measurements done on samples synthesized in a similar fashion.[17], [18], [37] The evolution with temperature of the peak position and the FWHM was studied over a large temperature range, something that has not been done so far in the literature. The line width continuously decreases with temperature, which is at least partly due to the fact that particles with a different resonance frequency than the main ones become superparamagnetic at lower temperatures.

Signal intensity evolution

In this section, the evolution of the signal intensity with temperature will be monitored. As a reminder, with increasing temperature some Co NPs do not give an IF NMR signal anymore due to the ferromagnetic/ superparamagnetic transition. The blocking temperature (T_B) of this magnetic transition strongly depends on the size of such a particle. It is therefore interesting to study the evolution with temperature of the IF NMR spectrum integral intensity, which is relative to the number of ferromagnetic nuclei at a particular temperature and might allow a quantitative analysis of the particle size distribution. In the literature, this method has already been used in order to study samples of non-interacting Co nanoparticles [20], [27]. The goal of this work is to extend it to the study of interacting particles and to characterize the influence of the particle interactions on the T_B. In the previous studies, the temperature variation between the NMR experiments was very large. In the

following, the results using small temperature variations are presented and compared to the histograms determined by TEM.

Due to the fact that at relatively high temperatures strong corrections for to the Boltzmann distribution and the T_2 relaxation were necessary, the signal intensity was sometimes low and noisy apart from the center of the main peak. In order to avoid an influence on the integral intensity of the relatively strong noise at high temperatures, the integral was measured in between the frequencies corresponding to the FWHM of the spectrum. As a check, the evolution with temperature of the integral calculated in this way was compared to the evolution when taking the integral over the complete spectrum. The same trend was observed for each sample, thus validating this way to assess the signal intensity.

Besides the FWHM of a spectrum, which continuously decreased with increasing temperature as already presented in **Figure 10** b), it is the peak height that was decisive for the integral intensity. The evolution with temperature of the maximum peak height of the different samples (except *NP_9nm*, which has not been studied quantitatively) is shown in **Figure 11** a). It can be seen that for *NP_6nm* the peak height decreased monotonically with the temperature, but for *NP_4nm_OAm* and *NP_4nm_C13* a maximum peak height could be observed at 65 K and 50 K, respectively, with a decrease towards higher and lower temperatures. As *NP_6nm* was studied at temperatures below 85 K, a maximum might also have occurred at lower temperatures for this sample. Besides for sample *NP_4nm_OAm*, for which the peak height at 65 K was particularly high and the one at 4 K particularly low, the peak height seemed less temperature dependent that the FWHM. Influenced by the FWHM and the peak height, the relative IF NMR spectrum integral intensity at the different temperatures for the three samples is represented in **Figure 11** b). It can be seen that the intensity generally decreased with the temperature. For the *NP_4nm* samples a maximum was observed between 20 K and 30 K and an additional maximum around 65 K could be observed for *NP_4nm_OAm*.

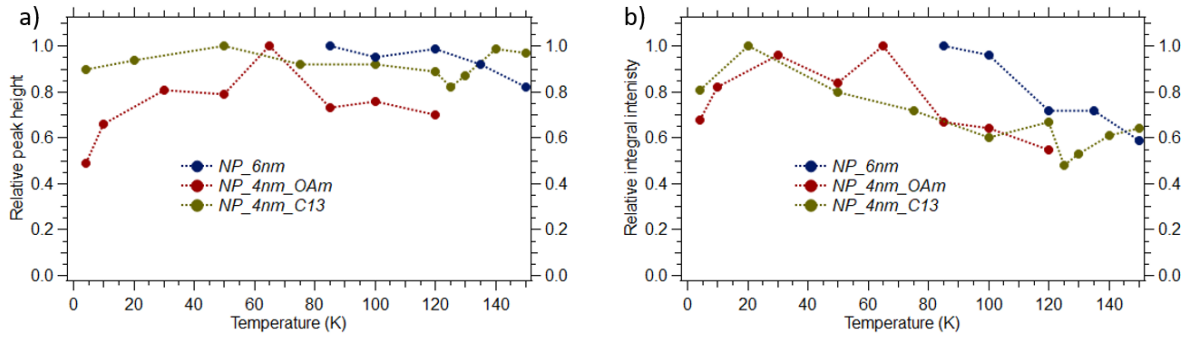

Figure 11: Evolution with temperature of a) the relative maximum peak height and b) the relative integral intensity of the ^{59}Co IF NMR spectra of the different samples.

The decrease of the integral intensity with temperature can be explained by the superparamagnetic transition of the magnetic NPs, as will be explained more in detail in the following paragraph. On the other hand, the increase with temperature of the integral intensity for temperatures between 4 and 20 K is quite surprising. A similar phenomenon has been observed recently by Meny and Panissod [48] when studying interacting Co NPs. They explained this phenomenon by the reduction of the magnetic anisotropy energy due to particle interactions towards low temperatures, a phenomenon already observed for weakly interacting particles when using Mössbauer spectroscopy [49] and AC susceptibility measurements [50] to determine the T_B. For IF NMR measurements, a lower magnetic anisotropy leads to a higher enhancement factor and consequently a lower pulse power necessary for an optimal excitation. Also in this work, the optimal power slightly increased with the temperature during the experiments in this temperature region, which is in line with this hypothesis. The signal increase observed for *NP_4nm_C13* for temperatures above 125 K was probably due to the low precision at those high temperatures. Especially the strong correction for T_2 introduced a strong error in this region, as explained in the next section.

Comparison of ^{59}Co IF NMR and TEM results

The evolution of the integral intensity should stand in a relationship with the particle size distribution due to the dependence of the superparamagnetic behavior on the particle volume. As the crystalline structure of the particles is *hcp* Co, the energy barrier for the flipping of the particle magnetic moment can be estimated by the uniaxial anisotropy energy: $\Delta E = K_{eff}(T) * V, K_{eff} \sim hcp$ magnetocrystalline anisotropy. The blocking temperature (T_B) of a particle can therefore be defined by Eq. (6.2), showing a direct relationship between T_B and the particle volume. This relationship is used to compare the particle size determination by TEM and the IF NMR spectrum integral of the samples *NP_6nm, NP_4nm_OAm* and *NP_4nm_C13*, as shown in **Figure 12** and explained in the following. First of all, the volume fraction particle volume distribution is determined based on the number fraction the of each particle diameter (red bars), determined by TEM as shown in **Figure 7** and **Figure 8**. This is done by considering all particles to be perfectly spherical. At a temperature where all the NPs are ferromagnetic, this distribution theoretically corresponds to the relative contribution of each particle size in the overall IF NMR signal, as it is proportional to the amount of Co nuclei. Via Eq. (6.2) this volume distribution is transformed into a distribution of theoretical T_B for the IF NMR measurements. This is represented in **Figure 12** by adding temperature *x*-axis, which is related to the volume *x*-axis by Eq. (6.2). The non-linearity between both axis is due to the temperature dependence of K_{eff}[40]. The black line in **Figure 12** represents the cumulative volume fraction as function of the particle volume, starting from the highest volume. Considering the temperature axis, this line

corresponds to the volume fractions of the particles that are blocked at a given temperature: All particles with a volume above the critical volume at this temperature (determined by Eq. (6.2)) are large enough to be ferromagnetic and give an IF NMR signal, all the particles with a volume below the critical volume are superparamagnetic and therefore should not give an IF NMR signal. For sample *NP_4nm_OAm* for example, around 60 % of the particle volume fraction has a volume superior to 45 nm³. By Eq. (6.2), 45 nm³ is the critical particle volume at around 180 K, meaning that smaller particles are superparamagnetic and bigger ones are ferromagnetic. As a result, in *NP_4nm_OAm* around 60 % of the particle volume fraction is expected to be ferromagnetic at 180 K according to Eq. (6.2).

For comparison to the TEM results, the evolution of the IF NMR integral intensity is represented in blue, normalized to 1 around the maximum integral intensity. If the particle size measurements by TEM gave a perfect overall picture of the sample and all the conditions of Eq. (6.2) were perfectly verified, both curves would perfectly overlap. However, it can be seen that for all samples, the ^{59}Co IF NMR integral decreased faster with temperature than predicted by the TEM particle size measurements. There are several factors that could explain this discrepancy:

- The most natural explanation would be the presence of smaller particles that were not observed by the localized TEM experiments but were detected by the sample-wide ^{59}Co IF NMR measurements. What is not in favor of this rational though, is the fact that the NMR signal is relative to the particle volume, meaning that there would be an unrealistically large number of small NPs that were not detected by TEM.
- Another, more probable, explanation was the presence Co NPs with a non-perfect *hcp* or even an *fcc* structure. Due to their lower magnetocrystalline anisotropy (K_{eff}), these particles should become superparamagnetic at a much lower temperature than particles of the same volume with a perfect *hcp* structure. As such particles also have a slightly different resonance frequency compared to the ones with a perfect *hcp* structure, the reduction of the integral intensity was at least partly due to a decrease of the FWHM, shown in **Figure 10** b). Nevertheless, the FWHM decrease already started at temperatures where the integral intensity was stable or increased with temperature, meaning that other factors also played a role.
- A third sample property that might explain the early integral decrease is the Co NP shape. By the TEM measurements a characteristic diameter was determined, which was then transformed into a volume considering a perfect sphere. A cubic particle with a diagonal d has an about 15 % reduced volume compared to a spherical particle with a diameter d, an effect that can be even more extreme for shapes like discs or needles for example. These particles would therefore shift downwards the particle volume distribution and became superparamagnetic earlier than predicted by the theory. In a

recent article, Liu et al.[27] explained the discrepancy between the TEM and IF NMR by this phenomenon, by dividing the theoretical T_B for a particle with a certain diameter by 2.5. Such a high correction factor seems exaggerated for the present samples, given the almost spherical character of most particles (**Figure 7** and **Figure 8**).

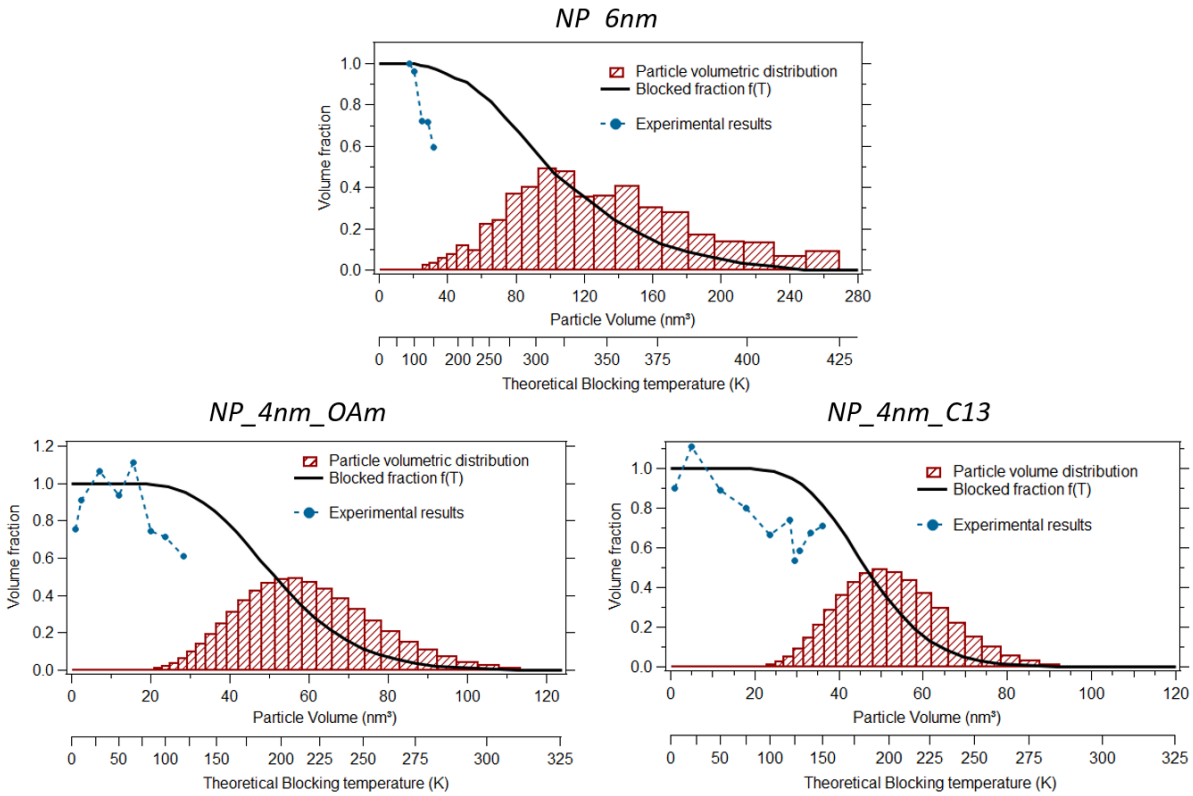

Figure 12: Representation of the fraction of Co atoms inside blocked (ferromagnetic) NPs (Black line), determined from the size distribution of volume fraction of the Co NPs (determined by TEM) (red bars) via the $T_B - V$ relationship in Eq. (6.2). The temperature axis is adapted to the volume axis in the same way. The evolution of the integral intensity of the IF NMR spectra at different temperatures (blue circles) is compared to this fraction. The volume distribution is normalized to 0.5 at its maximum for better visualization.

In summary, it can be said that for all the analyzed samples a decrease of the signal intensity before the temperatures predicted from TEM measurements and Eq. (6.2) was observed. Possible explanations for this early decrease are a non-spherical shape of the particles or a non-perfect *hcp* crystalline phase, leading to a reduced magnetic anisotropy. The main factor responsible for the decrease of the total signal intensity was not the height of the observed peak, but more its FWHM. This is a sign that the particles that become superparamagnetic at low temperatures have a slightly difference resonance frequency than the others. Such an effect was not observed by previous studies using ^{59}Co IF NMR to study the size of Co NPs.[20], [27] However, the evolution with temperature of

the FWHM and the signal intensity do not always follow the same trend, meaning that also different factors have an influence.

Transverse relaxation time

The transverse relaxation time (T_2) was measured at all temperatures for most of the samples shown in this work and the signal intensity was corrected to a zero interpulse delay. The evolution with temperature of the measured T_2 is represented in **Figure 13** a). It can be seen that T_2 decreased with temperature, going down from about 20 µs at 4 K to 4 µs around 150 K. For comparison, T_2 is generally around 20 µs at ambient temperature for bulk samples with signal arising from the excitation of domain walls. For non-interacting NPs studied by Yakovlev et al.[20], a slower decrease of T_2 from ~23 µs at 30 K to ~15 µs at 300 K was observed. When comparing the results obtained for the different samples, T_2 also seemed to be dependent on the average particle size of the analyzed sample, with T_2 being systematically higher for the *NP_6nm* sample than for the two *NP_4nm* samples. In addition, it was generally slightly higher for *NP_4nm_C13* than for *NP_4nm_OAm* at the different temperatures. It is tempting to attribute this difference to the slightly different average particle size, which is higher for the latter one, or due to the closer inter-particle distance for the former one. However, given the small differences observed in T_2 values, it might simply be due to experimental errors in the T_2 measurement.

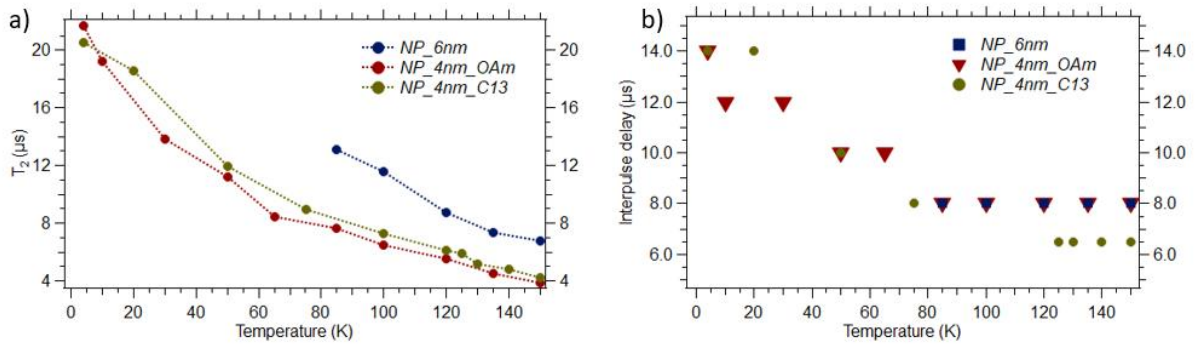

Figure 13: a) Evolution with temperature of the measured T_2 relaxation time for the different samples. b) The interpulse delays (τ) chosen for the experiments at the different temperatures.

In **Figure 13** b), the length of the interpulse delay (τ) chosen for the different experiments is displayed. As already mentioned in the experimental part of this chapter (Subsection 2.3), the interpulse delay had to be varied with temperature, due to an increasing dead time (t_{dead}) of the probe with decreasing temperature. When comparing these values to the corresponding T_2 that were measured, it can be seen that they were close to each other, τ was even above for some experiments. As a result, the

correction to a zero interpulse delay was important (explained in Chapter 3, Subsection 1.1), leading to quite large error of this correction even for small inaccuracies of the T_2 measurement.

It is noteworthy, that when measuring T_2 at a temperature close to the superparamagnetic transition of some particles in a sample, a systematic error appears. As during the T_2 measurement the interpulse delay τ is varied, the measurement time (τ_m) also changes. Consequently, some particles might be ferromagnetic for short τ, but become superparamagnetic for the later points of the relaxation curve. In **Figure 14** a), the T_2 relaxation curve measured from *NP_4nm_C13* at 130 K is represented, including the exponential fit of the curve. In red, the evolution of the critical volume (V_{crit}) as function of $\tau_m = (2\tau + t_p)$ is represented, calculated using Eq.(6.2). It can be seen that V_{crit} decreases with decreasing τ_m and goes from about 33 nm³ for $\tau_m = 45$ µs down to around 28 nm³ for $\tau_m = 5$ µs. More particles (even the smaller ones) might therefore be detected at the beginning of the relaxation curve (shorter τ). As shown in **Figure 12**, there are some particles between 28 and 33 nm³ in *NP_4nm_C13*, so theoretically more particles give a ferromagnetic signal for low τ.

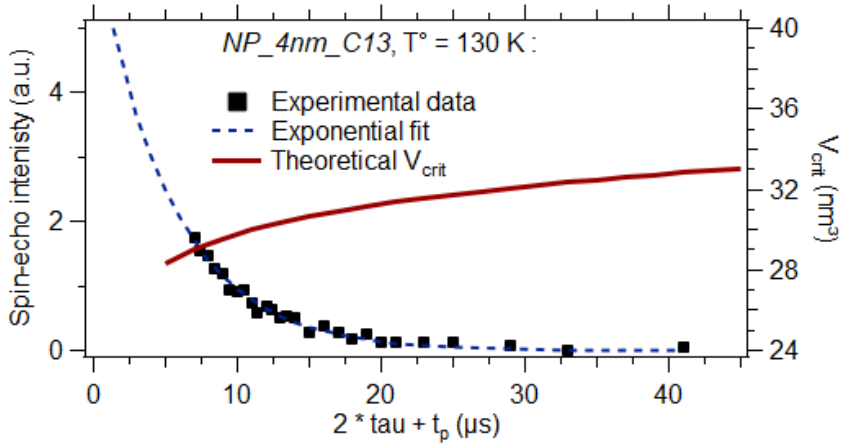

Figure 14: Representation of the exponential T_2 for sample *NP_4nm_C13* measured at 130 K. The red line gives the evolution of the theoretical critical volume as function of the $\tau_m = (2\tau + t_p)$ during the experiments. τ is the interpulse delay and t_p the pulse length.

Conclusions of the IF NMR analysis

First of all, the results of the ^{59}Co IF NMR analysis on the NPs indicate a predominantly *hcp* Co crystalline phase for these NPs. This was already suggested by electron diffraction measurements using TEM but was confirmed by the non-local NMR measurement. Moreover, some *fcc* or defaulted *hcp* crystalline phases were also detected. Based on Eq. (6.2) for non-interacting spherical particles, the analysis of the IF NMR measurements did not reproduce the particle size and T_B measurements

obtained by TEM and ZFC/FC magnetometry, respectively. Considering the superparamagnetic relaxation time calculation proposed in Eq. (6.2), the evolution of the NMR spectra with temperature indicated the presence of smaller particles than shown by TEM pictures. This could partly be explained by the non-spherical shape of the Co NPs, which lead to an overestimation of the particle size by TEM. In addition, the presence of crystalline phases different to perfect *hcp* might be responsible for an underestimation of the particle size by ^{59}Co IF NMR. Finally, the evolution of the T_2 time was monitored, which decreased with increasing temperature. Due to probe dead times of the same order of magnitude than the T_2 times, the precision of the quantitative integral intensity measurements were reduced.

4. Conclusions

In this chapter, close-packed monodisperse Co NPs have been studied using TEM, ZFC/FC magnetometry and ^{59}Co IF NMR experiments. While isolated Co NPs already have already been studied using this techniques, it is a novelty for close-packed ones. By TEM (including electron diffraction) the particle size, as well as the crystalline structure, of local parts of the sample have been studied. It shows different particle sizes with a more or less monodisperse size distribution and different interparticle distance as function of the synthesis conditions. The main crystalline structure is *hcp* for all conditions. The ZFC/FC magnetometry measurements show a T_B superior to the theoretical value, but no significant influence of the interparticle distance was observed. The ^{59}Co IF NMR allows first of all to confirm the predominantly *hcp* Co structure of the NPs, but also some non-perfect *hcp* phases were detected. Concerning the particle size, these measurements suggest that a lot of particles became superparamagnetic below their theoretical T_B, which can be explained by a non-spherical particle shape or particles with a magnetic anisotropy below the one of pure *hcp* Co. This discrepancy between the ZFC/FC and ^{59}Co IF NMR results could be explained by the different sample preparation: ZFC/FC samples were deposited on a film and dried, for IF NMR the solution was still present. Even though the NPs deposited on the tube borders, the presence of the solvent might still increase the interparticle distance and therefore reduce the particle interactions. A perspective is therefore the analysis of dried or deposited samples by NMR.

As a reminder, an initial goal of this chapter was to explain the T_B above its theoretical value observed by ^{59}Co IF NMR for Co particles inside conversion reaction battery materials. This observation was definitely not confirmed in the ^{59}Co IF NMR experiments performed on colloidal particles, which could be explained by the fact that the particles were not in contact. Therefore, only weak interactions exist

in between the particles, while the particles inside the battery materials are potentially in contact with strong interactions in between them. Weak interactions nevertheless can still reduce the magnetic anisotropy of the particles in some cases [49], [50], which might also be an explanation for the reduced T_B of the colloidal particles. The reason for this phenomenon is not very well understood, however. Quantitative information about the influence of particle interactions could not be determined here.

Overall, we have shown that the blocking temperature (T_B) depends on multiple parameters other than the particle size, such as the particle shape, particle interactions and the crystalline structure of a particle. The effects of these three phenomena are difficult to decorrelate, meaning that it is difficult to precisely measure a particle size inside an unknow system. Furthermore, the interplay between T_2 and T_B (*via* a variation of the measurement time τ_m during the experiment), particularly significant when the measuring temperature approaches T_B, introduces a systematic error when measuring T_2. This error influences the quantitative estimation of the number of ferromagnetic particles and therefore the T_B analysis based on Eq.(6.2). Thus, although in principle possible, the determination of particle size distributions by IF NMR measurements at various temperatures (as first suggested by [27]) appears to have some shortcomings.

A factor that reduced the precision of the quantitative interpretation of the ^{59}Co IF NMR results in thesis was the long dead time (t_{dead}) compared to the transverse relaxation time (T_2) of the observed signal. As a result, the chosen interpulse delay (τ) of the experiments was often of the same order of magnitude than T_2, leading to a low signal intensity and a large integral intensity correction for T_2. In addition, the precision of the T_2 measurement was also compromised, resulting in a less accurate T_2 correction. The precision of the experiments could therefore be increased using a probe with a shorter t_{dead}, by reducing its quality factor, for example. Nevertheless, precisely measuring signals with T_2 < 5 µs is challenging using classic NMR setups.

5. Supplementary Information

5.1. Brownian relaxation

Besides the Néel relaxation described previously, the magnetic moment of a single-domain ferromagnetic particle might also relax via rotation of the particle as a whole due to Brownian motion/ rotation. This type of relaxation is therefore only observed for magnetic particles in solution/ suspension. The comparison of both mechanisms is shown in **Figure 15**. Just as for Néel relaxation, if the Brownian relaxation a ferromagnetic particle is faster than the characteristic time of the measurement, the particle will not exhibit ferromagnetic behavior. The associated Brownian characteristic relaxation time for spherical particles suspended in a liquid is the following [51]:

$$\tau_B = \frac{3\,V'\eta}{k_B T} = \frac{4\pi\,(d'/2)^3\eta}{k_B T} \qquad (6.5)$$

with V'/d' the hydrodynamic volume/ diameter of the particle, η the dynamic viscosity of the suspending phase, k_B the Boltzmann constant and T the absolute temperature. For the current case of spherical particles in toluene and mostly stabilized by oleylamine, the hydrodynamic volume is a sphere with a radius equal to the sum of the particle radius and the length of the oleylamine chain in the solvent. As the interparticle distance at contact in oleylamine was measured to be equal to 4.1 nm [37], the length of the oleylamine chain is estimated to be equal to 2.0 nm. The dynamic viscosity (η) of toluene has been measured in the literature for values down to 213 K [52], a temperature still quite far above its freezing temperature of 178 K. As η might change drastically when approaching the freezing point, τ_B was not calculated for temperatures below 213 K. The effective characteristic relaxation time τ_{eff} is defined by [51]:

$$\frac{1}{\tau_{eff}} = \frac{1}{\tau_N} + \frac{1}{\tau_B} \qquad (6.6)$$

As a result, in case one of the relaxation times is much smaller than the other, the corresponding relaxation phenomenon is much faster and dominant over the other one.

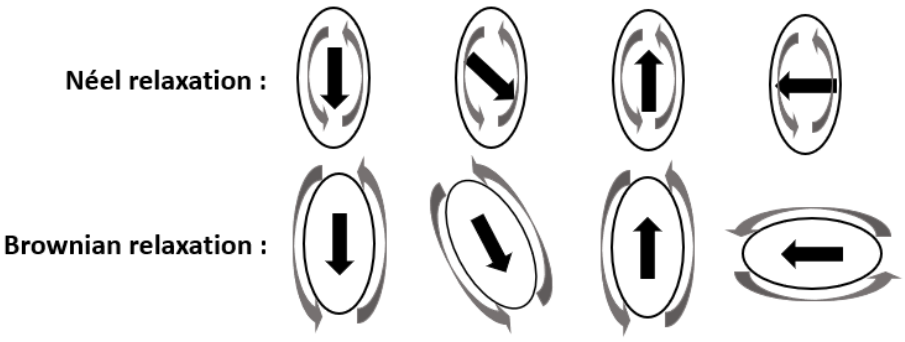

Figure 15: Comparison of the relaxation mechanisms of the Néel and Brownian relaxation for single-domain magnetic particles. The phenomena are represented schematically for ellipsoidal particles for better visualization, but also occurs for spheres.

In **Figure 16**, the theoretical evolution with the particle diameter (d) of the different relaxation times for *hcp* Co NPs stabilized by oleylamine in toluene for two different temperatures (213 K and 298 K) are represented. When comparing the Néel and Brownian relaxation times **Figure 16** a), it can be seen that τ_N ($\sim \exp(V) \sim \exp(d^3)$) varies much faster with the particle size than τ_B ($\sim V \sim d^3$). The Néel relaxation is therefore dominant for low particle diameters and the Brownian relaxation for higher particle diameters. For the presented example, the transition happens between diameters of around 4 – 5 nm, while in between both phenomena have a significant influence. Both relaxations are obviously faster at higher temperatures, with again a stronger dependence for τ_N ($\sim \exp(1/T)$) than for τ_B ($\sim 1/T$).

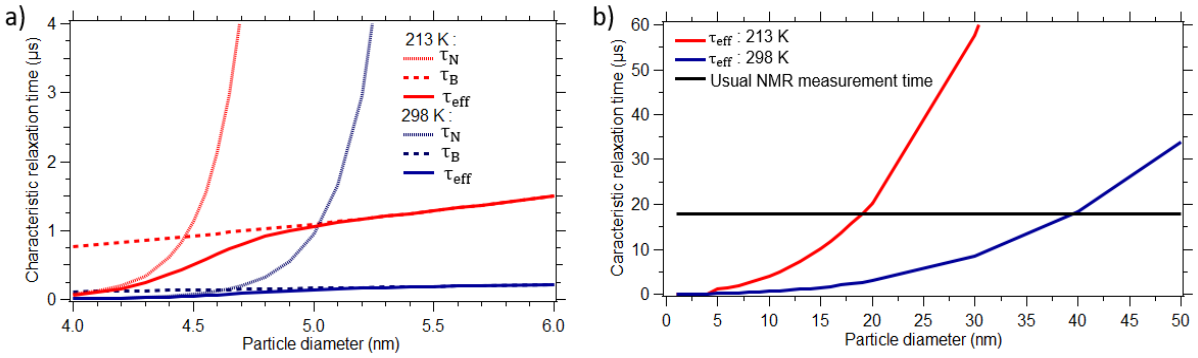

Figure 16: Theoretical evolution of the Brownian (τ_B), Néel (τ_N) and effective (τ_{eff}) characteristic relaxation times as function of the diameter of *hcp* Co NPs stabilized by oleylamine in toluene for two different temperatures. a) Zoom on the region where Néel and Brownian relaxation cross each other. b) Comparison of τ_{eff} to the typical IF NMR measurement time (18 µs).

In **Figure 16** b) the development of τ_{eff} with d is compared to the usual measurement time of our IF NMR experiments (18 µs). The critical diameter below which the relaxation is faster than the

measurement time is about 19 nm and 39 nm at 213 K and 298 K, respectively. **Figure 16** a), shows that the relaxation for these particle sizes is very much dominated by the Brownian movement. Considering the small size of the particles studied in this work (< 10 nm), the Brownian relaxation is faster than the NMR measurement time for all of them and no signal should be observed for most temperatures where toluene is in a liquid state. However, the analyzed Co NPs are not moving freely inside the toluene solvent and tend to sediment quite rapidly, organizing themselves on the tube bottom/wall. The particles are still stabilized by the oleylamine and are much more confined, resulting in a higher apparent viscosity. It is therefore considered that for most particles the behavior is dominated by the Néel relaxation. Nevertheless, some particles might still be in a relatively free suspension and therefore relax rapidly via Brownian motion and give no signal for the IF NMR measurements, even though they are not superparamagnetic considering only the Néel relaxation. As these particles are not exposed to Brownian motion anymore below the toluene freezing temperature, this might introduce and error to the quantitative measurements. In order to avoid the influence of Brownian motion, it is possible to remove the solvent by evaporation and only leave the stabilized particles behind. This is what was done for the TEM and the magnetic measurements, where the solution containing the particles was deposited on a support and the solvent evaporated. Brownian motion did thus not play a significant role in these experiments.

5.2. Complete ^{59}Co IF NMR spectra

In **Figure 17**, the complete ^{59}Co IF NMR spectra of samples *NP_9nm, NP_4nm_OAm* and *NP_4nm_C13* are represented. These spectra contain the results of the experiments at temperatures not presented in **Figure 9**. Given the high number of temperatures tested for sample *NP_4nm_C13*, the results were divided in two graphs. A detailed description of the sample synthesis conditions and characteristics can be found in Subsection 3.1 (**Table 1**). The main results of the spectrum interpretation and its evolution with temperature are described in Subsection 3.2.

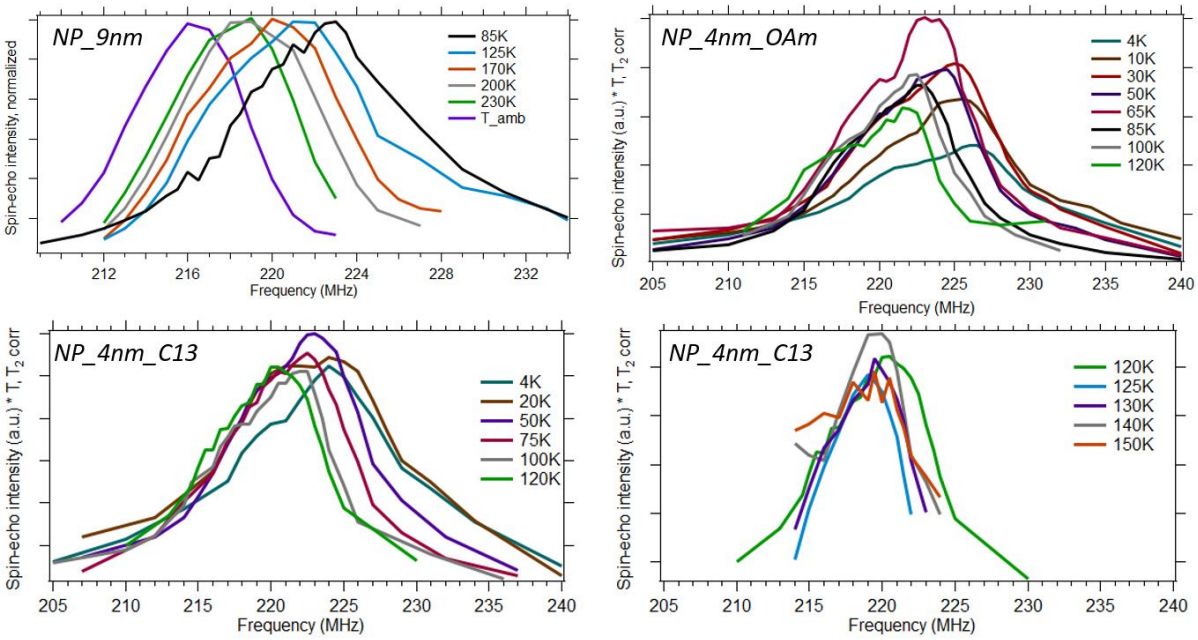

Figure 17: ^{59}Co IF NMR spectra at all the different tested temperatures of three Co NPs samples presented in this chapter. Except for the *NP_9nm* sample, all spectra have been corrected for the Boltzmann distribution (multiplication by the Temperature (K)) and the T_2 variation. The *NP_9nm* spectra have been normalized by their maximum.

6. References

[1] K. M. Krishnan *et al.*, "Nanomagnetism and spin electronics: materials, microstructure and novel properties," *J. Mater. Sci.*, vol. 41, no. 3, pp. 793–815, Feb. 2006, doi: 10.1007/s10853-006-6564-1.

[2] S. Oyarzún, "Spintronics in cluster-assembled nanostructures," Université Claude Bernard (Lyon 1), Lyon, 2013. [Online]. Available: https://tel.archives-ouvertes.fr/tel-01019680

[3] X. J. Wang, H. Zou, and Y. Ji, "Spin transfer torque switching of cobalt nanoparticles," *Appl. Phys. Lett.*, vol. 93, no. 16, p. 162501, Oct. 2008, doi: 10.1063/1.3005426.

[4] I. Florea, Y. Liu, O. Ersen, C. Meny, and C. Pham-Huu, "Microstructural Analysis and Energy-Filtered TEM Imaging to Investigate the Structure-Activity Relationship in Fischer-Tropsch Catalysts," *ChemCatChem*, vol. 5, no. 9, pp. 2610–2620, Sep. 2013, doi: 10.1002/cctc.201300103.

[5] Y.-P. Pei *et al.*, "High Alcohols Synthesis via Fischer–Tropsch Reaction at Cobalt Metal/Carbide Interface," *ACS Catal.*, vol. 5, no. 6, pp. 3620–3624, Jun. 2015, doi: 10.1021/acscatal.5b00791.

[6] S. Yan, J. Zhang, X. Yan, D. Pan, H. Ren, and X. Qu, "Catalytic coal hydrogasification by cobalt-calcium catalyst in a pressurized fluidized bed: Role of hydropyrolysis and catalysis process," *J. Anal. Appl. Pyrolysis*, vol. 135, pp. 251–259, Oct. 2018, doi: 10.1016/j.jaap.2018.08.028.

[7] M. Rahmati, M.-S. Safdari, T. H. Fletcher, M. D. Argyle, and C. H. Bartholomew, "Chemical and Thermal Sintering of Supported Metals with Emphasis on Cobalt Catalysts During Fischer–Tropsch Synthesis," *Chem. Rev.*, vol. 120, no. 10, pp. 4455–4533, May 2020, doi: 10.1021/acs.chemrev.9b00417.

[8] F. Chen *et al.*, "Selective cobalt nanoparticles for catalytic transfer hydrogenation of N-heteroarenes," *Chem. Sci.*, vol. 8, no. 9, pp. 6239–6246, 2017, doi: 10.1039/C7SC02062G.

[9] R. Hergt, S. Dutz, R. Müller, and M. Zeisberger, "Magnetic particle hyperthermia: nanoparticle magnetism and materials development for cancer therapy," *J. Phys. Condens. Matter*, vol. 18, no. 38, pp. S2919–S2934, Sep. 2006, doi: 10.1088/0953-8984/18/38/S26.

[10] P. Lukanov *et al.*, "CCVD Synthesis of Carbon-Encapsulated Cobalt Nanoparticles for Biomedical Applications," *Adv. Funct. Mater.*, vol. 21, no. 18, pp. 3583–3588, Sep. 2011, doi: 10.1002/adfm.201100364.

[11] Xu, "Carbon-covered magnetic nanomaterials and their application for the thermolysis of cancer cells," *Int. J. Nanomedicine*, p. 167, Mar. 2010, doi: 10.2147/IJN.S8306.

[12] M. A. Kazakova, "Fe/Co/Ni mixed oxide nanoparticles supported on oxidized multi-walled carbon nanotubes as electrocatalysts for the oxygen reduction and the oxygen evolution reactions in alkaline media," *Catal. Today*, vol. 357, pp. 259–268, 2020, doi: 10.1016/j.cattod.2019.02.047.

[13] Z. Yan *et al.*, "Co 3 O 4 /Co nanoparticles enclosed graphitic carbon as anode material for high performance Li-ion batteries," *Chem. Eng. J.*, vol. 321, pp. 495–501, Aug. 2017, doi: 10.1016/j.cej.2017.03.146.

[14] P. Poizot, S. Laruelle, S. Grugeon, L. Dupont, and J.-M. Tarascon, "Nano-sized transition-metal oxides as negative-electrode materials for lithium-ion batteries," *Nature*, vol. 407, no. 6803, Art. no. 6803, Sep. 2000, doi: 10.1038/35035045.

[15] M. Varón *et al.*, "Dipolar Magnetism in Ordered and Disordered Low-Dimensional Nanoparticle Assemblies," *Sci. Rep.*, vol. 3, no. 1, p. 1234, Dec. 2013, doi: 10.1038/srep01234.

[16] I. Lisiecki, D. Parker, C. Salzemann, and M. P. Pileni, "Face-Centered Cubic Supra-Crystals and Disordered Three-Dimensional Assemblies of 7.5 nm Cobalt Nanocrystals: Influence of the Mesoscopic Ordering on the Magnetic Properties," *Chem. Mater.*, vol. 19, no. 16, pp. 4030–4036, Aug. 2007, doi: 10.1021/cm070625x.

[17] A. Vivien *et al.*, "Role of Oleylamine Revisited: An Original Disproportionation Route to Monodispersed Cobalt and Nickel Nanocrystals," *Chem. Mater.*, vol. 31, no. 3, Art. no. 3, Feb. 2019, doi: 10.1021/acs.chemmater.8b04435.

[18] A. Sodreau, A. Vivien, A. Moisset, C. Salzemann, C. Petit, and M. Petit, "Simpler and Cleaner Synthesis of Variously Capped Cobalt Nanocrystals Applied in the Semihydrogenation of Alkynes," *Inorg. Chem.*, vol. 59, no. 19, pp. 13972–13978, Oct. 2020, doi: 10.1021/acs.inorgchem.0c01641.

[19] I. S. Edelman *et al.*, "FMR and TEM Studies of Co and Ni Nanoparticles Implanted in the SiO2 Matrix," *Appl. Magn. Reson.*, vol. 40, no. 3, pp. 363–375, May 2011, doi: 10.1007/s00723-011-0218-4.

[20] I. V. Yakovlev *et al.*, "Superparamagnetic behaviour of metallic Co nanoparticles according to variable temperature magnetic resonance," *Phys. Chem. Chem. Phys.*, vol. 23, no. 4, Art. no. 4, 2021, doi: 10.1039/D0CP05963C.

[21] A. A. Shmyreva, V. V. Matveev, and G. Yu. Yurkov, "Nuclear magnetic resonance in magnetic nano-materials as an effective technique to test and/or to certificate local magnetic properties," *Int. J. Nanotechnol.*, vol. 13, no. 1/2/3, Art. no. 1/2/3, 2016, doi: 10.1504/IJNT.2016.074527.

[22] W. Hines, J. Budnick, D. Perry, S. Majetich, R. Booth, and M. Sachan, "Nuclear magnetic resonance and magnetization study of surfactant-coated epsilon-Co nanoparticles," *Phys. Status Solidi B*, vol. 248, no. 3, Art. no. 3, Mar. 2011, doi: 10.1002/pssb.201046164.

[23] Y. D. Zhang, J. I. Budnick, W. A. Hines, S. A. Majetich, and E. M. Kirkpatrick, "Microstructure and magnetic behavior of carbon-coated Co nanoparticles studied by nuclear magnetic resonance," *Appl. Phys. Lett.*, vol. 76, no. 1, Art. no. 1, Jan. 2000, doi: 10.1063/1.125667.

[24] A. C. Gossard, A. M. Portis, M. Rubinstein, and R. H. Lindquist, "Ferromagnetic Nuclear Resonance of Single-Domain Cobalt Particles," *Phys. Rev.*, vol. 138, no. 5A, Art. no. 5A, May 1965, doi: 10.1103/PhysRev.138.A1415.

[25] H. Yasuoka and R. T. Lewis, "Temperature Dependence of Co 59 Nuclear Magnetic Resonance in Single-Domain Cobalt Particles," *Phys. Rev.*, vol. 183, no. 2, Art. no. 2, Jul. 1969, doi: 10.1103/PhysRev.183.559.

[26] V. V. Matveev, D. A. Baranov, G. Yu. Yurkov, N. G. Akatiev, I. P. Dotsenko, and S. P. Gubin, "Cobalt nanoparticles with preferential hcp structure: A confirmation by X-ray diffraction and NMR," *Chem. Phys. Lett.*, vol. 422, no. 4–6, Art. no. 4–6, May 2006, doi: 10.1016/j.cplett.2006.02.099.

[27] Y. Liu *et al.*, "Sampling the structure and chemical order in assemblies of ferromagnetic nanoparticles by nuclear magnetic resonance," *Nat. Commun.*, vol. 7, no. 1, Art. no. 1, Sep. 2016, doi: 10.1038/ncomms11532.

[28] J. P. Chen, C. M. Sorensen, K. J. Klabunde, and G. C. Hadjipanayis, "Magnetic properties of nanophase cobalt particles synthesized in inversed micelles," *J. Appl. Phys.*, vol. 76, no. 10, Art. no. 10, Nov. 1994, doi: 10.1063/1.358280.

[29] F. Wang *et al.*, "Conversion Reaction Mechanisms in Lithium Ion Batteries: Study of the Binary Metal Fluoride Electrodes," *J. Am. Chem. Soc.*, vol. 133, no. 46, Art. no. 46, Nov. 2011, doi: 10.1021/ja206268a.

[30] J. Cabana, L. Monconduit, D. Larcher, and M. R. Palacín, "Beyond Intercalation-Based Li-Ion Batteries: The State of the Art and Challenges of Electrode Materials Reacting Through Conversion Reactions," *Adv. Mater.*, vol. 22, no. 35, Art. no. 35, Sep. 2010, doi: 10.1002/adma.201000717.

[31] S.-H. Yu, S. H. Lee, D. J. Lee, Y.-E. Sung, and T. Hyeon, "Conversion Reaction-Based Oxide Nanomaterials for Lithium Ion Battery Anodes," *Small*, vol. 12, no. 16, Art. no. 16, Apr. 2016, doi: 10.1002/smll.201502299.

[32] Y. Fu *et al.*, "Nanostructure-Mediated Phase Evolution in Lithiation/Delithiation of Co_3O_4," *ACS Appl. Mater. Interfaces*, vol. 13, no. 24, pp. 28171–28180, Jun. 2021, doi: 10.1021/acsami.1c05591.

[33] J. Zhang, H. Jiang, Y. Zeng, Y. Zhang, and H. Guo, "Oxygen-defective Co3O4 for pseudo-capacitive lithium storage," *J. Power Sources*, vol. 439, p. 227026, Nov. 2019, doi: 10.1016/j.jpowsour.2019.227026.

[34] J. Mei, T. Liao, G. A. Ayoko, J. Bell, and Z. Sun, "Cobalt oxide-based nanoarchitectures for electrochemical energy applications," *Prog. Mater. Sci.*, vol. 103, pp. 596–677, Jun. 2019, doi: 10.1016/j.pmatsci.2019.03.001.

[35] S.-H. Yu, X. Feng, N. Zhang, J. Seok, and H. D. Abruña, "Understanding Conversion-Type Electrodes for Lithium Rechargeable Batteries," *Acc. Chem. Res.*, vol. 51, no. 2, Art. no. 2, Feb. 2018, doi: 10.1021/acs.accounts.7b00487.

[36] J.-M. Tarascon *et al.*, "On the Electrochemical Reactivity Mechanism of CoSb[sub 3] vs. Lithium," *J. Electrochem. Soc.*, vol. 150, no. 6, Art. no. 6, 2003, doi: 10.1149/1.1568737.

[37] L. Meziane, C. Salzemann, C. Aubert, H. Gérard, C. Petit, and M. Petit, "Hcp cobalt nanocrystals with high magnetic anisotropy prepared by easy one-pot synthesis," *Nanoscale*, vol. 8, no. 44, Art. no. 44, 2016, doi: 10.1039/C6NR05792F.

[38] L. Meziane, "Nanomatériaux mono et bimétalliques à forte anisotropie magnétique," Université Pierre et Marie Curie, Paris, 2016. [Online]. Available: https://hal.inria.fr/THESES-UPMC/tel-01885496v1

[39] Y. Barnier, "Contribution à l'étude des propriétés magnétiques du cobalt et des alliages de fer-cobalt (Thèse d'Ingénieur-Docteur)," Université de Grenoble, Grenoble, 1963. [Online]. Available: https://tel.archives-ouvertes.fr/tel-03372927

[40] E. P. Wohlfarth, "Iron, Cobalt and Nickel," in *Ferromagnetic materials*, vol. 1, North-Holland Publishing Company, 1980, p. 70.

[41] C. de Julián Fernández, "Influence of the temperature dependence of anisotropy on the magnetic behavior of nanoparticles," *Phys. Rev. B*, vol. 72, no. 5, Art. no. 5, Aug. 2005, doi: 10.1103/PhysRevB.72.054438.

[42] S. Bedanta, O. Petracic, and W. Kleemann, "Supermagnetism," in *Handbook of Magnetic Materials*, vol. 23, Elsevier, 2015, pp. 1–83. doi: 10.1016/B978-0-444-63528-0.00001-2.

[43] K. L. Livesey, S. Ruta, N. R. Anderson, D. Baldomir, R. W. Chantrell, and D. Serantes, "Beyond the blocking model to fit nanoparticle ZFC/FC magnetisation curves," *Sci. Rep.*, vol. 8, no. 1, Art. no. 1, Dec. 2018, doi: 10.1038/s41598-018-29501-8.

[44] R. Sappey, E. Vincent, N. Hadacek, F. Chaput, J. P. Boilot, and D. Zins, "Nonmonotonic field dependence of the zero-field cooled magnetization peak in some systems of magnetic nanoparticles," *Phys. Rev. B*, vol. 56, no. 22, Art. no. 22, Dec. 1997, doi: 10.1103/PhysRevB.56.14551.

[45] A. M. Portis and A. C. Gossard, "Nuclear Resonance in Ferromagnetic Cobalt," *J. Appl. Phys.*, vol. 31, no. 5, Art. no. 5, May 1960, doi: 10.1063/1.1984666.

[46] L. G. Hanson, "Is quantum mechanics necessary for understanding magnetic resonance?," *Concepts Magn. Reson. Part A*, vol. 32A, no. 5, pp. 329–340, Sep. 2008, doi: 10.1002/cmr.a.20123.

[47] A. S. Andreev, J.-B. d'Espinose de Lacaillerie, O. B. Lapina, and A. Gerashenko, "Thermal stability and hcp–fcc allotropic transformation in supported Co metal catalysts probed near operando by ferromagnetic NMR," *Phys. Chem. Chem. Phys.*, vol. 17, no. 22, Art. no. 22, 2015, doi: 10.1039/C4CP05327C.

[48] C. Meny and P. Panissod, "Nuclear magnetic resonance in ferromagnets: Ferromagnetic nuclear resonance; a very broadband approach," in *Annual Reports on NMR Spectroscopy*, vol. 103, Elsevier, 2021, pp. 47–96. doi: 10.1016/bs.arnmr.2021.02.001.

[49] S. Mørup and E. Tronc, "Superparamagnetic relaxation of weakly interacting particles," *Phys. Rev. Lett.*, vol. 72, no. 20, pp. 3278–3281, May 1994, doi: 10.1103/PhysRevLett.72.3278.

[50] J. L. Dormann, L. Bessais, and D. Fiorani, "A dynamic study of small interacting particles: superparamagnetic model and spin-glass laws," *J. Phys. C Solid State Phys.*, vol. 21, no. 10, pp. 2015–2034, Apr. 1988, doi: 10.1088/0022-3719/21/10/019.

[51] R. Kötitz, P. C. Fannin, and L. Trahms, "Time domain study of Brownian and Néel relaxation in ferrofluids," *J. Magn. Magn. Mater.*, vol. 149, pp. 42–46, 1995, doi: 10.1016/0304-8853(95)00333-9.

[52] M. J. Assael, N. K. Dalaouti, and S. Polimatidou, "The Viscosity of Toluene in the Temperature Range 210 to 370 K," *Int. J. Thermophys.*, vol. 20, no. 5, pp. 1367–1377, 1999, doi: 10.1023/A:1021428819290.

Conclusions and prospects

Conclusions and prospects

In this PhD work, cobalt containing systems of different nature and with applications in various scientific domains were studied. Given the wide range of applications, different properties needed to be tested for each system. The studied characteristics were the crystalline structure, including the presence of foreign atoms and defects, the magnetic domain and domain wall structure and the size of nanoparticles, which all could be determined using ^{59}Co internal field nuclear magnetic resonance (IF NMR). Even though the use and the development of this technique was the main focus of this work, all systems were also studied using different techniques for verification and to obtain complementary results, most often in collaboration with partner laboratories. As the concepts of the ^{59}Co IF NMR experiments and the interpretation of the resulting spectra are unfamiliar to many researchers, even working in the domain of NMR, an introduction to both was given in the first parts of the thesis. Then, the analysis of the different systems of interest was presented. Interesting results were obtained, also raising several new questions, as will be elucidated in the following.

In **Chapter 4**, the results of the analysis of Co-C composite materials were presented. The materials were produced by ball milling of carbon under a hydrogen atmosphere with the purpose of doing a carbon hydrogasification reaction with Co as a catalyst. Over the course of the milling, the evolution of the predominant Co crystalline structure and of the Co-C phase was studied and compared to the carbon hydrogasification reaction rate. To characterize Co-C bonding, ^{59}Co IF NMR provided complementary information compared to techniques like X-ray diffraction (XRD) or photoemission spectroscopy (PES).

First of all, it was found that the presence of Co-C intermediates in the Co material stabilized the *fcc* Co phase. This effect seemed to dominate over changes of the crystallite size over the course of the milling. Focusing on the Co-C intermediates, two different phases were distinguished: A Co/C interstitial solid solution and the metastable Co_3C phase. Over the course of the milling, a direct relationship between the reaction rate and the total amount of Co-C intermediates was observed. Both started at a very high level directly after the activation, decreased to a steady-state and then declined towards zero when almost no carbon remained inside the mill anymore. This observation confirms that the carbon dissociation and the Co-C bond formation generally is the limiting step of the carbon hydrogasification reaction. As this reaction step is strongly enhanced using the here presented mechanochemical process due to the high collision energy and the close contact between both phases (cobalt and carbon), the reaction rate is much superior compared to classical processes.

These conclusions show the great potential of ^{59}Co IF NMR to study the evolution of a catalyst over the course of a reaction. In the future, the here-presented carbon hydrogasification reaction might be

studied more in detail, as the milling parameters seemed to have a strong influence on the efficiency of the reaction. In addition, it is planned to simulate the evolution of the carbon content inside the Co particles, taking into account the carbon diffusion and surface reaction. In addition, the appearance of a signal at very low frequencies still needs to be understood. Besides the study of additional ^{13}C enriched and non-enriched samples, it is also a methodological challenge to precisely detect a signal at such low frequencies.

Finally, the potential of ^{59}Co IF NMR to study simultaneously the catalyst crystalline phase and the bond with the reactants is potentially of interest in different catalytic reactions as well. This is not only valid for cobalt, but also for iron- or nickel-containing catalysts. Both nuclei can also be studied using IF NMR, even though the ^{57}Fe and ^{61}Ni isotopes have a low natural abundance (2.2% and 1.14%).

In **Chapter 5**, cobalt nanowires produced by electrodeposition into the pores of membranes were studied. Their crystalline and magnetic structure as function of the deposition conditions and the wire geometry were analyzed using ^{59}Co IF NMR, in addition to XRD and magnetic hysteresis measurements. Two different types of porous membranes were tested: polycarbonate (PC) membranes with 50 nm pores and a low pore density, as well as anodized aluminum oxide (AAO) membranes with 200 nm pores and a high pore density. In addition, samples deposited into both membrane types were synthesized with two different deposition conditions: with and without the presence of organic additives in the electrolyte.

Independent of the membrane type, it was observed by ^{59}Co IF NMR that the deposition conditions had a big impact on the crystalline structure of the wires. While samples deposited in absence of organic additives in the electrolyte were composed of relatively big crystalline domains with a low grain-boundary density, the presence of organic additives resulted in a reduced crystalline domain size with a high grain-boundary density and potentially an inclusion of impurities in the structure. These observations were complementary to the results obtained using XRD experiments, indicating a preferential *hcp* Co phase with the *c*-axis perpendicular to the wire axis for samples synthesized in absence of organic additives and a preferential *fcc* Co phase for the others. Such a variation of the preferential crystalline phase was not observed using ^{59}Co IF NMR, which could be explained by the oriented character of the XRD analysis.

When analyzing the magnetic structure, it was observed that the strong shape anisotropy was predominant for the 50 nm samples and resulted in a magnetic easy axis oriented alongside the wire axis, independently of its crystalline structure. For the 200 nm wires on the other hand, the crystalline anisotropy played an important role, especially the orientation of the *c*-axis of the anisotropic *hcp*

structure. The wires deposited in absence of organic additives being composed of big crystalline domains including *hcp* Co phases with a *c*-axis perpendicular to the wire axis, their magnetic easy axis was perpendicular to the wire. In contrast, the wires deposited in presence of organic additives were detected to have a magnetic easy axis parallel to the wire. Based on the ^{59}Co IF NMR results, this change was not due to a different predominant crystalline phase but more because of a higher amount of grain boundaries and a decrease of the crystalline quality in presence of the additives, leading to a lower crystalline anisotropy.

The analysis of the magnetic easy axis orientation presented above was done by magnetic hysteresis measurements and confirmed by a novel approach using ^{59}Co IF NMR. By analyzing the excitation efficiency as function of the orientation between the *rf* field and the wire axis, the orientation of the magnetic domain walls could be determined. In the future, this new concept of analyzing the domain wall orientations using ^{59}Co IF NMR could be extended by application of a constant external field, to analyze 2D systems for example.

Additional prospects of these experiments are the study of the influence of interwire interactions on their magnetic structure, which could be done by varying the interwire distance. In addition, experiments with a variable applied external field would also help to push this study further and to study the orientation of the *hcp* Co *c*-axis by NMR (as already demonstrated by Strijkers et al.[1]) or to differentiate the signal from different magnetic domains.

In Chapter 6, assemblies of close-packed monodisperse Co nanoparticles (NPs) in suspension were studied. The NPs were synthesized by a disproportionation reaction, allowing a variation of the particle size and the interparticle distance. They were analyzed using transmission electron microscopy (TEM), zero-field cooling/ field cooling (ZFC/FC) magnetometry and ^{59}Co IF NMR.

The particle crystalline structure was determined using ^{59}Co IF NMR, allowing a sample-wide overview. Given the position of the main resonance frequency and its large width, the predominant structure was attributed to *hcp* Co in a single-domain magnetic structure. Samples with three different average particle sizes and the same interparticle distance were compared, as well as two samples with the same particle size but a different interparticle spacing. The different samples were studied using TEM in order to get information about the particle size and the interparticle distance. These results were then compared to ZFC/FC magnetometry and ^{59}Co IF NMR measurements, which allowed to estimate the particle size via the characterization of the ferromagnetic - superparamagnetic transition at the blocking temperature (T_B). ZFC/FC magnetometry measurements showed a mean T_B above the theoretical value determined based on the TEM size distribution. The ^{59}Co IF NMR experiments on the

other hand, indicated that many particles became superparamagnetic at a temperature below the theoretical value. This effect could be explained by the presence of non-spherical particles or by particles with a magnetic anisotropy below the one of pure *hcp* Co. This difference between the ZFC/FC magnetometry (higher T_B) and ^{59}Co IF NMR (lower T_B) results might be explained by the different sample preparations: For the ZFC/FC magnetometry measurements the sample was deposited on a film and dried, for the NMR analysis the solution was still present. An outlook is therefore the analysis of dried or deposited samples by NMR, which might lead to lower interparticle distance and stronger particle interactions.

An initial goal of this study was to analyze the observation of an increased T_B by ^{59}Co IF NMR for small Co NPs inside conversion reaction battery materials, an effect which was not observed in this study. Potential reasons are the fact that the particles inside the battery materials are in contact and therefore interact via strong (exchange) interactions, while the here-presented samples only interact weakly. Besides the analysis of dried samples, a prospect is therefore the analysis of model systems of particles in contact, which will also help to better understand the role of weak and strong interparticle interactions.

Finally, during the NP study the limitations of the performed quantitative T_B analysis by ^{59}Co IF NMR were shown. Especially at higher temperatures when already some particles were superparamagnetic, very low T_2 relaxation times were observed (< 8 µs), which were of the same order of magnitude than the electronic dead-time of the used probe, limiting the precision of the measurements. A prospect for future works would therefore be the employment of probes with lower electronic dead times. When being able to determine the evolution of T_2 more precisely, a possibility would be to study the origin of and the quantification of the low T_2 values with increasing temperature. Potential links between superparamagnetism and the relaxation behavior might be investigated.

In order to conclude, it can be said that using ^{59}Co IF NMR, different samples characteristics were studied in the three analyzed systems. Besides the crystalline structure, during the study of Co-C systems the focus was the study of the local Co environment, during the study of the Co nanowires the magnetic domain structure was determined and during the study of Co nanoparticles it was the particle size. This shows the great potential of this technique when studying cobalt, which is an important component in many applications of the modern society. As a consequence, hopefully more researchers will be interested to try this technique in the future. For example, experiments are already planned on Co containing magneto-ionic 2D layered systems. The Co metal structure that is forming inside is suited well to be studied by ^{59}Co IF NMR.[2]

Besides being relatively simple to perform in principle, this work also showed some limitations of the ^{59}Co IF NMR and elements that can be improved during further studies. During the analysis of Co NP, there seem to be several phenomena that have an influence: particle size, crystalline structure, interactions. In an unknown system, the effects of these three phenomena are difficult to decorrelate. During the study of Co-C nanocomposites, a very broad spectrum was obtained. Given the point-by point acquisition, these experiments were time-consuming. In the future, auto-tune or broadband systems would definitely increase the efficiency of these experiments.

[1] G. J. Strijkers, J. H. J. Dalderop, M. A. A. Broeksteeg, H. J. M. Swagten, and W. J. M. de Jonge, "Structure and magnetization of arrays of electrodeposited Co wires in anodic alumina," *J. Appl. Phys.*, vol. 86, no. 9, Art. no. 9, Nov. 1999, doi: 10.1063/1.371490.

[2] J. de Rojas *et al.*, "Magneto-Ionics in Single-Layer Transition Metal Nitrides," *ACS Appl. Mater. Interfaces*, vol. 13, no. 26, pp. 30826–30834, Jul. 2021, doi: 10.1021/acsami.1c06138.

Appendix

Relationship between B, H and M

In the literature there often seems to be a confusion between the use of the letter H or B when describing a magnetic field, even though these letters correspond to two distinct physical quantities with different units. This can lead to confusion when describing NMR phenomena. In addition, two types of unit sets are used in the literature, SI and CGS, leading to different formulations. Most of the information and annotations used here come from the first chapter of Guimarães A.P.: Magentism and Magnetic Resonance in Solids, p.227 - 242 (1998)[1]. Letters in bold correspond to vectors.

Magnetic induction

First of all, we want to define the magnetic induction **B**. By definition, it determines the Lorentz force that acts on moving charges (charge q and speed $\boldsymbol{v}$) in a given environment:

$$\boldsymbol{F}_L = q\boldsymbol{v} \times \boldsymbol{B} \qquad (\text{App. } 1)$$

$\boldsymbol{B}$ is often also called the “magnetic flux density” or simply the “magnetic field”. In this PhD thesis, when talking about the magnetic field it is always a magnetic induction $\boldsymbol{B}$ that is actually referred to. Its units are [T] (SI) and [G] (CGS), with 1 G → 10^{-4} T.

Magnetization

Secondly, the magnetization $\boldsymbol{M}$ is defined as the total magnetic dipole moment ($\mu_{\boldsymbol{dip}}$) of an object divided by its volume. It is thus the volumetric density of magnetic dipole moments. $\mu_{\boldsymbol{dip}}$ of an object is defined by the total torque ($\boldsymbol{\tau}$) experienced by an object inside a magnetic induction $\boldsymbol{B}$:

$$\boldsymbol{\tau} = \mu_{\boldsymbol{dip}} \times \boldsymbol{B} \qquad (\text{App. } 2)$$

The units of $\boldsymbol{M}$ are $\left[\frac{A}{m}\right]$ in (SI) or $\left[\frac{emu}{cm^3}\right]$ (CGS), with 1 $\frac{emu}{cm^3}$→ 10^3 $\frac{A}{m}$.

Magnetizing field

Lastly, the magnetizing field $\boldsymbol{H}$ corresponds to the difference between the total magnetic induction inside a medium and the magnetization induced by the medium itself. In SI units, this becomes:

$$\boldsymbol{H} = \frac{\boldsymbol{B}}{\mu_0} - \boldsymbol{M} \qquad (\text{App. } 3)$$

with $\mu_0 = 4\pi\ 10^{-7}\ \frac{H}{m}(SI)$ the vacuum permeability. And in CGS units:

$$\boldsymbol{H} = \boldsymbol{B}(/\mu_0) - 4\pi\boldsymbol{M} \qquad (\text{App. } 4)$$

with μ_0 = 1 G/Oe, so the vacuum permeability is generally not used with CGS units. The units of $\boldsymbol{H}$ are $\left[\frac{A}{m}\right]$ in SI and [Oe] in CGS, with 1 Oe → $\frac{10^3}{4\pi}\ \frac{A}{m}$. As it can be seen, the units of $\boldsymbol{M}$ and $\boldsymbol{H}$ are not the same in CGS, with the difference being a factor 4π. Other names for $\boldsymbol{H}$ are "magnetic field strength/ intensity" or even "magnetic field". This last term is used for both $\boldsymbol{B}$ and $\boldsymbol{H}$ and therefore responsible for the confusion between them, but in this PhD thesis this term is never used to describe $\boldsymbol{H}$.

Overview

When turning the definition of $\boldsymbol{H}$ around, one can say that the magnetic induction $\boldsymbol{B}$ inside a material is the sum of the magnetizing field $\boldsymbol{H}$ (generally from external sources) and the magnetization $\boldsymbol{M}$ of the material itself (often induced by $\boldsymbol{H}$). As a result, one can write:

SI: $\overbrace{\boldsymbol{B}}^{[T]} = \mu_0(\overbrace{\boldsymbol{H} + \boldsymbol{M}}^{[A/m]})$ with $\mu_0 \rightarrow 4\pi\ 10^{-7}\ \frac{H}{m}$ (App. 5)

CGS: $\overbrace{\boldsymbol{B}}^{[G]} = \underbrace{\boldsymbol{H}}_{[Oe]} + \overbrace{4\pi\underbrace{\boldsymbol{M}}_{\left[\frac{emu}{cm^3}\right]}}^{[G]}$ (App. 6)

As a result, free space ($\boldsymbol{M} = 0$), $\boldsymbol{B}$ and $\boldsymbol{H}$ are simply directly related via the vacuum permeability: $\boldsymbol{B} = \mu_0\boldsymbol{H}$ (SI) or $\boldsymbol{B} = \boldsymbol{H}$ (CGS).

Magnetic susceptibility/ permeability

The magnetic susceptibility of a medium ($\mathcal{X}$) is defined by the magnetization $\boldsymbol{M}$ of a medium that is under the influence of a magnetizing field $\boldsymbol{H}$:

$$\boldsymbol{M} = \mathcal{X}\boldsymbol{H} \qquad (\text{App. } 7)$$

The magnetic induction of this medium is defined by the magnetic permeability μ:

$$\boldsymbol{B} = \mu\boldsymbol{H} \qquad (\text{App. } 8)$$

Both parameters are generally not constant and depend on $\boldsymbol{H}$ and other parameters (temperature…).

When inserting both expressions inside the definition of $\boldsymbol{H}$, a relationship between $\mathcal{X}$ and μ can be found and a relative susceptibility μ_r is defined:

SI: $\mu_r = \frac{\mu}{\mu_0} = (1 + \mathcal{X})$ (App. 9) CGS: $\mu_r = \frac{\mu}{\mu_0} = (1 + 4\pi\mathcal{X})$ (App. 10)

For example, in free space $\mu_r = 1$ in a paramagnetic material, which has a positive $\mathcal{X}$, $\mu_r > 1$.

Lines of forces

In order to represent the evolution of $\boldsymbol{B}$ and $\boldsymbol{H}$ inside different magnetic materials, their lines of forces are represented. The lines of forces show the direction of vectorial property and the density of the lines is proportional to the intensity of the vectorial property. An important boundary condition of $\boldsymbol{B}$ is that its lines of force always have to be continuous, even at the interface between different materials. This condition is not valid for $\boldsymbol{H}$ and $\boldsymbol{M}$.

In **Figure 1** the lines of forces of $\boldsymbol{B}$ and $\boldsymbol{H}$ are represented for a paramagnetic material ($\mathcal{X} > 0$, $\mu_r > 1$) under the influence of a uniform external magnetic field. It can be seen that outside of the material both lines have the same intensity, as no $\boldsymbol{M}$ ($\mathcal{X} = 0$) is generated and therefore $\mu_r = 1$. Inside the paramagnetic material, however, a $\boldsymbol{M}$ (represented in red) parallel to $\boldsymbol{H}$ is generated as $\mathcal{X} > 0$ and the lines of $\boldsymbol{B}$ are denser than the ones of $\boldsymbol{H}$. The lines of $\boldsymbol{B}$ are continuous at interface between different materials which is not the case for $\boldsymbol{H}$. It seems clear that the total magnetic field seen by the nuclei inside the sample is $\boldsymbol{B}$ and that it differs from the magnetizing field $\boldsymbol{H}$.

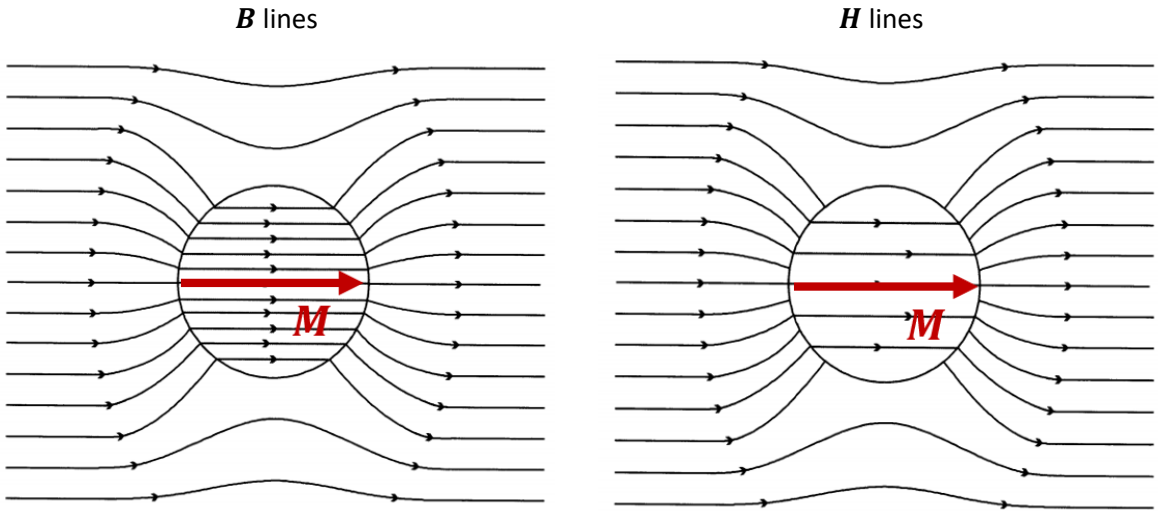

Figure 1: Representation of the lines of forces of $\boldsymbol{B}$ and $\boldsymbol{H}$ inside and outside of a paramagnetic material under the influence of an external magnetic field. The red arrow corresponds to the direction of the magnetization. Adapted from [1].

In **Figure 2** the lines of forces of $\boldsymbol{B}$ and $\boldsymbol{H}$ are represented inside and outside of a ferromagnetic material in absence of an external field. In such a ferromagnetic material an internal magnetization $\boldsymbol{M}$ (represented in red) is generated due to the alignment of the electron spins even in absence of an external field. $\boldsymbol{M}$ will generate a colinear magnetic induction $\boldsymbol{B}$ inside the material $\sim\mu_0\boldsymbol{M}$ (SI) or $\sim 4\pi\boldsymbol{M}$ (CGS). As the material is finite, free magnetic poles (S – N) will appear at the surface of the material. These poles are responsible for a magnetizing field $\boldsymbol{H}$ outside of the particle, called stray field, which is proportional to $\boldsymbol{B}$ in this case as $\mathcal{X}$ = 0 outside of the particle. This field also validates the continuity condition of $\boldsymbol{B}$. Inside the material, these poles create a magnetizing field $\boldsymbol{H}$ in the opposite direction of $\boldsymbol{M}$ (as $\boldsymbol{H}$ always N → S), which therefore reduces $\boldsymbol{B}$ inside the particle and is often called demagnetizing field. More details about this phenomenon will be given in the next section.

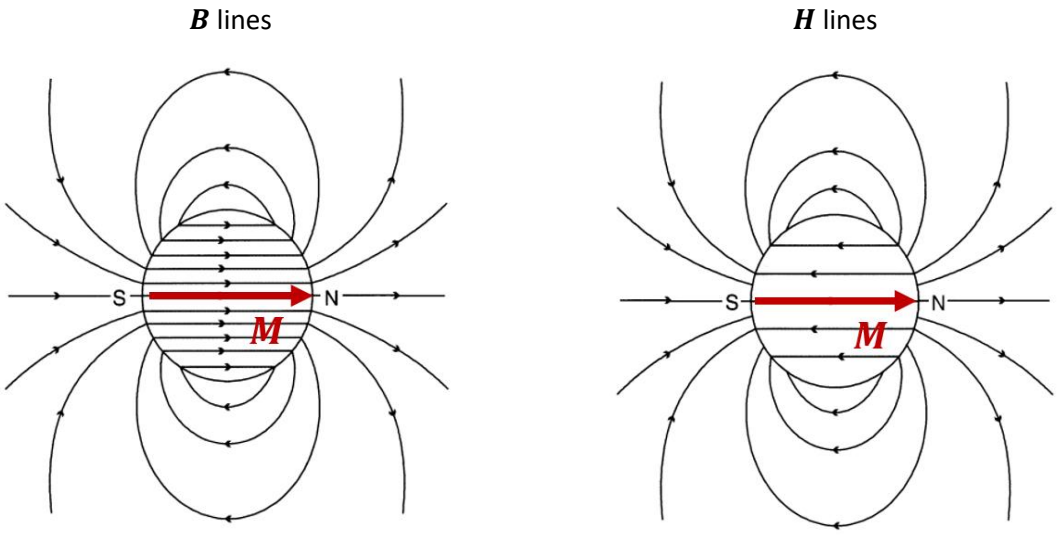

Figure 2: Representation of the lines of forces of $\boldsymbol{B}$ and $\boldsymbol{H}$ inside and outside of a ferromagnetic material in absence of an external field. The red arrow corresponds to the direction of the magnetization. S, N: Magnetic south and north pole. Adapted from [1].

Demagnetizing field

As described in the previous section, due to free poles at the surface of ferromagnetic particles a demagnetizing field appears inside the particle that reduces the magnetic induction $\boldsymbol{B}$ inside it. This demagnetizing field is directly dependent on the amplitude and the direction of the magnetization $\boldsymbol{M}$ inside the particle, but also on its shape. As there will be much more free poles at the surface of spherical particle compared to a long cylinder magnetized along its main axis, the demagnetizing field is bigger in the former case. The demagnetizing field therefore can be written as:

SI: $\boldsymbol{H}_{dem} = -N_d \boldsymbol{M}$ (App. 11) CGS: $\boldsymbol{H}_{dem} = -4\pi N_d \boldsymbol{M}$ (App. 12)

N_d is the demagnetizing factor or form factor and equal to 1/3 for a sphere, for example.[2]

A $\boldsymbol{H}$ is used in this case to describe the effect of the demagnetizing field, which could be a sign that it is $\boldsymbol{H}$ that should be used to the describe the field acting on the nuclei and not the magnetic induction $\boldsymbol{B}$. However, even though the effect of the free poles on the magnetic properties inside the material can be visualized well using a demagnetizing field $\boldsymbol{H}$, its physical effect is the reduction of $\boldsymbol{B}$ inside the material:

SI : $\boldsymbol{B}_{dem} = -\mu_0 N_d \boldsymbol{M}$ (App. 13) CGS: $\boldsymbol{B}_{dem} = -4\pi N_d \boldsymbol{M}$ (App. 14)

As a result, in this work $\boldsymbol{B}_{dem}$ is preferred in order to describe the demagnetizing field. Even though in the literature the term $\boldsymbol{H}_{dem}$ is more commonly used, its amplitude is generally given in [T] or [G], showing that the authors were actually discussing the magnetic induction and not the magnetizing field.

In order to conclude, it is a magnetic induction $\boldsymbol{B}$ that needs to be used to describe the field acting on the nuclei inside magnetic materials and not the magnetizing field $\boldsymbol{H}$. As shown in **Figure 1** and **Figure 2**, in order to obtain the total magnetic field inside a sample, not only the effect of external fields but also the effect of $\boldsymbol{M}$ also need to be taken into account.

[1] A. P. Guimarães, *Magnetism and magnetic resonance in solids*. New York: John Wiley & Sons, 1998.

[2] J. A. Osborn, "Demagnetizing Factors of the General Ellipsoid," *Phys. Rev.*, vol. 67, no. 11–12, pp. 351–357, Jun. 1945, doi: 10.1103/PhysRev.67.351.

Résumé substantiel en français

Les matériaux contenant du cobalt et en particulier des nanostructures de cobalt sont des matériaux importants dans de nombreuses applications de la société moderne. Ils sont utilisés dans les dispositifs de détection ou de stockage de données, ainsi qu'en catalyse et pour le stockage d'énergie. En fonction du type d'application, différentes propriétés sont nécessaires pour obtenir un résultat optimal, ce qui signifie que les matériaux se présentent sous différentes formes et structures cristallines. Dans le cas de la catalyse par exemple, une surface élevée de Co doit être disponible pour le réactif et le matériau doit donc contenir des nanoparticules de cobalt avec un rapport surface/volume élevé. En outre, l'efficacité de la réaction catalytique dépend souvent de la structure cristalline des particules de Co. Dans les mémoires à accès aléatoire, en revanche, des propriétés magnétiques sont visées.

En fonction de la propriété à analyser, ces matériaux ont déjà été étudiés par de nombreuses techniques analytiques. Les plus courantes sont la diffraction des rayons X pour analyser la structure cristalline, la microscopie électronique à transmission pour déterminer la taille des nanostructures, les mesures d'hystérésis magnétique pour quantifier les propriétés magnétiques, mais également beaucoup d'autres. Une technique puissante qui n'est que rarement utilisée est la RMN ^{59}Co en champ interne (IF NMR), également appelée RMN ferromagnétique (FNR). Elle permet d'étudier simultanément la structure cristalline, l'environnement local du cobalt et la structure magnétique des matériaux ferromagnétiques contenant du cobalt. Par conséquent, elle peut être appliquée pour caractériser beaucoup de matériaux différents. Dans ce travail, l'étude de structures différentes (assemblages de nanoparticules de Co en interaction, nanobâtons de Co, composites Co-C) a mis en évidence l'intérêt d'exploiter l'anisotropie de l'excitation des parois de domaines ainsi que l'importance des interactions entre particules. L'objectif de l'étude est de montrer le potentiel de cette technique pour analyser des structures variées et avec des caractéristiques différentes.

1. RMN en champ interne

Premièrement, les principes de la RMN en champ interne sont illustrés et le champ interne est décrit, ce qui permet de mieux comprendre l'interprétation des spectres et le potentiel de la technique.

Contrairement à la RMN classique, il n'est pas nécessaire d'appliquer un champ magnétique externe constant car le champ interne présent dans les composés ferromagnétiques suffit à polariser les spins nucléaires. Ce champ interne n'est pas statique, mais interagit avec l'aimantation nucléaire et le champ

radiofréquence (*rf*) de l'excitation. Lors de l'excitation, l'aimantation électronique, et par conséquent aussi le champ interne, suivent la direction du champ *rf,* à la même fréquence. Le champ d'excitation vu par les spins nucléaires est donc la composante transverse du champ interne ($B_{int}^{\perp}$) qui est beaucoup plus élevée que le champ *rf* initial (B_1). On peut donc définir le facteur d'amplification η :

$$\eta = \frac{B_{int}^{\perp}}{B_1} \tag{1}$$

De manière similaire, la réponse des spins nucléaires est également amplifiée par ce même facteur η, ce qui augmente la sensibilité. Dans le cas des parois de domaines, le champ radiofréquence engendre leur déplacement, ce qui donne un η plus élevé par rapport aux domaines. La puissance du champ *rf* nécessaire pour une excitation optimale est inversement proportionnelle à η, ce qui permet de différencier le signal des domaines et des parois.

La fréquence de résonance dans le cas de la RMN en champ interne peut être déterminée par les équations de Bloch d'un système couplée nucleus – électron. Dans la plupart de cas, elle peut être estimée par le produit du rapport gyromagnétique (γ_n) et le champ interne (B_{int}):

$$\Omega_n = |-\gamma_n B_{int}| \tag{2}$$

Dans le cas de la RMN en champ interne du Co, la valeur de B_{int} peut être divisé en deux contributions : le champ hyperfin (B_{HF}) et le champ dipolaire (B_{dip}). La contribution principale vient de B_{HF}, qui dépend de la structure cristalline et des voisins proches (différent du Co par exemple) d'un atome de cobalt. Une contribution importante à B_{dip} est le champ de démagnétisation, qui dépend de la forme de l'échantillon et de la structure des domaines magnétiques. Globalement, la valeur de B_{int} et donc de la fréquence de résonance donnera une information sur la structure cristalline, la structure du premier voisin et la structure magnétique.

Les valeurs exactes des fréquences de résonance sont difficilement calculables de manière précise, surtout pour des systèmes avec une structure cristalline non parfaite. L'attribution des pics dans les spectres se fait donc principalement par comparaison avec des références dans la littérature. Pour des structures de Co pur, différents pics sont généralement distingués à température ambiante : un pic autour de 213 MHz (Co *fcc* multi-domaine), autour de 216 MHz (Co *fcc* mono-domaine), un pic large autour de 219 MHz (structure Co *hcp,* mono- et multi-domaine à la fois). La présence de défauts et d'atomes étrangers dans la structure réduit généralement la fréquence de résonance. [1]

2. Composites Co-C produits par broyage à billes

Le premier système étudié est constitué des particules de carbure de cobalt. Les matériaux ont été produits par broyage à billes avec l'objectif de la préparation de l'hydrogénation du carbone (CHG). Ce travail a été réalisé en collaboration avec Dr. Gao-Feng Han et Prof. Jong-Beom Baek de l'Ulsan National Institute of Science and Technology (UNIST, Corée du Sud), qui ont synthétisé les échantillons.

La CHG est un processus connu depuis plusieurs décennies et permet de produire du méthane proprement sur base de sources de carbone comme le charbon, le coke et des déchets. Dans le passé, ce processus a souvent été catalysé par Co ou d'autres métaux de transition dans des réacteurs à lit fixe, mais des travaux récents de Han et al. (en préparation) ont montré que l'utilisation d'un procédé mécanochimique (broyage à billes) augmente fortement le taux de réaction. Pendant ce procédé, du graphite est broyé sous une atmosphère d'hydrogène avec des particules de Co comme catalyseur. Pour estimer le taux de réaction, la production de méthane est surveillée tout au long du procédé. Cependant, avant le début de l'hydrogénation, le graphite et le cobalt sont broyés sous une atmosphère inerte pour activer l'échantillon. Les billes sont faites de deux matériaux différents : WC et ZrO_2. Dans ce travail, l'évolution de la phase Co à différentes étapes du broyage a été étudié par ^{59}Co IF NMR, ce qui a permis d'analyser l'évolution de la phase cristalline prédominante du Co et de caractériser les différents intermédiaires Co/C.

Avant de pouvoir analyser par ^{59}Co IF NMR, les phases présentes dans un composé Co-C, la décomposition d'un spectre doit être étudiée, comme celle-ci n'est pas encore unifiée dans la littérature. En **Figure 1**, le spectre ^{59}Co IF NMR d'un échantillon broyé (avec des billes ZrO_2) pendant 15,5 h après activation est représenté, y compris une proposition de décomposition du spectre en différents environnements de cobalt (lignes pointillées). Le pic principal centré autour de 213,5 MHz est attribué au cobalt *fcc* pur, comme il a déjà été reporté dans la littérature.[1] En outre, la décomposition montre un petit pic autour de 219 MHz, indiquant la présence d'une petite quantité de cobalt *hcp* également.[1] Dans la même figure, le spectre est comparé à celui de la poudre de Co initiale, non broyée. Il présente les mêmes caractéristiques dans cette gamme de fréquence mais est beaucoup plus étroit, ce qui peut s'expliquer par une variation de la qualité de la structure cristalline et de la taille des cristallites. Dans la poudre de Co initiale, le cobalt était composé de gros grains avec peu de défauts cristallins. Dans l'échantillon activé, le broyage pendant plusieurs heures a réduit la taille des cristallites et augmenté la densité des défauts, ce qui a augmenté la largeur des pics.

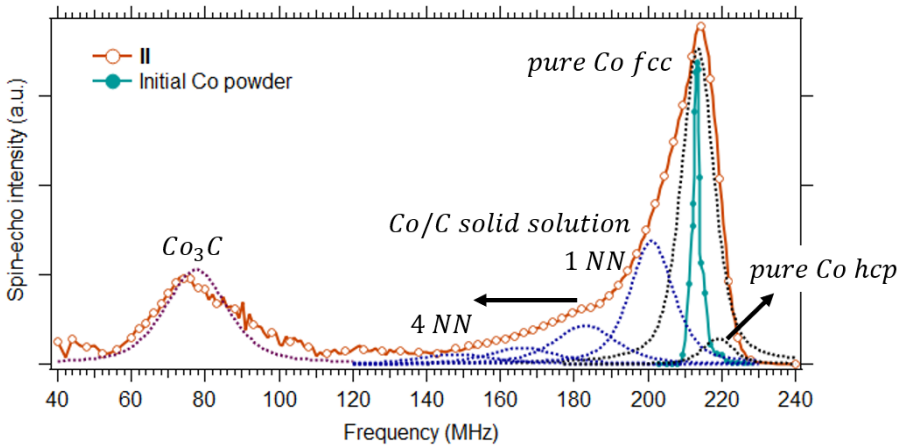

Figure 1: Spectre ^{59}Co IF NMR d'un échantillon broyé (avec des billes ZrO_2) pendant 15,5 h après activation: ligne orange avec cercles vides. Il est comparé au spectre obtenu à partir de la poudre de cobalt initiale, sans aucun broyage : ligne turquoise avec cercles pleins. Les lignes pointillées correspondent à la décomposition proposée du spectre après activation → noir : Co *fcc* & Co *hcp* purs, bleu : Co *fcc* avec 1 - 4 C comme NN en solution solide (négligeant les contributions d'autres voisins), violet : Co_3C.

Dans le spectre de l'échantillon broyé dans **Figure 1**, le signal ne diminue que lentement dans la région de fréquence située sous le pic principal du Co *fcc*. Le signal dans cette région est attribué à une solution solide cobalt/carbone. La présence d'un ou plusieurs carbones sur un site interstitiel voisin (le plus proche du Co) perturbe la structure électronique du cobalt et réduit ainsi le champ magnétique vu par le noyau ^{59}Co. Cet effet a bien été étudié pour des alliages Co/métal (par substitution), pour lesquels un décalage en fréquence constant du signal ^{59}Co IF NMR par premier voisin (NN) remplacé par un atome étranger est observé. Par contre, le cas du système Co-C (solution solide par insertion) est peu étudié dans la littérature par ^{59}Co IF NMR. Pour des échantillons avec une teneur en carbone allant jusqu'à 1,1 at.%, Cadeville et al.[2] ont observé des lignes satellites à des fréquences 14 MHz et 34 MHz en dessous du pic du Co *fcc* pur, attribuées au cobalt avec un et deux carbones sur ses sites interstitiels NN. Le spectre de l'échantillon broyé dans la **Figure 1** peut être ajusté avec deux pics à 201 MHz et 183 MHz, correspondant à un décalage vers les basses fréquences similaire à ceux observés par Cadeville et al. et donc assignés au Co avec un et deux C NN, respectivement. Le spectre en dessous de ces fréquences est ajusté avec deux pics supplémentaires à 165 MHz et 148 MHz, correspondant au cobalt avec trois et quatre C NN, respectivement. Le dernier signal qui doit encore être attribué est la large bosse centrée autour de 80 MHz. Un signal à cette fréquence a déjà été observé par Hiraoka et al. [3] lors de l'analyse d'alliages Co-C, produits par broyage à billes, et attribué à la présence d'une phase Co_3C.

Globalement, l'analyse ^{59}Co IF NMR des matériaux composites Co-C permet donc de distinguer 4 environnements : Co *fcc*, Co *hcp*, Co/C solution solide (Co avec 1 - 4 C comme NN) & Co_3C. L'attribution a été vérifiée par des expériences de diffraction des rayons X (DRX) et de spectroscopie photoélectronique (PES).

Les résultats présentés dans la suite correspondent à l'analyse des échantillons broyés avec des billes en WC. En **Figure 2** a), l'évolution de la quantité de carbone présente à l'intérieur du récipient de broyage est représentée (bleu). Cette quantité a été estimée par mesure de la quantité de CH_4 présent dans le récipient après différents temps de broyage et on peut observer qu'elle diminue continuellement et est proche de 0 après 30 h de broyage. La courbe rouge correspond au taux de consommation de carbone, égale à la pente de la courbe bleue. Ce taux est très élevé juste après l'activation, descend rapidement vers un plateau et tend vers 0 à la fin. Les lettres **A** à **F** correspondent aux moments où la phase Co a été analysé par ^{59}Co IF NMR.

Les résultats de la décomposition de ces spectres RMN sont représentés en **Figure 2** b). On peut observer qu'après l'activation (temps 0), la forme cristalline de l'échantillon est le Co *fcc*, mais une grande partie est en solution solide Co/C et il existe même un peu de Co_3C. Globalement, la quantité totale de composés Co-C diminue avec le broyage. Seul le point **E**, après 24 h de broyage, semble ne pas suivre cette tendance. La composition de la phase cristalline de Co semble d'être directement liée à la quantité des composés Co-C : la présence de carbone dans la structure de Co semble stabiliser la phase Co *fcc*. Dans l'échantillon **F**, broyé pendant longtemps avec peu de carbone dans le récipient, il n'y a plus de composés Co-C et la phase cristalline prédominante est Co *hcp*.

Lorsque l'on compare le taux de consommation de carbone avec l'évolution de la quantité totale de composés Co-C (Co avec C en solution solide ou Co_3C), la forme des deux lignes semble similaire. Elles commencent toutes deux à une valeur très élevée, diminuent rapidement vers un état d'équilibre, puis redescendent pour atteindre quasiment zéro à la toute fin. Ceci permet d'expliquer pourquoi le processus de broyage à billes donne un taux de réaction aussi élevé par rapport à un processus d'hydrogénation de carbone classique : l'étape limitante du processus classique est la dissociation de carbone et sa réaction avec du cobalt, ce qui est fortement augmenté en affinant les grains de cobalt et de carbone et en les maintenant en contact étroit. De plus, la formation d'une grande quantité de défauts à l'intérieur du cobalt est connue pour améliorer sa réactivité avec le carbone.

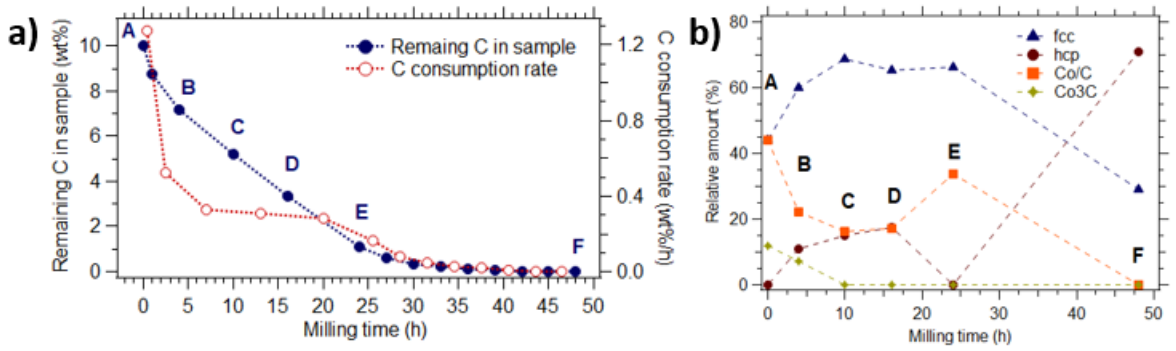

Figure 2: Analyse d'une série d'expériences sur un seul échantillon : Broyé avec des boules de WC après activation. a) En bleu, l'évolution en fonction du temps de broyage (0 h = directement après activation) de la teneur en carbone restant à l'intérieur du récipient de broyage est représentée. Les lettres **A** à **F** correspondent aux moments où une petite quantité de l'échantillon a été retirée du broyeur afin d'effectuer des expériences de RMN. Le taux de consommation de carbone correspondant entre les mesures est représenté en rouge (cercles creux). b) Estimation à partir de la ^{59}Co IF NMR des différents environnements du Co : Co *fcc* & *hcp* pur, solution solide Co/C, Co_3C.

3. Nanobâtons de Co synthétisés par électrodéposition

Le deuxième système étudié est une structure de nanobâtons de cobalt orientés parallèlement entre eux. Les nanobâtons sont synthétisés par électrodéposition de Co dans les pores des membranes poreuses. Ce travail a été réalisé en collaboration avec le Dr. Alberto Quintana et l'équipe de Prof. Kai Liu de Georgetown University, qui ont synthétisés les échantillons et faits les mesures de magnétométrie.

Les nanobâtons ferromagnétiques avec des propriétés magnétiques accordables ont fait l'objet d'intenses recherches, non seulement parce qu'ils soulèvent d'intéressantes questions de physique fondamentale, mais aussi parce qu'ils sont utilisés dans des dispositifs électromagnétiques à l'échelle nanométrique ou microscopique. Les propriétés magnétiques des nanobâtons de cobalt métallique synthétisés par électrodéposition dépendent non seulement de la géométrie des nanobâtons, mais également des conditions de synthèse. Deux types de membranes sont utilisés comme support de déposition : des membranes en polycarbonate (PC) avec des pores de 50 nm et une faible densité de pores, ainsi que des membranes en oxyde d'aluminium anodisé (AAO) avec des pores de 200 nm et

une forte densité de pores. Pour les deux types de membranes, deux conditions de dépôt différentes ont été testées : avec et sans la présence d'additifs organiques dans l'électrolyte.

Dans ce travail, la ^{59}Co IF NMR est utilisée pour étudier la structure cristalline et magnétique des différentes nanobâtons et les résultats sont comparés à ceux des techniques les plus utilisées dans la littérature : la diffraction des rayons X (DRX) et la magnétométrie.

En **Figure 3**, l'exemple d'une analyse ^{59}Co IF NMR d'un échantillon déposé dans les pores de 200 nm des membranes AAO, en présence des additifs organiques dans l'électrolyte, est représentée. Le spectre (a)) montre que l'échantillon est composé d'une quantité équivalente de Co *fcc* & *hcp*. Le pied du spectre vers les fréquences basses indique la présence d'impuretés et de joints de grains. L'évolution avec la fréquence de la puissance d'excitation optimale est constante et montre que toute la structure est multi-domaine. En comparant la puissance optimale en fonction de l'orientation entre l'axe de bâtons et le champ radiofréquence (*rf*), on peut observer que plus de puissance est nécessaire pour une orientation perpendiculaire. Comme le déplacement des parois de domaines est plus efficace pour un champ magnétique parallèle aux domaines, ceci signifie que l'orientation des domaines de la structure multi-domaine est parallèle à l'axe du bâton. Cette méthode pour déterminer l'orientation de l'axe facile d'aimantation dans des nanobâtons est nouvelle et a été confirmée par des expériences de magnétométrie.

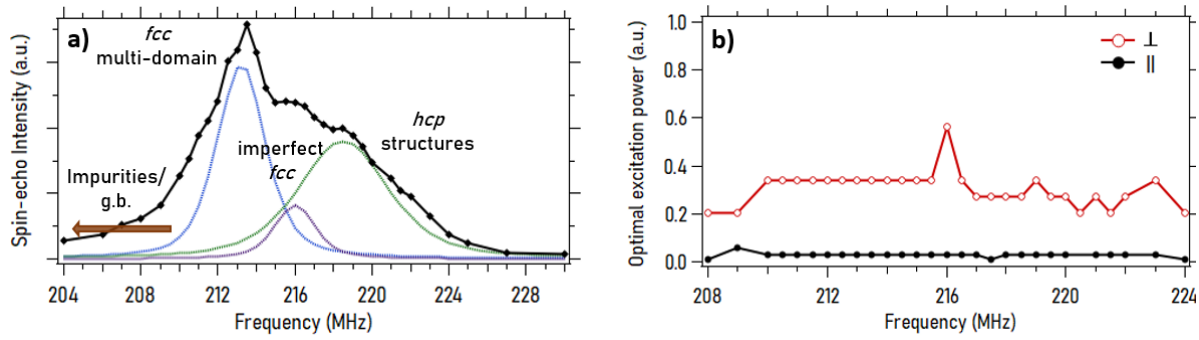

Figure 3: a) Spectre ^{59}Co IF NMR d'un échantillon déposé dans des pores de 200 nm de membranes AAO, en présence d'additifs organiques dans l'électrolyte. Une tentative de décomposition du spectre est présentée également. b) L'évolution avec la fréquence de la puissance d'excitation optimale en fonction de l'orientation entre l'axe des bâtons et le champ radiofréquence (*rf*).

Les étapes d'analyse décrites précédemment ont été faites pour tous les échantillons. Les caractéristiques spectrales de l'IF NMR ont été comparées aux résultats de l'analyse de diffraction des rayons X, et l'anisotropie de la puissance d'optimale d'excitation de l'IF NMR aux résultats de la

magnétométrie. Alors que le comportement magnétique des nanobâtons de 50 nm était dominé, comme prévu, par une anisotropie de forme avec des domaines magnétiques orientés sur l'axe, l'analyse des 200 nm s'est avérée plus complexe. La ^{59}Co IF NMR a révélé que la différence déterminante entre les échantillons électrodéposés en présence ou en l'absence d'additifs organiques n'était pas la structure cristalline dominante (*fcc* ou *hcp*) mais les tailles et les limites cohérentes des domaines cristallins. En présence d'additifs organiques, les domaines cristallins de Co sont plus petits et présentent des joints de grains défectueux, comme le révèlent les résonances inférieures à 210 MHz. Cela a empêché le développement de la forte anisotropie magnétocristalline dans la partie Co *hcp* de l'échantillon, qui a été observée en l'absence d'additifs organiques. En présence d'additifs organiques, même dans des nanobâtons aussi larges que 200 nm, le comportement magnétique est resté déterminé par l'anisotropie de forme avec une anisotropie magnétique effective positive et une forte anisotropie du facteur d'amélioration RMN.

En résumé on peut dire que l'étude ^{59}Co IF NMR complète bien les expériences de diffraction des rayons X et de la magnétométrie pour cette structure. Une particularité du travail a été l'utilisation de la RMN pour déterminer la structure des parois de domaines magnétiques à l'intérieur du bâton en variant l'orientation entre le champ d'excitation et l'axe du bâton. La ^{59}Co IF NMR a prouvé que ce n'est pas seulement la géométrie du bâton et sa phase cristalline qui sont responsables de sa structure magnétique, mais aussi la taille et la qualité des cristallites.

4. Assemblages de NPs de Co

Le troisième système étudié sont des assemblages de nanoparticules (NPs) de cobalt. Les NPs sont synthétisées par une réaction de dismutation d'un précurseur. Les NPs sont stabilisées par un ligand et dissoutes dans du toluène. Ce travail a été réalisé en collaboration avec le Dr. Alexandre Sodreau de l'équipe de Prof. Christophe Petit et Dr. Arthur Moisset de l'équipe de Dr. Marc Petit de l'université Sorbonne, qui ont synthétisé les échantillons et effectué les analyses de microscopie électronique en transmission (MET) et de zero field-cooling/ field-cooling (ZFC/FC).

Des assemblages de NPs de cobalt trouvent des applications dans de nombreux domaines scientifiques, par exemple en catalyse [4], en médecine[5] et dans les matériaux de stockage d'énergie[6]. Dans la plupart de ces applications, la structure cristalline et la taille des nanoparticules sont des paramètres cruciaux. En particulier, avec la distance et les interactions interparticulaires, ces paramètres ont une influence sur les propriétés magnétiques d'un assemblage de nanoparticules. Une technique peu utilisée pour analyser ce genre de NPs est la ^{59}Co IF NMR, qui permet d'obtenir une vue

d'ensemble de la structure cristalline des particules des échantillons. En outre, elle permet de déterminer la taille des particules *via* la transition superparamagnétique - ferromagnétique à la température dite de blocage. Au cours de l'analyse des nanoparticules de cobalt dans les matériaux des batteries à réaction de conversion, il a été observé que dans certains cas, des nanoparticules de petite taille présentent un signal ferromagnétique au-dessus de leur température de blocage théorique, ce qui pourrait être expliqué par des interactions entre les particules. Afin de valider cette hypothèse, des assemblages compactes de nanoparticules de cobalt avec différentes tailles de particules et distances interparticules ont été étudiés dans ce travail. Les résultats des analyses ^{59}Co IF NMR sont comparés à ceux obtenus avec des techniques plus utilisées dans la littérature : MET et ZFC/FC.

Plusieurs échantillons différents ont été testés : 3 avec de l'oléylamine (4.1 nm distance interparticule) comme ligand et un diamètre moyen des NPs de 8.6, 5.5 et 4.5 nm et un dernier avec du tridécanol comme ligand et un diamètre moyen de 4.4 nm. Les diamètres ont été déterminés par MET, montrant également que la distance interparticule est fortement réduite si le tridécanol est le ligand.

Pour chaque échantillon, des expériences de ^{59}Co IF NMR à différentes températures ont été réalisées. En **Figure 4**, les résultats de l'échantillon *NP_4nm_C13* (tridécanol comme ligand et Ø 4.4 nm) sont présentés comme exemple. Une première observation concerne la position du pic principal des spectres (**Figure 4** a)), qui indique une structure Co *hcp*. La fréquence du pic diminue avec la température à cause de la diminution de l'aimantation et donc du champ interne, un effet déjà étudié dans la littérature. La variation avec la température de l'intégrale du spectre permet de tirer des conclusions sur les tailles des NPs dans l'échantillon. En raison de la transition superparamagnétique à ferromagnétique, on considère que seules les particules à des températures inférieures à leur température de blocage (T_B) donnent un signal. Pour les températures supérieures, l'énergie thermique induit un basculement du moment magnétique de la particule, qui est plus rapide que le temps de mesure de la ^{59}Co IF NMR. Cette particule semble être superparamagnétique et ne contribue donc pas au signal observé. Si l'on compare maintenant les spectres observés à deux températures différentes (T_x et T_y par exemple), on peut en tirer des informations différentes. Comme les spectres à T_x et T_y correspondent au signal de toutes les particules dont la T_B est inférieure à T_x et T_y, respectivement, la soustraction des deux spectres représente le signal de toutes les particules ayant une T_B intermédiaire.[7] La valeur de T_B peut être liée à un volume critique de particule théorique *via* le temps de relaxation de Néel [8] pour des particules Co *hcp* isolées, ce qui permet d'estimer la distribution de tailles dans l'échantillon.

En **Figure 4** b), l'évolution de l'intensité de l'intégrale du spectre avec la température est représentée en bleu. On voit que globalement l'intensité diminue avec la température, ce qui est attribué à des NPs de Co qui deviennent superparamagnétique avec l'augmentation de la température. L'axe de volume est déterminé par la relation entre le volume critique et la T_B théorique calculée. Pour comparaison, la distribution de la taille des NPs déterminée par MET est représentée en rouge. La ligne noire représente la fraction volumique cumulée de la taille des particules présentes dans l'échantillon, en partant du volume le plus élevé. En considérant l'axe des températures, cette ligne correspond aux fractions volumiques des particules qui sont bloquées à une température donnée. Toutes les particules dont le volume est supérieur au volume critique à cette température sont suffisamment grandes pour être ferromagnétiques et donner un signal ^{59}Co IF NMR. Toutes les particules dont le volume est inférieur au volume critique sont superparamagnétiques et ne devraient donc pas donner de signal ^{59}Co IF NMR. Si les mesures de la taille des particules par TEM donnaient une image globale parfaite de l'échantillon et que toutes les conditions de l'équation de la relaxation de Néel étaient parfaitement vérifiées, les deux courbes se superposeraient parfaitement. Cependant, on peut voir que l'intégrale ^{59}Co IF NMR diminue plus rapidement avec la température que ce que prédisent les mesures de taille de particules par TEM. La même observation a été faite pour tous les échantillons. Les explications possibles de cette diminution précoce (T_B en-dessous de sa valeur théorique) sont une forme non sphérique des particules ou une phase cristalline Co *hcp* non parfaite, conduisant à une anisotropie magnétique réduite.

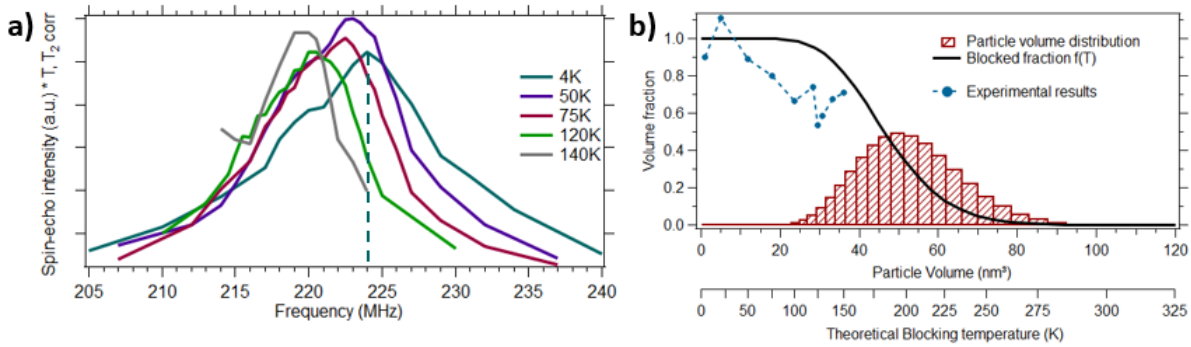

Figure 4: Résultats de l'analyse ^{59}Co IF NMR de l'échantillon *NP_4nm_C13* (tridécanol comme ligand et Ø 4.4 nm) a) Spectre ^{59}Co IF NMR obtenu à différentes températures, corrigé pour le facteur de Boltzmann et la relaxation transverse (T_2) et donc quantitative. b) Comparaison de l'évolution de l'intensité intégrale des spectres ^{59}Co IF NMR à différentes températures (cercles bleus) avec la fraction de particules de Co à l'intérieur des NPs bloquées (ferromagnétiques) (ligne noire), déterminée à partir de la distribution de taille de la fraction volumique des NPs de Co (déterminée par TEM) (barres rouges) *via* l'équation de la relaxation de Néel.

Pour rappel, un des objectifs initiaux de ce chapitre était d'expliquer pourquoi la T_B était au-dessus de sa valeur théorique. Ceci a été observé par ^{59}Co IF NMR pour des particules de Co à l'intérieur de matériaux de batteries à réaction de conversion. Cette observation n'a absolument pas été confirmée dans les expériences de ^{59}Co IF NMR réalisées sur des particules colloïdales, ce qui peut s'expliquer par le fait que les particules ne sont pas en contact. Par conséquent, seules des interactions faibles existent entre les particules, alors que les particules à l'intérieur des matériaux de la batterie sont potentiellement en contact avec des interactions fortes entre elles. Les interactions faibles peuvent néanmoins réduire l'anisotropie magnétique des particules dans certains cas [9], ce qui pourrait également expliquer la réduction de la T_B des particules colloïdales. La raison de ce phénomène n'est cependant pas entièrement comprise. Des informations quantitatives sur l'influence des interactions entre les particules n'ont pas pu être déterminées ici.

[1] A. S. Andreev, J.-B. d'Espinose de Lacaillerie, O. B. Lapina, and A. Gerashenko, "Thermal stability and hcp–fcc allotropic transformation in supported Co metal catalysts probed near operando by ferromagnetic NMR," *Phys. Chem. Chem. Phys.*, vol. 17, no. 22, Art. no. 22, 2015, doi: 10.1039/C4CP05327C.

[2] M. C. Cadeville and C. Lerner, "On the electronic structure of interstitial transition-metal based alloys with boron and carbon impurities: Part I. Experimental study," *Philos. Mag.*, vol. 33, no. 5, Art. no. 5, May 1976, doi: 10.1080/14786437608221917.

[3] K. Hiraoka, A. Oota, and H. Jinushi, "NMR and Magnetic Studies of Mechanically Alloyed Co $_{75}$ C $_{25}$," *J. Phys. Soc. Jpn.*, vol. 77, no. 7, Art. no. 7, Jul. 2008, doi: 10.1143/JPSJ.77.074705.

[4] Y.-P. Pei *et al.*, "High Alcohols Synthesis via Fischer–Tropsch Reaction at Cobalt Metal/Carbide Interface," *ACS Catal.*, vol. 5, no. 6, pp. 3620–3624, Jun. 2015, doi: 10.1021/acscatal.5b00791.

[5] R. Hergt, S. Dutz, R. Müller, and M. Zeisberger, "Magnetic particle hyperthermia: nanoparticle magnetism and materials development for cancer therapy," *J. Phys. Condens. Matter*, vol. 18, no. 38, pp. S2919–S2934, Sep. 2006, doi: 10.1088/0953-8984/18/38/S26.

[6] P. Poizot, S. Laruelle, S. Grugeon, L. Dupont, and J.-M. Tarascon, "Nano-sized transition-metal oxides as negative-electrode materials for lithium-ion batteries," *Nature*, vol. 407, no. 6803, Art. no. 6803, Sep. 2000, doi: 10.1038/35035045.

[7] Y. Liu *et al.*, "Sampling the structure and chemical order in assemblies of ferromagnetic nanoparticles by nuclear magnetic resonance," *Nat. Commun.*, vol. 7, no. 1, Art. no. 1, Sep. 2016, doi: 10.1038/ncomms11532.

[8] C. de Julián Fernández, "Influence of the temperature dependence of anisotropy on the magnetic behavior of nanoparticles," *Phys. Rev. B*, vol. 72, no. 5, Art. no. 5, Aug. 2005, doi: 10.1103/PhysRevB.72.054438.

[9] S. Mørup and E. Tronc, "Superparamagnetic relaxation of weakly interacting particles," *Phys. Rev. Lett.*, vol. 72, no. 20, pp. 3278–3281, May 1994, doi: 10.1103/PhysRevLett.72.3278.

RÉSUMÉ

Contrairement aux techniques classiques de RMN, la RMN du champ interne (IF), également appelée RMN ferromagnétique (FNR), ne nécessite pas l'application d'un champ magnétique externe constant, car le champ interne présent dans les composés ferromagnétiques suffit à polariser les spins nucléaires. Elle permet d'étudier simultanément la structure cristalline, l'environnement local du cobalt et la structure magnétique des matériaux contenant du cobalt. Par conséquent, elle peut être appliquée pour caractériser tous les différents types de matériaux contenant du Co, qui sont des matériaux importants dans de nombreuses applications de la société moderne. Dans ce travail, nous avons étudié une grande variété de structures, avec le but ultime d'évaluer le potentiel de la RMN IF pour étudier le cobalt dans les matériaux de batterie.

Le premier système d'intérêt étaient des composites Co-C produits par mécanochimie pour l'hydrogénation du carbone (CHG). La RMN ^{59}Co IF a notamment permis d'analyser l'évolution des différents intermédiaires Co-C (solution solide Co/C & Co_3C) présents à l'intérieur de l'échantillon tout au long de la réaction CHG. Une relation directe entre la quantité totale d'intermédiaires Co-C et la vitesse de la réaction CHG a été trouvée, ce qui signifie que la formation de la liaison Co-C est l'étape déterminant la vitesse.

Le second système était une structure constituée de nanobâtons de Co parallèles. Outre la détermination de la structure cristalline, une nouveauté de ce travail est la détermination de la structure de la paroi du domaine magnétique à l'intérieur du fil par la variation de l'orientation entre le champ d'excitation RMN et l'axe du fil. L'analyse RMN IF du ^{59}Co a prouvé que ce n'est pas seulement la géométrie du bâton et sa phase cristalline qui sont responsables de la structure magnétique, mais aussi la taille et la qualité des cristallites.

Enfin, des assemblages modèles de nanoparticules de Co ont été étudiés. La RMN IF a fourni une vue d'ensemble des structures cristallines des particules à l'intérieur de l'échantillon. En outre, la transition superparamagnétique - ferromagnétique à la température dite de blocage (T_B) permet de déterminer la taille des particules. Au cours de l'analyse des nanoparticules de cobalt dans les matériaux de batteries à réaction de conversion, il a été observé dans certains cas que les nanoparticules de petite taille présentent un signal ferromagnétique au-dessus de leur T_B théorique, ce qui pourrait être expliqué par des interactions entre les particules. Lors de l'étude d'assemblages modèles compacts de nanoparticules de Co, aucune augmentation de la T_B n'a été observée, ce qui met en évidence la différence entre l'effet des interactions faibles et fortes entre les particules.

MOTS CLÉS

IF NMR, FNR, cobalt, nanomagnétisme, nanoparticules, nanobâtons, catalyse, carbure de cobalt, batteries

ABSTRACT

In contrast to classical NMR techniques, internal field (IF) NMR, also called ferromagnetic NMR (FNR) requires no applied constant external magnetic field as the internal field present in ferromagnetic compounds suffices to polarize the nuclear spins. It allows to simultaneously study the crystalline structure, the local Co environment and the magnetic structure of cobalt containing materials. As a result, it can be applied to characterize all different kinds of Co containing materials, which are important materials in many applications of the modern society. In this work, the initial goal was to assess the potential of IF NMR to study cobalt in battery materials but, as a preliminary, a large variety of structures has been studied to assess clearly the potential of the method.

The first system of interest was Co-C composites produced by ball milling under a hydrogen for carbon hydrogasification (CHG) was studied. Amongst others, ^{59}Co IF NMR allowed to analyze the evolution of the different Co-C intermediates (Co/C solid solution & Co_3C) present inside the sample throughout the CHG reaction. A direct relationship between the total amount of Co-C intermediates and the CHG reaction rate was found, meaning that the formation of the Co-C bond is the rate determining step.

The second system was a structure made of parallel Co nanowires. Besides the determination of the crystalline structure, a novelty of this work is the determination of the magnetic domain-wall structure inside the wire by variation of the orientation between the NMR excitation field and the wire axis. The ^{59}Co IF NMR analysis proved that it is not only the wire geometry and its crystalline phase that are responsible for the magnetic structure of the wire, but also the crystallite size and quality.

Finally, model assemblies of Co nanoparticles were studied. IF NMR provided a sample-wide overview of the particle crystalline structures inside the sample. In addition, the superparamagnetic – ferromagnetic transition at the so-called blocking-temperature allows to determine the particle size. During the analysis of cobalt nanoparticles inside conversion reaction battery materials, it has been observed in some cases that small sized nanoparticles exhibit a ferromagnetic signal above their theoretical blocking temperature, which might be explained by particle interactions. During the study of close-packed model assemblies of Co nanoparticles no increase of T_B was observed, highlighting the difference between the effect of weak and strong particle interactions.

KEYWORDS

IF NMR, FNR, cobalt, nanomagnetism, nanoparticles, nanowires, catalysis, cobalt carbide, battery